TECHNISCHEN UNIVERSITÄT MÜNCHEN
Fakultät für Elektrotechnik und Informationstechnik
Lehrstuhl für Nanoelektronik

PRINTED COMPONENTS FOR ORGANIC OPTOELECTRONICS

Aniello Falco

Vollständiger Abdruck der von der Fakultät für Elektrotechnik und Informationstechnik der Technischen Universität München zur Erlangungen des akademischen Grades eines

Doktor-Ingenieurs (Dr.-Ing.)

genehmigten Dissertation.

Vorsitzender: Prof. Dr.-Ing. Wolfgang Kellerer

Prüfende der Dissertation:

1. Prof. Paolo Lugli, Ph. D
2. Prof. Luca Larcher, Ph. D, Università degli Studi di Modena e Reggio Emilia, Italien

Die Dissertation wurde am 29.09.2016 bei der Technischen Universität München eingereicht und durch die Fakultät für Elektrotechnik und Informationstechnik am 21.10.2016 angenommen.

To my parents, Giovannino and Orsola,
To my brother, Luigi,
To my other half, Angela.
And to my first half, me.

"The game of science is, in principle, without end. He who decides one day that scientific statements do not call for any further test, and that they can be regarded as finally verified, retires from the game."
- Karl Popper

Abstract

Deutsch

Ziel dieser Arbeit ist die Anwendung von Organische Elektrische Bauelemente in der Neuroelektronik, sowohl in vivo wie in vitro. Der erste Schritt ist die Entwicklung von Organische Fotodioden (OFD) auf beliebige Substrate. Der entwickelte Prozess ist frei von Verdampfungsprozesse. Diese Eigenschaft erlaubt die Herstellung von OFDs ohne Einschränkung der Konfiguration oder Form. Nachfolgend würde die Stabilität in Luft Atmosphäre ohne Verkapselung, mit einer Standard Glass/Harz Verkapselung und mit einer Neuartiger Feuchtigkeit- und Sauerstoffbarriere, geprüft. Desweiterem würde die Degradierung der Elektroden, über die Zeit, als einer der Hauptfaktoren identifiziert, die für die Reduzierung der Lebensdauer verantwortlich ist. Um die Eiwendbarkeit der OFDs in physiologischen Medium zu prüfen, müsste die Biokompatibilität der Metallelektroden erforscht werden. In Folge dieser Untersuchungen wurde bewiesen, dass die Verwendung von Polymerische Haftvermittler, sowohl die Biokompatibilität die Langzeitstabilität erhöhen kann. Nachkommend wird der Fokus, auf die Integration von Organische Elektrische Bauelemente in komplexe Systeme, verlagert. In diesem Zusammenhang würden Polarisatoren, im Sichtbarem Lichtspektrum, in OFDs und in Organische Lichtdioden integriert um selbst-polarisierte Licht Emitter und Detektoren zu herstellen. Schlussendlich wird die Vereinigung von 3D gedrückten Objekte und organische Dünnschicht Bauelemente realisiert. Als Machbarkeitsstudie wird eine semitransparente Heizkammer hergestellt entstehend aus eine 3D gedruckte Kammer und eine PEDOT:PSS Schicht.

English

In this work we aim at utilizing Organic Electronic (OE) devices in neuroelectronics applications, in vivo and in vitro. To achieve this goal, we first develop a process for fully-solution processable Organic Photodiodes (OPDs) on arbitrary substrates. This process, free of any evaporation step, allows us to obtain OPDs with any desired shape and in any configuration, with a quick and cost-effective fabrication process. We subsequently analyze the stability of such devices in air, without encapsulation, with classical resin/glass lid encapsulation and with a novel in-line moisture and oxygen barrier. Furthermore, we identify the degradation of the electrodes as one of the main causes for the reduction of the life time of such devices over time. In order to assess the suitability of OPDs in physiological environment, we investigate the biocompatibility of the metallic electrodes employed for their fabrication. Furthermore, we demonstrate how the employment of a polymeric adhesion layer beneath the metal can enhance both the biocompatibility and the stability over time. Successively, we focus on the integration of Organic Electronics in more complex systems. In this context, we embed visible light thin film polarizers in OPDs and OLEDs, in order to obtain self-polarized light emitters and detectors. Finally, we prove the viability of the integration of 3D-Printing and Spray-Deposition, to realize printed objects with organic thin film devices. As a proof of concept, we present a fully printed semi-transparent heating chamber, with a 3D printed well and a spray-deposited PEDOT:PSS layer.

Contents

Chapter 1

Introduction

During the last decade, the field of Printed Electronics (i.e. the branch of electronics based onto the diverse stacking, integration and functionalization of solution processable materials like polymers, nanowires, oxides and quantum dots) has been experiencing a great expansion, due to several characteristics which candidate it as either a low-cost and green substitute of conventional inorganic electronics, or as a big player in the definition of new markets.

The main driver for the attention Printed Electronics has been receiving so far is an intrinsic characteristic of the material there employed: flexibility and softness. The use of polymers or small molecules coupled with nanowires, for instance, can lead to the realization of bendable or conformal light emitting surfaces aimed to general purpose electronics. This aspect has been recently exploited by several consumer electronic companies which presented to the market curved or bendable light sources and displays, based on Organic Light Emitting Diodes (OLEDs). This technology is, however, also attracting the interest of many research fields, traditionally not bound to electronics, such as biology and life sciences in general.

Since 2007, when the term "Organic Bioelectronics" has been coined by Berggren and Richter-Dahlfors [1], the number of biocompatible functional materials and the description of new possible applications has been steadily increasing [2]–[4], and did not lose yet its momentum over the years [5], [6]. In fact, while on the one hand, out-of-the-body applications such as Lab-on-a-Chip or body-motion control devices significantly benefit from the use of OLEDs and Organic Photodiodes (OPDs) [7]–[11], bicompatible, flexible and soft materials have the potential to be used in a wide spectrum of *in-body* applications. In this particular field, Organic Bioelectronic devices have been employed as electrodes or amplifiers for the detection/stimulation of neural signals [3], [12], [13], for the realization of optical prostheses [14], [15] or for flexible sensors able to

monitor pH and single ion levels in a medium, which could be implanted for effective health monitoring [16], [17].
Furthermore, since the election in 2010 of Optogenetics as Method of the year by the prestigious journal “Nature”, [18], the integration of OLEDs and organic electronic devices with living system has been considered as a particularly attractive challenge. While successful attempt of integrating rigid probes with optogenetic system have been recently reported [19], [20], their main limitation, which inhibits them from real clinic applications, is the immune reaction of the brain to such external, stiff objects [21]. Conversely, the employment of soft and flexible organic polymers, has been recently been proved as a viable and effective alternative to conventional electronics because of enhanced functionality and damped immune response [22].
A further stimulus to the growth of the organic electronic research is given by the ease of material production and device fabrication even up to large scale, which could reduce the devices’ cost and extend the availability of point-of-care bioelectronic system also to developing markets [23]. Methods like roll-to-roll [24], ink-jet printing [25], spray deposition [26] and screen printing [27] are leading to the realization of large-scale production lines, with the undiscussed benefit of working at low temperatures, atmospheric pressure and overall relaxed ambient conditions.
The dissertation is embedded within this framework and positions itself on a bridge between the world of biology and nanotechnology, with its overall aim of the realization of devices and processes capable of simplifying the way to organic neuroelectronics: once the concepts are defined, one of the main barriers separating the ideas from real-life applications is the ability to fabricate in a reliable, durable and cost-effective manner the needed devices. While for *in vivo* bioelectronics the main focus is on the *reliable* and *durable* part of the last sentence, for *in vitro* and *point of care* applications it is shifted on the latter part, namely the *cost-effectiveness*.
In order to achieve this ambitious goal, or at least to provide some tools useful for its future fulfillment, the thesis is structured in seven chapters.

Chapter 2, which immediately follows this introduction, is its natural continuation and will give a more in depth view of some of the concepts we briefly mentioned here. First, we will give more details on the world of organic semiconductors, describing the basic phenomena behind their behavior and outlining the main differences with respect to the classical inorganic electronics. We will then give an overview on some of the most used processing techniques, describing the basic working principles, the main advantages and flaws.

Once the potential of flexible and conformal electronics is clear, the question arising is how to fabricate arbitrarily shaped devices on flexible substrates and how to integrate them with complex systems. An attempt at answering this multi-faceted question is done by Chapter 3, where we pursue the goal of fully solution processable organic electronic devices. We will focus on a special kind of device, the organic photodiodes (OPDs), but, by the end of the thesis work it will be clear that the developed techniques can be utilized, in principle, for the realization of any printed electronic device. In the last part of this chapter, we will provide a proof of concept for an OPD deposited on plastic foil and integrated with a digitally custom-tailored printed circuit.

Nevertheless, for the application of any device in a clinical environment, the functionality is, per se, not enough. An essential prerequisite is, in fact, the durability. Organic electronic devices tend to modify their behavior over time, becoming eventually unusable for any practical scope after a relatively short time. Chapter 4 is focused on understanding the degradation phenomena of both functional layers and metal electrodes, proposing integrable and cost effective solutions: the in-line encapsulation of OPDs and adhesion layers to prevent the delamination of metal electrodes.

The last forming block of the thesis, divided in two chapters for practical convenience and topic similarity, can be synthesized by the word *integration*. The scope of Chapter 5 and Chapter 6 is to provide tools able to render easier and more effective the integration of separate parts into an unitarian system.
Particularly, in the former we will discuss the concept of *vertical integration*, in the meaning of monolithic integration of separate devices which in many application work coupled as one. In our particular case, we explored the viability of embedding optical field polarizers in organic optoelectronic devices. Through numerical simulations and practical implementation we will introduce a new class of devices, defined *polarized Organic Photodiodes* and *polarized Organic Light Emitting Diodes* (*pOPD* and *pOLED*, respectively), which are composed by a classical device stack, with the only (major) difference residing in the substitution of a thin transparent electrode with a wire grid polarizer. This latter element, produced *in-house* with a simple soft-lithographic technique, acts contemporaneously as electrode and as selective optical window for the optoelectronic devices.
Chapter 6, on the other hand will we centered on the concept of *horizontal integration*, an idea well embraced by Lab-on-a-Chip devices and consisting in the flawless (and as effortless as possible) integration of different devices which share the same horizontal plane. The idea behind is to simplify the cumbersome techniques used so far to interface organic electronic devices to microfluidic chips, developing a practical framework able to combine the worlds of fast prototyping and organic electronics. We will develop

a method (and build a simple machine) to realize 3D-printed object with embedded organic devices, and with a very limited need for intervention of an human operator. Subsequently, we will briefly describe one of the most fascinating, but at the same time straightforward, applications of such process: the realization of a fully printed perfusion chamber.

Finally, in Chapter 7 we will briefly summarize the main findings of the work, sketching possible strategies to further develop the concepts and processes here described.

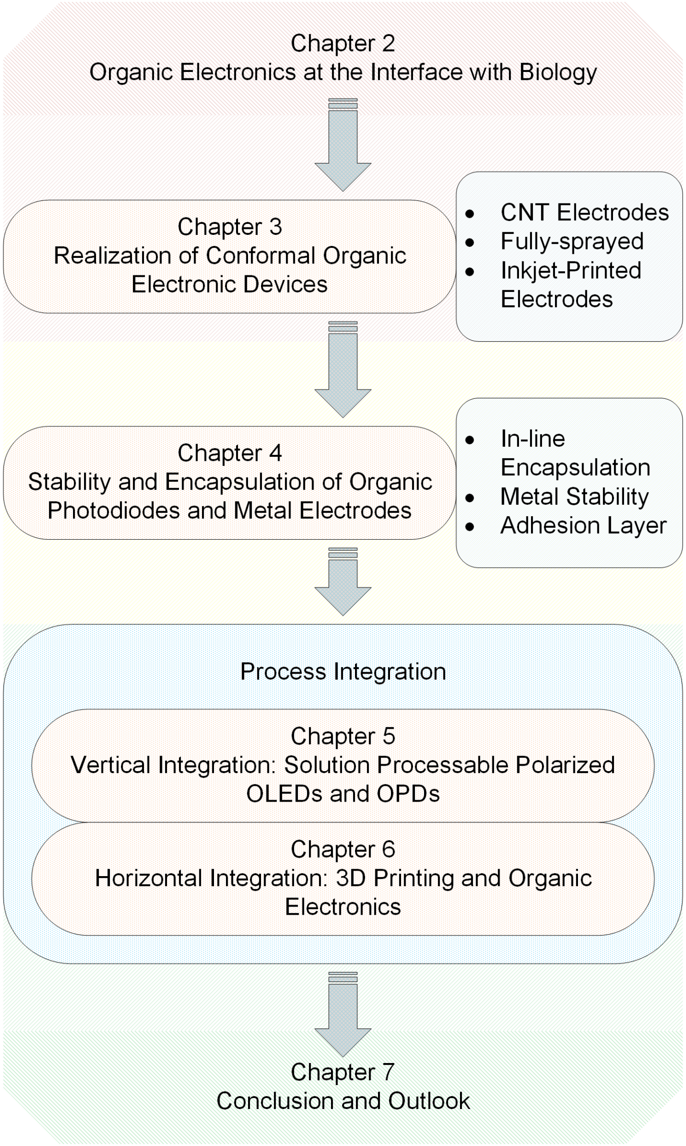

Chapter 2

Organic Electronics

This chapter will give a overview on Organic Electronics, briefly describing the working principles on which organic semiconductors are based and highlighting the biggest advantages and disadvantages with respect to classic, inorganic semiconductors. Among these advantages, one of the most significant resides in the possibility of fabricating organic semiconductor layers with means of solution-based processes: by doing so, Organic Electronics enables the fabrication of flexible and conformal devices, which are of paramount importance for bioelectronics.

In order to better understand the potential of such processing techniques, we introduce two significant examples of successful employment of printed and organic electronics to the life sciences: a flexible wearable patch for health monitoring and an implanted electrode array for the electrical readout of neurons.

The practical fabrication of these devices, is, however, subordinate to the implementation of reliable processes able to deposit arbitrary solution-processable materials onto a number of different substrates. To further clarify how, we will briefly describe three important deposition techniques (namely, spin-coating, inkjet-printing and spray-deposition), which represent the most widely utilized methods for the fabrication of organic devices on a lab-scale.

2.1 Organic Semiconductors

2.1.1 Organic Semiconductors

Organic Electronics is a branch of science and engineering based on the employment of *Organic Semiconductors*, a class of plastic materials (mainly based on carbon and

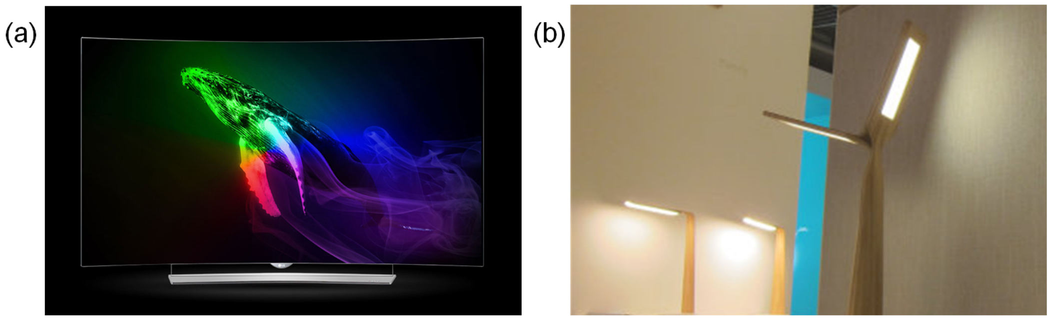

Figure 2.1: Two commercial applications of Organic Electronics (a) a curved AMOLED TV panel produced from LG [28] and a wooden luminary with flat white light produced by (b) OSRAM [29]

hydrogen atoms) with semiconducting characteristics [30]. An early report about the luminescence of some organic compounds dates back to 1906, due to the pioneering work of the Italian researcher A. Pochettino [31], who reported, for the first time, the persistent green luminescence of Anthracene and other molecules. It took, however, until 1963 before the electroluminescence of such materials was exploited in a short but remarkable work by Pope et al. [32], where $10\mu m$ to $20\mu m$ thick Anthracene crystals were connected to silver electrodes and subject to an external field, presenting a marked electroluminescence, although only for voltages higher than 400 V.

The necessity of high operational voltages arose from the elevated thickness of the crystals, which at the same time yield a poor reproducibility of the results. At the beginning of the 1990, nevertheless, organic macro-molecules were substituted by conjugated polymers (e.g PPV), which presented two substantial advantages: they have an higher electroluminescence efficiency, and they can be easily deposited from solution. For instance, in the work of Burroughes et al. [33], $100nm$ PPV thin films were obtained on top of a semi-transparent ITO glass via spin-coating deposition technique; the devices were completed by the evaporation of a reflective Al-layer and presented a strong electroluminescence in the yellow-green region of the spectrum, already activated below $15V$.

A further stimulus for the development of organic materials and their employment in electronics came in 1977 with the first demonstration of electrical conductivity in Doped Polyacetylene by Heeger, MacDiarmid, and Shirakawa [34], awarded in 2000 with the Nobel prize in chemistry [35]. Indeed, with the conjunct use of organic semiconductors and organic conducting polymers, it has been possible, in the last decades to obtain a number of products and devices which would have been sharply limited in performances, if not impossible to realize, such as active matrix (O)LED displays [36] or flexible and conformable solar cells [37].

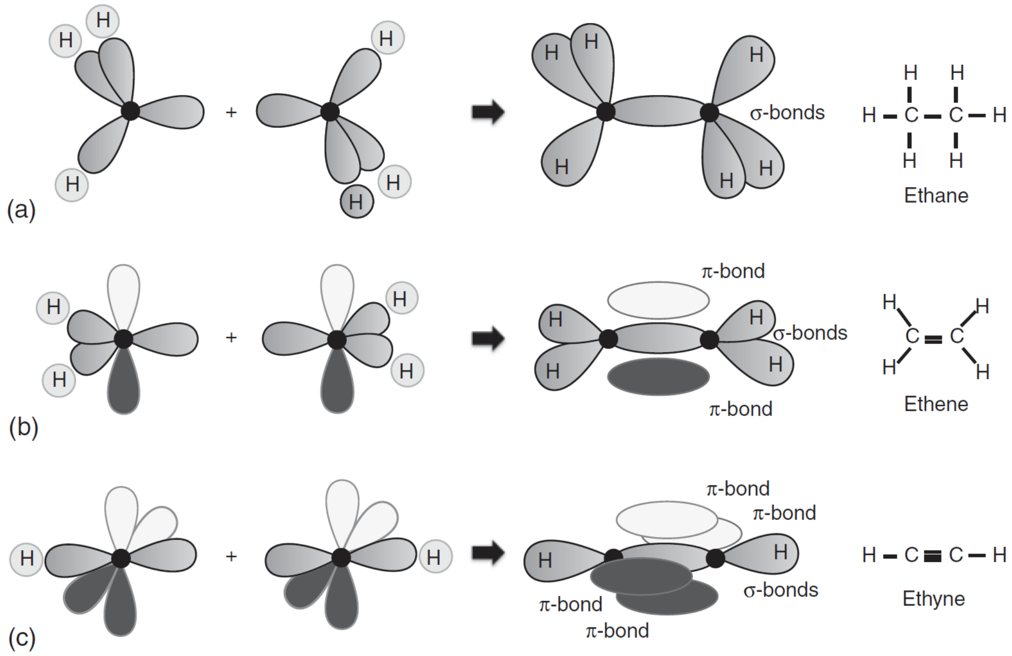

Figure 2.2: Molecular structure and hybridization states of Ethane (a), Ethene (b) and Ethyne (c), with the $\sigma-$bonds depicted in light gray and the different states of $\pi-$bonds are in white and dark gray, respectively. Figure extracted with permission from the book *Electronic Processes in Organic Semiconductors, An Introduction* [30]

2.1.2 Conjugated Polymers

The main building block of organic semiconductors is constituted by carbon and hydrogen atoms, which do not possess intrinsic conducting or semi-conducting properties. Nevertheless, the insertion of these atoms in more complex molecules yields to a process (defined as *hybridization*) which leads to the formation of free charge.
Carbon, in its ground state, has six electrons arranged in a $1s^2 2s^2 2p_x^1 2p_y^1$ configuration, which is the most energetically stabled for an insulated carbon atom, and renders the atom prone to constitute two covalent bonds. This number could be increased to four in case it was possible to provide the necessary energy for the promotion of one of the 2s electrons to the free 2p state, (say $2p_z$). This condition is met in almost any practical case, hence, whenever carbon is placed in contact with any other species, the energy provided to the atom is enough to remove the electron from the 2s state, creating a new *hybrid* energetic configuration, where the 2s and the 2p orbitals interfere. To mathematically represent this interference, also known as *hybridization*, a new orbital description is introduced, with the notation sp, sp^2 and sp^3 is used when two, three or all four orbitals are involved, respectively. This process is schematically represented in Figure 2.2 [30], where all the possible hybrid states are described for very simple

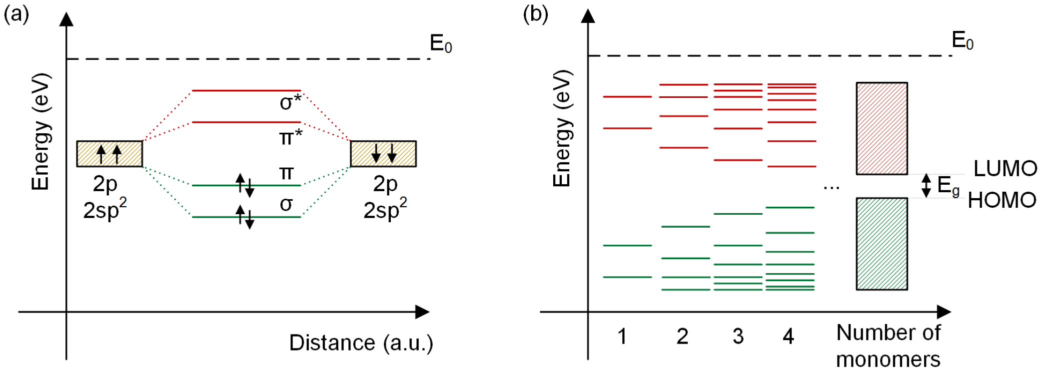

Figure 2.3: Panel (a) shows the formation of bonding and anti-bonding states for π and σ carbon bonds. The drawing in panel (b) represents the formation of band structures and band gap in polymers, as described by van Mullekom et al [38]

organic molecules only based on C and H atoms: Ethane, Ethene and Ethyne.
In the first case, the three H atoms will bond to three of the hybrid states, while the last valence electron will create a σ-bond between two C atoms. All the bonds of the Ethane molecule are characterized by the alignment of the wavefunction of each electron over the axis connecting two atoms and bring to the formation of *σ orbitals*.
However, the bonds occurring in Ethene and Ethyne are of a different nature. Consider, for example, the former case: since each carbon atom is bond to three other atoms, the hybridization configuration will be sp^2 and will yield in the formation of three sp hybrid orbitals, leaving still one free $2p_z$ orbital. Two of former will connect to the H atoms, while the third one will constitute a σ-bond with the correspondent sp^2 orbital of the carbon atom. The remaining $2p_z$ orbitals (one per each carbon atom) are disposed orthogonally to the molecular axis and will form a so called $\pi-$bond, where the wavefunctions of the shared electrons are distributed above and below the axis. This kind of bond is weaker and the electrons cannot be attributed to one of the two C atoms, forming a delocalized state.
It must be noted that, regardless from the kind of bonding, from a mathematical point of view, the formation of any molecular orbital is the linear combination of two wavefunctions, which can lead to constructive or destructive interference. The former, characterized by a higher charge density, is defined as *bonding state*, and has an intrinsic bonding behavior. In the latter case, however, the repulsion of the atomic nuclei is only mildly shielded by the low charge density, and for this reason this state, also solution of the Schrödinger equation, is defined as *antibonding state* and in standard notation is indicated with an asterisk [30].

The presence of these two co-existent states is the fundamental reason behind the semi-

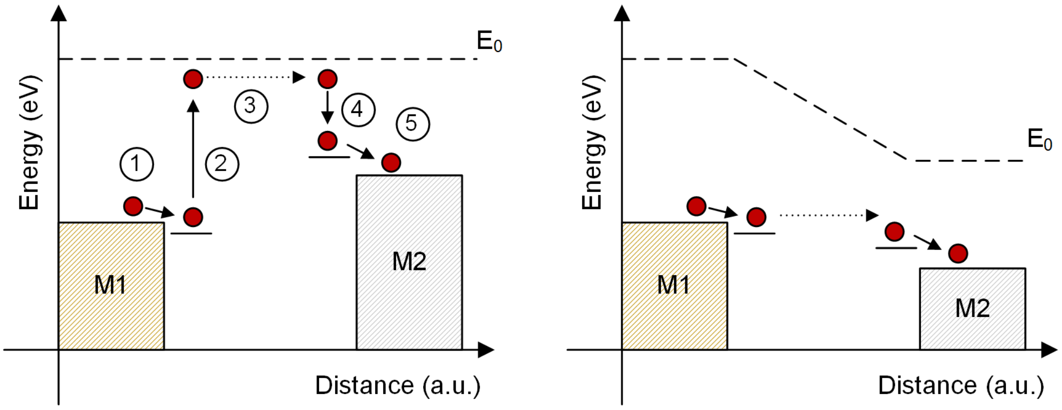

Figure 2.4: Schematic representation of the phonon assisted hopping in absence (a) or presence (b) of an externally applied electric field

conducting in organic molecules: at the thermodynamical equilibrium, and in absence of external forces, for each bond there will be an energy range composed of bonding states only and one composed of anti-bonding only. The bonding states, given the positive interference of the wavefunctions, will have a high probability of being occupied by electrons, while the anti-bonding states will have a high probability of being unoccupied.

Connecting a replica of this molecular structure to the original one, in theory, should result in the appearance of duplicate bonding and anti-bonding states at the same energetic level. However, because of the Pauli's exclusion principle, the states will be subject to a slight mismatch: as shown in Figure 2.3 (b), increasing the number of single cells will result in a band-like structure, where the final energetic difference between the highest bonding state and the lowest anti-bonding state can be seen as a band-gap. Since the top of the *Valence Band* is the molecular orbital of the highest bonding state, we will refer to it as *Highest Occupied Molecular Orbital (HOMO)*, while the bottom of the *Conduction Band*, being the lowest anti-bonding state, will be referred to as *Lowest Unoccupied Molecular Orbital (LUMO)*

Nevertheless, given the limited number of repeatable cells for energetically stable molecules, the density of available levels is rather low, especially if compared to inorganic semiconductors. As a result, the description of the phenomena happening in organic electronics in terms of band structures and band gap is not physically accurate, although it can be employed for the empirical qualitative description of most of the "macroscopic" devices.

2.1.3 Conduction Mechanism

As just described, the repetition of simple organic structures as the ones we just described, also known as *monomers*, result in the alternation of π and *sigma* bonds, with the formation of a high number of repeated delocalized states and the insurgence of many “free” carriers. This leads to the formation of a quasi-band structure and to the possibility of one-dimensional conduction throughout the polymeric chain. However, since the low number of available states and the disordered nature of a polymeric system, the description of charge transfer with means of a simple drift-diffusion mechanism is correct in a first approximation, but physically immotivated.
A more accurate description of the conduction process in disordered solids, known as *hopping*, is provided by a work of Miller and Abrahams [39], where the transport of charge from a localized impurity state to a neighboring one is analyzed and mathematically modeled. In this model a charge carrier trapped into a state with an energy E_i, can move to another state with energy E_j (without lack of generality, consider $E_i < E_j$) only in presence of an external work, which can be provided via thermal or electrical excitation. The derived model describes the *hopping rate*, i.e. the probability of an hopping event to happen, as follows:

$$\nu = \nu_0 \nu_{ext}(E_{ext}) exp\Big(-2\alpha R - \frac{E_j - E_i}{k_B T}\Big) \tag{2.1}$$

Where ν_0 is the maximum hopping rate, ν_{ext} is a term which takes in account the externally applied electric field, R is the spatial distance between the two states and α is the tunneling decay characteristic constant. The amount of transfered charges along the chain, hence, is influenced by how far away on the polymeric chain the delocalized sites are and from their energetic difference. The dependence from temperature is typical for *phonon assisted* conduction mechanisms, where, because of thermal agitation, a phonon can transfer energy to a charge carrier: when the “excited” electron reaches the energetic level of the free neighboring state, a quantum tunneling process is possible and the electron reaches the target state. This process is represented in Figure 2.4 in absence (a) and presence (b) of an external electric field. In the example, two metals with different work functions are separated by two localized states. The drift of an electron from Metal 1 to the first trap state is energetically favorable and happens spontaneously. When a phonon with sufficient energy impacts the electron, its energetic level can be higher than the the level of the second trap state: in these conditions, quantum tunneling is possible. After tunneling, the carrier will be spatially localized in proximity of the second trap state, but, in general, at higher energy; the extra energy

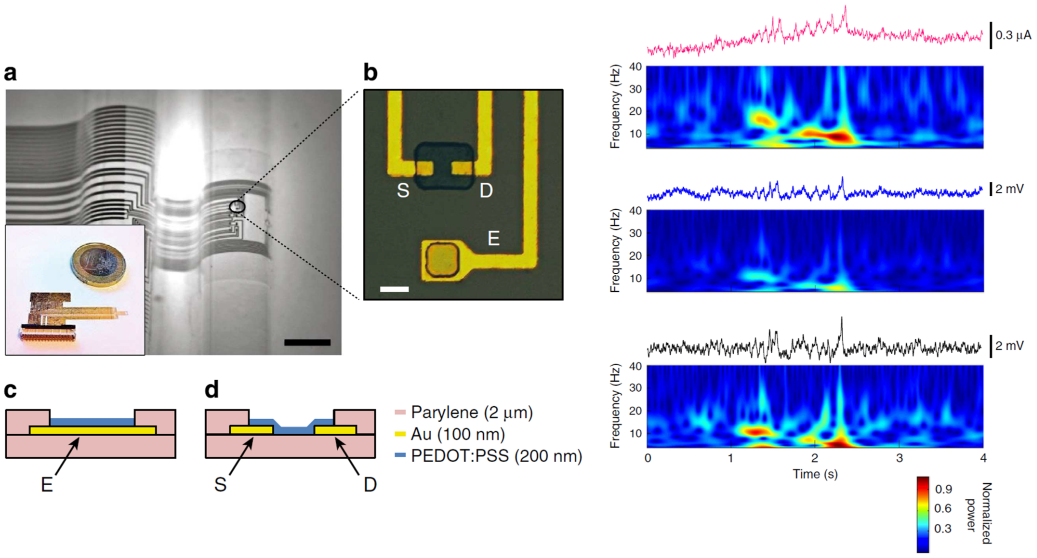

Figure 2.5: (a) Optical micrograph of the flexible transistor array, the scale bar indicates 1 mm. (b) A zoomed micrograph of the electrolyte-gated transistor, with its golden source and drain electrodes, and the PEDOT:PSS semiconducting layer, and a reference electrode, used as comparison to validate the use of a transistor structure over a simple electrode. (c) and (d) are the cross-sectional views of the electrode and the transistor, respectively. The three panels on the right are spectrograms of the same signal sensed from the OECTs (top), the passive electrodes (middle) and Ir-penetrating electrodes (bottom). Figures extracted from the work of Khodagholy et al. [12], CC BY-NC-ND

is released (*thermalization*) and the electron will reach the trap level.

In case an external field is applied, the energetic difference between the two states can be reduce, or even become negative, which will result in enhanced hopping probability, since the electron transfer can happen already with very low phononic energy. One of the main implications of this complex conduction process, is that the charge transfer within an organic semiconductor is not as fast and as efficient as in the inorganic ones [40]. Length of the polymeric chain, distance between the delocalized carriers, molecular weight, are only some of the parameters which affect the conductivity of such materials, and this big availability of degrees of freedom is at the same time one of the great potentials of Organic Electronics, and one of its stronger limits.

2.2 Organic Bioelectronics: Two Case Studies

2.2.1 Printed Electronics at the Interface with Biology

In this section we will see, throughout two main examples, how the employment of the methods of Organic and Printed Electronics in bioelectronics enables the realization of

novel important devices.
The first application is constituted by the work of Khodagholy et al. [12], who developed a flexible and conformal electrolyte-gated transistor array for the detection *in vivo* of brain signals. The transistors, obtained with a thin layer of cross-linked PEDOT:PSS and Au source and drain electrodes, were fabricated on a $2\mu m$ thick plastic film (Parylene C), which was employed both as substrate and passivation layer. After the thin film system was fabricated, it was implanted in the skull of living rats, to evaluate its capability of detecting brain very dim electrical oscillations in the neurons potentials, which, if characterized by a certain shape, frequency and amplitude, could indicate brain distress, and even the insurgence of epileptic seizures. The organic electrochemical transistors, were compared to reference Au electrodes (which until then were the only flexible detection technique available for this kind of signals) and to state-of-the-art rigid Ir-penetrating probes. The latter, although providing a high Signal to Noise Ratio (SNR), and a rich electrophysiological signal, are fabricated with not entirely biocompatible materials and, being rigid, can procure cuts and severe damage into living and moving animals.
The overall results, presented on the right side of Figure 2.5 show how the PEDOT:PSS transistors have a SNR and an harmonic content comparable to the one of the state-of-the art electrodes and significantly better than the golden electrodes. Furthermore, since they are fabricated via standard lithography techniques on foil, the plastic-based OECTs are conformal and the array can be designed in arbitrary shapes. Any desired number of transistors could be integrated and employed, for instance to be used for in vivo high resolution electrophysiological activity monitoring. Finally, given the possibility of tailoring the characteristics of organic semiconductors, the transistor array could be extended with the employment of differently functionalized films, in order to simultaneously detect different quantities, like pH and glucose. Such a multi-purpose device could be a “neuroelectronic swiss knife” employable for both basic research (e.g. in the understanding of the signaling mechanisms which take place in the brain) and life-savers applications (e.g. detection of epileptic seizures).

The second application we briefly review is a *smart bandage*, developed by Honda et al. [41], and it is represented in Figure 2.6. It is a complex multilayered system which integrates a temperature sensor, a capacitive touch sensor, a wireless coil for the transmission of the data and a drug dispensing pump, hence integrating sensing and actuating capabilities. The interconnecting lines and electrodes were realized by printing Ag ink, while the temperature sensor has been obtained with a mixture of PEDOT:PSS and Carbon Nanotubes. The different foils were laminated together and

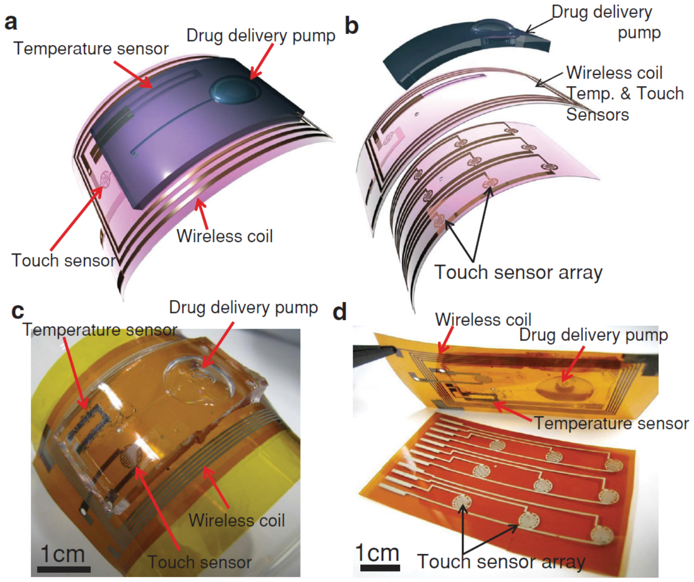

Figure 2.6: Several views of the design and fabrication of a flexible smart bandage with printed temperature sensor, touch sensor, wireless coil and drug delivery pump. The fabrication has been carried out without any lithographic process and the vertical integration has been achieved with means of foil lamination and laser cuts. Figure reproduced with permission from the work of Honda et al. [41]

the via holes for the connection of each sub-system to the other were performed with means of a laser-cutting machine.

Every part has been obtained by directly on-foil lithography-free techniques, giving to this approach for the fabrication of smart objects the potential of becoming cost effective and highly customizable. Although the single functions implemented in the device are not novel, nor with extraordinary performances, what renders this work of special appeal is the total monolithic integration of the components, while still preserving the single functionality and the structural flexibility.

These two examples, which are remarkably different both in the applied methodologies and in the specific significance, have been chosen to give a direct introduction to the main topics which will be developed in this dissertation: realization of conformal and flexible organic electronics, to provide easy insertion *in* the bodies or *on* the bodies of living animals. Evaluation of the stability and biocompatibility of each material. Horizontal and vertical integration of processes and components. Before the advent of organic bioelectronics, many of these topics were never considered or applied to electronics, and thus require a strong research effort.

However, once the main issues will be solved, it will be possible to design full-body systems, where for instance, an abnormal brain activity is sensed by the OECTs and wirelessly transmitted to a smart armband. This latter subsystem could in turn immediately dispense a drug through microneedles, while contemporaneously saving the event in a log and transmitting it to a physician.

2.2.2 General Advantages and Drawbacks

Some of the main advantages of organic semiconductors over inorganic ones are either evident from these two examples, or have been already introduced in the Introduction. An extensive list of properties and caveats lyes beyond the purpose of this thesis, however, here we propose a short list of important properties (with relative bibliographic references) which will be relevant for our work.

- Mechanical softness and flexibility, which is enables the realization of conformal devices for consumer electronics and for bioelectronics [37], [42], [43].
- Facile and superior spectral tunability of the molecules' bandgap, which allows the realization of arbitrarily emitting and absorbing optoelectronic devices [36], [44].
- Solution processing, which on the one hand relaxes the process constraints [45]–[47] and, on the other hand, allows facile material blending and intermixing [48]–[50].
- Proven biocompatibility and ability to conduct ionic currents, which make them ideal for the applications in bioelectronics [2], [3], [22], [51].
- Low mobilities (especially for electrons) if compared to inorganic semiconductors [40], [52], [53]
- Subject to degradation over time, with progressive degeneration of the core properties, until complete hindering of the functionality [54]–[56]

2.3 Relevant Deposition Techniques

2.3.1 Spin-Coating

As previously stated, one of the main advantages of polymeric electronics is the wide range of processing technology which can be employed for the realization of thin films. One of the biggest breakthrough for the real application of organic devices was, indeed,

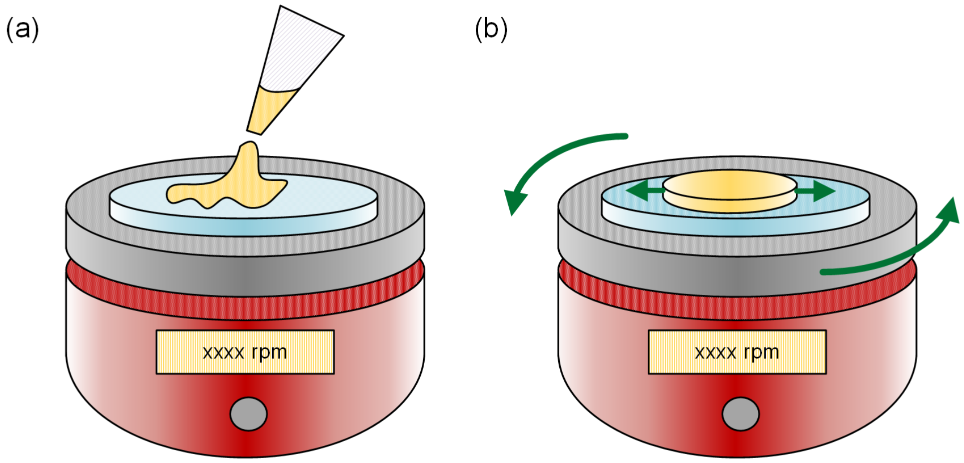

Figure 2.7: The drawing conceptualizes Spin-Coating process: (a) in a first phase the material is dispensed on the sample, then (b) the centrifugal force spreads the liquid over the surface forming a thin film

the demonstration that thin film stacks, with single layer thickness in the range of few hundred of nm, could be built with means of spin-coating [33].

Spin coating is a well-established method for the deposition of thin ($> 200nm$) and ultrathin ($< 200nm$) films, commonly employed for the deposition of polymeric films in the microelectronic industry [57], [58] and successfully applied in a number of processes the organic and printed electronics [47], [59]–[62]. The method, described by the drawings in Figure 2.7, is conceptually simple: the material, in liquid form (from now on also *ink*), is dispensed on top of a sample, which is attached to a chuck with means of a strong air suction. When the dispensing is ultimated (or, in some applications, while it is still in progress), the chuck starts its rotation and, with means of centrifugal forces, the solution is spread across the substrate, leading to the formation of a thin film. The rotation phase (spinning) itself, is composed of different stages: an acceleration time lapse, when the rotating plane is brought to the steady state speed, during which most of the material is flung out from the sample; a second phase where the decided rotation speed is kept for a certain amount of time (typically at least 30 seconds), setting the thickness of the layer; a last segment of time, when the air flow dries out the residual solvent and helps to provide a solid film. Given its simplicity, the technique has been extensively studied, and it is possible to find mathematical models which relate the thickness of a final polymeric layer to the original characteristics of the ink and to the processing parameters (steady state speed, acceleration, deposition time) [63], [64]. The main caveat of spin-coating as process for printed electronics is its inherent lack of up-scaling possibility: the maximum sample size is limited to the chuck size and the radial nature of the phenomena involved contribute to reduce the uniformity of

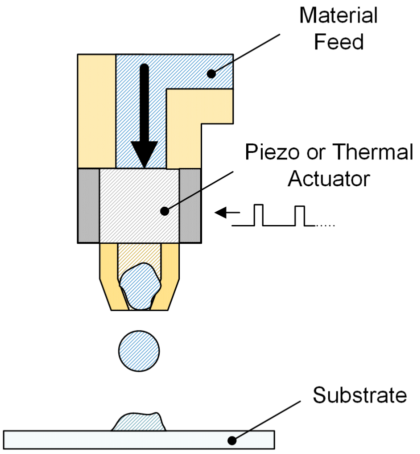

Figure 2.8: In an Inkjet printer, the material is fed through a pipe to an actuator which regulates the injection. The droplet is formed at the nozzle and released towards the surface of the substrate

the position with increasing sample size. Albeit this main limitation, however, it is the most widely employed technique for lab-scale research and development of organic electronic devices.

2.3.2 Inkjet-Printing

While the term “coating" refers to the full coverage of a substrate with a material, the term “printing" involves the definition of pattern or shapes, as in the process of *printing* a text-book or a figure. This concept, not related to conventional, inorganic semiconductors, becomes extremely important in organic electronics, where the preferred process flows is based on the direct fabrication of structures and devices, with the minimal possible amount of post-processing. Inkjet-printing, schematically represented in Figure 2.8 is the technology which, at the current state, better embraces this idea: a computer defined design can be directly transferred to a sample and immediately used as it is or for subsequent deposition steps. Reduced to its most simple dynamics, the working principle of inkjet printing is the following: the desired ink is brought to a *printing head* which contains a small actuator. Whenever a pulse is given to the actuator (which can be based on thermal principles or on piezoelectricity), it will change the dimension of the feeding chamber, gradually modifying it from “totally closed” to “totally open” and then back to the original position. As a result of this perturbation, a well defined amount of material is transfered from the feeding pipes to the nozzle of the injector and, once it is released, is let fall towards the substrate. Moving the printing head along the x and y direction, leads to the juxtaposition of

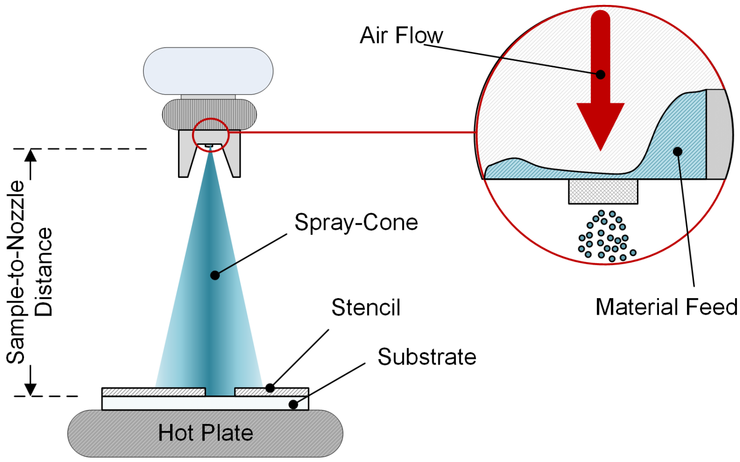

Figure 2.9: The spray gun is set to an well defined distance from a hotplate where the substrate lays on a hotplate. A stencil can be used to define a certain shape. In the chamber, the atomization is obtained with means of a pressurized air flow which impacts the material in the atomization nozzle

tiny droplets which form, in case of correct processing conditions, a closed layer in the desired pattern. Given the high versatility of the method, inkjet printing has been employed in a wide variety of applications [65], ranging from printed photoactive devices [66] to transistors [67], from conductive lines [68] to semi-transparent electrodes [69]. The main disadvantage of inkjet printing, however, is its overall operating speed, and the lack of systems to finely tune the thickness of the obtained layers (besides changing the rheological composition of the ink). Furthermore, since the realization of a complete layer is delegated to the merging of linearly arranged droplets, the printing process is not robust, since in case of malfunctioning injectors, the film will present *holes*, which might hinder the functionality of the printed device [69].

2.3.3 Spray-Deposition

Spray deposition is a fairly established technique for many industrial uses, ranging from the dispensing of glues to the deposition of paints or finish coatings [70]. It has been, however, attracting increasing interest in the world of organic and printed electronics because of some key characteristics, among which we can enumerate the easy up-scalability, the wide choice of employable materials (essentially, any material which can be put in solution) and the fine possible control over the layer thickness (in the range of tens of nanometers) [26], [45], [47], [71]–[76].

The deposition is obtained via *atomization* (i.e. the decomposition in small droplets) of a liquid, with means of a pressurized air flow or vibrating actuators. In the former case, a stream of compressed air (typically nitrogen), impacts the material in solution

and, with means of its kinetic energy, disintegrates the liquid and creates the spray. In the latter case, a piezoelectric plate oscillates in the ultrasound ranges, directly transferring the energy to the fluid, which is dismembered in very fine droplets and directed to the samples with means of a pressurized carrier gas.
However, regardless from the atomization method, the overall concept is similar: the atomized material is forced out from an orifice and assumes the shape of a cone (*spray cone*) which is directed towards a substrate, typically positioned on a heating element. The droplets impact on the surface and, ideally, merge together in such a way that when all the solvent is evaporated an homogeneous closed film is left on the substrate. The quality, thickness and roughness of the deposition are influenced by many parameters, some of which are common to both spray-deposition classes, namely the nozzle-to-sample distance, the temperature of the hot plate and the material flow rate. This last quantity is in turn affected by some method-specific factors; for instance, in the case of air atomizers, schematically represented in Figure 2.9, the atomizing air pressure, the material feed pressure and the nozzle opening are the main responsible for the obtainment of the desired droplets size and distribution [70].
As a matter of principle, for each new introduced material, the parameters have to be adjusted in order to achieve the correct deposition regime. A reliable, although simplified approach, resides in describing three different working regions - wet, dry and intermediate - and chose the most adequate one to the process requirements [75]. The three deposition regimes are defined on the basis of some key characteristics: in a *dry* process, for a given material flow and nozzle-to-substrate distance, either the kinetic energy or the hotplate temperature are too high, and the solvent dries before even reaching the substrate. In these conditions, the layers will be characterized by rough and separated material clusters which seldom form a closed film. The opposite extreme is represented by the *wet* deposition regime: either the kinetic energy of the spray or the temperature of the hotplate are too low, and the resulting layer needs time to dry up, leading to hard-to-control film thickness and roughness. Finally, a so-called *intermediate* deposition regime is achieved when all the parameters are balanced: the droplets reach the substrate when they are still in liquid form, merge with previously deposited material islands and quickly dry up. Working in this deposition regime, the formed layers tend to be close and relatively smooth, and it has been the deposition regime of choice for all the applications presented in this thesis.

Finally, some variations of the *soft lithography* technique will be discussed in Section 5.3 and 6.1, where their introduction is more pertinent, and will not be repeated here.

2.4 Summary

In this chapter we described the working principle of Organic Electronics. After a short historical review, we introduced the concept of molecular orbital hybridization, which is behind the formation of delocalized states in organic materials. Along with it, we discussed the concept of a pseudo-band structure for polymers. Although this simplified model does not take in account all the phenomena occurring on the molecular level, it is accurate enough to empirically describe the effect of macroscopic Organic Electronics. Within this context, we also described one of the most important conduction mechanisms in disordered solids, typically applied to amorphous materials and successfully employed for the modeling of the charge transfer in organic semiconductors.

We then used two examples from previous literature, to describe the width of the application spectrum of organic and printed bioelectronics. The first one is an in vivo application to sense small bioelectrical signals, while the second one is a smart armband with multiple sensing capabilities and a drug dispenser. These two case studies gave an overview of some amongst the biggest advantages of organic and printed electronics, and we used them to compile a short list of important characteristics of organic devices.

Finally, we described three of the fabrication techniques we will use throughout the dissertation: spin-coating, inkjet-printing and spray deposition. The importance of each method is highlighted, along with its drawbacks, and a particular focus is put on the key parameters affecting the quality of spray-deposited films.

Chapter 3

Realization of Conformal Organic Electronic Devices

In the first section of this chapter, we will see the main reasons motivations which render Organic Photodetectors are an outstandingly appealing technology. As seen in Chapter 2, the potential of this devices does not reside only in the possibility to be used as cost effective alternatives of their inorganic counterparts, but in their capability to enable new applications and solve old issues in preexistent market niches. We will discuss how this *enabling capability* of OPDs is related to the inherent characteristics of organic electronic devices: spectral tunability, possibility of fabrication on flexible substrates, assessed biocompatibility.
Subsequently, we will utilize some approximations to describe the behavior of OPDs in terms of “classical" band diagrams, and with means of this simplifications, we will qualitatively present the working principle of such devices. Typical characteristics of OPDs fabricated with a standard material system will be introduced and the most important parameters and figures of merit will be highlighted and explained.

In the remaining part of the chapter, effort will be put to realize devices able to fulfill the needs stated in the premise: the fabricated OPDs must be prepared through easy, green and cost-effective processes; they need to be flexible and conformal, at the same time retaining the original characteristics of the rigid OPDs; finally, they have to be realizable in arbitrary shapes and design, and integrable in more complex systems which can be, eventually, used in the field of bioelectronics.

3.1 Need for Conformal Photodetectors

3.1.1 Hybrid Applications of Organic Photodetectors

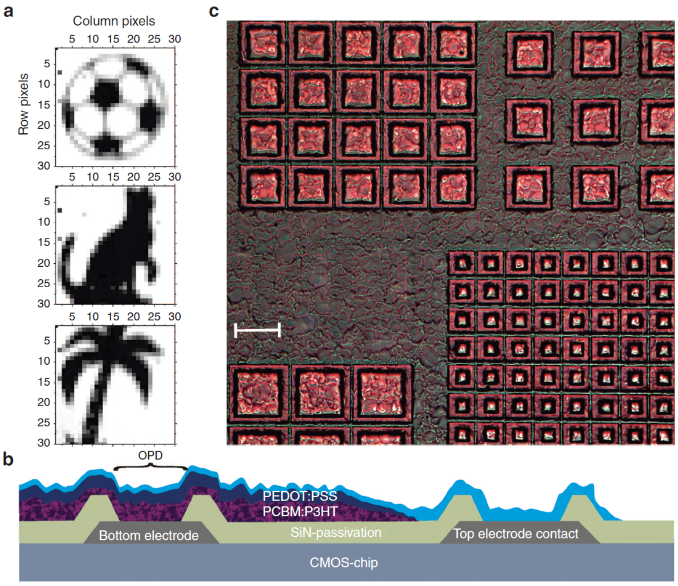

Figure 3.1: The figure has been reproduced with permission from the work of Baierl et al. [77]. Panel (a) shows the low resolution images projected and detected by the hybrid CMOS chip, while panel (c) shows a microscope image of the array with the spray-deposited polymer. Panel (b), finally, shows the cross-section of the device, and the different parts of the chip are there labeled. The OPD is created with an evaporated bottom electrode, a spray-deposited layer of photoactive blend and a conductive polymer on top. The conductive polimer lines are then brought to the “top electrode contact” which is localized outside from the active area of the detector

Photodetectors, are, generally speaking, transducers able to transform light in an electrical signal. Inorganic photodetectors are needed and utilized in a number of applications in science and in consumer electronics, for instance the production of scanners, cameras or ambient light sensors. They are, however, obtained through cumbersome processes and produced on relatively heavy and rigid chips. Furthermore, although there is a wide range of inorganic semiconductors, able to cover every part of the spectrum, their fabrication is normally expensive and their compatibility with the CMOS technology very limited. On the other hand, the molecules used for organic electronics can be synthesized from scratch to obtain a certain absorption in a given wavelength range, and they can be deposited on almost any substrate or lattice. A good example in this direction has been provided by the work of Baierl et al. [77], who investigated the feasibility of an hybrid CMOS light sensor, where the problems related to low pixel fill factor and spectral sensitivity of Silicon were solved by the introduction

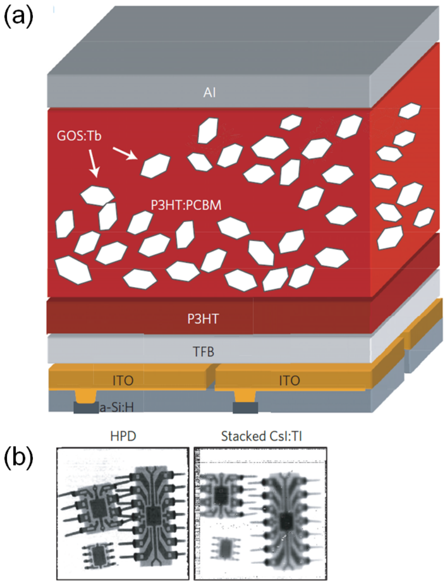

Figure 3.2: The figure has been reproduced with permission from the work of Buchele et al. [78] and presents the single pixel stack (a) and the comparison of an X-rays image acquired with the system proposed by them (b, left hand side image) and a more classical stacked device (b, right hand side image)

of fully-solution processable Organic Photodiodes (OPDs) on top of CMOS chip. The chip was designed and realized in conventional $0.35\mu m$ CMOS technology and included the pixel pads and all the readout electronics. On top of the pixel pads, inverted OPDs were fabricated and characterized, showing full functionality, reproducibility and spectral sensitivity. This proof of concept, although does not create a novel category of devices, is the starting point to understand the potential of the integrability of organic photodiodes with more complex systems. One of the most striking achievements in this direction is the integration of OPDs for the realization of X-Rays detectors on foil [78]–[80]. The main advantages of this technology, besides the cost-effectiveness, are related to the flexible and light-weight nature of both the substrates and the employed materials: the X-Rays detectors are portable and flexible and could be used for an entire new sets of applications. Medical machinery for panoramic radiographies, for instance might be substantially simplified by the employment of these large area, conformable thin film absorbers. In a remarkable work by Buechele at al. [78], it is shown how a scintillator can be integrated into a polymeric matrix to be used as high density X-Rays detector array. The devices were composed by an amorphous silicon backpane with ITO contacts, on top of which the photodetector has been realized: first two polymeric interlayers (needed for the reduction of the dark current) were deposited and then the mixture of P3HT:PCBM (materials photosensitive in the visible range) and GOS:Tb (nanomaterial sensitive to X-excitation) was fabricated through spray-coating. The device was finalized with the evaporation of Al top contacts by thermal evaporation and is summarized in Figure 3.2 (a). Since the scintillator is directly integrated *into* a micrometer thick photodetective layer, the resolution achievable is much higher than the one obtainable with traditional cost-effective technologies, where a scintillator film (usually some hundreds of micrometers thick) is placed on top of a photodetectors backpane. The fabricated 256 x 256 arrays presented very low optical crosstalk and sensitivities comparable to state of the art a-Se direct X-Rays converters, but with far more relaxed constraints on the applied voltage and on the production process. This remarkable result further confirms what had already emerged from the previous work: the integration of organic photodetectors in hybrid structures, more than the complete substitution of conventional electronics, is the key to obtain novel devices with outstanding performances.

3.1.2 Fully Solution Processable OPDs

As emerged from the two examples presented so far, a crucial point for the real-world application of organic photodetectors (and photodiodes in particular) resides in the adaptation of the deposition process and the ability to create OPDs on (almost) any kind of substrates. In both works, the deposition of thin interlayers and thick active materials was obtained through spray-deposition, indicating this method as one of the most versatile to produce working organic devices on preexisting systems. Since the goal of this work was the creation of a framework where the world of neurosciences could be interfaced with bioelectronics through organic optoelectronic devices, the most natural deposition choice for most of the realized devices is spray-deposition.

Spray-deposited OPDs, indeed, can be directly deposited on microfluidic chips, in order to realize fully integrated fluorescent probes for biological markers [7], [81], [82] or directly employed in *in-vivo* implants. The functionality of these implants could be the realization of prostheses, as already stated in the introduction, or as control circuits for optogenetic applications. Figure 3.3 shows one of these possibilities. With means of solution processable techniques it could be possible to print an antenna on a biocompatible tissue and integrate it with a microcontroller. When the antenna is excited by an external tag reader, the microcontroller is activated and provides energy to the OLED in order to start an optogenetic raction. The OLED light intensity, however, is susceptible to phisiological variations, given by the overall conditions of the chip and aging effects: using a well encapsulated OPD, it could be possible to use its photocurrent as a feedback signal to modify the energy provided to the OLED

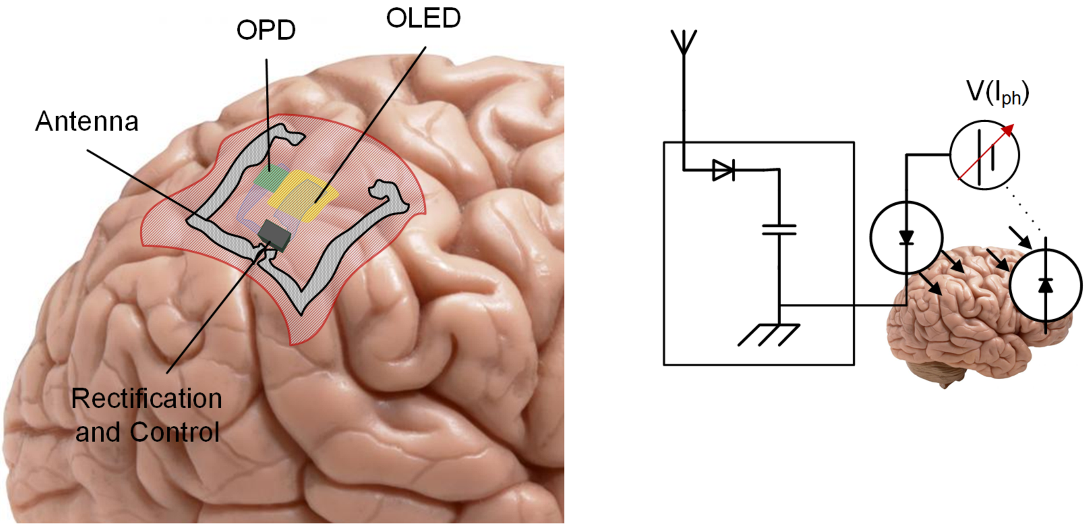

Figure 3.3: The figure shows a conceptual application of a bio-tag fitted with an antenna, a small elaboration unit with rectifier, an OLED and an OPD. When the tag is activated by an external reader, the OLED emits light to initiate an optogenetic reaction; at the same time, the OPD records the light intensity and activates a feedback circuit, to make certain that the required level of illumination is achieved

and obtain safer operational conditions. Through successive optimization processes, at the end of the present chapter, we will demonstrate, through a proof of concept, the feasibility of such devices. The realization and characterization of such device constitute a starting point for the development of more "smart" and integrated flexible chips which denote significant potential in the field of bioelectronics.

3.2 Organic Photodiodes

3.2.1 Working Principle of Organic Photodiodes

As seen in Chapter 2, the world of organic electronics is based on physical phenomena substantially different from the ones regulating the conventional, inorganic electronics. However, up to a certain extent, it is possible to abstract from the atomistic or molecular effects and consider the behavior of the devices on a more macroscopic level. If considered on the whole, an organic electronic device can be described through the classical models which are applied in inorganic electronics, and provide valuable qualitative understanding. Under this directive it is possible to approximate the complex localized states structure of an organic semiconductor as its inorganic counterpart, with the definition of *Conduction Band* and *Valence Band* which assume the names of LUMO and HOMO respectively. With this approximation, the working principle of an OPD

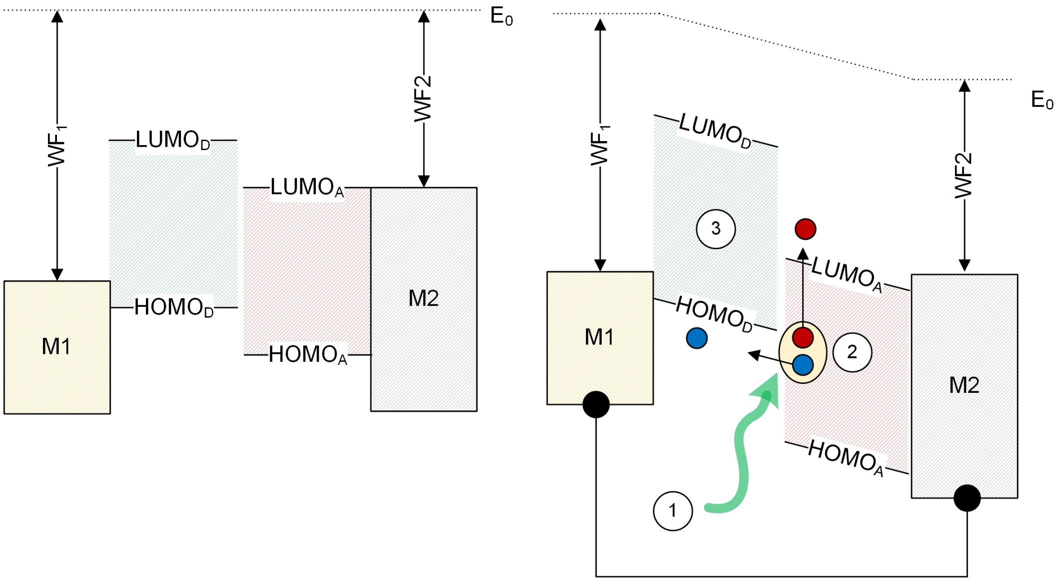

Figure 3.4: Simplified view of an organic photodiode formed with means of one single semiconductor layer at the thermodynamical equilibrium (a) and in short circuit conditions (b). The right hand side of the figure also shows a sequence of the basic phenomena happening: an electron with enough energy is incident on the material (1), the exciton is formed and separated at the interface (2), electron and hole are driven by the built-in field to the respective electrodes (3)

can be explained in terms of band diagrams and the transport can be modeled through familiar drift/diffusion mechanisms.

An organic photodiode is a device composed by the stack of at least four materials: a donor semiconductor, an acceptor semiconductor, a conductor whose work-function is aligned to the the HOMO of the donor (from now on also “anode” or “high work-function electrode”) and a conductor whose work-function is aligned to the LUMO of the acceptor (from now on also “cathode” or “low work-function electrode”) [44], [83]. This structure can be visualized in Figure 3.4 at the thermodynamic equilibrium (a) and when the electrodes are short-circuited (b). The unbalanced electrodes lead to the formation of a built-in potential: in case a photon with sufficient energy will shine on the material and an electron-hole pair is formed and separated, the carriers will flow towards the respective electrode. Differently from inorganic semiconductors, however, where the electron and the hole are immediately separated at ambient temperature, in organic semiconductors, the generated electron-hole pairs are attracted by strong Coulomb attraction. The bounded electron-hole pair is defined as “exciton”, and an energy greater than the binding energy is required in order to separate the carriers [84]. Typical values of the binding energies in organic semiconductors are in the range of some hundreds of eV [85], [86] and can be as high as 1eV, rendering the exciton

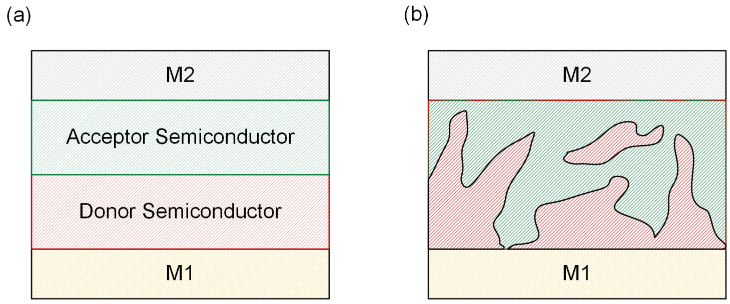

Figure 3.5: Section schematic of a planar heterojunction (a) and a bulk heterojunction (b)

impossible to separate by thermal oscillations at room temperature. Inside a multi-material stack, energy high enough to separate the electron-hole pair can be found at the interface between materials with different ionization potential or electron affinities: in the example sketched above, this would happen only at the interface between the two semiconductors or between one of the semiconductors and anode or cathode. In order to obtain charge separation, then, the exciton must be generated within diffusion length from one of the three interfaces. Measured values for the diffusion length of excitons in organic semiconductors is in the order of 10 nm [87], which renders the conversion efficiency of a single semiconductor layer photodiode very poor because of two competing effects: to maximize the absorption of light (which is regulated by the Lambert-Beer law), the thickness of the active layer should be increased as much as possible; but the thicker the absorber layer, the smaller is the fraction of excitons generated within diffusion length from one of the interfaces.

3.2.2 Bulk Heterojunction

A natural evolution of this concept resides in the idea of *Bulk Heterojunction (BHJ)* [88]. In a BHJ, the two semiconductor materials are mixed in the liquid phase, in order to create an interpenetrated network. When the layer is fabricated and the solvent dried up, the resulting layer will be a composite made of many nanometer-sized domains of the donor and the acceptor, leading to a multitude of consecutive interfaces. The number of the domains will strongly influence the separation efficiency, while their size will affect the collection efficiency. There is, hence, a trade off on the size of the two different phases, and working on how the solution is prepared, or how the layer is deposited an dried, is considered to be a promising research field to enhance the efficiencies of photodetectors [44], [89], [90]. A schematic of the BHJ is presented in Figure 3.5: given the elevated number of junctions, regardless from where in the sample

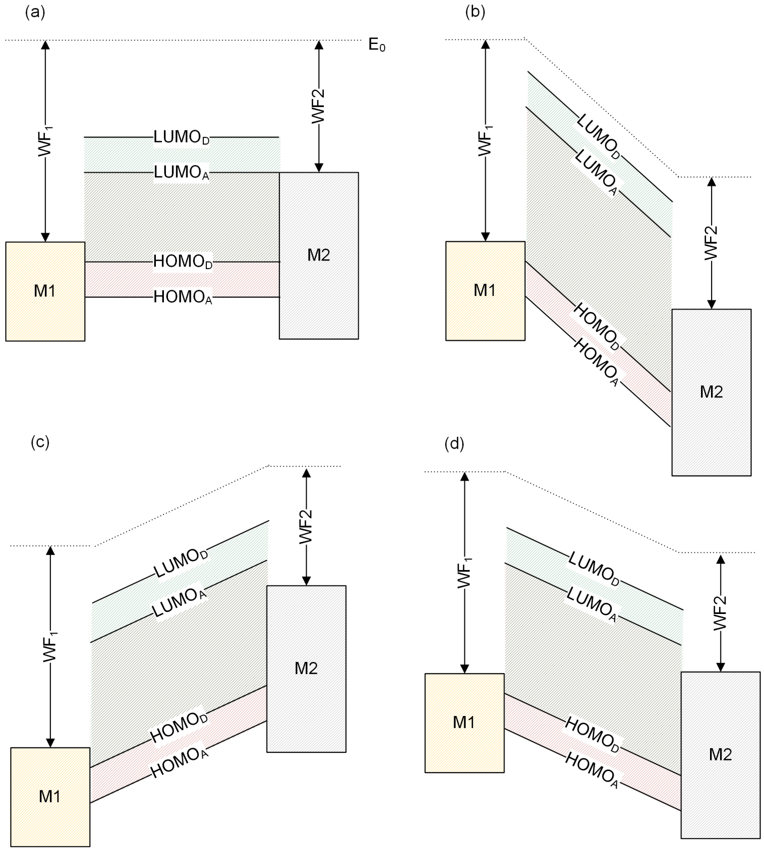

Figure 3.6: Bulk heterojunction under different bias conditions: open circuit (a), reverse bias (b), forward bias (c), short circuit (d)

the photon is absorbed, the exciton can easily reach an interface and be separated. Once the separation efficiency is optimized, it can be safely assumed that, even at ambient temperature, all the excitons are separated and the carriers can be considered as free electron and hole. In this condition, the behavior of a BHJ organic photodiode can be studied with the band structure analogy, where the HOMO/LUMO level of the donor and the acceptor are spatially overlapping.

Figure 3.6 shows the band structure of a BHJ under different voltage biases. When a negative voltage is applied to the anode (b), in dark condition, the charge transfer from anode to cathode or vice versa is energetically non-favorable. However, if a photon with sufficient energy shines on the structure and generates an exciton, once the electron and the hole are separated, the strong electric field will direct them to their respective electrode: in this bias mode, also known as *reverse bias mode*, the photodiode is expected to yield a current as low as possible when in dark conditions, while it should convert in electrical signal any incident photon. Panel (c) shows the band structure when a positive bias is applied to the anode. In this case, even in dark conditions, the charge transfer from anode to cathode and vice versa is energetically

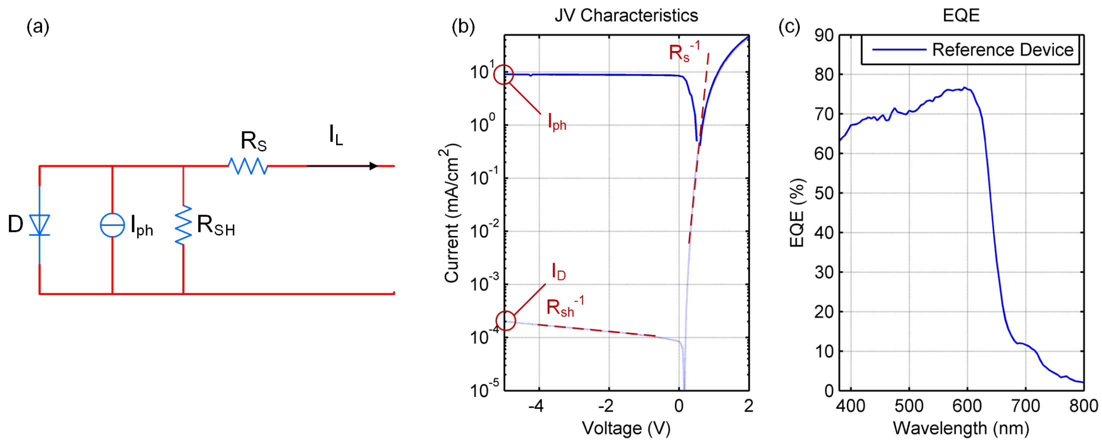

Figure 3.7: Diode equivalent circuit (a) and typical JV characteristics of a P3HT:PCBM photodiode in dark conditions and under 1 sun illumination (b)

favorable and the current rises exponentially with the applied bias. Finally, when a zero bias is applied (d), because of the different work-function of the electrodes, a built-in potential is generated and the band bending is somehow similar to case (b), although the electric field will be much weaker and the collection efficiency is significantly lower than under reverse bias.

3.2.3 OPDs Important Parameters

As a result of these observations, it can be inferred that the empirical description of the optoelectronic behavior of an OPD, albeit originated by complex phenomena, can be assimilated to a classical diode model. Figure 3.7 (a) shows the equivalent circuit of a photodiode and typical charcteristics of an OPD fabricated with standard processing techniques (b). The materials utilized are Indium Tin Oxide as transparent electrode, LiF/Al as cathode and a bulk heterojunction of the polymer P3HT and the fullerene PCBM as photoactive layer. For more details on the utilized materials, we ask the interested reader to refer to Appendix A.
From the JV characteristics, it is possible to extract some important figures of merit, which will be used throughout the chapter to evaluate the quality of OPDs.

- *Dark Current*: with the term “dark current” we will refer to the current density of the OPD under a specified reverse bias, when it is not subject to any kind of illumination. The dark current depends on the band alignment, on the intrinsic characteristics of the polymers and on the presence of shunt paths between anode and cathode [44], [83], [91]. Typical values of dark current density of a P3HT:PCBM OPD are in the order of $10^{-4} mA/cm^2$

- *Shunt Resistance*: with the term “shunt resistance” we will refer to the resistance calculated from the slope of the dark current in regime of strong reverse bias. It indicates the degree of shunt paths through the BHJ.

- *Illuminated Current*: with the term “illuminated current"” (also photocurrent, I_{ph}) we will refer to the current of the OPD under a specified bias when is subject to illumination. Unless differently stated, we will refer to the illumination under the standard AM1.5G one sun spectrum. Typical values of illuminated current density are in the order of $10 mA/cm^2$

- *Rectification Ratio*: with the term “rectification ratio” we will refer to the ratio of the dark current when the diode is biased at +2V to the same quantity when the diode is biased to -4V. Typical values are between 4 and 5 orders of magnitude.

- *Serial Resistance*: with the term “serial resistance” we will refer to the resistance calculated from the slope of the dark current in forward bias. It depends on the materials interface and on the resistivity of the two electrodes [43], [83]

Another important figure of merit for the quality of an OPD, is depicted in Figure 3.7 (c): the *External Quantum Efficiency (EQE)*. It is defined as the ratio of the number of extracted charges to the number of incident photons (at a given wavelength) in the time unit and, besides some special cases, is a quantity lower than one. Its value is influenced by many factors, among which it is worth naming the number of transmitted photons through the electrode, the percentage of absorbed photons which is effectively separated in electron-hole pair (this value is also known as *Internal Quantum Efficiency, IQE,* and is a property of the Donor:Acceptor system) and the collection efficiency. Ideally a photodiode should have one completely transparent electrode and a collection efficiency of 100%: in this case, the EQE will be equal to the IQE.

Once all the important parameters are introduced and clarified, it is possible to proceed to the realization of such OPDs and to the optimization of the fabrication processes. The main goal of the rest of this chapter will be the realization of arbitrarily-shaped, fully solution-processable OPDs, in such a way to have a flexible, green and cost-effective procedure for their realization, which, however, does not penalize the key figures defined in this section.

3.3 Fabrication of CNT based OPDs

3.3.1 CNTs Random Networks as Transparent Electrodes

The last years have seen a surge in the research interest in random networks of carbon nanotubes (CNT), which quickly become an exciting material for the organic and printed electronics industry. The unique and variegate properties of such networks have rendered them the preferable material for a wide range of applications in science and engineering [92]–[94]. For the objective of this doctoral work, one of the most interesting employments of CNT was found to be in the field of solution-processable transparent conductors. With CNT thin films, it is possible to obtain alternative transparent electrodes in organic optoelectronic devices, achieving reasonable trade-offs with respect to sheet-resistance and transmittance [71], [95], [96]. As electrodes, CNT networks are less effective with respect to the most used material, Indium Tin Oxide (ITO), which is extremely transparent and with a high conductivity, but opposed to CNTs it is brittle, rare and difficult to pattern, due to its hardness [97], [98].

As we have previously discussed, one of the goals of this work is to avoid complex lithographic techniques in order to achieve a process able to produce printed electronics based on organic semiconductors and nanomaterials, with high-throughput and low-cost production onto a wide range of substrate materials. Although, as reported in Chapter 2, spray-deposition is a promising candidate for such attainment, extensive research and development is still required to achieve reliable and reproducible realization of multilayer stacks of different functional materials. The fabrication of fully-sprayed photosensitive devices, with the minimal introduction of non-sprayed process steps, would embrace the philosophy of process simplification and integration, and would pave the way for fully-autonomous and high-throughput production lines. Indeed, important bottlenecks which limit the throughput are constituted by vacuum-based steps, or by technologies, such as spin-coating, which are inherently working on small areas. Albeit the feasibility of CNT based transparent electrodes has been previously investigated for organic solar cells (OSC) [71], [99] and light emitting diodes (OLED) [96], their use in OPDs was largely neglected. Very promising results in the realization of OSCs, for instance, have been obtained through the use of air-assisted [47] and ultrasonic spray technology [71] for the deposition of CNT networks, and our work is initiated by this research branch. The optimization of the material ink *per se* is crucial for the obtainment of a smooth and effective electrode. As well-known [94], the single CNTs are strongly attracted by Van der Waals forces, this fact leading to the formation of clusters (or *bundles*). As a powder, a typical CNT commercial product will be very flaky and entangled, and needs to be put into solution together with an insulating dispersing agent. After spraying, the dispersant is chemically removed and a network of randomly oriented CNTs is formed. If the density of CNTs is high enough, the percolation threshold is reached [71], [94] and electric paths are established throughout the whole film. There are many dispersants used with a multitude of purposes and in a range of applications [94], however, the ones most largely employed for the realization of conductive films are carboxymethyl cellulose (CMC) and sodium dodecyl sulphate (SDS). The former is a stronger dispersant, which almost totally avoids bundles, and leads to smooth, repeatable films. An important consequence is that the roughness of the CNT film is considerably lower for CMC with respect to SDS [46], suggesting this dispersant as a more viable solution for the fabrication of CNT electrodes to be applied in multilayer devices. However, while SDS can be simply removed via immersion in water for circa half an hour, in order to remove the CMC from the as-prepared film, it is necessary to employ a long (>12 h) and aggressive nitrid acid treatment.

In both cases, however, once the film has been deposited and the dispersant removed, it can be electro-optically characterized measuring its sheet resistance and transmittance spectrum. The relationship between transmittance and sheet resistance in a CNT film, as well as in many other transparent-conductive films, can been analyzed through the Tinkhams formula 3.1 [100]:

$$T = \left[1 + \frac{\zeta_0}{2R_{sh}}\frac{\sigma_{op}}{\sigma_{DC}}\right]^{-2} = \left[1 + \frac{\zeta_0}{2R_{sh}}\frac{1}{\gamma}\right]^{-2} \tag{3.1}$$

Where σ_{DC} is the DC conductivity, assumed to be independent of thickness, and σ_{OP} is the optical conductivity of the film. The ratio between σ_{DC} and σ_{OP} is referred to as γ and it is used as a figure of merit for the quality of the film: an higher γ corresponds to a lower sheet resistance at a given transmittance value. Figure 3.8 shows the experimental values of transmittance at 550 nm and sheet resistance for films of different thickness. These values are then fitted to the Tinkham formula, and values for the figure of merit γ are obtained. Tho outcome of the fits confirms the first-glance impression given by the plots, showing γ values of 18.77 and 12.38 for CMC and SDS, respectively. For fairness sake, it must be noticed that the nitric acid treatment used to remove the CMC also introduces a further p-doping to the CNTs due to the oxidative nature of the process, increasing the number of carriers and inducing an increased overall film conductivity [94], [102]. Observing the curves, it was possible to choose reasonable CNTs thickness working points, with sheet resistances below $200\Omega/\square$ and transmittances above 80%. Particularly, it is possible to fabricate films characterized

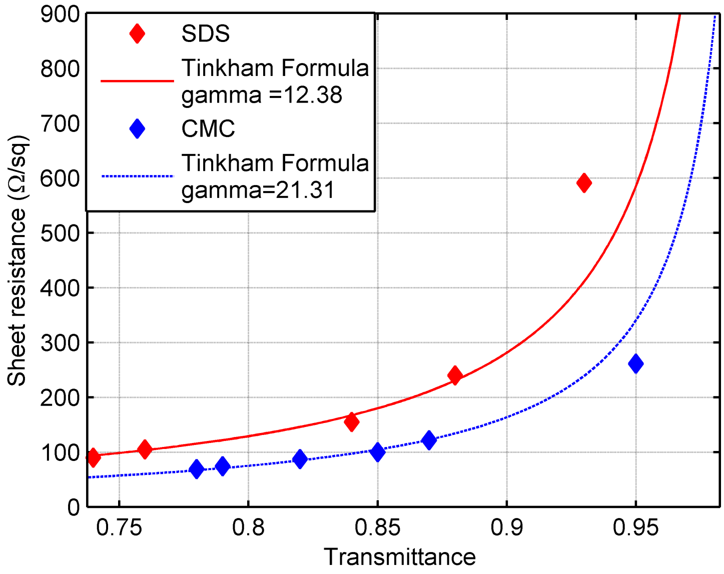

Figure 3.8: Experimental data (markers) and Tinkham formula fit (lines) for CNT films from SDS and in CMC dispersed solutions with no further doping after dispersant removal [101]

by 120Ω/□ with a transmittance of 85% and 160Ω/□ with a transmittance of 84% for CMC and SDS, respectively. The resistance values are high if compared to ITO (which typically presents sheet resistances lower than 20Ω/□) and they would probably not be suitable for the use in OSCs or OLEDs. The peculiarity of OPDs, however, is that they work under reverse bias, where the influence of serial resistance is negligible, up to a certain extent. Finally, since the differences between the resistance of the thin films obtained with the two dispersants are not particularly marked, especially in the the range where we intend to operate, the choice of the one over the other can be motivated with different arguments then mere electro-optical considerations. In general, it is beneficial to keep the process as simple as possible, and avoiding acid treatments would move in that direction. This choice would have the additional benefit of keeping the process more cost effective and green, beside guaranteeing the absence of acid residuals on the sample, which could be harmful in bioelectronics applications. All considered, the selection od SDS as the preferred CNT dispersant seems to be the most natural choice.

3.3.2 Optimization of the PEDOT:PSS Interlayer

Although the work-function of CNTs has been reported to be as high as 5 eV [94] for thin semiconducting films, values measurable for thick conductive networks are significantly lower, being as low as 4.7 eV [103]. In order to optimize the band alignment throughout the device, the necessity of a Hole Transport Layer arises. As reported in the previous section, a typical material employed for this purpose is a mixture of PEDOT:PSS with the highest possible ratio of PSS to PEDOT [104]. As a result, once the anode contact has been deposited, the PEDOT:PSS interlayer must be fabricated on top of it. The optimization of the parameters for spray-deposition of a new material is a long and complex iterative process. Many of the physical characteristics to be tuned have contrasting effects on the film quality and must be finely balanced. Furthermore, the deposition quality is strongly dependent on the topmost layer and its surface free energy [70]. The straight-forward fabrication of photodiodes using PEDOT:PSS in aqueous solution on a CNT film, resulted in a yield, here defined as the ratio between the number of functioning devices over the number of fabricated devices, lower than 50% (See Table 3.1). The devices considered to be working (i.e. the ones whose current under illumination was at least one order of magnitude higher than the dark current), are shown in Figure 3.9 and present acceptable, albeit poor performances. Average peak EQE comprised between 45% and 55%, dark currents densities of 10-3 mA/cm^2 at -5V and rectification ratios of 3 orders of magnitude. It must be here noticed that the high hydrophobicity of CNTs [47], [105] is a known issue. In our case, the PEDOT:PSS in aqueous solution presented a contact angle of 50° (Figure 3.10) on the bare CNT film. This value is, in absolute terms, not particularly high, but contact angles lower than 30° are normally needed to have a flawless deposition [70]. In literature it is possible to find several proposed solutions for the reduction of the contact angle and the improvement of the deposition of a thin film of top of CNTs. The different approaches, either enhancw the hydrophilicity of the CNT layer, or reduce the surface tension of the formed droplets by tuning the ink formulation. To the first class of methods belong pre-wetting of the sample with water-soluble alcohols [47] or plasma treatment of the surface [105], while to the second class of solutions belong the employment of wetting agents or the elaboration of a so-called “two-solvent system” [73]. In order to find an optimal deposition process, both categories of approaches were explored and among the many trials, we report here two of the most interesting ones. The first one relies on the alteration of the free energy of the surface through a mild oxygen plasma treatment, and has been successfully employed in the past for the modification of materials commonly used in organic electronics, such as P3HT:PCBM [106], ITO [107] and even CNTs [105]. Once more, however, there is a trade-off in the formulation of the process: the oxygen plasma must be strong enough to have sufficient surface activation, but mild enough to avoid excessive damage of the CNTs. In our

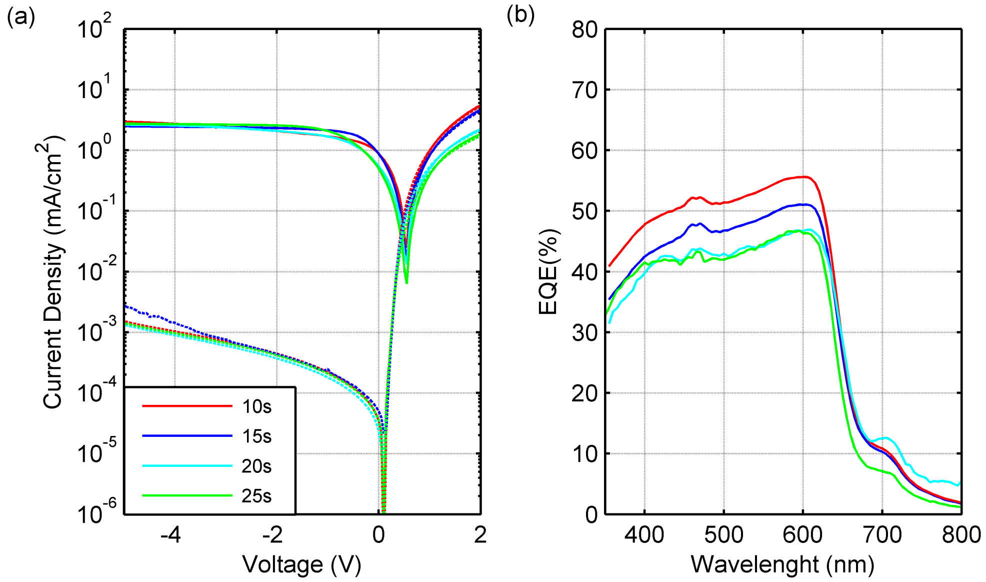

Figure 3.9: Dark (dashed lines) and illuminated (solid lines) JV characteristics of OPDs obtained spray-coating PEDOT:PSS in aqueous solution and P3HT:PCBM blend on structured CNTs, increasing spraying time of the PEDOT:PSS layer b) EQE of the same samples

case, the mildest attainable plasma intensity, was through a 100 W remote microwave plasma generated in a chamber with 0.3 mbar of oxygen. We found that exposures longer than 12 s did not bring to any further improvement in the contact angle, hence we set 12 s as last working parameter for the plasma exposure. The contact angle of PEDOT:PSS on the film was measured prior to spray-deposition of the inter-layer. Afterwards, optical micrographs have been acquired to evaluate the quality of the film. The results of both experiments can be seen in Figure 3.10, and show how a very mild microwave oxygen plasma treatment in a faradaic cage is effective in making the CNT network surface extremely hydrophilic. The most evident consequence of the plasma treatment is a strong reduction in the contact angle to 16° and a substantially better merging of the droplets, evident from the optical microscope. Please note that the films imaged in Figure 3.10 (d) and (e) were obtained with the same ink and identical spray-parameters. Nevertheless, the reduced contact angle and the better spreading of the droplets, did not imply the awaited improvement in the characteristics of the diodes. If compared to the OPDs realized on untreated CNT electrodes, the peak of the EQE is even reduced, being on average below 50%, as shown in Figure 3.11. As a further concern, the linear characteristics of the photodiodes show a strong s-shape in proximity of the zero-crossing. Although this region of the JV characteristics is not normally considered for the operation of photodiodes, the degradation of the fill-factor is a symptom of the induction of charge accumulation in correspondence of traps and

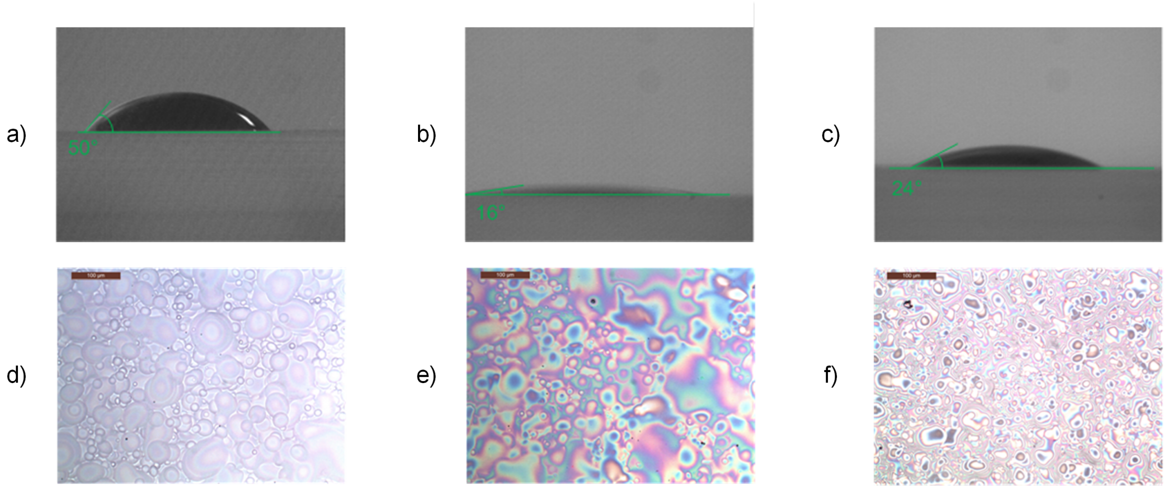

Figure 3.10: Dark (dashed lines) and illuminated (solid lines) JV characteristics of OPDs obtained spray-coating PEDOT:PSS in aqueous solution and P3HT:PCBM blend on structured plasma treated CNTs, increasing spraying time of the PEDOT:PSS layer b) EQE of the same samples

defects [106]. There is, however, a significant benefit in the employment of this approach, and it resides in an increase of the fabrication yield up to 60% attributable to the improved planarization and layer coverage.

The insurgence of charge accumulation, in not fully motivated yet, nonetheless. The phenomenon is quite peculiar, since a macroscopic view of the films would have led to think to an almost perfect deposition, and for this reason a more in-depth analysis has been performed. First, the sheet electro-optical characteristics of the film have been assessed, then its surface properties were investigated through Raman spectroscopy. Sheet resistance measurements of the CNT film before and after plasma treatment demonstrated how the resistance of the films increased of circa 30%, whereas the transmittance of the film stayed constant. This finding has manifold implications: primarily, it can be observed that the film has not been etched, since its transmittance, associated to the solid content of CNTs on the surface is unaltered. In a second instance, the change in resistance is not significant enough to justify a marked reduction in the EQE plots. Finally, the charge accumulation at the interface, could be due to the introduction of defects in the CNT film originated by the plasma treatment: these defects render the film more hydrophilic, but, at the same time worsen the interface. To find confirmation for this hypothesis, and, in general, to shed more light on this phenomenon, the CNT films were investigated with Raman Spectroscopy, before and after the mild O_2 plasma treatment. The ratio of the peak in the G-band over the peak in the D-band of the Raman spectrum is a figure of merit for the CNT film (the higher

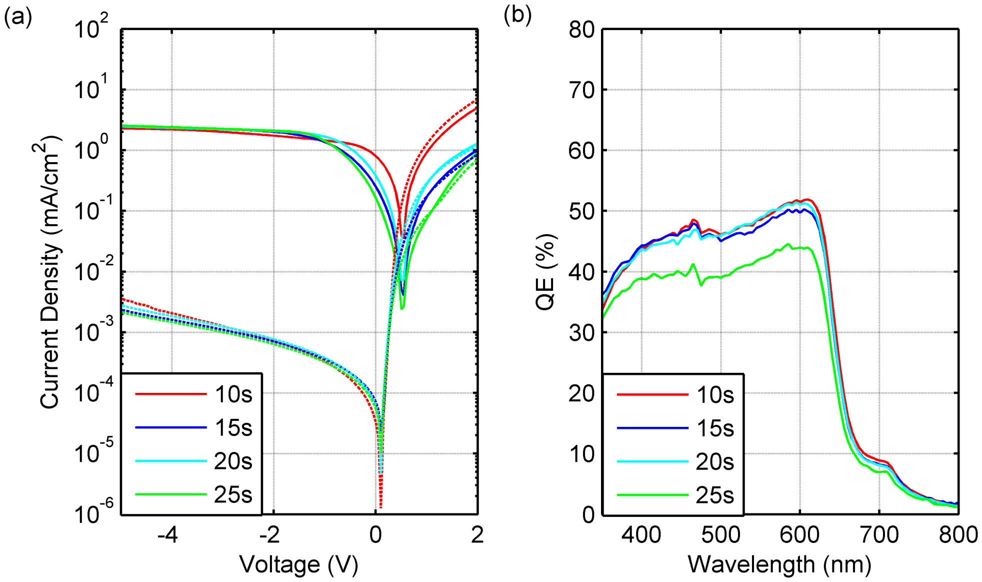

Figure 3.11: Dark (dashed lines) and illuminated (solid lines) JV characteristics of OPDs obtained spray-coating PEDOT:PSS in aqueous solution and P3HT:PCBM blend on structured CNTs, increasing spraying time of the PEDOT:PSS layer b) EQE of the same samples

the ratio, the more defect-free the film). Figure 3.12 shows the Raman spectra of the untreated and treated CNT films. Differently shaped G and D peaks are observable, and just considering the ratio of their peak values leads to a strikingly clear conclusion: the figure of merit is 16.83 and 50, for treated and untreated samples, respectively, and indicates a severe degradation of the film's quality. The hypothesis is hence confirmed: applying a plasma strong enough to modify the free surface energy on top of the CNT layer, leads to the formation of defect centers, which, in turn, worsens the electrical and chemical interface between CNTs and PEDOT:PSS. The performances inevitably decline, and, as a consequence, even if the yield is increased at around 60%, the plasma treatment cannot be considered a viable solution. As stated above, nevertheless, there is a number of works in literature where a "two-solvent system" is found to significantly ameliorate the deposition of a sprayed layer [66], [73]. This strategy consists in mixing a solvent with high boiling point and low vapor pressure (primary solvent) to a solvent with a lower boiling point and a higher vapor pressure (secondary solvent). In this composite, the secondary solvent reduces the surface tension and evaporates faster enhancing the merging of the droplets, while leading to a better uniformity and substrate coverage by means of Marangoni flows.

A major advantage of commercial PEDOT:PSS is that it can be purchased in aqueous solution. This choice contemporaneously gives a ready-to-use environmental friendly material and a solution with a good miscibility to 2-Isopropyl Alcohol (IPA). Given

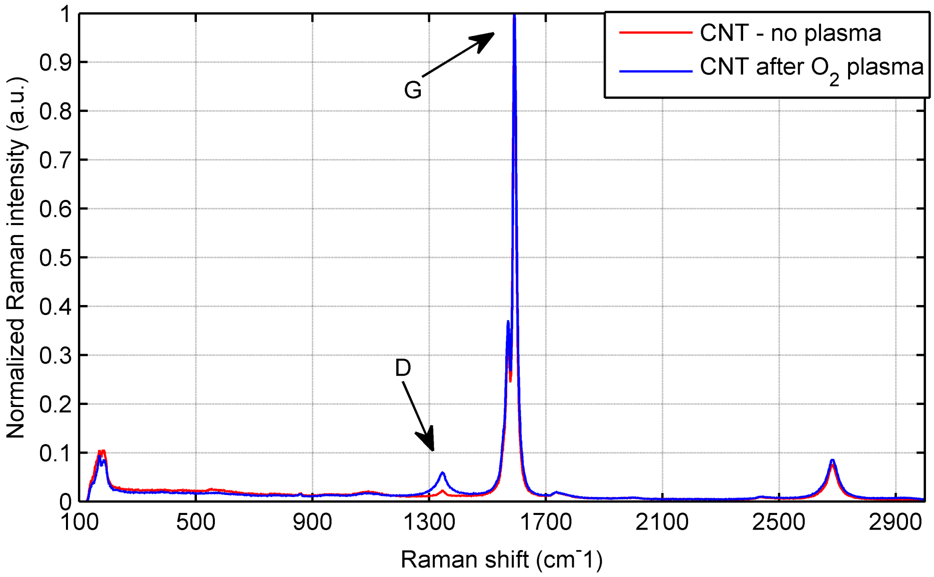

Figure 3.12: Raman spectra of a CNT film before (red line) and after plasma (blue line)

the joint characteristics of water and IPA, these two solvents constitute a perfect "two-solvent system": IPA has by a boiling point of 82.6°C and a vapor pressure of 13.33 kPa at 40°C while water presents a boiling point of circa 100°C and a vapor pessure of 7.4kPa. The ratio of 1:3 (1 part of aqueous PEDOT:PSS in 3 parts of IPA) was found to be optimal for ultrasonic spray-deposition on ITO substrates [73] and was taken as a starting point for our investigation. Through the employment of this simple ink modification, the contact angle was reduced from 50° to 24°, and optical microscope and profilometer inspections confirm the desired enhancement, as presented in Figure 3.10. Finally, Figure 3.13 presents the JV characteristics and the EQE spectra of OPDs fabricated with this current ink formulation and through an optimized "intermediate" spray regime. The characteristics are significantly better with respect to the previously analyzed ones, with dark current densities in the order of magnitude of $10^{-3} mA/cm^2$ at -5V, average rectification ratios of 4 orders of magnitude and EQE up to 65%. Furthermore, the issue related to the "S-shape" at the zero-crossing in the JV characteristics seems to be solved (Figure 3.14), and the curve resemble a classical diode shape, indicating the formation of a cleaner interface between the nanotubes and the organic layers. Moreover, the fabrication yield rose to circa 70%, indicating a better coverage of the sample and less short-circuits between anode and cathode.

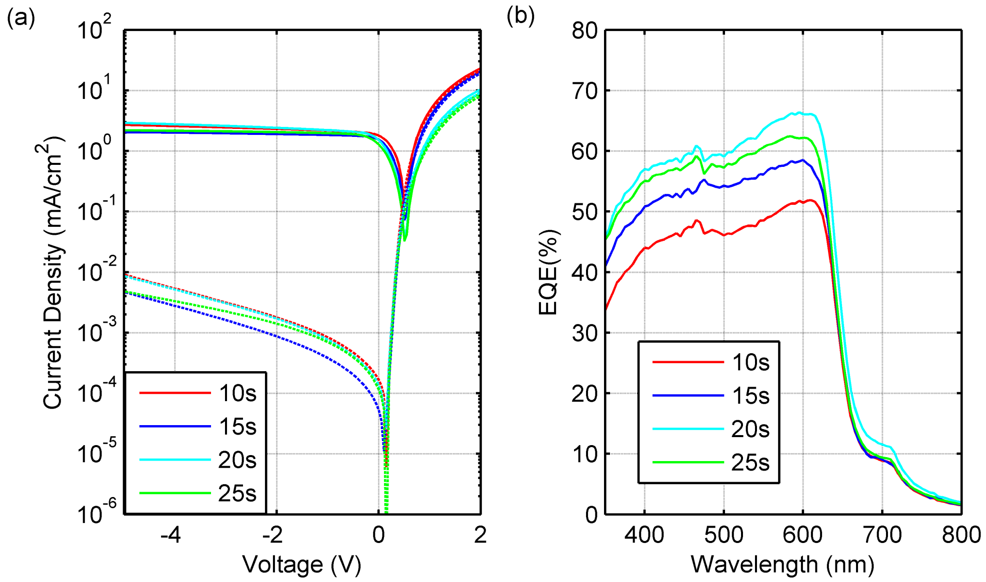

Figure 3.13: Dark (dashed lines) and illuminated (solid lines) JV characteristics of OPDs obtained spray-coating PEDOT:PSS in aqueous solution and P3HT:PCBM blend on structured plasma treated CNTs, increasing spraying time of the PEDOT:PSS layer b) EQE of the same samples

3.3.3 Optimization of the P3HT:PCBM Layer

The process presented so far was aimed at ameliorating the performances of the photodiodes. One of the side effects of enhanced performance was a higher fabrication yield, however, even in the best case, the number of working devices was never higher than 75%. Furthermore, although the EQE and the serial resistance of the OPDs had significant benefits from the realization of more conformal PEDOT:PSS layers, the dark current is still significantly higher than the one reported in the Section 3.2 for OPDs fabricated on ITO electrodes. A phenomenon which could associate the overall low yield to abnormal dark currents is the systematic insurgence of shunt paths. Since the RMS roughness of the CNT layers (a fem tens of nm in the worst cases) is not enough to justify an excessive amount of shunt paths through the devices [46], the rise in dark current can be related to the bundles of nanotubes “spiking” through the bulk heterojunction. Given the small diameter of the CNTs (in the order of few nanometers), a direct experimental confirmation through electron microscopy could be far-fetched. However, if the hypothesis is correct, the presence of strong irregularities could create local paths with a lower shunt resistance and low photoreactivity, resulting in a higher dark current and a locally lower photocurrent. Moreover, if these bundles are long and numerous enough to form a complete conductive path from cathode to anode electrodes, the devices will present very high dark current and insignificant rectification behavior.

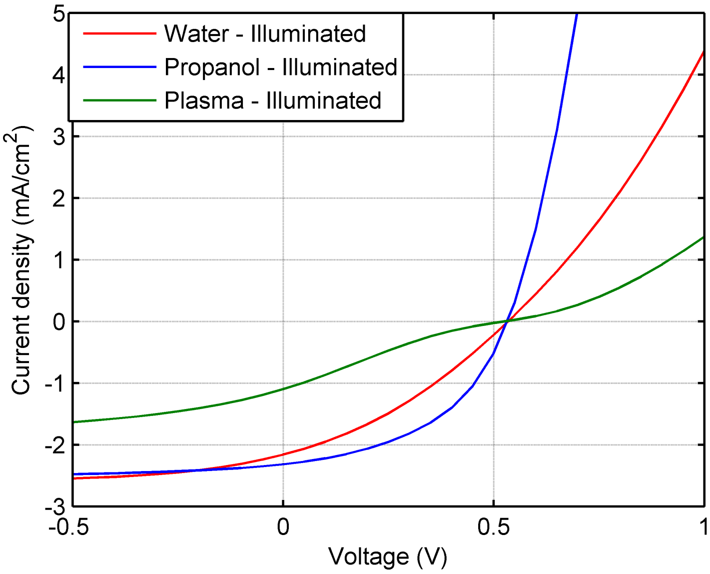

Figure 3.14: Comparison of the illuminated J-V linear characteristics at the zero crossing for typical photodiodes fabricated using PEDOT:PSS in aqueous solution on untreated CNTs (red line), on plasma treated CNTs (green) and using diluted PEDOT:PSS 1:3 in IPA (blue line). The V_{OC} of the diodes is, as expected, not related to the quality of the PEDOT:PSS layer and is constant to 0.55V. The photodiodes with plasma-treated CNTs exhibit a strong modification of the shape in proximity of the zero crossing and overall worse performances

These issues are normally encountered when processing multi-stacked devices based on nanowires or nanotubes networks, as reported for instance by Lee et al. [108] and by Leem et al. [109]. One of the possible solutions reported in the latter work, consisted in fabricating devices with thick PEDOT:PSS layers. Although this approach solves is effective in solving the issues associated to the fabrication yield, it results in a further reduction of the EQE (due to the low conductivity of the PEDOT:PSS interlayer) and in an increase of dark current. Another approach, which is the one we pursued, is increasing the thickness of the bulk-heterojunction. This would not be a solution for solar cells, since they are supposed to be operated in photovoltaic mode (i.e. without any applied bias), and very thick layers might lead to substantial recombination. However, since a high reverse bias can be applied to the OPD, the electric field in the BHJ is still strong enough to provide charge separation and carrier transport through the whole bulk heterojunction. An indirect method to test the goodness of this approach resides in two kind of optoelectronic experiments::

- Measurement of the JV characteristics in dark condition and under illumination, to evaluate the overall influence of thickness on the devices' characteristics and the fabrication yield.

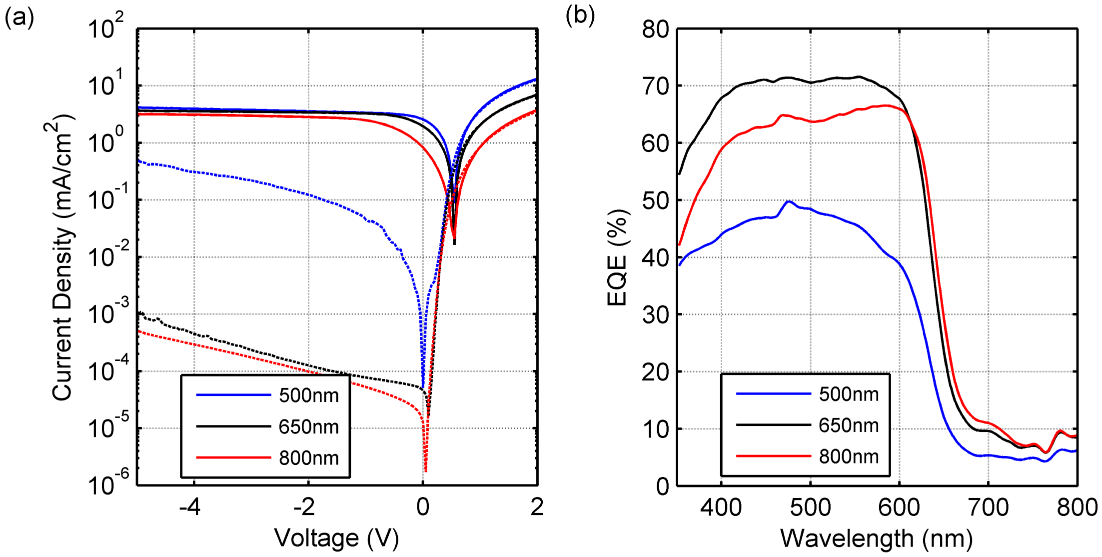

Figure 3.15: Dark (dashed lines) and illuminated (solid lines) J-V characteristics of OPDs for different thickness (500nm, 650nm, 800nm) of the active layers

- Measurement of a spatially resolved EQE, keeping the sample in dark condition and moving a focused light spot on the active area of the sample. The generated photocurrent is then recorded and related to the light intensity. This method can provide with a map where the presence of *hot spots* could be easily identified.

Figure 3.15 shows the experimental evidence related to the first experiment, i.e. a comparison of the JV characteristics of devices with different active-layer thickness. When the thickness of the active layer was kept below 600 nm, the devices presented very high dark currents (above $10^{-}2mA/cm^{2}$ at -5V) and low on-off and rectification ratios (less than 2 orders of magnitude). The best devices could be fabricated with BHJ thickness of 650 nm and 800 nm, in correspondence of which the dark currents lowered down to $4 \times 10^{-4} mA/cm^{2}$ in the case of the thickest devices. Associated to these results, we found a correspective increase in the fabrication yield, which rose to 94% in the case of the thickest active layer, on IPA based PEDOT:PSS electrode. Although this first macroscopic data shows how the performances of the photodiodes improved, still nothing can be stated on the spatial uniformity of the light responsivity and the hypothesis of the presence of shunt paths cannot be confirmed. The second experiment, however, is aimed at assessing the spatial uniformity of the photocurrent. The setup used for this measurement, located in the Optoelectronics Lab of University of Rome, “Tor Vergata”, is composed of a xenon arc discharge white light, attached to a monochromator. The monochromatic light, at a selected wavelength (in our case

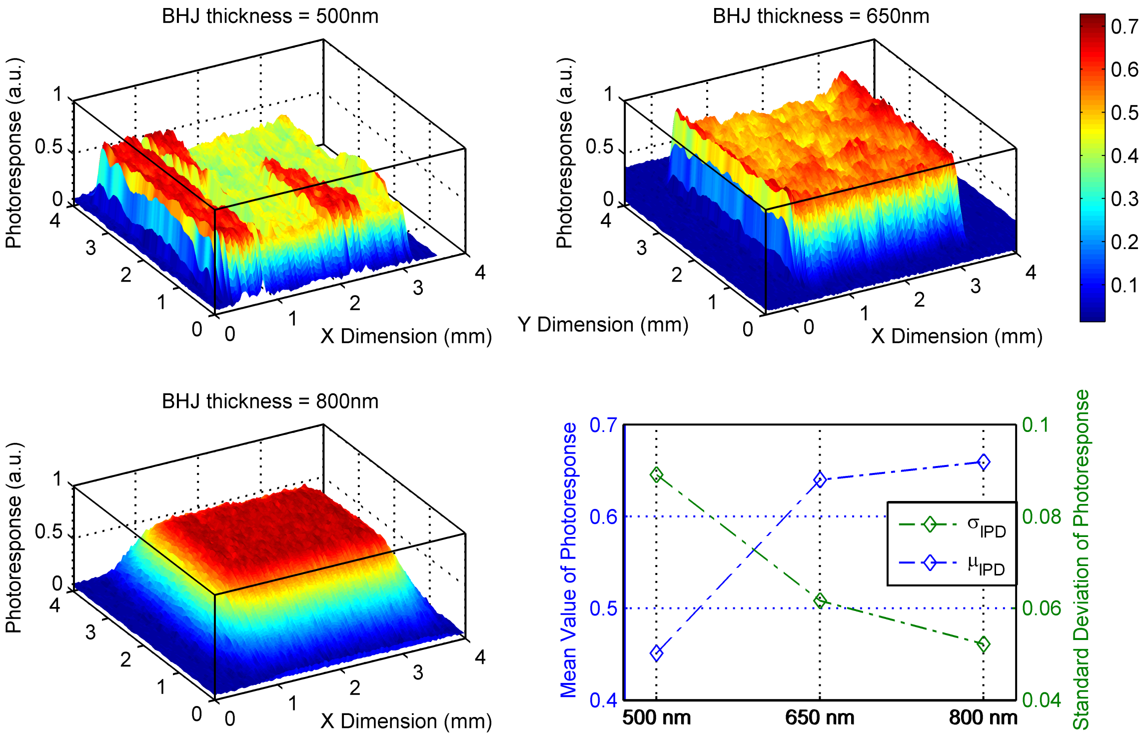

Figure 3.16: Spatially resolved EQE on the active area for different blend thickness: a) 500 nm b) 650 nm c) 800 nm

$\lambda = 550nm$), is redirected through an inverted microscope: by selecting an appropriate magnification lens, the spot size could be reduced to a circle with a diameter of roughly $30\mu m$. The motorized step of the microscope can move in the X and Y direction with a step of $30\mu m$ and it was used to scan the entire $3mm \times 3mm$ area of the photodetector. Figure 3.16 shows how the thinnest measurable device (500 nm active layer thickness) presented strong non-homogeneities and extensive areas in which the response to light was very modest. Increasing the thickness of the BHJ to 650 nm (Figure 3.16 (b)) leads to a higher uniformity and to significant reduction of hot and cold spots. Further increasing the thickness leads to a totally uniform EQE on the entire area of the considered sample (Figure 8(c)), to a yield above 90% and still to a high overall EQE (above 65%) and dark currents as low as $10^{-4} mA/cm^2$. Finally, Table 3.1 shows the yield for the different combination of thickness and fabrication methods presented in this work.

CNT Treatment	**PEDOT:PSS Formulation**	**Blend Thickness**	**Fabrication Yield**
Untreated	1:3 in H_2O	650 nm	$\approx 38\%(6/16)$
O_2 **Plasma**	1:3 in H_2O	650 nm	$\approx 56\%(9/16)$
Untreated	1:3 in IPA	800 nm	$\approx 94\%(15/16)$
		650 nm	$\approx 75\%(12/16)$
		500 nm	$\approx 50\%(8/16)$
		350 nm	$\approx 19\%(3/16)$

Table 3.1: Process Yield for the different used deposition approaches, defined as the ratio of the number of properly functioning devices to the total number of fabricated device with a given treatment combination

3.3.4 Transmittance-Sheet Resistance Trade Off

A final optimization of the performances can be obtained understanding how to cope with the trade-off posed by the inverse relationship between transmittance and sheet resistance. In an ideal photodiode, the EQE is not affected by a change in serial resistance, since the shunt resistance is infinitive. However, if the shunt resistance is constant (since is set by the physical characteristics of the bulk heterojunction), high in magnitude, but still finite, the effect of serial resistance on the EQE cannot be neglected. Moreover, the external quantum efficiency is influenced by the amount of photons which effectively reach the bulkheterojunction (and, hence, from the transmittance of the semitransparent electrode). As we have seen at beginning of the chapter, however, an increase in transmittance corresponds to a more than proportional increase in sheet resistance, according to the Tinkham formula and the choice of an arbitrary (T, R_{sh}) couple on a given Tinkham curve is obtainable by regulating the thickness of the CNT film. This flexibility gives one more degree of freedom that has to be taken in account and optimized. High sheet resistance means high serial resistance and, hence, electric losses. On the other side, low sheet resistance, corresponds to lower transmittance, meaning that less photons can reach the bulk of the photodiode, and, in turn, optic losses. This effect can be examined by means of the simple diode circuital model.

The generated current, in ideal conditions is only related to the ability of the active layer to absorb photons and convert them in charge carriers. Adding shunt and serial resistance helps to take in account the non-ideality of the active layer (shunt paths, imperfections in the polymer), while the serial resistance is strictly correlated to the resistance of the electrodes. Considering $\eta_0()$ as the internal quantum efficiency, it must be taken in account that the layer of CNTs absorbs part of the incident light, hence, its transmittance must be included in the formula.

$$EQE(\lambda) = \eta_0(\lambda)T_{CNT}(\lambda)\frac{R_p}{R_p + R_s} = \eta_0(\lambda)T_{CNT}(\lambda)\frac{1}{1 + \frac{R_s}{R_p}} \tag{3.2}$$

The serial resistance can be considered, at least in a first order approximation, proportional to the sheet resistance, since its main contribution is the resistance of the electrode and the 3.2 can be rewritten as:

$$EQE(\lambda) = \eta_0(\lambda)T(\lambda)\frac{1}{1 + \alpha R_{sheet}} \tag{3.3}$$

Where $\alpha = \frac{R_s}{R_p R_{sheet}}$. Introducing the Tinkham formula (Equation 3.1) in the equation, the whole expression can be rearranged to be only a function of the sheet resistance, which, for the fixed wavelength $\lambda = 550nm$ yields:

$$EQE(\lambda = 550nm) = \eta_0 \frac{1}{\left[1 + \frac{\zeta_0}{2R_{sheet}}\frac{1}{\gamma}\right]^2 \left[\frac{1}{1+\alpha R_{sheet}}\right]} = \tag{3.4}$$

$$= \eta_0 \frac{\gamma^2 R_{sheet}^2}{\left(\alpha R_{sheet} + 1\right)\left(\gamma R_{sheet} + 60\pi\right)^2} \tag{3.5}$$

For a given sheet resistance, the factor α can be calculated through the experimental

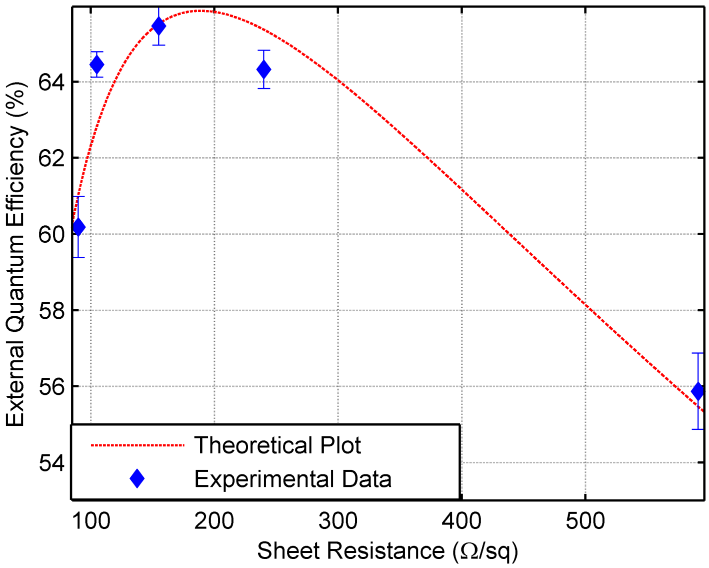

Figure 3.17: Experimental data (diamonds) and plot of the function (solid line) of the EQE as a function of sheet resistance. $R^2 = 0.92$

evaluation of serial and shunt resistance. To this purpose, for each point, 8 OPDs have been fabricated and measured, and the characteristic resistances have been extrapolated from the JV curves through a first order approximation. Since the shunt resistance was almost identical for all the considered OPDs, α resulted to be proportional to the ratio of R_s to R_p and nearly constant at a value of $\alpha = (950 \pm 20) \times 10^{-6} \Omega^{-1}$. Setting a reasonable value for $\eta_0(0.9)$ it is possible to obtain an empirical formula which represents the trade-off between transparency of the layer and resistance of the electrode, and is characterized by an absolute maximum. Utilizing this formula and the associated curve, it is possible to predict the optimal couple $\big(T, Rsheet\big)$ for a given material set. The theoretical curve, among with the experimental values are plotted in Figure 3.17.

3.3.5 Realization of Flexible OPDs

After optimizing the deposition on glass, one of the major advantages of spray-deposition over other fabrication techniques was exploited: a certain process can be easily *ported* from one substrate type to the other, with only minor adjustment of the parameters. This aspect was demonstrated to be true, since the deposition on Polyethylene Terephthalate (PET) thin foil was achieved simply reducing the annealing temperature of the P3HT:PCBM blend, to avoid impairment of the plastic substrate. The structure consists of two stripes of CNTs with a sheet resistance of circa $200\Omega/\square$, 50 nm PEDOT:PSS, 800 nm P3HT:PCBM, 1 nm of LiF and 120 nm of Aluminum, just as the best ones on glass. Figure 3.18 presents the JV characteristics and the external quantum efficiency of such devices. The overall performances are comparable to the devices fabricated on glass, with dark current densities lower than $5 \times 10^-4 mA/cm^2$ and EQE as high as 65%. The inset in Figure 9(b) shows the mechanical flexibility of the PET based OPDs. The device characteristics, however, quickly degenerated during the first 24 h after the fabrication of the device, because of the lack of a flexible encapsulation technique.

Demonstrating the feasibility of fully sprayed devices on plastic substrates paves the way for the simple and cost-effective realization of conformable devices such as flexible scanners or curved photodetectors to be used in biomedical applications. Although similar devices are already reported in literature [110], they can currently only be fabricated through small molecule evaporation and the use of expensive and brittle TCOs.

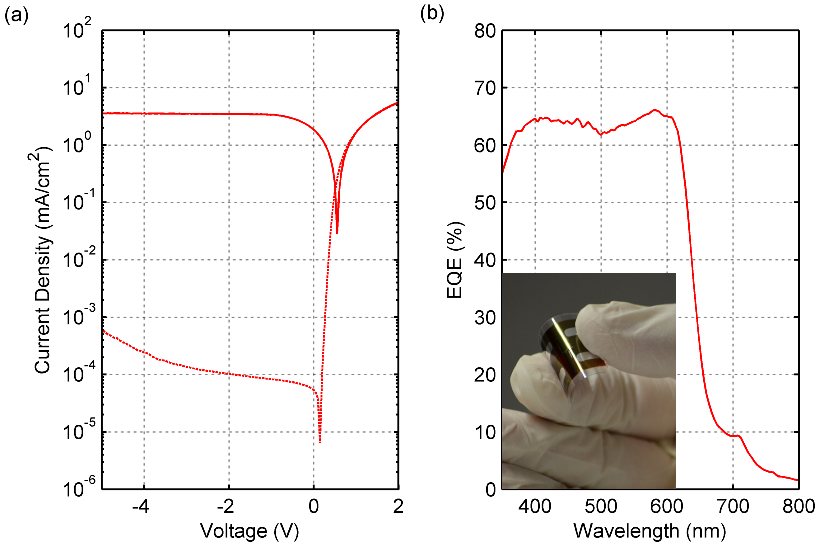

Figure 3.18: Dark (dashed lines) and illuminated (solid lines) JV characteristics of OPDs obtained spray-coating PEDOT:PSS diluted in IPA and blend on PET substrate. The inset shows the fabricated flexible photodiodes

3.4 Fully-solution processable OPDs

3.4.1 Need for Work Function Modifiers

In the last section we have demonstrated how the realization of transparent conductive films does not need to be relegated to the use of the expensive and brittle ITO. We have shown how semitransparent CNTs based electrodes can be realized and employed for the realization of the anode of an OPD. CNTs, however, are not the only material which can be employed to obtain such a goal and in the last years an effort has been put towards the use of alternative materials, e.g. silver nanowires [111] or blends of conductive polymers [112]. However, although the technology for the realization of solution-processable anodes is now quite mature, the cathode contact, is still mostly realized with LiF/Al or Ca/Ag, leading to a reduced scalability of the process and increased cost and complexity. An interestingly evaporation-free approach was, however, presented by La Notte et al. [113], where the spray-pyrolysis of TiO_2 is exploited, and fully functioning spray-deposited organic solar cells are produced. While the need of vacuum steps is avoided, the need of FTO substrates and the high temperatures needed by the spray-pyrolysis (above $300°C$) contrast the cost effectiveness of the spray coating, and exclude the employment of most of the commonly used flexible substrates. Nevertheless, a particularly promising solution to this issue has been proposed by Zhou

Material	Pristine WF (eV)	WF with spin-coated PEI (eV)
Au	5.05	4.00
Al	4.15	3.60
Ag	4.40	3.90
ITO	4.70	3.90
PEDOT:PSS	4.7	4.05

Table 3.2: Work-function measured for the pristine materials and the same material modified with a 11 nm thick layer of PEI

and coworkers [114], which investigated the effectiveness of Polyethylenimine (PEI) and Polyethylenimine ethoxylated (PEIE)as universal work function modifier. Due to the induction of a permanent dipole at the interface with a conducting material, the work-function of the latter is reduced by more than 1eV, converting typical p-type conductors such as ITO or PEDOT:PSS in n-type conductors. This finding has then been applied in the realization of spin-coated organic solar cells [114], [115], TFTs [114] and OLEDs [116]. Moreover, a remarkable work by Azzellino et al. [66] shows how PEIE can be used as a workfunction stabilizer into silver-based ink-jet printed organic photodiodes.

In all these reports, however, the PEI and PEIE layers are obtained solely by spin-coating technique, which at the same time slows down the process and limits the range of application. Indeed, spin-coating is inherently a full-sample technique, which cannot be utilized to fabricate a layer on a small portion of a sample. This can be harmful when there is the need of realizing more electronic devices with different characteristics on one single chip, and can either compromise the functionality of the other devices, or complicate the sequence of steps to obtain the complete circuit. The solution we propose is to build a reliable spray-deposition process for the fabrication of thin film work-function modifiers, allowing the realization of the first fully-spray deposited OPDs.

Primarily, the deposition parameters must be optimized and some performance benchmarks must be defined. The first information to take into account is that PEI is an insulating polymer. Although when deposited in thin layers is a very effective work function modifier, if deposited in an excessive thickness can severely increase the serial resistance of the photodiode. In second instance, the use of PEI is aimed at reducing the work-function of a given electrode, hence the work-function of the resulting layer must be evaluated by means of Kelvin Probe. Finally, since this layer will be underneath a complex stacked structure, its roughness must be low, in order to simplify the deposition of the following layers. To set a benchmark, first PEI was diluted in ethanol and spun on a glass sample with parameters commonly used in litarature [114]. The obtained layer on glass had a thickness of 11nm (as determined by AFM investigation) and an RMS roughness of 7nm. Spin-coating the polymer on top of Ag, Al, Au, ITO and PEDOT:PSS electrodes yielded the expected outcome, substantially reducing the work function of the electrodes, as reported in Table 3.2.

3.4.2 Spray Deposition of PEI

The optimization of the spray-deposited layer followed a procedure similar to what already described for other materials in the previous section. In this particular case, since ethanol is a solvent with a particularly low boiling point ($78°C$), and after atomization easily evaporates even at ambient temperature, the heat-plate was set to the minimum stable point guaranteed by the setup, which was $40°C$. The nozzle-to-sample distance and the atomization pressure were set to the maximum value which was still able to yield wet droplets on the substrate (15cm and 1.5bar, respectively). Since the choice of these parameters was essentially forced by the material system, the residual degrees of freedom were the spraying time and the material concentration only. A main advantage of decreasing the PEI content in solution, for instance, is that it would lead to thinner layers for a given spray time, which gives enhanced control on the deposition rate. On the other hand, when the polymer ratio is too small, the amount of PEI content in the single droplets can be too small to form connected films. To evaluate the optimal dilution rate and deposition time, several layers were spray-deposited onto ITO-covered glass with different concentrations of PEI in ethanol (namely, 0.4 %wt, 0.2 %wt, 0.1 %wt and 0.05 %wt) and with different spraying times (5 s, 10 s, 15 s, 20 s). As shown by 3.20, for a fixed concentration, the thickness is almost linearly increasing with the deposition time. Particularly, the minimal achieved thickness is 5 nm with 5s spraying time and a PEI concentration in ethanol of 0.05 %wt, while the maximum is 55nm achieved with 20s spraying time and a PEI concentration in ethanol of 0.4 %wt. Through the contemporaneous observation of the AFM images presented in Figure 3.19 and the roughness levels reported in Figure 3.20 it is possible to draw some important indications on the optimal choice of parameters. For instance, it is safe to state that all the layers obtained with a spraying time of 5 s, besides from the case with 0.4 %wt PEI in ethanol, were characterized by a high roughness, presented several non-homogeneities and a low coverage. Remarkably, 3.21 shows how these layers led to a relatively small variation of Work Function with respect to the bare ITO (which presents a measured work-function of 4.78eV). Even in the best case, i.e. when the PEI to ethanol ratio is maximum, the coverage of the ITO layer is poor. The

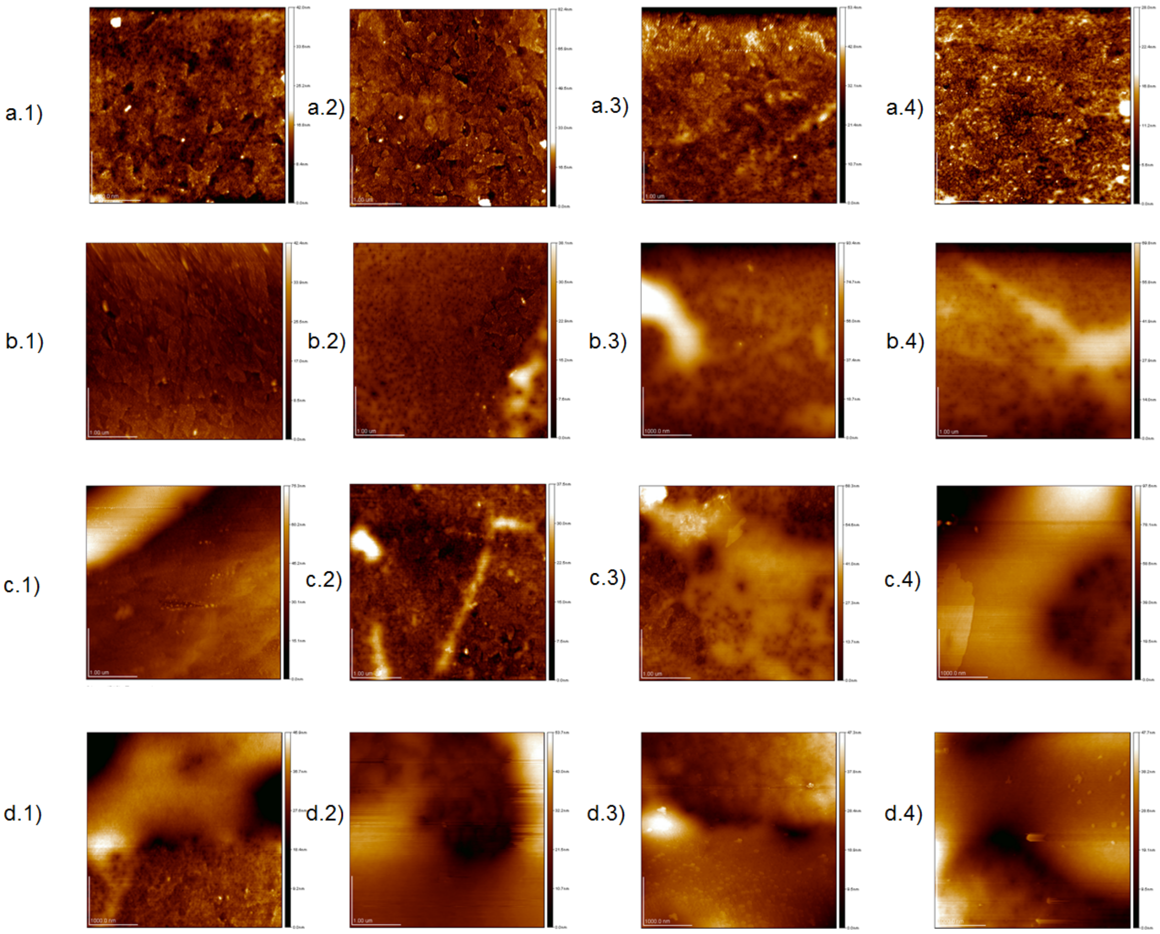

Figure 3.19: AFM topography images of spray-coated PEI in different concentrations and with different spray-time. The layers presented on a single row were obtained with constant PEI concentrations (0.05 %wt, 0.1 %wt, 0.2 %wt, 0.4 %wt A,B,C,D, respectively), whereas the layers presented on a single column were obtained with constant spray time (5s, 10s, 15s, 20s 1,2,3,4, respectively).The z scale is linear and the higher bound (a) is 82.4 nm, 42 nm, 28 nm, 53.4 nm for row A, 42.4 nm, 38.1 nm, 93.4 nm, 69.8 nm for row B, 37.5 nm, 75.3 nm, 68.3 nm,97.6 nm for row C and 45.9 nm, 53.7 nm, 47.3 nm, 47.7 nm for row D [117]

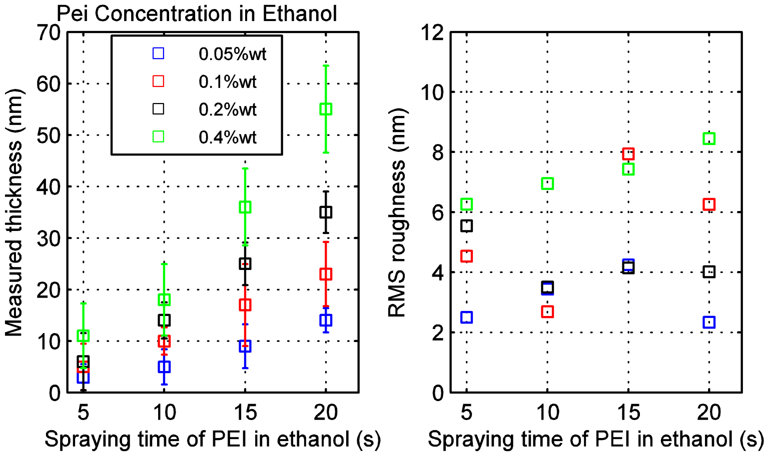

Figure 3.20: Thickness and roughness of the fabricated layers measured throughout AFM measurements. The measurement has been conducted on layers fabricated with different concentration of PEI in Ethanol (different colors) and with increasing spraying time

described effects are most likely due to the very short deposition time choice: although the droplets might contain enough PEI to reduce the work function of the material, their distribution will be uneven, since there is not enough time to make certain that the whole sample is uniformly covered. Since spray-deposition is method based on the stochastic overlapping of differently sized droplets, the number of ejected droplets must be statistically significant. When this coverage threshold is not reached, the material is prone to agglomerate in separate islands [70]. Sub optimal coverage might then result into local hot spots where the work function is higher, issue which could reduce or compromise the performances of any kind of stacked device. A successful process with almost total coverage can, however, be obtained by spraying for longer than 10 s with any PEI concentration above 0.05 %wt and to an increased thickness corresponds a marked decrease of work-function, which moves down to a plateau and saturates when the PEI thickness is circa 20 nm, in accordance with some reports found in the recent literature [66], [114], [115]. Furthermore, Stolz and coworkers [116] suggested that a preeminent factor for the work-function tuning is represented by the coverage of the underlying material with PEI. The results emerging from the AFM characterization and the work-function measurement are also consistent with this hypothesis, and from this point of view, the spray-deposition of PEI was demonstrated to be equivalent to spin-coating, since a closed layer can be already fabricated with a 10nm thin film.

In order to further test the uniformity of the spray-coated layers, a larger area investigations have been performed with means of a white light interferometer which demonstrated an overall low RMS roughness and a limited number of outliers over an area of $313\mu m \times 235\mu m$ [117]. Particularly, the RMS roughness for a 10 nm thick layer

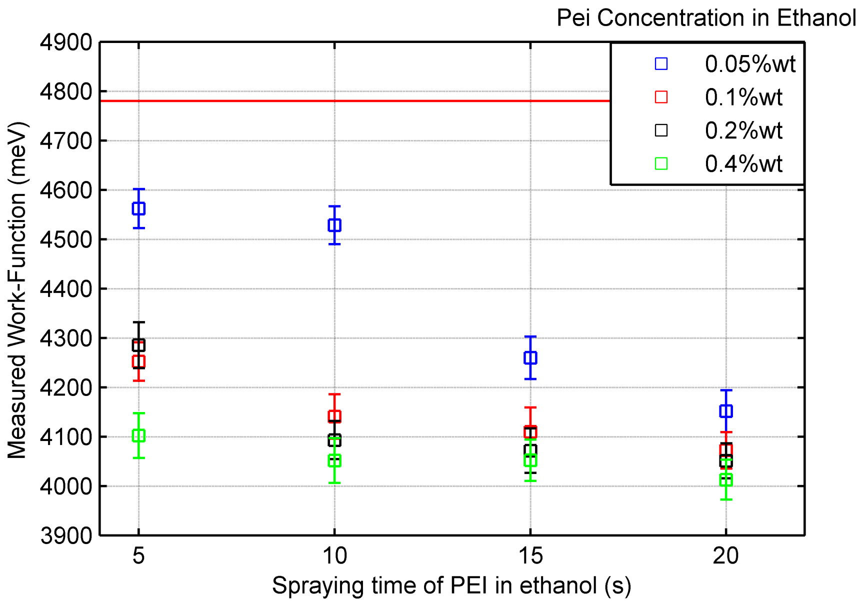

Figure 3.21: Measured Work-Function as a function of the PEI concentration in Ethanol (different colors) and as a function of the spraying time. The red line indicates the measured work-function of bare ITO

was found to be in the order of 5 nm, and the presence of outliers was scarce and of minor entity.

3.4.3 Realization of Fully-sprayed OPDs

As the optimization of the spray-deposition of the work-function modifier has now been performed, it is finally possible to move towards the realization of fully solution-processable OPDs. Among the several material combinations while carrying out this part of the work, in the following paragraphs we will present only the most insightful onesm which provide us with information concerning the effect of the PEI thickness on the OPDs characteristics. The two different combinations, depicted in Figure 3.22, represent a needed step to assess the process (i.e. the modification of a stable material such as ITO for the realization of the transparent cathode) and the ultimate goal of the section (i.e. a fully solution processable OPD), respectively. In the first approach for the fabrication of OPDs free of any vacuum step, the work-function modifier is applied on ITO which is known for its stability and relatively high conductivity. To do so, first, a 10nm-thick layer of PEI has been spun onto patterned ITO, to be used as a benchmark, while the and the remaining parts of the stack (active layer, hole conducting layer and anode) were spray-deposited according to the procedures reported in Section 3.3. Prior to the deposition of the top PEDOT:PSS electrode, however, it was necessary to

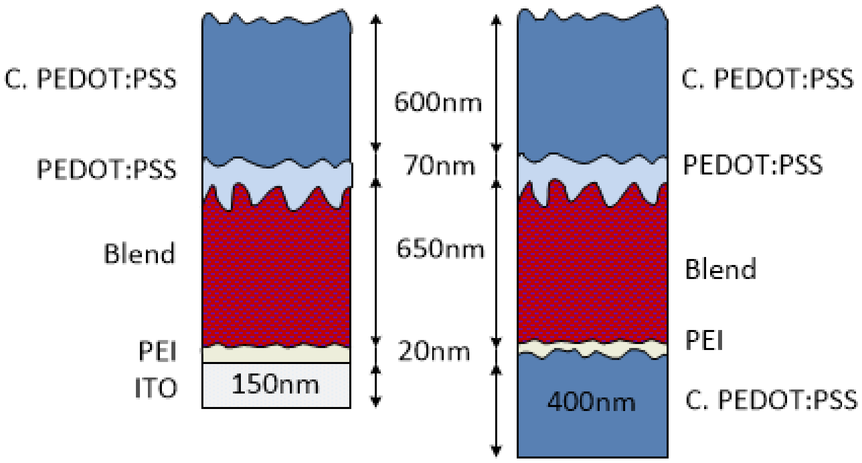

Figure 3.22: Fully-spray coated photodiodes. The left-hand-side proposed stack is a photodiode obtained starting from a glass with structured ITO on whom 15nm of PEI are spray-coated, then 650nm of P3HT:PCBM blend, 70nm of HCL PEDOT:PSS and circa 600nm of conductive PEDOT:PSS as anode electrode. The right-hand side stack differs from the first one because the ITO is not needed anymore since it is substituted by a 400nm thick layer of spray-coated conductive PEDOT:PSS.

activate the surface of the P3HT:PCBM blend through mild oxygen plasma treatment [106]. The OPDs obtained with this method, have characteristics comparable, for instance, to spray-deposited OPDs with PEDOT:PSS anode and evaporated cathode [112]. Successively, the spin-coated PEI layer was substituted by a spray-deposited counterpart. Given the versatility of the method, different thicknesses for the work-function modifier could be achieved tuning the deposition parameters. We opted for a dilution rate of 0.1 %wt of PEI in ethanol, which demonstrated to be the more versatile, and selected deposition times long enough to obtain roughly 5 nm, 10 nm, 15 nm and 20 nm thick PEI layers.

The results are summarized in Figure 3.23, where the JV characteristics and the EQE of the fabricated devices are presented. Remarkably, when the thickness of the spray-deposited PEI is comparable to the thickness of the spin-coated one, the differences between the fully spray-deposited photodiodes and the ones with one spin-coating layer are minimal. In both cases dark currents lower than $10^{-4} mA/cm^2$ are obtained, and the External Quantum Efficiency is as high as 65% at -4V, comparable to OPDs obtained with similar material stacks [77], [112]. A slight variation in the thickness of PEI, however, can lead to strikingly different behaviors of the overall device. Too thin and sparse work-function modification layers, lead to the formation of large areas where the ITO is not covered by the PEI layer at all, nullifying the work-function difference between the two electrodes and reducing the built-in potential. The photodiode is effectively transformed in a photoconductor, and the characteristics change accordingly:

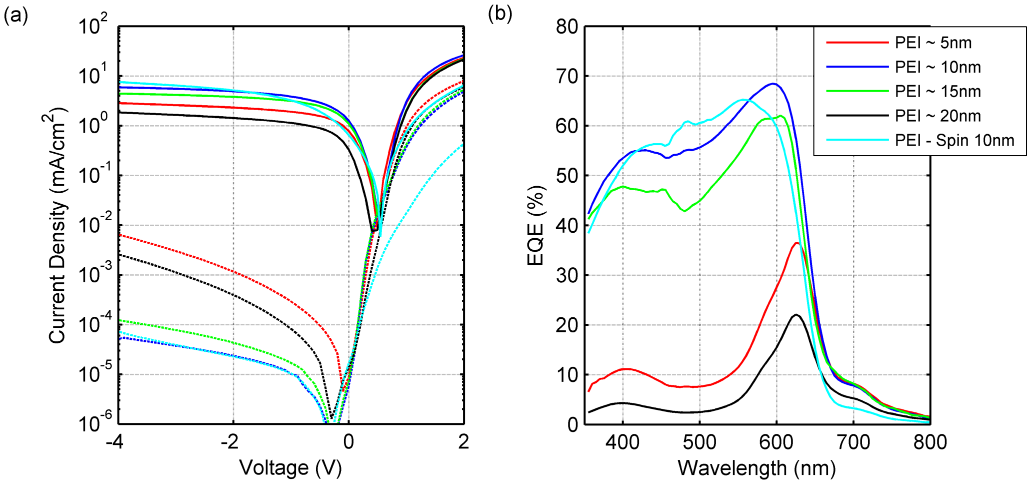

Figure 3.23: Dark (dashed lines) and illuminated (solid lines) JV characteristics of OPDs obtained spray-coating PEI with different thicknesses. The cyan line represents a reference photodiode obtained spin-coating the PEI and spray-coating the uppermost layers of the stack b) EQE at a bias of -4V for the same samples The shift of the EQE peak of OPDs with spray-coated PEI with respect to the ones with spin-coated PEI is most likely due to a different effective thickness of the blend. The effect is reproducible on several samples with the same material stacks and processing steps and is attributable to the different surface characteristics of the spin coated and the spray coated layers.

the dark currents rise (in the order of $10^{-2} mA/cm^2$) and the separation/collection of charge to become largely non effective, as shown by the low illuminated current and the shape of the EQE.

In the other direction, although a 15 nm thick PEI layer only marginally affects the characteristics, a further 5 nm increase of its thickness results in a dramatic change. When the thickness of this amorphous and rough insulating layer increases a bulk insulator is created between the electrode and the semiconductor. With an augmented number of traps and recombination sites due to the higher volume of PEI, it is likely to trigger trap-assisted conduction mechanisms. [91], [118]. The effect will be very significant when the device is kept under dark conditions, since not all the traps are filled, and the intermediate defect states can enhance the hopping probability of a carrier from the semiconductor to the electrode. Because of these conduction paths, the reverse current in dark conditions increased up to $10^{-3} mA/cm^2$. On the other hand, when the samples are under illumination, the traps are readily filled, and this leads to a double effect: first, the charge accumulation partially shields the electric potential, thus weakening the field assisted transport through the device; in second instance, once the defect states are full, the trap assisted hopping paths are occupied and the 20 nm thick PEI layer behaves as an insulator. This phenomenon leads to

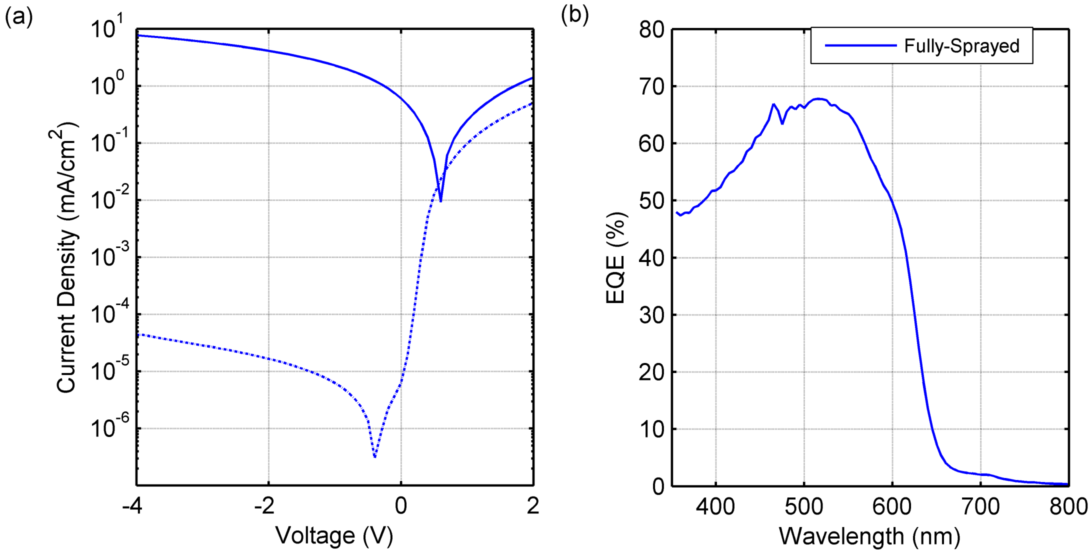

Figure 3.24: Dark (dashed lines) and illuminated (solid lines) JV characteristics of the first fully-sprayed organic photodiodes. Dark currents lower than 10-4 mA/cm2 are obtained b) EQE at a bias of -4V for the same sample.

the diminution of the charge collection and to a severe increase in serial resistance. As a result, the illuminated currents dropped and the EQE is circa a third than what achievable with the optimum material set. As a result of the analysis so far conducted, the optimal thickness of the PEI layer is to be set between 10 nm and 15 nm, and the former is the thickness utilized for the fabrication of the second set of OPDs. In fact, although the first class of OPD was free from any explicit vacuum step, it still relied on pre-patterned ITO samples. This bottleneck can be overcome by the use of any other transparent conductive material, and we decided to use a conductive PEDOT:PSS mixture, in order to reduce the palette of different material needed for the fabrication of the device. Figure 3.24 shows the final result of the optimization and the stacking procedure. First, a 400nm thick layer of PEDOT:PSS is deposited, then a PEI layer of approximatively 15nm, and then the bulk heterojunction, the hole transport layer and the top electrode are successively spray coated. Although the higher sheet resistance of the polymeric cathode induces an increase of the serial resistance, resulting in a reduced forward current, the significant figure of merits of a photodiode are only marginally affected. The fully-sprayed OPDs present, in fact, dark current lower than $10^{-4} mA/cm^2$ and EQE higher than 60%, all performance resembling the ones of the spray-coated photodiode on ITO electrode.

The devices obtained through the developed process are free from any evaporated or sputtered material, free from cumbersome lithography processes, do not involve the use

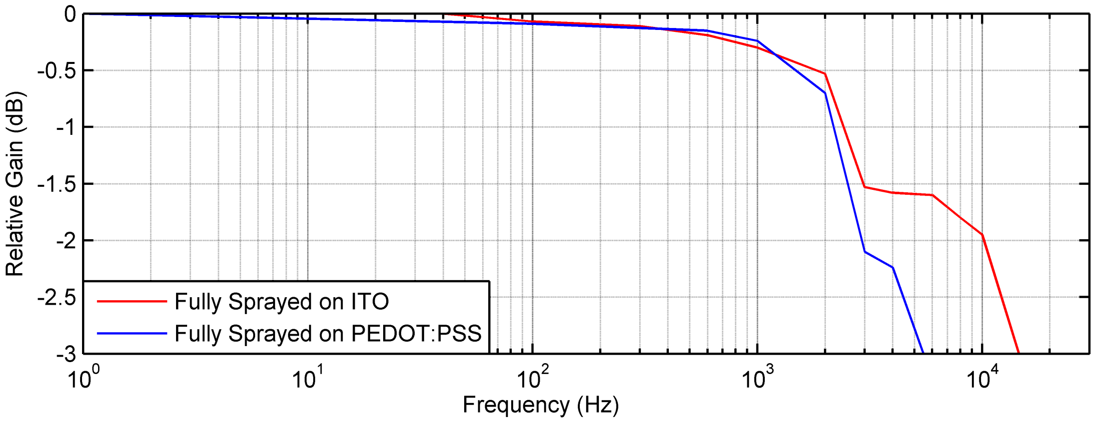

Figure 3.25: Cutoff frequency for the fully sprayed photodiodes. The red line is the frequency response of the photodiode depicted in 3.22 (a), while the blue line is the frequency response of the photodiode depicted in 3.22 (b). The decrease in cut-off frequency is mostly due to the increased serial resistance of the photodiode due to the polymeric cathode which reflects in an higher time constant of the system

of any acid or aggressive etchant. The whole fabrication is carried out with solution processable materials and, as such, can be performed onto arbitrary substrates. The only major difference between the fully-solution processable diode and the ones based on semi-transparent ITO electrodes, resides in the cutoff frequency. This parameter is dependant on the serial resistance of the diode and, hence, on the sheet resistance of the electrodes: since the PEDOT:PSS electrode is almost one order of magnitude more resistive than the ITO one, such an effect was expected. Nonetheless, the measurement presented in 3.25, show how the cut-off frequency of such diodes is in the range of 6 kHz. Although this value is not high in absolute terms, it is comparable to the one measured for similar devices with evaporated cathode and spray-deposited anode [112]. Finally, a last remarkable observation can be made. Since both anode and cathode electrodes are PEDOT:PSS based, they are both semi-transparent and the device can be illuminated contemporaneously from both sides. This kind of photodiode could be used, for instance, for sensing two independent optical signals, yielding to an output electric signal (photocurrent) which is composed by the sum of the conversion of the two input signals. Moreover, the transmittance of the electrodes can be modified by choosing appropriate spraying times or by selecting spectrally differentiated electrode materials (e.g. CNTs [43]). To push the concept even further, the two electrodes could be combined to color or polarization sensitive filters. Figure 3.26 shows the output curves of the fully-sprayed photodiode when a ramp is shining on the bottom side and a square wave is shining on the top side, and vice versa. The shapes and the different current amplitudes can be clearly inferred, achieving the proposed goal of summing up

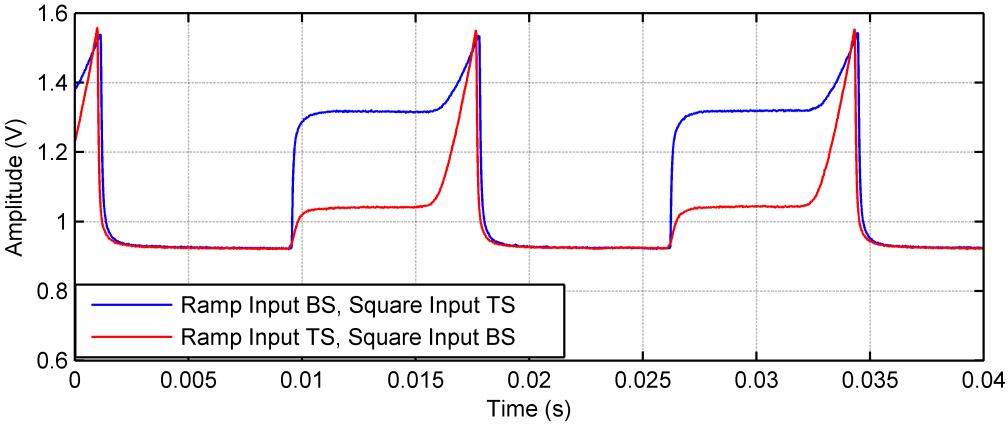

Figure 3.26: Output obtained when a green light (530nm) is shining onto both electrodes at the same time. The Bottom Side (cathode) was engineered to be thicker and hence with a lower transmittance than Top Side. The mismatch in transmittance directly implies a mismatch in amplitudes, that allows, in principle, the realization of side-sensitive photodetectors

the signals and fabricating a side-sensitive fully-sprayed organic photodiode.

3.4.4 Inkjet-printed Electrodes for OPDs

The only limitation imposed by the fully spray-deposited organic photodiode is in the design of the layouts. Although the realization of arbitrary shapes is possible mith means of spray deposition through a stencil, this approach is not optimal for fast prototyping. In fact, the desired shape must be laser-cut into metal thin foils and this process can be expensive and tedious.

When precise and arbitrary patterns are needed, the most flexible employable technique is ink-jet printing. As discussed in Chapter 2.3, there is a wide range of inkjet-printable materials, among which thick carbon inks and silver nanoparticle inks are the most commonly used [65]. The latter ink is made of a suspension of nanoparticles with a variable size (typically comprised between 30 nm and 80 nm) and can then be used for the deposition of relatively thin and smooth conductive layers [68]. With this method it is possible to achieve sheet resistances in the order of $55m\Omega/\square$, which are comparable to the ones of thin evaporated metallic films. Once the circuital design is prepared, it can immediately be printed and after a sintering step (typically thermal or photonic) is ready to use. Here we decide to exploit these advantages for the realization of arbitrarily shaped, fully solution processable Organic Photodetectors and to integrate them with a folded dipole antenna for remote sensing.

The overall system, shown in Figure 3.27 (a) comprises of a dipole antenna, of metal pads for the insertion of a discrete chip and a metal stripe to be used as the cathode of

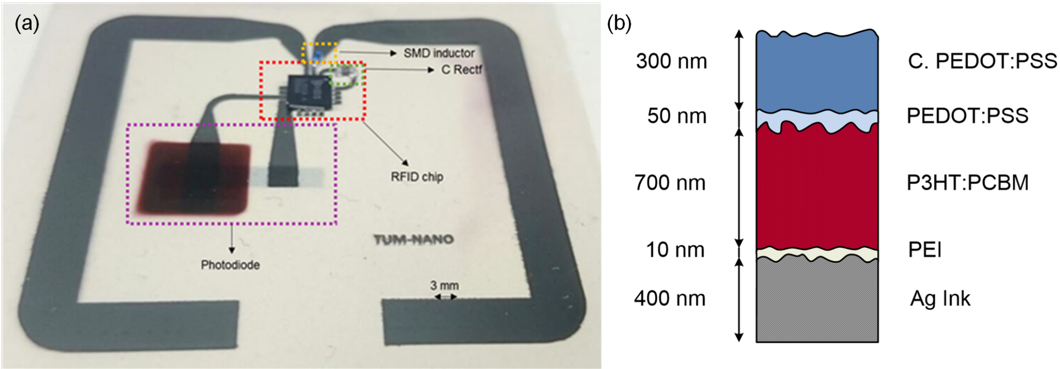

Figure 3.27: (a) Image of the tag with all its elements labelled, (b) Cross-sectional view of the OPD. An inkjet printed Ag line modified with spray-coated PEI is used as reflective bottom-electrode, while a 700nm thick blend of P3HT and PCBM is used as photoactive layer. The top semi-transparent electrode is obtained via a mixture of the conductive polymer PEDOT:PSS.

the OPD. The measured work function of the Ag line, however, is too high ($\approx 4.4eV$) for the realization of functioning photodiodes. Utilizing the process developed in the previous subsection, it is possible to selective deposit PEI only on the electrode's area and the functionality of all other components is not compromised. Subsequently to the deposition of the PEI film, a 700 nm thick P3HT:PCBM film as active layer has been sprayed, followed by a 50 nm thick hole injection layer and a 300 nm thick PEDOT:PSS anode: the stack is represented in Figure 3.27 (b). For comparison's sake, tags with PEI and without PEI were realized and the characteristics of both devices are plotted in Figure 3.28. The JV curve of the OPD fabricated on the non-modified electrode, clearly shows a substantial difference in the dark current (more than two orders of magnitude), associated with an overall instability in time, which is reflected in the noisy and irregular shape of the characteristic curve. On the other hand, the JV curve of the photodiode with the PEI interlayer is well aligned to the ones we described so far. Figure 3.28 (b) shows the external quantum efficiency of the functioning device, which presents a flat response in most of the range and a peak value resenting 70%. Although the realization of such device is remarkable on itself, it is here necessary to stress the importance of the obtained integration of different technologies and devices. The final device is, indeed, not only a photodiode, but a tag which can be remotely sensed, thanks to the antenna and the RFID chip. Such flexible devices could be utilized as remotely readable biosensors which can be implanted into living tissues and do not need direct contact for the read-out. To demonstrate this aspect we realized a prove of concept: the chip was put under different conditions of illumination (dark, one sun and variable intensity of yello monochromatic light), the feedback resistance was

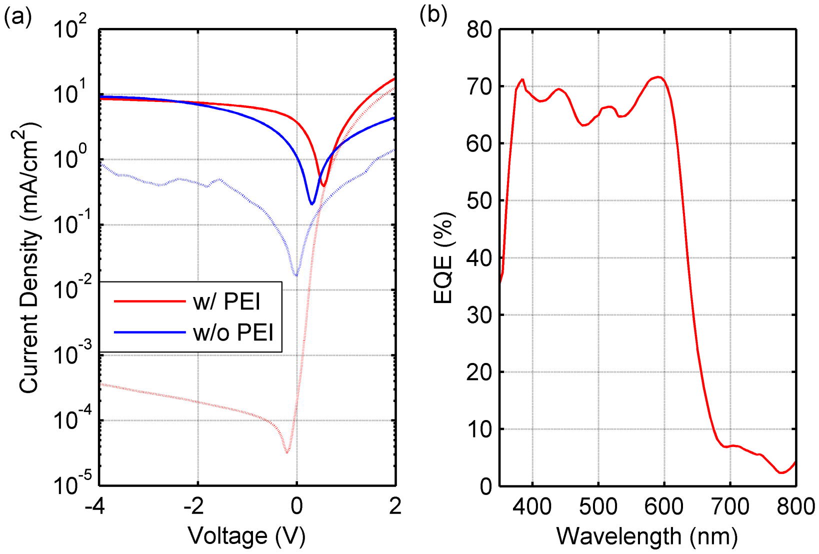

Figure 3.28: Dark (dashed lines) and illuminated (solid lines) JV characteristics (left) and EQE (right) of the fully-sprayed organic photodiode with and without PEI. Current density as low as 5x10-4mA/cm2 have been reliably achieved.

digitally set and the level of photocurrent was remotely estimated. To reduce the need of power, the OPD was operated in photovoltaic mode (i.e. without any external bias). Table 3.3 synthesizes the obtained values and shows how in any illumination condition, it was always possible to distinguish the different values. Particularly, with the settings optimized for the reading of high photocurrents, the dark current corrisponded to 0 bits of the ADC, while the current under illumination corresponded to 810 bit of the ADC converter. Analogously, reducing the feedback resistance to optimize the reading under dim monochromatic light, illumination levels of $0.02mW/cm^2$, $0.04mW/cm^2$ and $0.06mW/cm^2$ corresponded to 0 bits, 256 bits and 884 bits, respectively

Device / Configuration	**Optical Power Density** (mw/cm^2)	**ADC Count (Bits)**
Sun simulator	0	0 ± 0
$R_{FB} = 185k\Omega$		
$V_{ref1} = 0mV$	100	810 ± 1
$V_{ref1} = 410mV$		
	0.02	0 ± 0
Monochromator		
(600 nm)		
$R_{FB} = 3875\Omega$	0.04	256 ± 8
$V_{ref1} = 0mV$		
$V_{ref1} = 410mV$		0.06 ± 10

Table 3.3: Sensor performances in the RFID tag

3.5 Summary

In this chapter we have first introduced the subject of organic photodetectors, explaining why they are needed in bioelectronics, how they can be used and what are the biggest challenges to overcome. Afterwards, we briefly presented the working principle of Organic Photodiodes, along with a short description of the most widely accepted theory on the conduction mechanisms in organic devices.

Once the theoretical framework has been set, we showed the development, in several steps, of a fabrication process which enabled us to produce fully solution processable photodiodes with arbitrary shapes, on plastic foil. The first stage of the process development was in the realization of TCO-free spray-deposited organic photodiodes on flexible substrates incorporating CNT based anode electrodes. Understanding the critical aspects of multilayer spray deposition was of foremost importance in order to obtain state-of-the-art photodiodes with high yields. The most crucial point was the optimization of the CNT/PEDOT:PSS interface, which was achieved through an enhanced ink formulation.

Although the process led to the reliable fabrication of OPDs on foil, it still presented one major bottleneck: the cathode electrode is obtained through Physical Vapor Deposition. In the following section, we overcome this barrier by demonstrating for the first time spray-deposited ultrathin PEI layers. These layers act as work-function modifiers and, after the reported process optimization, have been employed for the realization of *fully sprayed* OPDs, where no pre-deposited material or vacuum step was involved. These devices presented comparable performances to OPDs realized with similar stacks and reported in previous literature.

Since this process yielded the expected results, the concept of fully solution processable photodiodes could be pushed even further. In the last part of the chapter we developed a complex RFID tag with inkjet-printed dipole antenna and an integrated fully spray-deposited photodetector. This kind of system, albeit just a proof of concept, could pave the way to the realization of autonomous, remotely readable sensors (and particularly biosensors), realized with arbitrary shapes and design and through reliable and cost-effective fabrication techniques.

Chapter 4

Materials Stability and Encapsulation

In this chapter we briefly examine the degradation mechanisms of organic semiconductors, in order to summarize the causes of the low life-time of such devices and at the same time identify the possible solutions. After pinpointing the desirable encapsulation characteristics, particularly for OPDs, we develop a method to obtain the in-line fabrication of protecting barriers, through the spray-deposition of polymers and the evaporation of sufficiently thick oxides. The effectiveness of each new method is evaluated through a one-month degradation study on the main characteristics of OPDs and a figure of merit, defined as *effective Transmission Rate (eTR)*, is introduced to qualitatively compare the obtained results to the literature.

However, in an organic device, the semiconductor is not the only part which might be sensitive to the effects of external agents. The metals used as electrodes, especially when in contact with highly reactive environments such as the cellular culturing media, could also degrade and hinder the functionality of the final device. In the second part of the chapter, hence, we prove that some of the metals commonly used in bioelectronics applications (Ag, Al and Au), especially the ones with lower work-function, when immersed in culturing medium are subject to strong degradation in terms of their work-function and conductivity. Furthermore, they are sometimes subject to delamination during long time experiments. To solve this last issue, we investigate the feasibility of the usage of a polymeric adhesion layer, and we optimize the deposition process to obtain a better adhesion and a proven biocompatibility.

4.1 Need for Encapsulation

4.1.1 Degradation Mechanisms

As previously seen, the efficiency and application range of organic electronic devices has been steadily improving in the last years, due to the multiplication of the efforts in the research in this field. However, although most of the devices present conspicuous advantages over their inorganic counterparts and have reached sufficient scalability and fabrication yield, their presence on the market is somewhat limited to few, specialized applications. As reported by some observers, one of the major reasons which stands behind this lack of commercial interest in organic electronics resides in the low life time of a typical device [119].

Organic materials and metallic electrodes are, indeed, sensitive to many environmental factors, among which UV light, oxygen and water vapor are the most harmful and difficult to eliminate. The reaction of those two gases with the bulk heterojunction or with low work function electrodes results in the formation of insulating oxides or in the creation of radicals, which alter the device characteristics and can bring, eventually, to devices which are unusable for any practical purpose. To prevent these phenomena to take place, or at least to limit their occurrence rate and to extend the life-time of organic devices, there is a need for *encapsulation*, i.e. the creation of a barrier which slows down the diffusion of the dangerous substances in the material stack. Practical barriers, are, however, far from ideal. Furthermore, the exposure to UV light, strongly present in the solar spectrum or in many analytical applications, serves as a catalyst for irreversible chemical reaction to happen. Although many other effects should be taken into account to understand the lifetime cycle of organic devices, the photochemical activation of oxidation reactions have been proved to be crucial in the alteration of the polymeric devices functionality [54]

Indeed, since P3HT and similar polymers are characterized by a low photochemical stability, providing optical energy in presence of singlet oxygen leads to irreversible photosensitisation. The singlet oxygen reacts with the thienyl group of the P3HT, and the reaction byproducts decompose in many simpler but reactive compounds, such as ketone and sulfine, which disrupt the π conjugation. As a result, the number of free delocalized carriers is reduced, the conduction through the polymer is hindered, and the visible absorbance spectrum of P3HT is irreversibly changed. The extensive and systematic work of Manceau et al. [120] confirms this theory through thorough experiments. Particularly, they show how the exposure of P3HT based films to O_2 or H_2O has limited hindering of the quality of the final device, as long as it is not exposed to UV light. In fact, in presence of UV light and one of the two gas, the peak P3HT absorbance in the visible spectrum is reduced to the 15% of the original value after only 80h of light exposure. Through IR spectroscopy studies, oxidation fingerprints were identified and it was possible to formalize the reaction sequences which bring to the oxidation of the alkyl-side chains and of the sulfur atom present in the P3HT and conclude that the polymeric backbone itself is decomposed.

As a further consequence, given the disruption of the polymer, the whole organic layer is subject to expansion, leading to a non isotropic swelling of the stack, affecting all the interfaces, including the delicate semiconductor/metal interface. When the thin surface of the electrode is modified, the metal tends to crack and the metal grains to move far apart, at the same time increasing the resistivity of the conductive film, worsening the charge transfer to the semiconductor and weakening the mechanical stability of the system[54], [55].

Besides the changes in the polymeric compounds, the UV-oxygen interaction hinders the functionality of non-polymeric materials as well. For instance, the fullerenes, such as PCBM, undergo doping and oxidation. The most notable degradation effect resides in the incorporation of oxygen in the carbon cage of PCBM, reported already few months after the isolation and stable synthesis of fullerenes in 1990 [121]. Oxygen acts as a strong p-dopant and as electron trap, at the same time reducing the number of free carriers and the effective mobility, leading to an overall reduction of the electron conductivity of more than one order of magnitude [54], [55]. Furthermore, the combination of PCBM's oxidation and P3HT's decomposition, induces, in presence of relatively high working temperatures (in the range of $80°C$) the crystallization and growth of spherulitic structures that scatter light and decrease clarity. These grains act as insulating chromophores, which alter the spectral reactivity of the polymeric mixture and hinder the charge separation and electrical transfer.

Finally, the goal of encapsulation is to avoid the diffusion of oxygen and water vapor through microscopic pinholes and diffusion paths. The fabrication of OPDs or OSCs in inert environments such as a glove box can limit the initial presence of these reactive species and the combination of a good encapsulation with savvy production processes can help to improve the lifetime of the devices and their mechanical stability [54], [55].

4.1.2 Encapsulation Requirements

Since OLEDs and TFTs are now present in commercial applications, their encapsulation requirements are quite clear and can be defined in terms of Water Vapor Transmission rate (WVTR) or Oxygen Transmission Rate (OTR). As an example, for

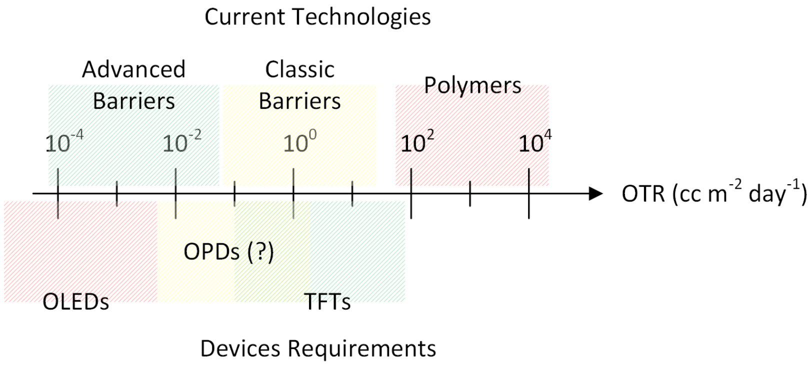

Figure 4.1: The schematic summarizes the barrier strength requirements for organic devices and what is currently achievable with the available technology. Simple polymeric encapsulations are not enough for any organic device, while classic thin film barriers suffice for TFTs. No rigorous study has been conducted on OPDs, rendering the requirements uncertain, albeit confined in a reasonable range

OLEDs, these figures should be confined in the range of $10^6 \rightarrow 10^4 gm^{-2}day^{-1}$ and $10^5 \rightarrow 10^5 cm^3m^{-2}day^{-1}$, respectively. For organic solar cells, the requirements are not yet well defined, although they can be roughly approximated to the ones of the OLEDs, given the similar material stacks and layer thicknesses [54], while for Organic Photodiodes no previous research effort can be found. It has to be noted that the needed barrier effectiveness can be defined through application oriented criteria: OLEDs for displays and solar cells are supposed to work uninterrupted for several months and up to years.
Conversely, OLEDs and OPDs for analytical applications, for instance for point-of-care biological applications, can be short-lived. Here we propose a working definition for Organic Photodiodes on flexible substrates for analytical applications, considering a possible encapsulation technique as viable, if after one week out from inert atmosphere (which could be a glovebox, as well as a vacuum package) the device still preserves at least half of its original photosensitivity. Figure 4.1 shows the range of obtainable transmission rates with current technologies, as well as the barrier requirements for OLEDs and TFTs, as well as a guessed value for OPDs, which will be confirmed at the end of the chapter.

In addition to provide insulation from oxygen and water, an encapsulation layer must also be transparent, mechanically robust, and eventually flexible, in case of conformal devices. These last features render the glass transition temperature (Tg) a very important characteristic of the material, since it is a measure for chain stability. In particular climatic conditions, such as torrid summers, the mechanical integrity and the barrier effectiveness can be compromised in case the material presents a low Tg, rendering the device temporarily unusable or leading it in a state of irreversible malfunction.

In summary, the encapsulation materials should present easy processability, high dielectric constant, low water absorptivity and permeability, high resistance to ultraviolet (UV) degradation and thermal oxidation, good adhesion, mechanical strength and chemical inertness [24]. Inorganic materials are most commonly used as encapsulanting agents since they exhibit a good combination of the above mentioned properties and they have an established history of acceptable durability and ease of processing. Nevertheless, thick oxides are brittle and cannot be used in conformal application. Furthermore, they tend to have hydrophilic behavior, being partially ineffective to block water permeation. Organic barrier materials have few advantages over their inorganic counterparts, among which we can count an even superior ease of deposition, energy level tuning, they are easy to dispose and, in general, they present a lower negative impact on the environment [55]. They also tend to be partially hydrophobic, representing then good barriers to water, although their porous nature is favorable to the diffusion of oxygen. As evident by just listing the characteristics of the two different kinds of encapsulation, the use of either on or the other cannot lead to effective barriers.

In fact, although single layer encapsulations are attractive due to their simplicity in processability compared to multilayer encapsulations, they create efficient pathways for water and/or vapor to penetrate. This phenomenon can be described by many analytical models, among which the most widely accepted ones are based on a solution-diffusion models [54], [122]. In the case of organic barriers, for instance, the gas molecules dissolve in the layer and start a diffusion process due to a concentration gradient in the barrier. The permeation rate is inversely proportional to the barrier thickness. But just increasing the thickness is not an option due to higher cost, longer processing time and enhanced reflection of light.

Concerning the materials used, most state of the art inorganic single layer encapsulations consist of Si, Al2O3, SiO2, MgO typically deposited by Atomic Layer Deposition [123]. It can be shown that simply increasing single layer thickness leads to a non-zero asymptotic value of OTR controlled by the number of defects present in the barrier layer [54], [124]. Due to these defects, single layer encapsulations are intrinsically inefficient, and the realization of successively stacked inorganic layers is a partial solution to the issue: the defects of the underlying layer are covered by the successive one.

If a multilayered inorganic barrier is accompanied by an insulating polymeric layer, the drawbacks of each typology of material are compensated by the other, and the strengths add up. As a result, hybrid organic/inorganic structures are by far the most

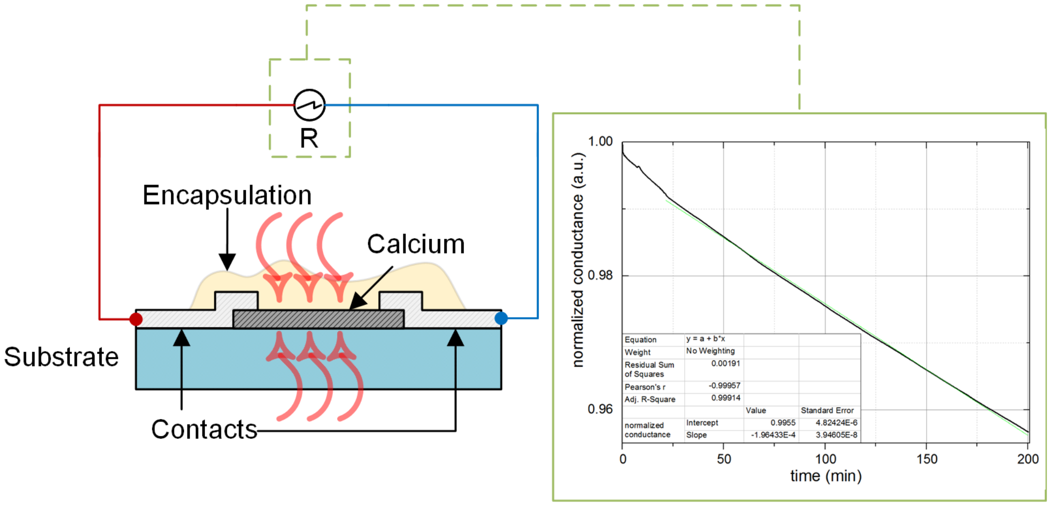

Equation	y = a + b*x		
Weight	No Weighting		
Residual Sum of Squares	0.00191		
Pearson's r	-0.99957		
Adj. R-Square	0.99914		
		Value	Standard Error
normalized conductance	Intercept	0.9955	4.82424E-6
	Slope	-1.96433E-4	3.94605E-8

Figure 4.2: Typical configuration used to perform a Calcium Test. The resistance of the encapsulated calcium is measured over time, and the slope is a function of the permeation rate

efficient and most widely used. Polymers such as Parylene, PMMA, PVA and PS are commonly used as organic interlayers and WVTR as low as $10^{-6} gm^{-2} day^{-1}$ can be readily obtained [55], [123], [125].

4.1.3 Calcium Test

Once the material stack has been decided and the processing technique selected, the encapsulating barrier must be tested, in order to find the permeation rates. In the past, colorimetric permeation assays were used for the estimation of WVTR. These methods, however, are relatively expensive and limited to a sensitivity of $5 \times 10^{-4} gm^{-2} day^{-1}$ for (WVTR)[126]. To measure lower Transfer Rates, in the last decade, the socalled *Calcium test*, a method developed by Paetzold et al. [127] in 2003, has been gaining increasing attention. The method allows measurement of WVTRs down to $10^{-6} gm^{-2} day^{-1}$ by in situ monitoring of corroding Calcium (Ca) films. The working principle is relatively simple and is based on a fundamental observation: since Ca exhibits a very low work function, it is highly reactive and prone to quick oxidation in presence of water or oxygen. Indeed, the description of the reactions of Calcium with oxygen and water, as described by Schubert et al. [126] leads to:

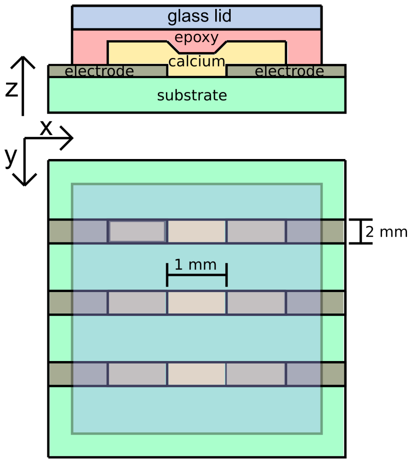

Figure 4.3: Layout for the realization of the Calcium test. The resistance of three separate calcium lines is measured in parallel and averaged at the end of the experiment

$$2Ca + O_2 \rightarrow 2CaO \tag{4.1}$$

$$Ca + H_2O \rightarrow CaO + H_2 \tag{4.2}$$

$$CaO + H_2O \rightarrow Ca(OH)_2 \tag{4.3}$$

Calcium is then promptly oxidized and its resistivity will proportionally increase. Constantly monitoring the change in resistance of a Ca stripe with known geometrical parameters, under a certain encapsulation method, leads to a curve that can be used to extrapolate the Transmission rates. Although the comparison of the degradation curves already serves the purpose of highlighting qualitative differences between barriers (the slower the degradation, the better the encapsulation), Paetzold developed an empirical formula quantitatively relating the slope of the Calcium conductance over time to the permeation rate of a generic species in gas form [127]:

$$P = -n\frac{M(reagent)}{M(Ca)}\delta\rho\frac{l}{b}\frac{d\left(\frac{1}{R}\right)}{dt} \tag{4.4}$$

Where n is the molar equivalent of the degradation reaction. According to equation 4.3, each Calcium atom can react with half an oxygen molecule (n = 0.5) and with up to two water molecules (n = 2). M(reagent) and M(Ca) are the molar masses of the permeating agents and of Ca respectively, denotes the Ca resistivity, is the density of Ca, l is the length and b is the width of the Ca layer stripe. The last part of the equation takes in to account the dependence of the permeation rate on the change in resistivity of the Ca layer.

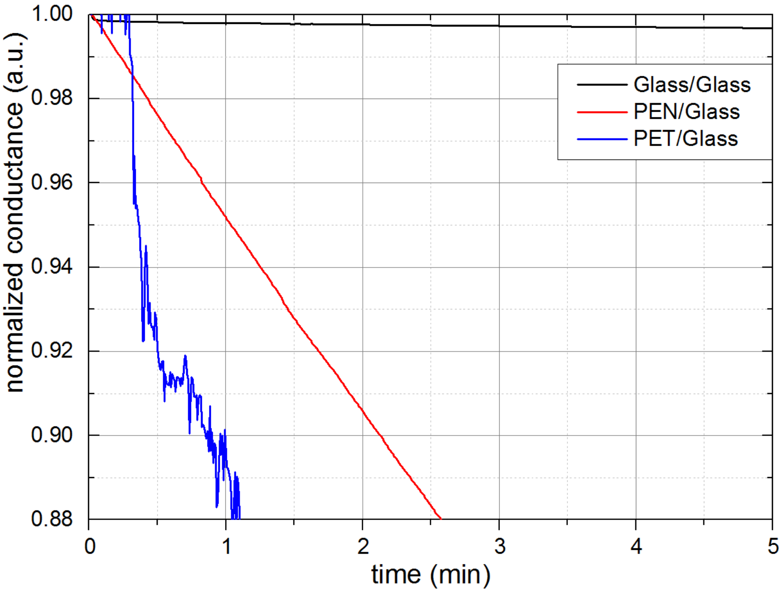

Figure 4.4: Comparison of normalized conductance for different substrates, encapsulated with a glass lid and epoxy glue

Figure 4.2 shows a typical Calcium test setup. A thick Calcium layer (>100 nm) is deposited on the desired substrate, then a pair of stable metallic electrodes are evaporated to contact the calcium and the encapsulation is performed. Silver is typically used as a contact electrode, given its stability to oxidation and its contained cost, if compared to gold or platinum [127]–[129] In our particular case, depicted in Figure 4.3, three stripes of 200 nm thick, 1 mm long and 2 mm wide Ca stripes were thermally evaporated on top of 100 nm thick Al layers, previously structured on the chosen substrate.

Although many researchers prefer Silver to Aluminum [127]–[129], in our experience, as well in some previous report, no significant difference in the permeation rates calculated with Al or Ag were encountered [126]. The choice of a relatively thick Ca layer (200 nm) was dictated by the will of measuring the degradation of calcium for very bad encapsulating barriers as well: this thickness guarantees at least 20 minutes of measurable resistance before Ca is completely transformed in CaO.

The thermal evaporation setup is placed inside a glovebox, which is an inert atmosphere with less than 1 ppm of H_2O and O_2, therefore the encapsulation could be calmly performed in a controlled environment before transferring the samples to room environment. Figure 4.2 shows a simplified circuital schematics to perform the resistance measurement. At this stage, the calcium test has been employed to test the permeability of the flexible substrates: PET and PEN are, in fact, porous materials and they are expected to perform poorly as barriers. To achieve this goal, the Ca-test

M(H_2O)	**M(O_2)**	**M(Ca)**	δ	ρ	l	b
18 g/mol	32 g/mol	40 g/mol	$1.55 g/cm^3$	$3.4 \times 10^{-6} \Omega m$	1 mm	2 mm

Table 4.1: Summary of the parameters employed for the evaluation of the permeation rates

structure was evaporated on top of PET and PEN film and a “Perfect barrier” made of epoxy resin and a glass lid was prepared on top. In this way, since the top side of the sample is well encapsulated, any deterioration of the conductivity of calcium is due to H_2O and O_2 permeating from the substrate itself.
After encapsulation, the samples were transferred to a measurement setup consisting of a sourcemeter controlled by a LabVIEW computer program. The sorurcemeter was connected to the electrodes with the use of crocodile clamps and the resistance of the stripes was measured at a repetition rate of 2Hz, applying a DC voltage of 100 mV.

Figure 4.4 presents a comparison of the normalized conductance curves for Calcium tests on the three considered substrates. As expected, the conductance of Ca on PET and PEN dropped significantly after few minutes, hinting to the poor barrier capability of simple polymeric films. After the fit to Formula 4.4 and the calculations of the parameters, the resulting oxygen permeation rates are $3 \times 10^{-3} \frac{g}{m^2 d}$, $3.9 \times 10^{-1} \frac{g}{m^2 d}$ and $1.74 \frac{g}{m^2 d}$ for glass substrates, PEN substrates and PET substrates, respectively. These results, in line with similar studies reported in literature [126], indicate that although the top encapsulation (epoxy and glass lid) is an almost ideal barrier, the polymeric substrate do not substantially hinder the permeation of oxygen and water.

4.1.4 Degradation of the JV characteristics

To verify whether these values of OTR are sufficient for the encapsulation of OPDs, a series of photodiodes has been realized onto the three different samples with the “ideal barrier” encapsulation. As a negative control, a series of OPDs was fabricated also on glass, but without any top encapsulation. The results are summarized in Figure 4.5, which shows the evolution of the JV characteristics of these diodes on a extended timespan of 28 days. As expectable, the samples encapsulated with epoxy and a glass lid presented little to no variation in terms of biased photocurrent and dark current, while other parameters, such as the serial resistance have been degrading over time. This condition is most likely due to the oxidation of the cathode, as this phenomenon is hard to avoid even with more advanced encapsulation techniques [54].

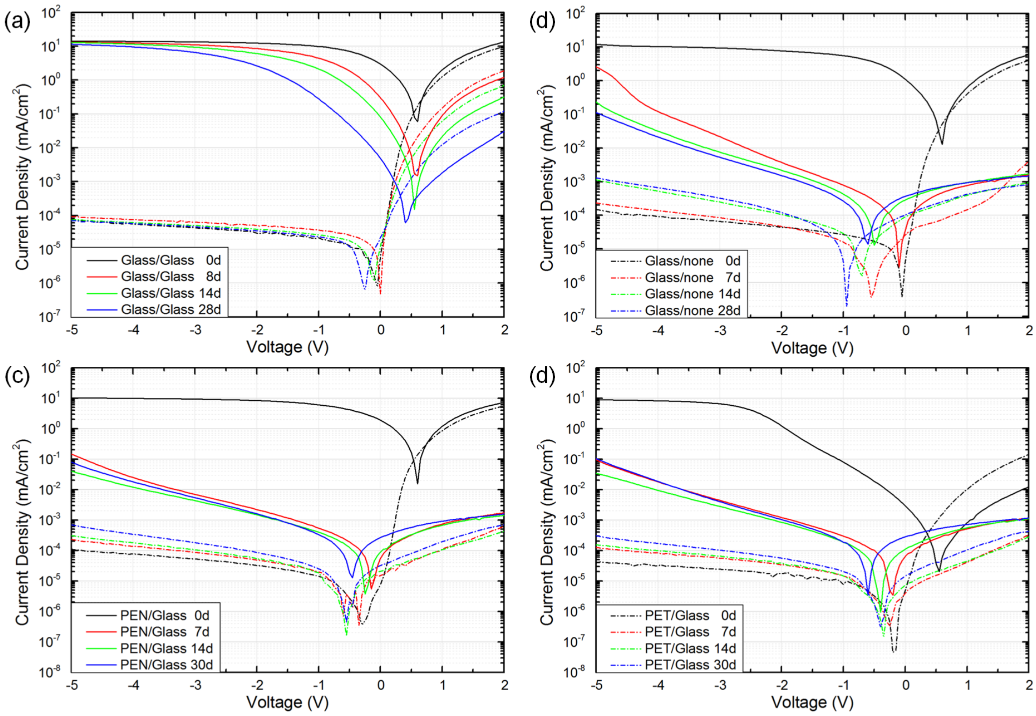

Figure 4.5: Modification of the JV characteristics over a time window of one month for OPDs on glass substrate with epoxy/glass encapsulation (a) and without any encapsulation (b). Panels (c) and (d) show the same study carried out onto OPDs realized on PEN (c) and PET (d) substrates, respectively

In contrast to glass, however, the OPDs fabricated on PEN and PET with glass encapsulation underwent a significant modification of the illuminated current under bias, leading to a diminution of more than 2 orders of magnitude in less than one day. The behavior of these *encapsulated* samples is comparable if not worse than what can be observed by the JV characteristics of devices fabricated on glass and without any encapsulation.
As it is possible to infer from the JV characteristics, the EQE of the devices fabricated on glass did not manifest any particular change in the considered timespan, while the EQE of the diodes on flexible substrates are subject to a consistent drop when measured after one week. In Figure 4.6 is plotted the EQE of devices produced on PET in different time points, and the evolution of the curves shows how not only the intensity of photoconversion is decreased, but also the peak is shifted in the spectrum. These findings are compatible with the alterations expected in both the P3HT and PCBM due to backbone decomposition and oxygen absorption, respectively.

Among the many parameters representative of the quality of a photodetector, the

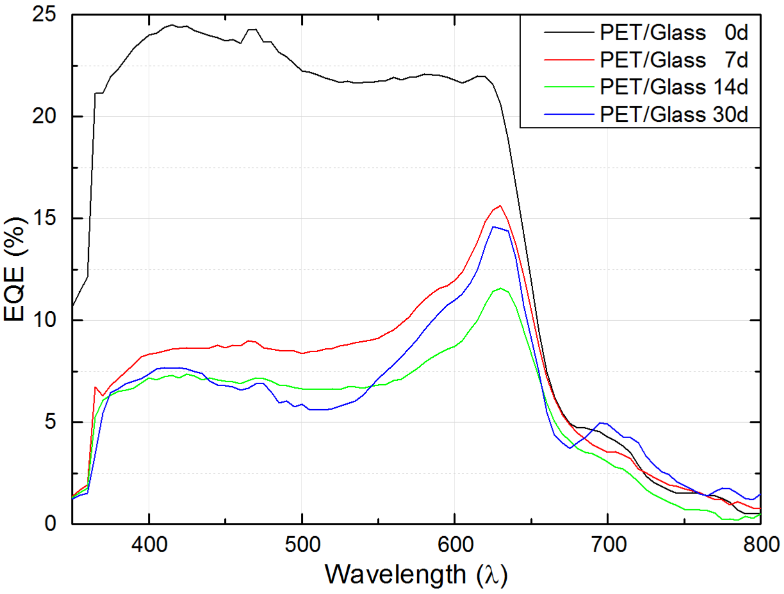

Figure 4.6: Degradation of the EQE at 0V as a function of time

easiest to analyze in a systematic and automated fashion are the ones related to the JV characteristics and to the EQE. Particularly, we have considered for our study the variation of Illuminated and dark current under bias, the serial and shunt resistance, the open circuit voltage and the average EQE in the visible range. Figure 4.7 shows all the parameters extracted from the JV curves plotted in Figure 4.5 and gives, in a single glance, an idea of how dramatic is the difference between OPDs fabricated on glass substrates and the ones fabricated on plastic. After 4 weeks, OPDs on glass substrates with glass encapsulation remain at 85% of their original IC. For OPDs on PEN and PET with glass encapsulatio,n a drop of the illuminated current to nearly 0.1 mA/cm^2 after only 3 days can be encountered. This degradation is even worse than OPDs on glass substrates without any encapsulation. The serial resistance (RS) was derived from the dark current slope in the range of 1 V to 2 V. Ideally it should be as small as possible, however, OPDs on flexible substrates or on glass without any encapsulations, present an a rise in serial resistance to very high values after a few days.

Shunt resistance (RSH) was derived from the dark current slope in the range of -5 V to -2 V. This parameter should ideally be close to infinity and stay as stable as possible. Consistently, OPDs on glass with glass encapsulation exhibit very high RSH values and keep them during the whole long time measurement. OPDs on flexible substrates show a fast drop in shunt resistance in a few days time and settle two orders of magnitude below the reference values obtained on glass.

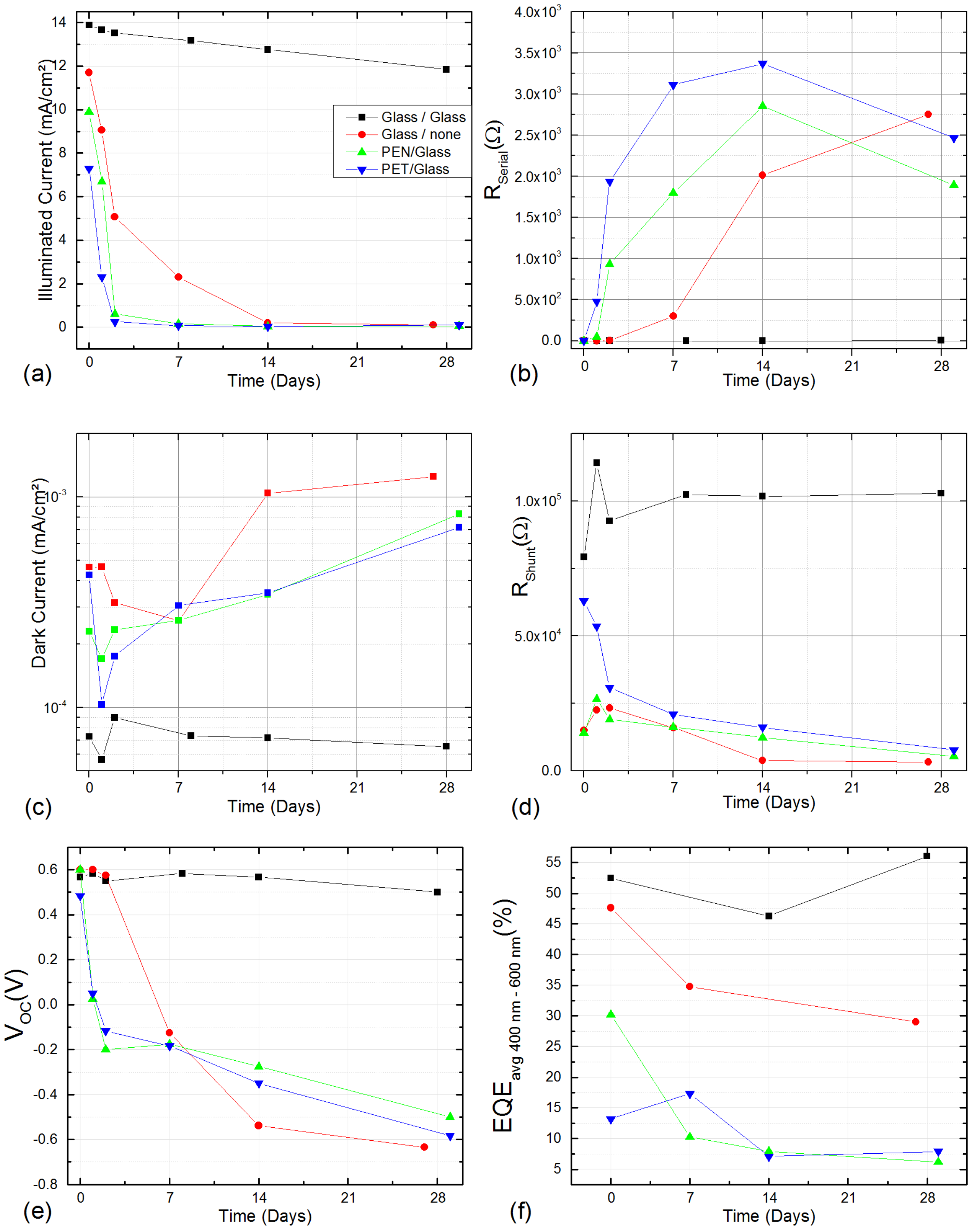

Figure 4.7: Evolution of the most important parameters for an OPD over a timespan of one month. The figure presents the Illuminated current (a), the serial resistance evaluated in the forward bias region (b), the dark current at -4 V (c), the shunt resistance evaluate under dark conditions (d), the V_{OC} and the average EQE (e)

Furthermore, Figure 4.7 (e) presents the open circuit voltage for all the considered photodiodes. Once more, the glass encapsulation on glass yields an almost perfect encapsulation, with a very small drop in the V_{OC} after one full month of shelf life. Vice versa, the V_{OC} of all remaining devices drops quickly to zero, degenerating to negative values when the effects of the cathode's oxidation add up to the degradation of the photoactive layer.

Finally, Figure 4.7 (f) presents the external quantum efficiency (EQE) averaged over a region of 400 nm to 600 nm. The drop of EQE follows with fidelity the drop in illuminate current and shows how, overall, devices on glass substrates, even without encapsulation, present better resistance to environmental agents than the encapsulated plastic based ones.

4.2 In-Line Thin-film Encapsulation

4.2.1 Encapsulation of OPDs on glass substrates

As discussed in the previous section, the typical methods used to preserve the functionality of organic devices over time rely on the use of hybrid resins a rigid glass lids.These materials are easy to process thorough drop casting or screen printing and have high encapsulation effectiveness and yield to "perfect barriers" towards both oxygen and water vapor. However, they present a major disadvantage: they form a thick rigid layer on top of the electronic device. For many stand-alone applications, such as Solar Cells and OLEDs for illumination purposes, the latter aspect does not constitute an issue, being instead a strength, since it guarantees enhanced mechanical stability. For flexible devices, however, this path cannot be followed, since it would hinder the flexibility and significantly increase the weight of the structure. Furthermore, the thickness of the resins can be up to several hundred μm, increasing the insertion losses in multilayered opto-electronic systems. The main goal of this section is to verify whether scalable, in-line and flexible encapsulation methods can be developed and applied to the fabrication of OPDs and whether the vapor transfer rates are low enough to guarantee a preservation of half of the photosensitivity after one week of shelf life. As a first trial to obtain working encapsulations, barriers have been produced with inorganic layers. The deposition has been performed through high rate electron beam evaporation of SiO_2 and/or AlO_3, a fast method normally implemented in evaporation chambers compatible with in-line processing. The major drawback of this technique resides in the high energy needed to allow the electron beam to dissociate the oxides and let them sublimate in order to deposit on the sample. When the material is separated from the crucible, it is still characterized by an high kinetic energy, which might damage the underlying materials. This concern was demonstrated to be true in the case of AlO_3, where the electron beam needed to be utilized to its maximum power: the devices encapsulated with AlO_3 only, presented a photocurrent on average 80% lower than all the other considered devices. SiO_2, on the other hand, was easier to sublimate and the process did not procure any damage to the organic layers. To verify the effectiveness of these thin inorganic barriers, the oxides have been used by themselves (200 nm thick AlO_3 or 200 nm thick SiO_2) and then in a stacked structure where SiO_2 was deposited first, in order to avoid damages due to the impact of the highly energetic AlO_3. For comparison's sake, the overall thickness of the encapsulating barriers was always kept constant to 200 nm, even when oxide layers were stacked together. The cases considered in this study are the alternance of two oxide layers (100 nm SiO_2 and 100 AlO_3), four layers (two repetitions of 50 nm SiO_2 and 50 AlO_3) and eight oxide layers (four repetitions of 25 nm SiO_2 and 25 AlO_3). As visible in figure 4.8, although the layer thickness of all oxide encapsulations was kept constant, multilayers with four and eight layers showed big improvements over single layer encapsulations in respect to retainment of the photocurrent level, especially during the the first week of experiments. As anticipated by the theory, however, the transfer rates are not low enough to be considered as sufficient encapsulations. In the same direction, a selection of organic single layers materials has been utilized for the realization of encapsulating layers. The organic materials were obtained by spray-deposition and their thickness has been kept constant to 1 μm. The spray-deposited Polystyrene, ABS, PVA and PMMA were compared to the "ideal barrier" encapsulation and to a 20 μm thick dropcasted hybrid polymer (Ormostamp). Figure 4.9 shows the normalized illuminated current over time for all the encapsulating polymers, along with the reference OPDs and non-encapsulated diodes. The most surprising outcome is that not only the polymers did not increase the lifetime of the OPDs with respect to the non-encapsulated cases, but they further reduced it, most likely because of non controllable chemical reactions at the interface between the OPD and the spray-deposited polymer.

The only exception to this pattern is constituted by the Ormostamp, which is, however 20 times thicker than the other polymers (albeit still one order of magnitude thinner than the epoxy resin) and the reduction of the transfer rate is totally consistent with the solution-diffusion model.

The next natural step is the combination of all the polymeric layers with the best oxide choice (constituted by the alternation of eight 25 nm thick layers), in order to identify the polymer which is best suitable to achieve hybrid encapsulations. The

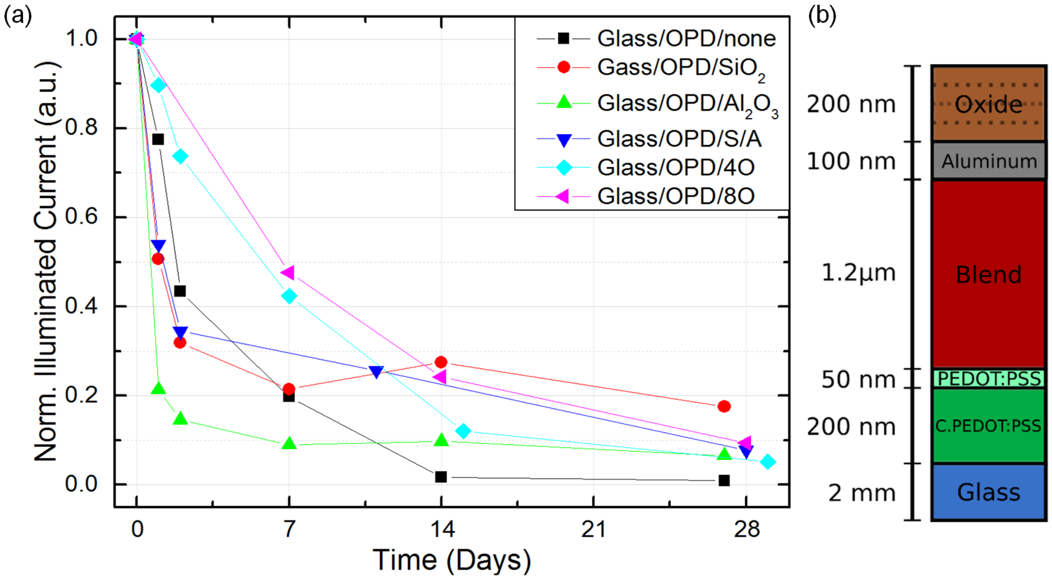

Figure 4.8: (a) Degradation of the illuminated current over time for OPDs fabricated on glass and with a thin evaporated oxide encapsulation. The blue, cyan and magenta markers represent stacks where Silicon Oxide and Aluminum Oxide are alternated once (a total of two oxide layers), twice (a total of four oxide layers) and four times (a total of eight oxide layers). In any case, the total thickness of the oxide is kept equal to 200 nm. Panel (b) depicts the material stack used in this experiment

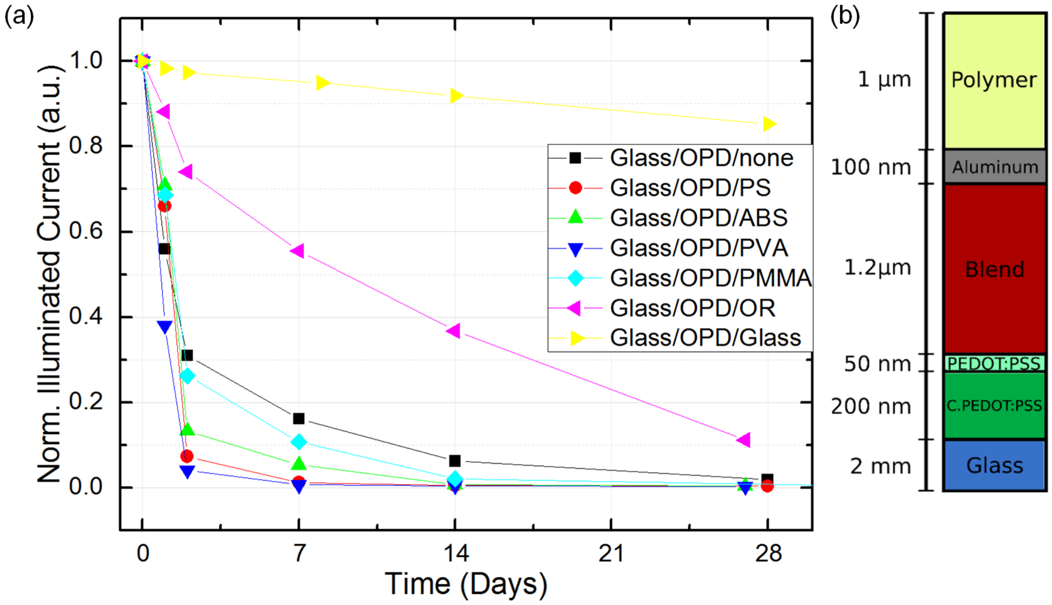

Figure 4.9: (a) Degradation of the illuminated current over time for OPDs fabricated on glass and with a thin spray-deposited polymeric encapsulation. Panel (b) depicts the material stack used in this experiment

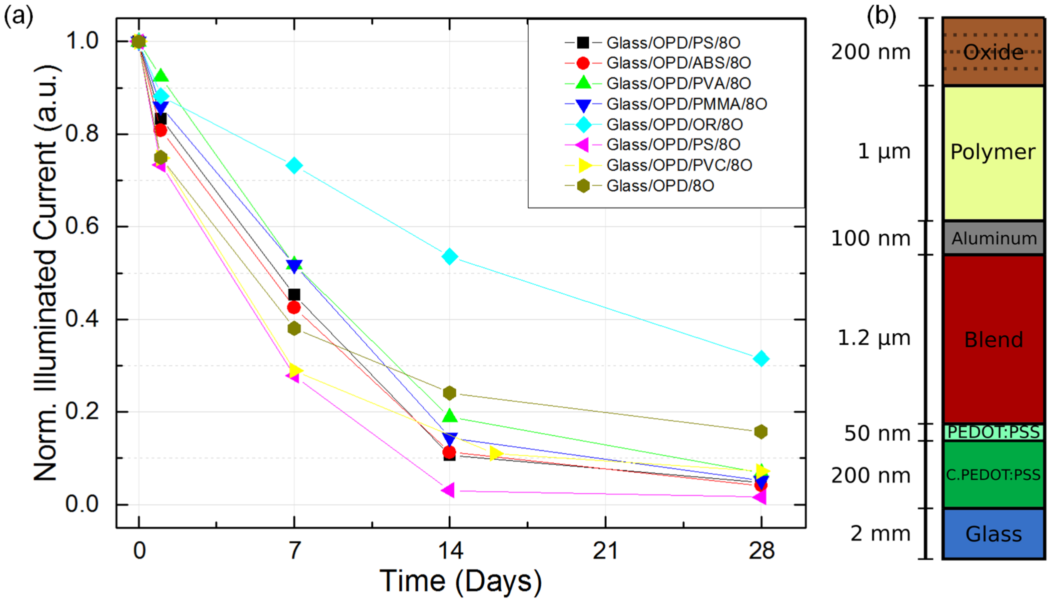

Figure 4.10: (a) Degradation of the illuminated current over time for OPDs fabricated on glass, with a thin spray-deposited polymeric encapsulation and eight alternated oxide layers. Panel (b) depicts the material stack used in this experiment

results, presented in Figure 4.10, show how the combination of Ormostamp with eight oxides, yields a substantially better encapsulation effectiveness with respect to any other polymer. Nevertheless, also PMMA respects the lifetime benchmark we set at the beginning of the chapter, keeping the photocurrent of the OPDs to drop below half of its initial value after the first week of operation. This result is remarkable, since PMMA is an easily available polymer and it is already commonly used for organic and printed electronics (e.g. as insulator for transistors and capacitors).

Finally, we replicated the same experiment with inverted photodiodes (i.e. photodiodes where the cathode is evaporated on the substrate and the rest of the device is built on top of it). In this configuration, the most reactive electrode is placed to the bottom of the device and is less exposed to the penetration of oxygen and water vapor [130]. In such a structure, the effect of metal oxidation is limited and most of the impairment of the performances of the OPD is due to the unavoidable degradation of the polymer, resulting in an extended device lifetime [54]. The devices were fabricated evaporating 100 nm of Aluminum as bottom electrode, followed by the spray deposition of the active layer. Since the P3HT:PCBM blend is strongly hydrophobic, in order to proceed with the spray-deposition of the PEDOT:PSS electrode on top, a mild plasma has been performed, as reported in other contexts [117], [131]. The results are summarized in Figure 4.11 and show how inverted OPDs on glass, encapsulated with a combination of eight oxide layers and Ormostamp or PMMA can retain their

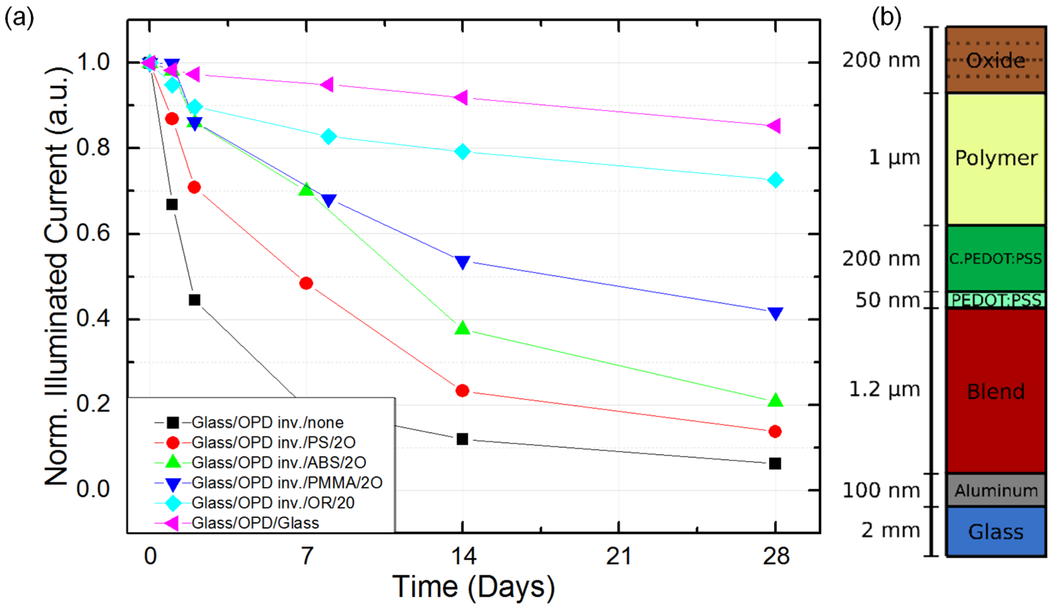

Figure 4.11: (a) Degradation of the illuminated current over time for inverted OPDs fabricated on glass, with a thin spray-deposited polymeric encapsulation and eight alternated oxide layers. Panel (b) depicts the material stack used in this experiment

functionality up to one month of shelf life.

4.2.2 Encapsulation of OPDs on flexible substrates

The results presented in the last subsection are remarkable, although they have only been obtained on rigid substrates. The evolution to flexible substrate is not necessary straightforward, for several reasons. Primarily, in the former case the glass substrates provided an almost ideal bottom encapsulation: the process concerns had only to be directed towards the attainment of an effective top encapsulation. This assumption does not stand in the case of flexible substrates. In fact, we have shown how PEN and PET are by themselves very ineffective barriers (the transmission rates are more than three orders of magnitude higher than the ones of glass). Given the OTR of the two polymeric substrates ($3.9 \times 10^{-1} \frac{g}{m^2 d}$ and $1.74 \frac{g}{m^2 d}$, for PEN and PET, respectively), PEN represents a natural choice, since it is four times a better barrier than PET.

The direct fabrication of OPDs on PEN substrates, yielded disastrous outcomes: none of the fabricated devices with in-line encapsulation, kept its normalized photocurrent above 50% of the original value for more than two days. A first step towards better devices is to create a “bottom encapsulation” as well as the usual top one. A first attempt, presented in Figure 4.12 introduces the evaporation of different oxide layers on the PEN prior to the fabrication of the OPD. The devices fabricated on this “reinforced

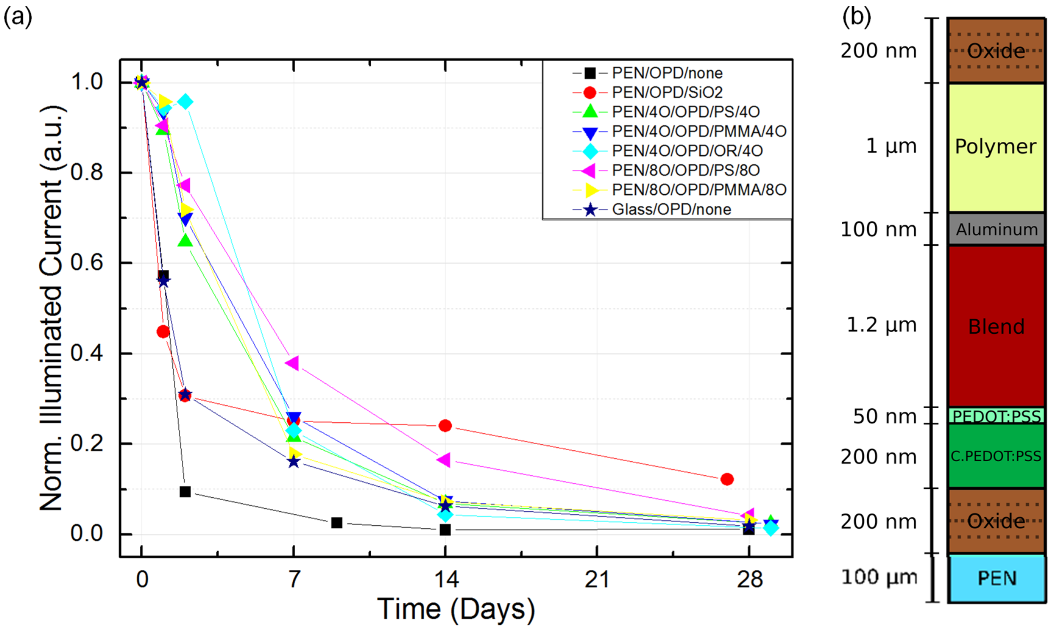

Figure 4.12: (a) Degradation of the illuminated current over time for OPDs fabricated on PEN, with different combinations of oxides and polymers. Panel (b) depicts the material stack used in this experiment

PEN" all still retain more than 20% of their original photosensitivity after one week, while the non-encapsulated ones fall below 5% in the same timespan.

To further stress the concept of bottom encapsulation, we performed an experiment where on top of the PEN substrate, a 5 to 15 μm thick layer of PMMA was spray-deposited, followed by the evaporation of 200 nm thick oxides layers. Above this bottom encapsulation, the rest of the photodiode was processed and protected with the same material stack used on the bottom (5 to 15 μm PMMA and 200 nm oxide). The results of this strategy can be extrapolated by Figure 4.13, which reports the evolution of the normalized photocurrent of these devices with respect to time. This stack with a sandwiched encapsulation is able to achieve the minimum results we set at the beginning of the chapter and can be considered as a satisfactory barrier. Notably, increasing the thickness of PMMA led to an amelioration of the durability of the devices (and, hence, a decrease of the transmission rates), as to be expected from the solution-diffusion model.

Finally, as the inverted structure demonstrated to be particularly effective on glass, the same concept has been applied to PEN substrates. The inverted OPDs were encapsulated with a "sandwich encapsulation approach" similar to the one reported in Figure 4.13 and characterized on a one month time-span. The percentage of photocurrent after one week was very similar to the one obtained in the non-inverted case, but, strikingly, the inverted structures are able to retain 40% of their photosensitivity after 2 full weeks and resulted to be still viable at the end of the month, when the photocurrent had decreased to 30% of the original value, but was stable and measurable.

One last observation on the Ormostamp polymer is due. Although in many of the experiments it rendered the best barrier in terms of vapor transmission rates, its use in flexible and conformable devices is limited. When exposed to UV light, the polymer crosslinks, and albeit this leads to a more effective barrier, it also makes the polymer stiffer and brittle. The risks of delamination or unintentional cracking during handling are very high, and only the 30% of the devices encapsulated with Ormostamp were working at all after fabrication. This aspect, along with the poor scalability of the Ormostamp process, does not allow us to consider it as a possible solution for the realization of in-line encapsulation processes. A thick layer of PMMA, however, is able to obtain similar encapsulation properties, without sacrificing transparency, scalability and flexibility.

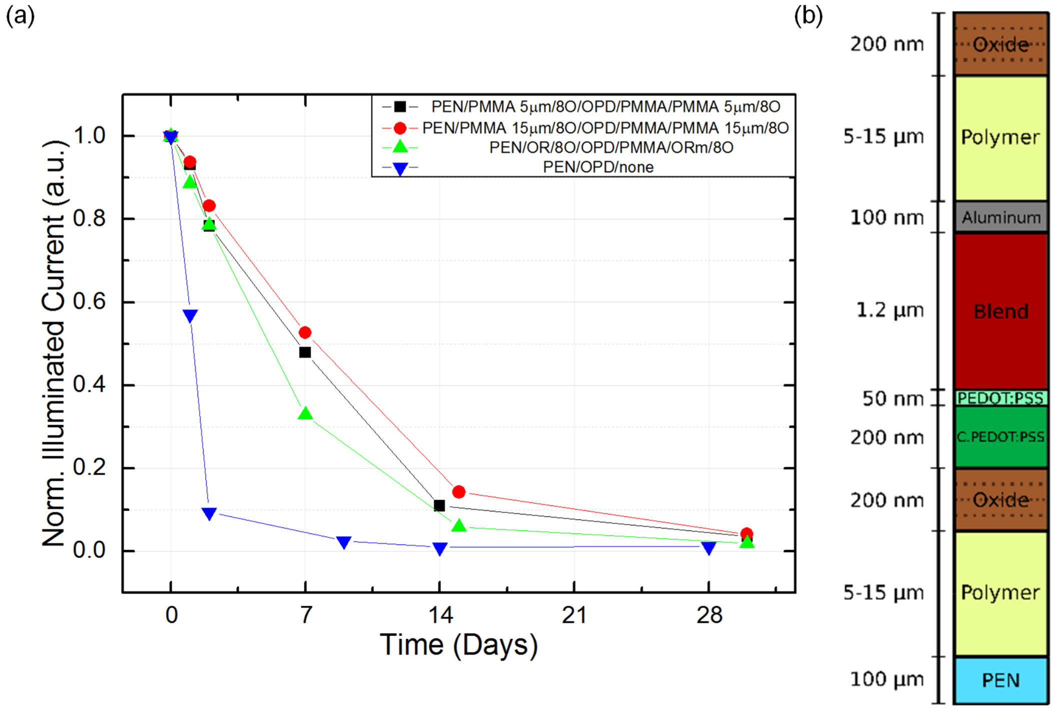

Figure 4.13: (a) Degradation of the illuminated current over time for OPDs fabricated on PEN, with eight alternated oxides and different polymer thickness. Panel (b) depicts the material stack used in this experiment

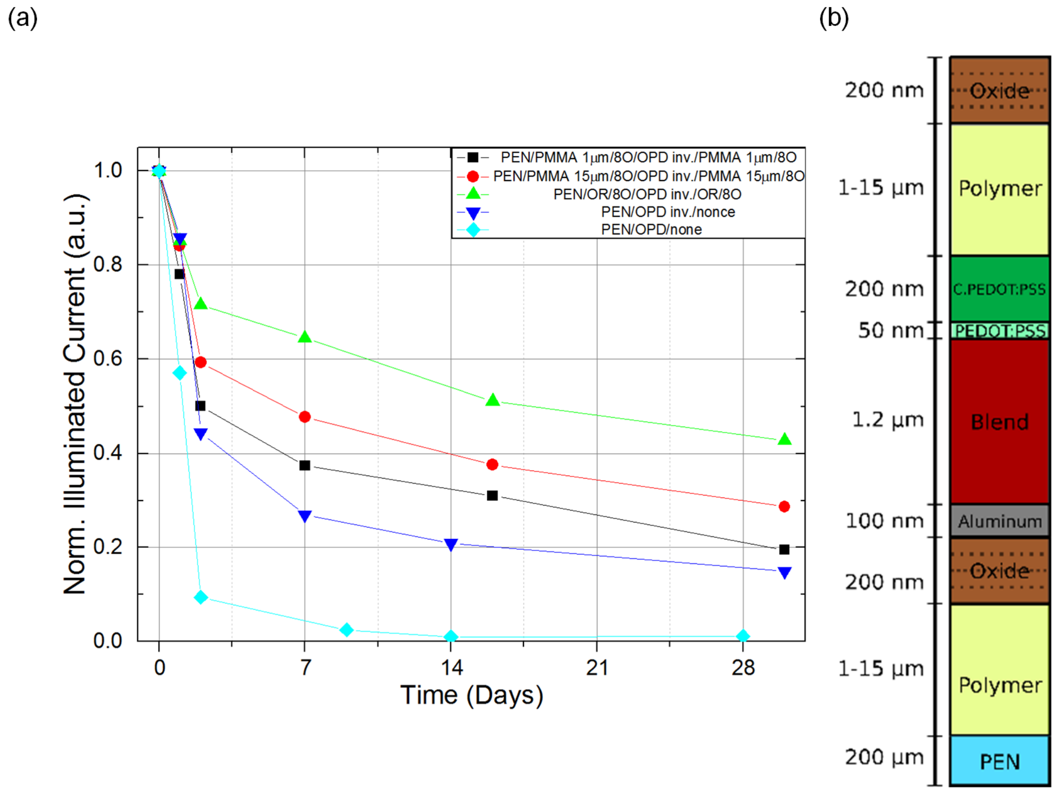

Figure 4.14: (a) Degradation of the illuminated current over time for inverted OPDs fabricated on PEN, with eight alternated oxides and different polymer thickness. Panel (b) depicts the material stack used in this experiment

4.2.3 Estimation of *effective Transmission Rates*

Since the necessity of a bottom encapsulation is now clear, the Calcium test on flexible substrates can be reiterated including this new finding. At this purpose, the usual 200 nm thick layer of Calcium was evaporated on top of bare PEN, PEN with eight oxide layers and PEN with an hybrid structure made of 8 oxide layers and a thick PMMA film. The evolution over time of the normalized conductance of the metal lines on the different substrates are reported in Figure 4.15. While a "non-reinforced" PEN reduces its conductance to half of the starting value in less than 15 minutes, the conductance of the flexible substrate with the inorganic barrier reaches the same level in 100 minutes and, finally, the hybrid barrier keeps this quantity above 50% for circa 120 minutes. From the slopes of these curves, it is possible to extract the OTRs, which are $9.3 \times 10^{-2} \frac{g}{m^2 d}$ and $8.4 \times 10^{-2} \frac{g}{m^2 d}$ for the inorganic and the hybrid barriers, respectively.

Finally, the plot of the evolution of the photocurrent of the OPDs over time encapsulated with the same material stacks utilized for the Calcium test, closely resembled

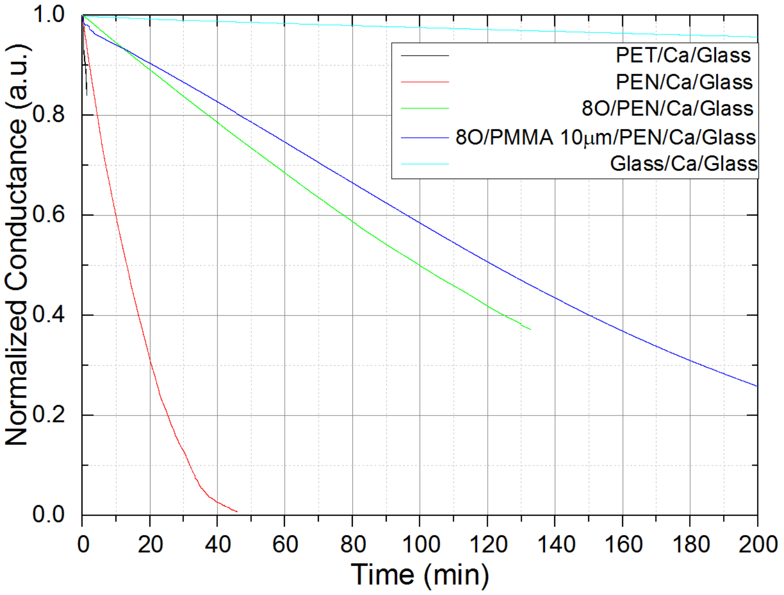

Figure 4.15: Normalized conductance curves of Ca test conducted on the most complex barriers

the decay of conductance due to the oxidation of calcium, although on a totally different time scale. This remarkable similarity, suggested an empirical relationship which could correlate the ability of a given encapsulation stack to retain the photocurrent over time to the OTR, namely:

$$eOTR = c \times \frac{dI_{ph}}{dt} \tag{4.5}$$

The fitting parameter $c = -1.2176(gm^{-2}d^{-1})$ has been found as the average value of the ratios of the OTR to the illuminated currents' slope over time. Using this empirical formula it has been possible to relate the degradation time to an *equivalent Oxygen Transition Rate* which can be used as a figure of merit for the encapsulation quality for any given method. The eOTR for all the inline encapsulation methods evaluated in this chapter are reported in Figure 4.16. The use of a figure of merit such as the eOTR gave us the chance to quantitatively compare all the encapsulation methods developed during the work and to confirm that an inverted structure with hybrid encapsulation based on thick PMMA is the configuration which guarantees the longest lifetime of the OPDs. Furthermore, using the extrapolated eOTRs, it is possible to reply to one of the main open questions of the chapter: what is the minimum OTR necessary to protect the OPD well enough to have still 50% of its original photosensitivity after one week? On PEN, this condition was satisfied by the sandwich encapsulation with $15\mu m$ thick PMMA, which corresponds to an eOTR of $7 \times 10^{-2} \frac{g}{m^2 d}$.

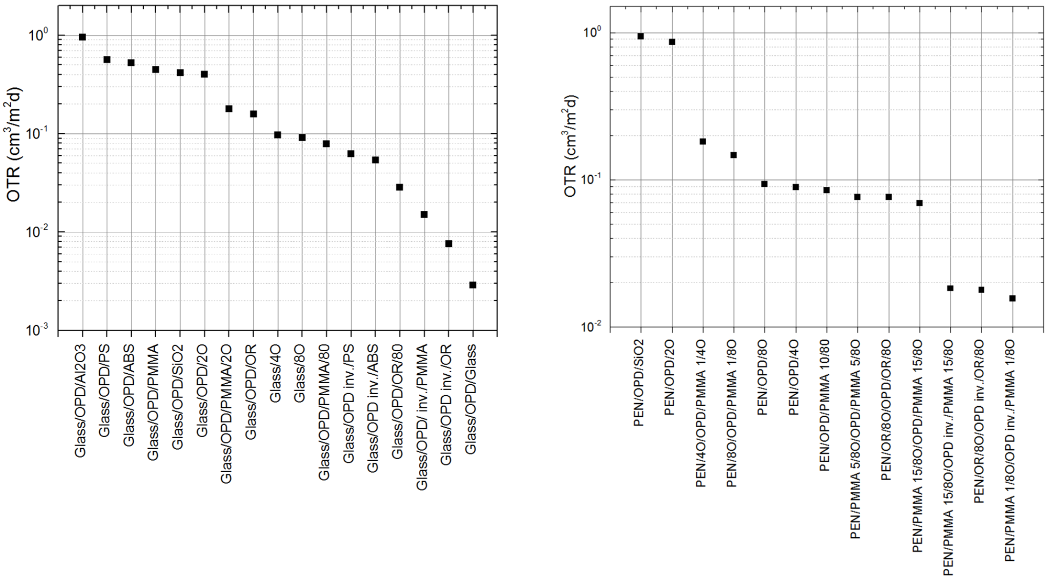

Figure 4.16: The eOTRs evaluated for glass substrates (left hands side panel) and PEN substrates (right hand side panel) are reported.

4.3 Stability and Biocompatibility of Metals in Different Media

4.3.1 Electrodes for Bioelectronics

The integration of organic electronics and optoelectronics with biological systems, such as simple cells or complex tissues can undergo two main general strategies, both of which aim at maintaining the electro-optical properties critical to device performance such as work function, conductivity, and transmittance. The first of these approaches, encapsulation, has been described so far and aims at insulating the electrodes from external harsh environments. The main disadvantage of such strategy, however, is that it prevents the device to be in *direct contact* with the biological system, precluding many applications which might exploit the peculiarities of organic electronics.

A second strategy, which has been more and more frequently pursued in the last years, is the material optimization, which aims at finding materials inherently stable in their functional environment. In any case, devices such as organic-photodiodes (OPD) [43], [44], [91], [112], organic light emitting diodes (OLEDs) [96], [107], [116], organic transistors (OT)[12], depend on keeping high conductivity of the electrodes, and, even more importantly, on the balance of the two electrode's work functions [44], [83]. Moreover, novel applications for sensing and actuation of the bioelectrical and biochemical activity of cells have a high need for transparency to be compatible with established techniques of biological laboratories, such as fluorescence microscopy [13], and as a prerequisite for integration with living tissues or cultures, must be biocompatible.

In this section we will focus on the stability of commonly used electrode materials in bioelectronics when immersed in physiological media, which are, in essence, high saline and biologically active aqueous systems. In such media, the strong polarizability of water gives room for many forms of electrochemical activity, the latter being amplified by the rich ionic composition of biological media, creating an overall environment where metals are very prone to corrosion and oxidation. One of the possible examples includes the readily reduction of Ag+ in presences of Cl- ions, a prevalent component of biological media. Aluminum, like silver, is very sensitive to reduction by aqueous chloride [132] and, given its low work function, is prone to easy and quick oxidation in presence of singlet oxygen. In a similar direction, it has been shown how gold may be dissolved by thiol-containing biological molecules like cysteine and glutathione [133]. Albeit these effects have been observed and reported in many contributions in the last decades, so far no comprehensive and comparative study has been carried out on the implications that these phenomena have on the stability of the main figure of merit for electrodes to be used in organic optoelectronics.

In this section, planar electrodes made of Gold (Au), Silver (Ag), Aluminum (Al) and Indium-Tin-Oxide (ITO) are immersed for one month in different media (DI water, Phosphate Buffer Solution and cell culturing medium). Conductivity, work function and optical transmittance are measured in different steps during the whole timespan and trends about the stability of these key parameters are sketched and analyzed. The selected media are very rich and complex in their ionic and biomolecular composition and range from a control in air, to phosphate buffered saline (a commonly used experimental solution in biology) through Dulbecos culturing medium (a more complex solution closely mimicking internal environment of organisms).

4.3.2 Electro-Optical Stability

The electro-optical characteristics of the chosen electrode materials have been measured after 24h, 48h and 168h (1 week), 336h (2 weeks) and 672h (4 weeks), to provide an exhaustive picture of the occurring phenomena and to be able to extrapolate the presence od eventual trends. However, it must be noted that although all investigated materials remained stable in air over the 4 week period, Au and Ag samples in PBS and medium underwent severe delamination, which prevented a complete set of measurements from being obtained. This factor, commonly observed in thermally evaporated thin Au layers, proves equally problematic for Ag, and points at the necessity to fab-

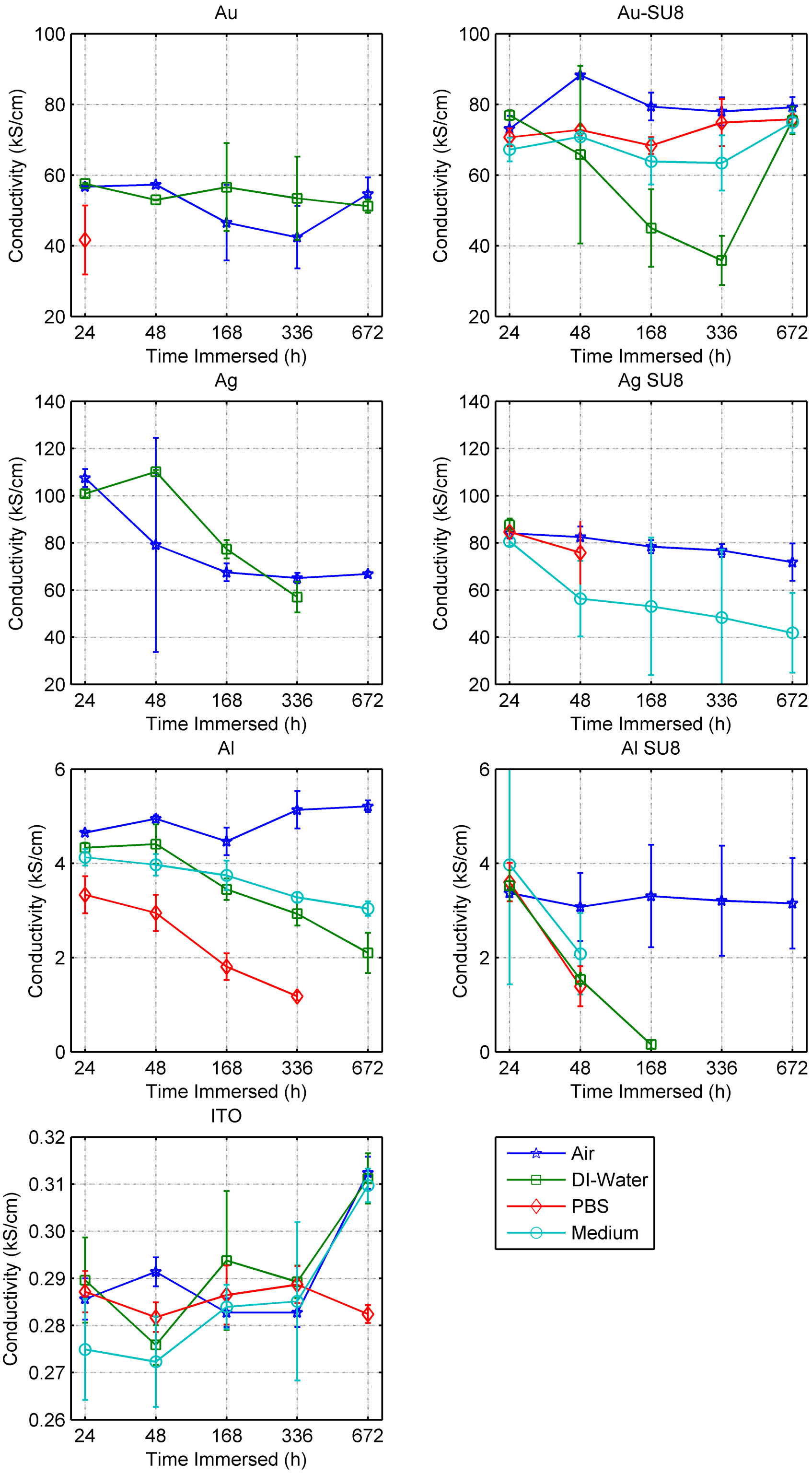

Figure 4.17: Conductivity of the electrode materials in distinct media (See legend) at 24h, 48h, 168h, 336h, 672h. The results for Au and Ag in PBS and Medium are missing due to delamination of the films [134]

ricate an adhesion layer between the metal electrode and the substrate's substrate to preserve the integrity of the film.

Typical solutions encountered in literature involve the deposition of oxidative metals such as Chromium or transparent polymers compatible with the usual fabrication steps employed in the organic electronics research and industry. [17], [135]. Albeit very effective in promoting the adhesion, Chromium presents some major caveats from a bioelectronics perspective, which are related to a poor transparency, entangled patterning procedures including several lithography steps and a proved high toxicity, hence the choice of a polymer over Chromium could be more appropriate. Amongst the many possible polymers to be employed in such application, we selected the commercial negative tone photoresist SU-8 because of its transparency and clarity and its easy patterning through a simple expose and develop process.

Figure 4.17 shows how as long as the material is attached to the glass substrate, the variation in conductivity is somehow limited. Even a reduction of 50% with respect to the original value can be considered acceptable, given the low bulk resistivity of the chosen materials. ITO, on the other hand, has variations below 10% from its initial value in every medium and at any time point, and can be effectively considered stable, given the harsh environmental conditions. The only material undergoing to visible changes in its conductivity is the Al deposited on SU-8, whose resistance become impossible to measure when immersed for few days in any liquid medium. Figure 4.18 shows the change in work function over time for each of the electrode in any media. The first insightful information which can be extracted from the plots is that the work function in air of each material stays almost constant for the whole month. The oxidative effect of the oxygen in the air does not seem to affect the work function of the electrodes, including Al. However, the immersion of the samples in different media caused significant changes in their properties. Particularly, each material, after only 24 hours of exposure to any liquid environment, has been subject to a significant drop in work function. The work functions of Au-glass, Au-SU8, Al-glass and Al-SU8 experience a reduction of roughly 200 meV in only one day. Surprisingly, the work function of Silver stayed very stable in water for one week, however, by the end of the second week it had dropped to 80% of its original value.

The use of SU-8 as adhesion layer, strongly enhanced the stability of the work function of the samples with evaporated Au and Ag, which were less prone to delamination and, besides the initial drop, likely to keep a constant value. Once more, it was not possible to measure the electrical behavior of Aluminum on SU-8, because of the poor quality of the film after immersion in many of the media. The main reason for this problem

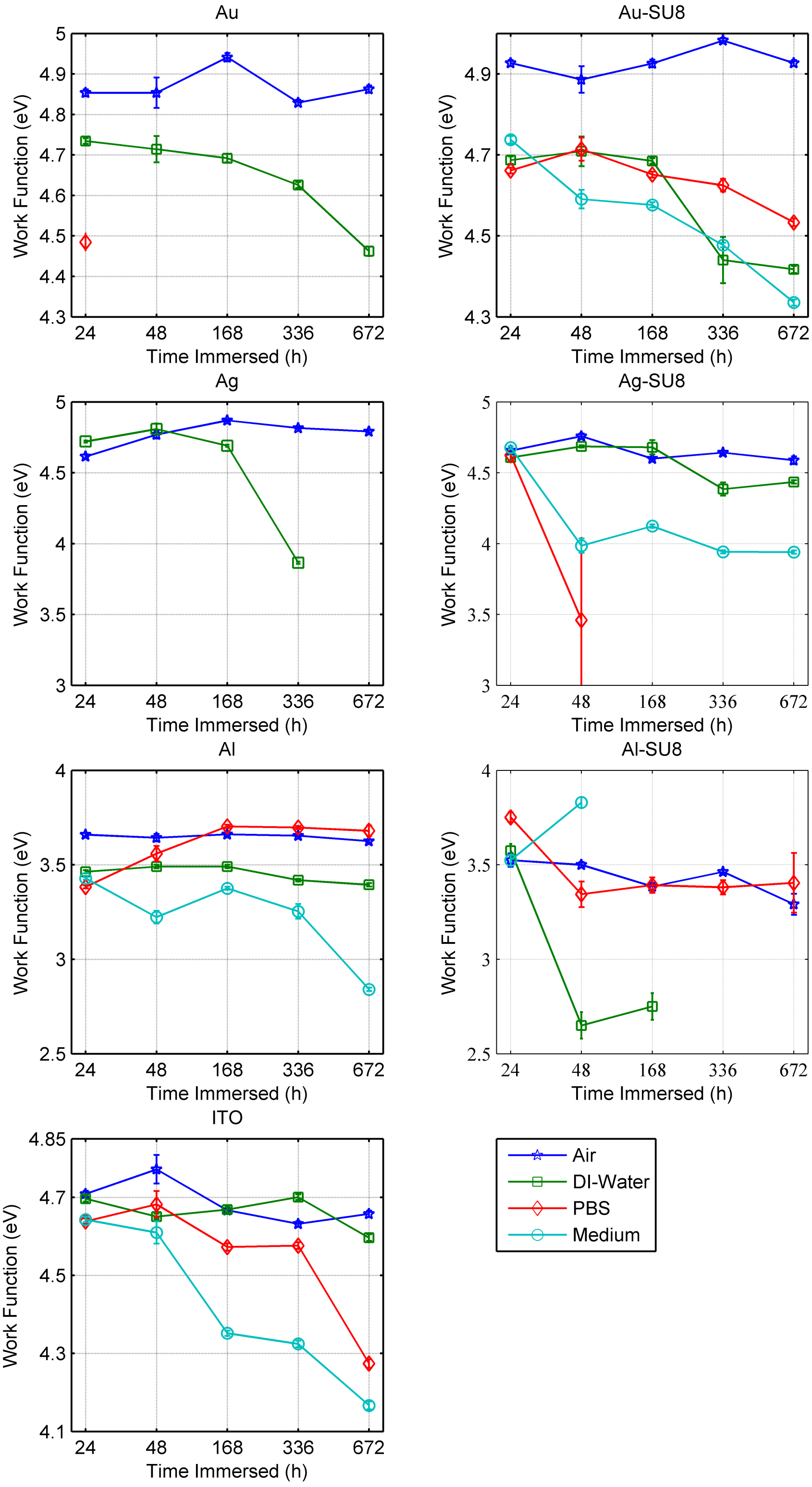

Figure 4.18: Work Function of the electrode materials in distinct media (See legend) at 24h, 48h, 168h, 336h, 672h. The results for Au and Ag in PBS and Medium and Al-SU8 are missing due to delamination or strong morphology changes of the films

resides in the delamination of the Al layer from the SU-8 film. From optical inspection it was evident that the adhesion of this metal to the polymeric interlayer was poorer than the its adhesion on glass. This aspect has been confirmed through transmittance measurements on the visibile spectrum. Figure 4.19 shows the transmittance value (averaged on the wavelengths between 350 nm and 800 nm) for each material in every condition. In these plots, the time of *complete* delamination is highlighted with solid markers to provide a visual reference. Clear increases in the transmittances of Ag in DI-water and Al in every medium were observed, suggesting partial delamination or strong oxidation of the film. Furthermore, when deposited on bare glass, Gold and Silver in PBS and culture medium show a complete delamination within 48 h.

The film of gold deposited on SU-8 showed almost no change in its average transmittance, however, at an optical inspection, clear cracks and wrinkles on the surface, and their presence cannot be detected through simple average transmittance measurements, since they do not cover enough surface to alter tangibly the measurement.

4.3.3 Morphological Stability

Figure 4.20 presents transmission and reflection mode optical micrographs of the SU-8 based samples after the one month immersion in Dulbecco's medium, while the small insets show the same image taken on the sample before the immersion. The defects are evident and predominantly on the edges of the samples, but present, although in a lower number, also in the middle.

The microscope picture, however, are not enough to identify whether these defects are wrinkles or cracks and what is their thickness or depth. In order to further investigate the phenomenon and to have clearer insights on the surface modifications of the metal layers deposited on the thin SU-8 layer, the surface roughness has been characterized with the aid of a mechanical profilometer. Figure 4.22 typical profiles of the three metals on SU-8 before the immersion in any medium and after 672h of immersion in Dulbeccos Modified Eagles Medium.

All metals, at the baseline, are substantially flat, while at the end of the immersion period, there is the formation of sharp protuberances tens of microns wide and with thickness ranging from some hundreds of nm to more than $1.5\mu m$. These "wrinkles" are not localized in specific parts of the sample, but well spread on the whole area, for every metal and in every medium and are more likely related to modifications of the SU-8 than to clustering of the metals on the surface. To obtain an even deeper characterization of the effect on the different metals, the roughness of the samples has been measured with means of an Atomic Force Microscope. The area affected by

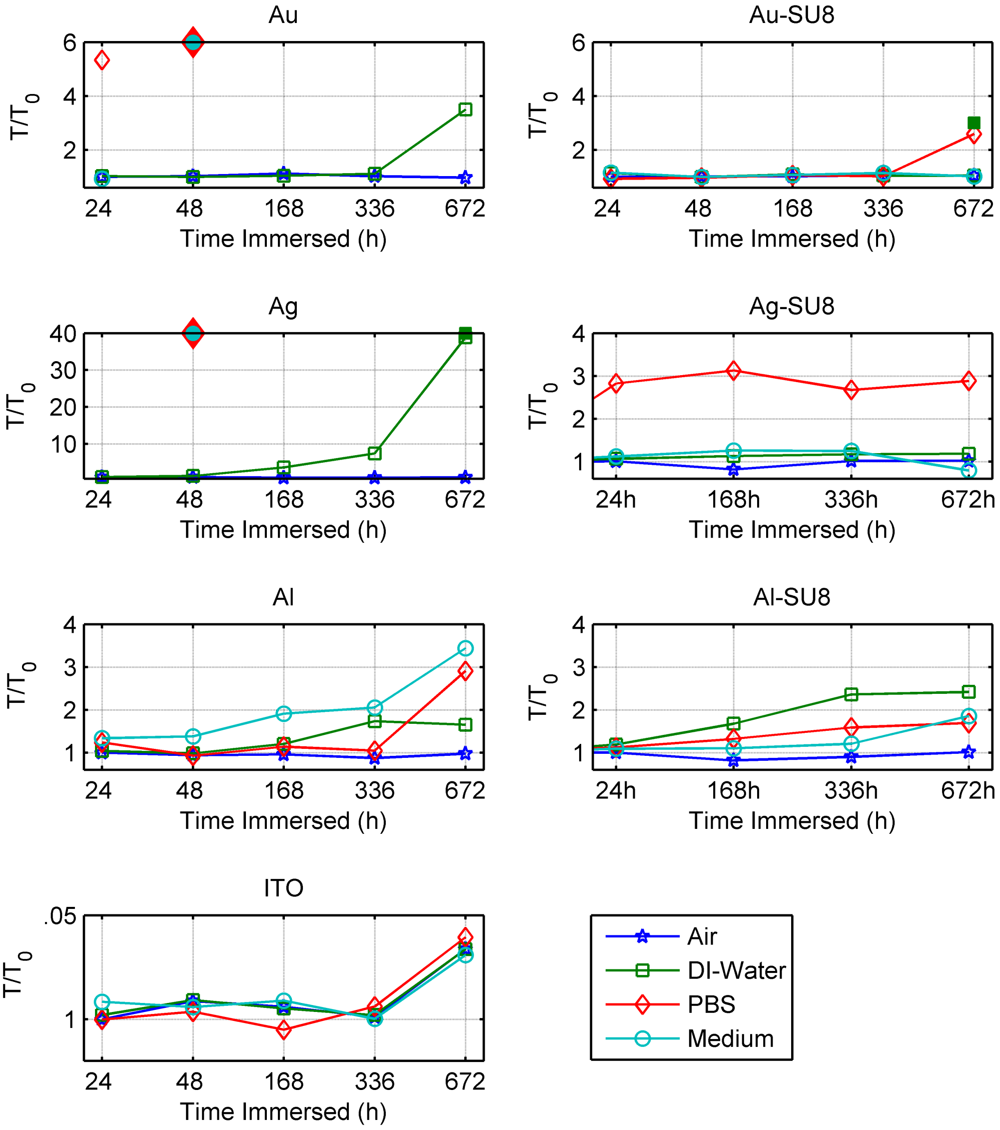

Figure 4.19: Transmittance spectra of the electrode materials in different media. The black solid lines represent the initial transmittance spectra, the solid lines represent the spectra of the materials after 24h of immersion, and the dashed lines represent the last measurable spectrum before delamination.

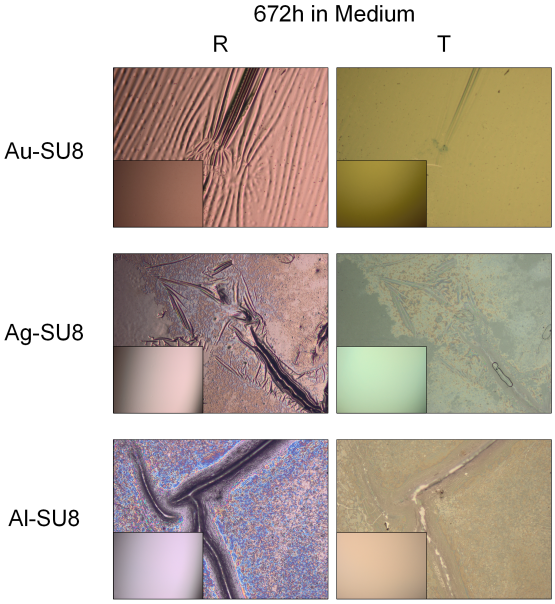

Figure 4.20: Reflection and transmission optical microscope image of the electrode materials after 672h in medium, with a magnification of 10x. The images clearly show the formation of wrinkles and cracks in the SU-8 layer, which determine a deterioration of all the considered electro-optical parameters. The insets show the images taken with the same parameters at the baseline.

the wrinkles could not be investigated, due to the excessive peak to peak roughness, nonetheless, the areas macroscopically flat, were observed and gave useful information in terms of RMS roughness. The estimated roughness is identical for the baseline samples and the ones kept in air and it is below 2 nm, while every metal immersed in a liquid medium is characterized by a rise in roughness up to one order of magnitude. Furthermore, from the analysis of the AFM images, no modification of the grain size is encountered for both immersions in DI water and Dulbecco's medium. The immersion in PBS, however, gives different results. From the AFM images of Ag and Al on SU-8, the formation of big clusters and agglomeration with peak heights above 100nm is evident. This finding sheds new light on the transmittance data presented in Figure 4.19, where the Ag-SU8 and Al-SU8 samples present an increase in transmittance up to 3 times with respect to the baseline. This phenomenon can now be associated to the removal of silver layers and their accumulation in bigger clusters.

4.3.4 Biocompatibility

Finally, in order to assess the biocompatibility of the electrode materials, two measures of cytoxicity were used. For both experiments, we employed glass as positive control, and polyethylenimine (PEI) as a negative control [136], [137]. The first method utilizes

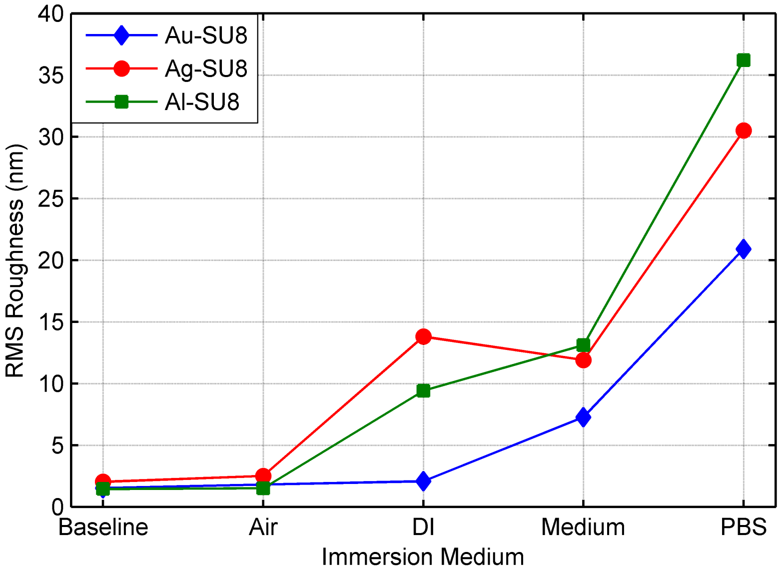

Figure 4.21: RMS roughness of materials after 672h of immersion in the different media. The samples in air are, in terms of RMS roughness, almost identical to the baseline, while the immersion in DI water and Medium leads to a substantial increase of roughness in the cases of Ag and Al. Although Au seems to be robust to immersion in water, the immersion in Medium leads the RMS roughness to rise from a baseline value of 1.53nm to a value of 7.27nm. Finally, the immersion in PBS results in a particularly enhanced roughness, namely 20.9nm, 36.2nm and 30.5nm for Au, Ag and Al, respectively.

a set of 3 fluorescent probes to quantify the number of attached cells, and the proportion of those cells which are viable. The effect of the 3 fluorescent probes is summarized in the drawing in Figure 4.23. Hoechst die labels DNA and as it is able to permeate the cell and nuclear membranes of healthy and dead cells, it serves to indicate cells regardless of their condition, and can be used to quantify cell adhesion.

The fluorescence assays carried out 24 and 48 h after cell plating revealed a particularly low cell adhesion on PEI (Figure 4.24, middle panel) when compared to the positive control sample on glass. All the electrode materials revealed similar levels of cell adhesion, with the exception of ITO, where the cell density was still higher than the one of PEI, but 30% lower than the control values. The next fluorescent die, Fluorescein diacetate (FDA) is a non-fluorescing cell-permeant enzymatic substrate for esterases. Upon hydrolysis by intracellular esterase enzymes that are present and functional in healthy cells, FDA is converted to a fluorescent product which is excited and detected to report on cell viability. After both 24 and 48 h, cell viability remained above 99% for cells attached either on glass or on metal substrates as revealed by concurrent Hoechst and hydrolyzed FDA signal (4.24, top panel). On the other hand, apart from the low cell attachment, a propidium iodide signal was strongly detected after 48 h in cells

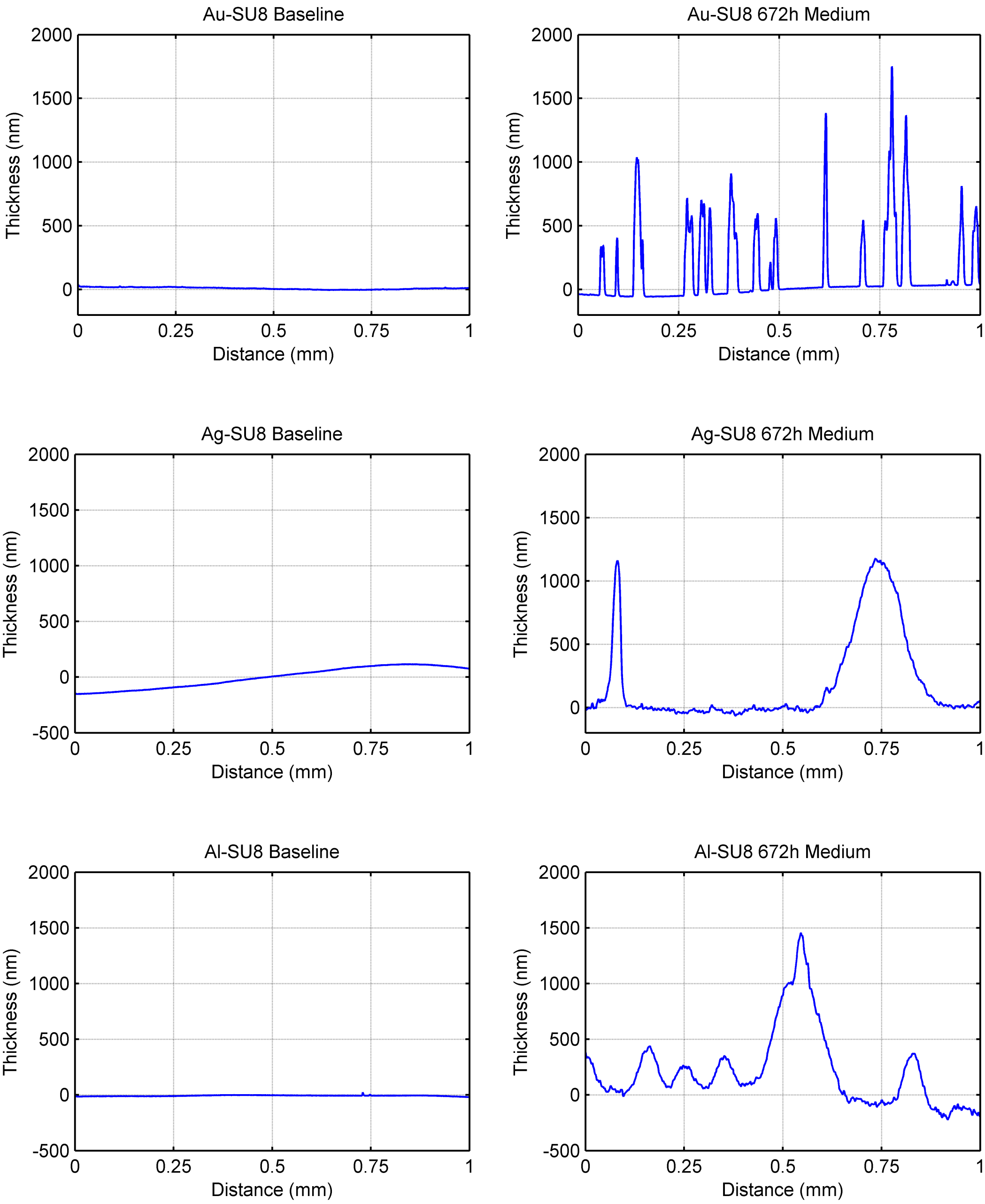

Figure 4.22: Typical profiles of the materials measured over a 1mm long line. The panels on the left side are relative to the baseline measurement, which shows almost completely flat surfaces without any wrinkling or cracks. A similar analysis performed on the samples with SU-8 immersed in any medium for 672h show the formation of protuberances characterized more than 1ţm high.

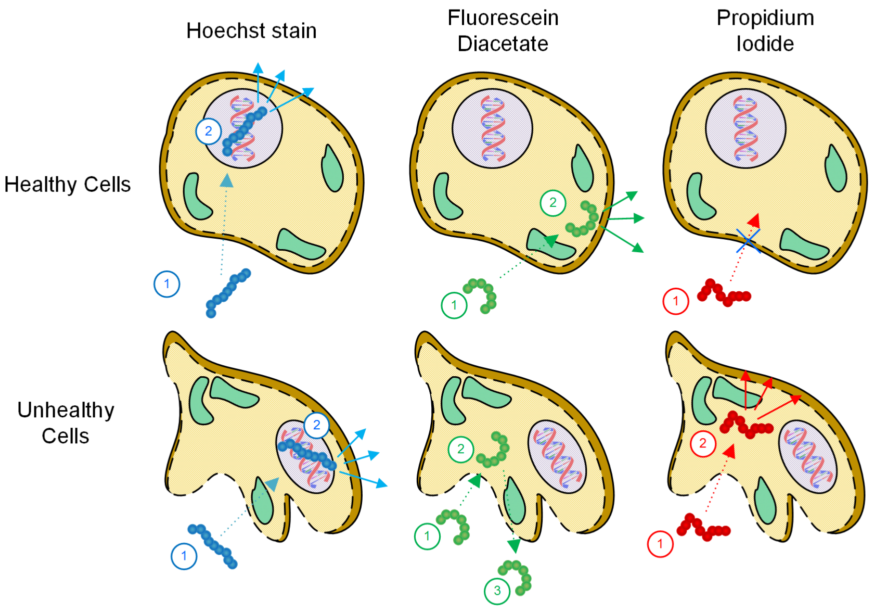

Figure 4.23: The cartoons represent the behavior of the three employed fluorescence assays: Hoechst penetrates the nuclei of healthy and unhelthy cells, FDA is only fluorescent in Healthy cells, while PI can only penetrate the membranes of unhelathy cells

grown on PEI. This final fluorescent reporter is not permeable to healthy cell membranes, and as such serves to report on cell death, which has two common pathways, apoptosis and necrosis. Necrotic cells are characterized by cell swelling and membrane rupture. Necrotic cells do not show FDA signal, as the esterases required for hydrolysis cannot be contained in the cytosol of the rupture cells. Apoptosis on the other hand results in cell membrane blebbing, and the progressive loss of cell membrane to apoptotic bodies. Besides the PEI, all groups presented levels of cell viability and mortality comparable to that of glass, hinting to a good biocompatibility of the metals. The data from electrophysiological experiments reflected the same trend. Patch clamp technique, a method commonly used to record potential or currents across a cell membrane through a glass micropipette, is used in this case to evaluate the membrane resting potential and its resistance. Significant differences in membrane resistance are observed in HEK293 attached on PEI. No such differences were found between glass and gold, or glass and ITO. These data, taken together with the fluorescent assays state quite clearly the biocompatibility of the chosen materials and finally assess their usability as electrodes for bioelectronics.

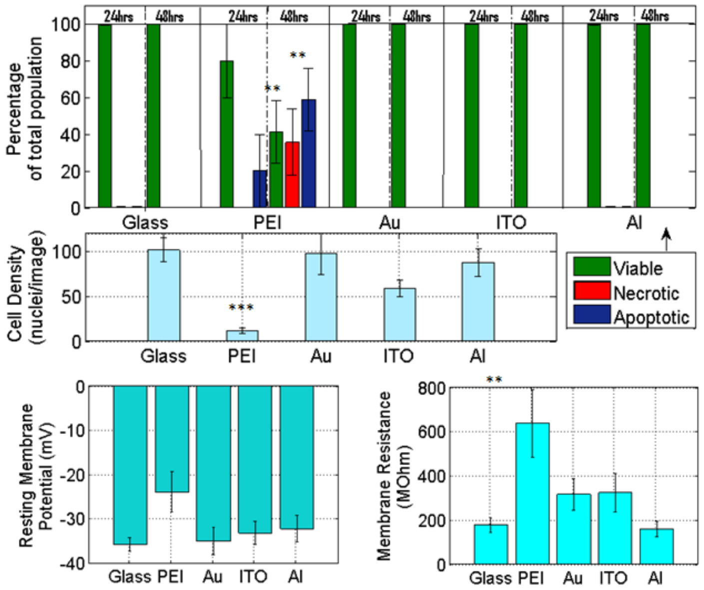

Figure 4.24: Top: time-course of FDA, PI, Hoescht viability assay on the various electrode substrates. Middle: average number of attached cells per acquired image. Bottom: basic cell membrane parameters (left: resting potential and right: input resistance) assessed by patch clamp. Statistical analysis was performed using one-way ANOVA followed by the Dunnett's multiple comparison test versus glass controls

4.4 Adhesion Layers to Promote the Stability

4.4.1 Importance of SU-8 Crosslink

As the morphological analysis of the samples' surface in previous section exposed, the adhesion and the morphological stability of the metal electrodes over interlayers is important and, at the same time, not granted. Particularly, although SU-8 seems to be promising because of its many advantages as adhesion layer, it has a tendency to develop wrinkles and cracks on the surface after prolonged periods of immersion in culturing medium. In this section we show that the adhesion of Au on SU-8 may be controlled by varying the amount of energy provided to the the polymer before the evaporation of the gold layer and we identify an optimized protocol which maximizes the uniformity of the surface. Furthermore we will show that the viability of neurons grown on SU-8 is much greater than the one of neurons grown on chromium, implying that any localized loss of the gold layer will be less harmful in the case of SU-8 with respect to bare Chromium.

SU-8 is composed by a mixture of an epoxy-based monomer, a solvent and a photosensitive component. When the material is exposed to UV light, the photosensitive component initiates a reaction which, eventually, yields to a cross-linked polymer. Mod-

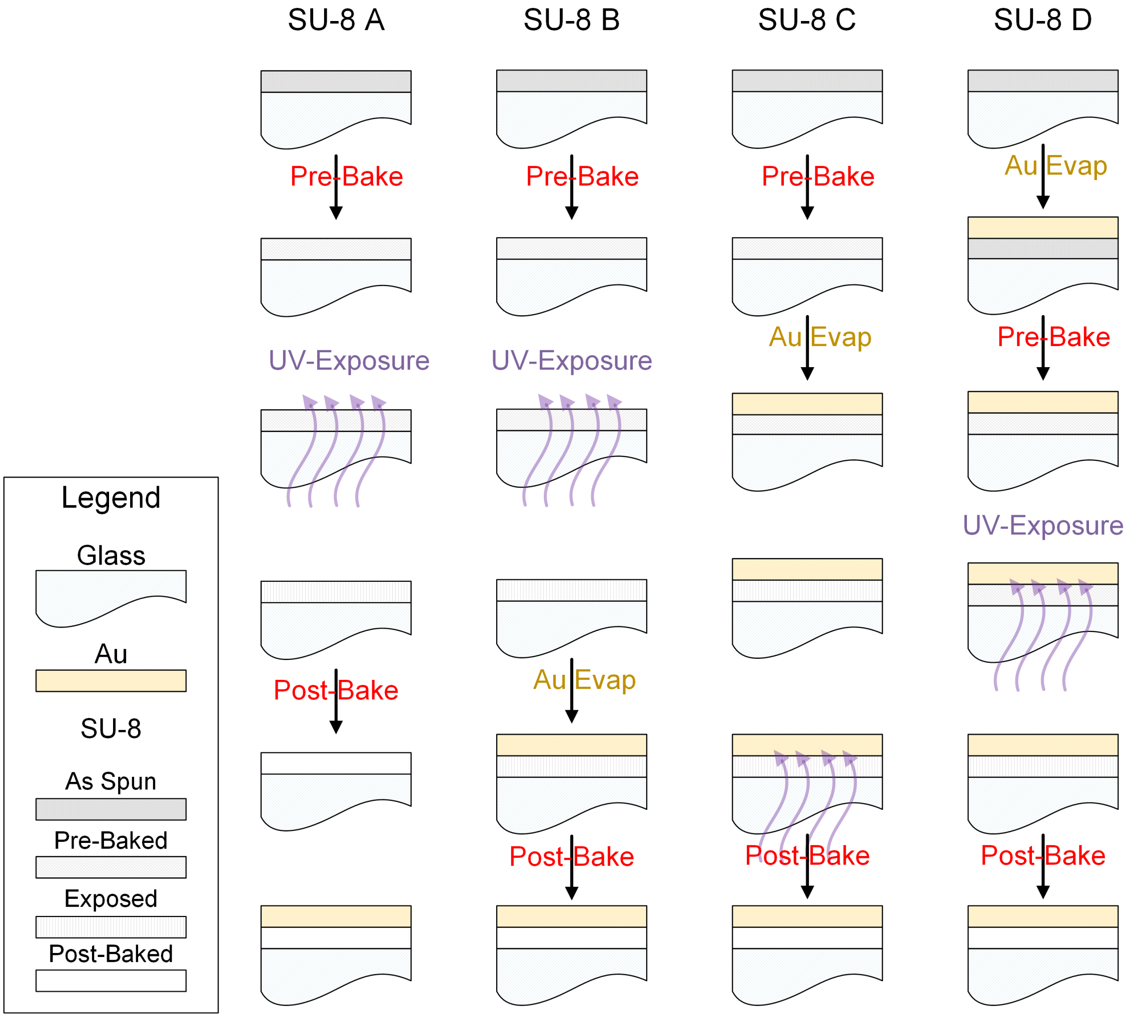

Figure 4.25: Step of deposition of gold on differentially photo-crosslinked SU8-2.

ifying the illumination dose and the curing time, the mechanical characteristics of the film can be tuned, particularly, a longer or more intense exposure would yield a harder film. The conventional process for the deposition of SU-8 involves the dispensing of the material through spin- or spray-coating, afterwards the SU-8 is soft baked with a temperature of $\approx 65^{\circ}C$ and ramped to $\approx 95^{\circ}C$ to let the excess solvent evaporate. Prior to the exposure to UV light, the sample is let cool down to ambient temperature. Once the exposure is performed, a second round of baking is set, utilizing the same temperature ramps employed for the soft bake. Only at this point the metal is evaporated and the sample is developed to remove the superfluous non cross-linked photoresist. In the current case, however, using the process as it is, yields to an over-cross-linked SU-8 which cracks and wrinkles after a long exposure to a liquid medium. The research question then arising is whether the changing point when the gold is evaporated could lead to an enhanced stability and adhesion of the SU-8/Au electrode or not. To find

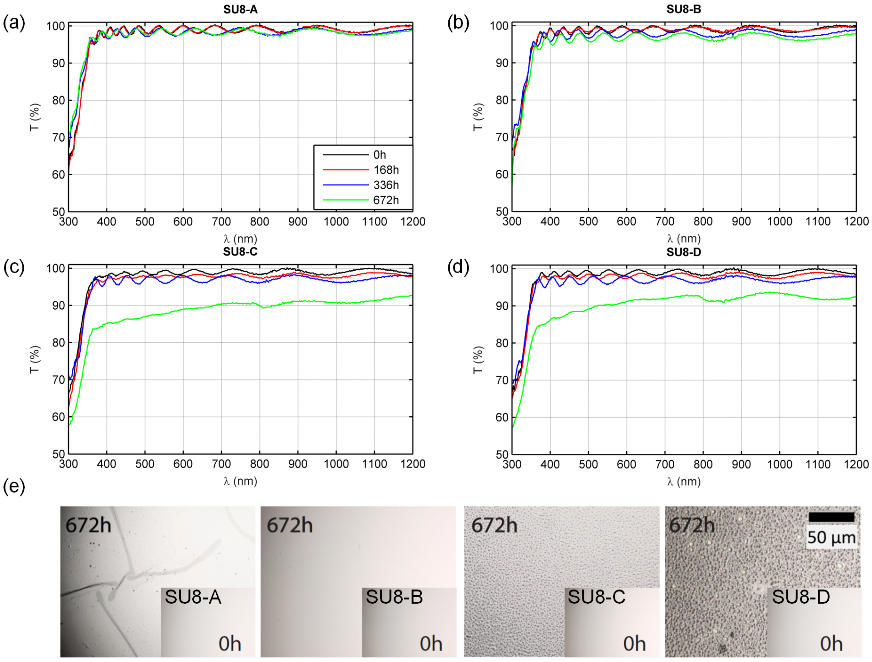

Figure 4.26: Stability of the transmittance spectra of SU8-A (a), SU8-B (b), SU8-C (c), SU8-D (d) in culturing medium for one month. Panel (e) presents the respective optical micrograph at the end of the experiment (bigger image) and at day zero (inset)

a possible solution to this question, four series of SU8 samples were fabricated with varying degrees of cross-linking prior to gold deposition: the first series (A) was subject to the whole cross-linking protocol; in the second series (B), the hard baking was performed only after the gold deposition; the third series (C) was prepared with the evaporation of gold right after the soft bake and prior to the light exposure; finally, the last set (D) was prepared evaporating the gold on the SU-8 after the the mildest part of the soft-bake.

The schematic in Figure 4.25 summarizes the different preparation steps utilized for the realization of the different samples. The UV dose was set to $100mJ/cm^2$, while all the annealing steps were 5 minutes long. Since the energy provided to the system at the moment of Au deposition, when passing from SU8-A to SU-D, reduced progressively, the polymeric film passed from a fully cross-linked hard state to a soft and “sticky” non cross-linked film.

In order to assess the suitability of SU-8 as a substrate material and its qualities as adhesion layer, two sets of samples were prepared: a first set where the polymer was deposited according to the above mentioned protocols, but not including the gold evaporation, and a second which included the gold evaporation and the successive preparation steps. Similarly to what already presented in the previous section, the samples have been submerged in cellular medium for a timespan of one month, being temporarily removed at certain time points, in order to measure UV-Vis transmittance and to take optical microscopy images. At the baseline, all samples appeared uniform under an optical microscope and exhibited consistent transmission spectra with peaks in the transmittances of above 90% in the wavelength range 400 1200 nm, as reported in Figure 4.26 (a)-(d).

Nevertheless, the different cross-linking conditions led to different behavior over time and significant differences are visible in both the transmission spectra and the optical micrographs after 672 h. Specifically, the most cross-linked sample (A) presented the insurgence of cracks and wrinkles on its surface, although this factor did not hinder its transparency. The least cross-linked samples (C and D), on the other hand, present a grainy look with the emergence of “bubbles” and the alternation of brigher spots to darker spots. The transmittance is strongly affected by this phenomenon and it is significantly reduced over the whole visible spectrum. Finally, only sample (B) seems to be not affected at all, both in terms of transmittance and of the optical micrographs. It is clear from this first set of experiments that the deposition of gold onto a fully cross-linked SU-8 might lead to cracks and wrinkles (as reported in the previous section), while the evaporation of gold onto a layer which has not been cross-linked enough, might induce a good adhesion, but a reduction of the transmittance, due to the presence of scattering sites.

4.4.2 Gold Stability

The relevant date of the second set of experiments is summarized in Figure 4.27. The initial spectrum is the typical visible range transmittance of a gold thin film. Besides SU8/Au-A, the spectra recorded at different time points are almost indistinguishable from the base line, indicating that in terms of “average” behavior, the gold layer is adhering fairly well to the underlying polymer. There is, however, a substantial difference in the transmittance of SU8/Au-A after 672 h, with respect to its baseline. In addition to the recognizable Au spectrum, there is an oscillatory behavior, probably due to interference originated by micro-delaminations of the film.

Panel (e) of Figure 4.27 shows one of these possible defects. At first, the defect is presented with the insurgence of parallel diagonal lines. The following week, the regular shape has been distorted to a more circular pattern; finally, after 672 h, the tensile stress due to the immersion in the medium breaks the film and leads to subsequent delamination. It cannot be stated, from these images, whether the Au thin film is peeling off from the underlying SU8 or the whole film is detaching from the glass sample, but the result is the formation of a microcavity which at the same time alters the

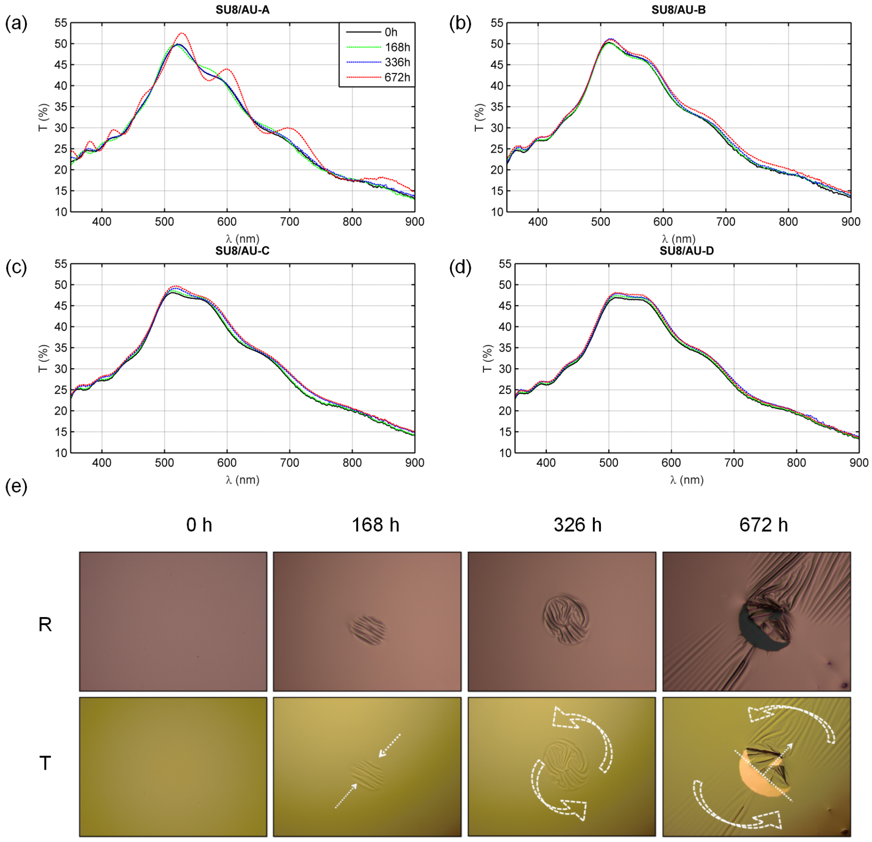

Figure 4.27: Stability of the transmittance spectra of Au evaporated on SU8-A (a), SU8-B (b), SU8-C (c), SU8-D (d) in culturing medium for one month. Panel (e) shows the optical micrographs in transmittance and reflectance mode of the evolution of a typical defect on the Au surface

transmittance and is an accumulation point for the insurgence of further defects.

Figure 4.28 shows full sample transmittance and reflectance analysis of each sample, along with a magnification of typical defects on the surface, after 672 h of immersion in the cellular medium. Observing the images it is possible to qualitatively state that samples SU8/Au-A, SU8/Au-B and SU8/Au-D have undergone similar deterioration processes. The main difference between the most and the least cross-linked ones, however, is size of the cracks and wrinkles: while samples A and B present small, numerous and diffused defects, sample D presents a lower number of defects, with significantly bigger dimensions. Remarkably, sample C seems to be largely unaffected by the submersion in cellular medium and its surface is as smooth and defect-free as it was at the baseline.

Combining the results of these two experiments, strong indications for the choice of a good protocol for the deposition of SU-8 can be extrapolated: the SU-8 film requires enough cross-linking to be able to adhere to glass and retain its optical properties,

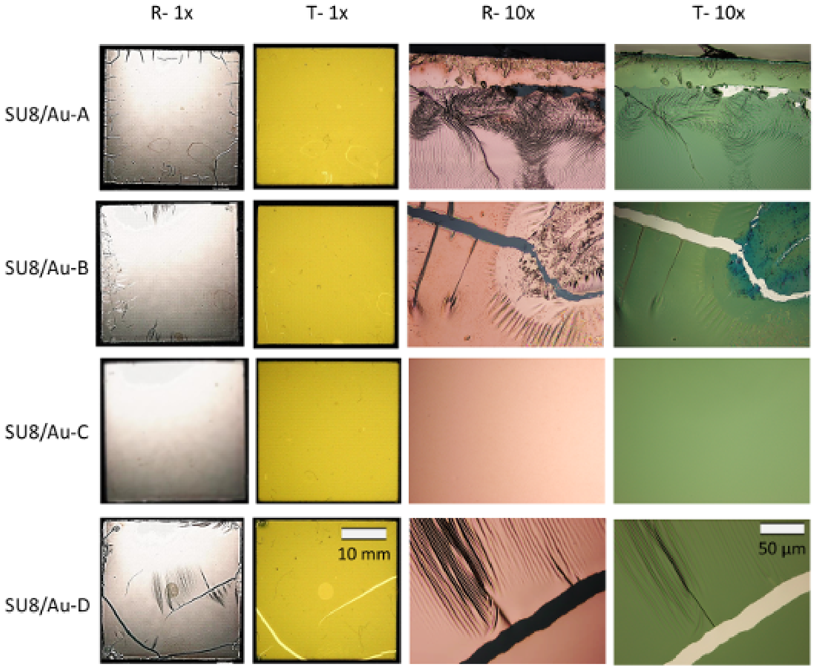

Figure 4.28: Macro (Full Sample 25x25 mm2) and micro (microscope x10) imagery of the gold thermally evaporated upon the differently processed SU8/AU after a month fully immersed in cell culture media. SU8-A/AU; SU8-B/AU and SU8-D/AU partially delaminated with cracks and wrinkles observed, while SU8-C/AU sustained perfectly smooth.

while too much cross-linking induces strais in the film, which, ultimately, leads to the formation of defects.

The resilience of the SU8/Au films to mechanical disturbances was investigated using peel testing. A strip of adhesive tape was applied to the surface of the gold and then peeled from the gold film at a constant speed of 50 mm/s at an angle of 90° to the surface. The process was repeated fifty times or until delamination of the gold film occurred. Samples A and B, which were subject to the highest cross-linking energy prior to the gold deposition, were severely delaminated after a single peeling step, indicating that Au does not adhere strongly to heavily cross-linked SU8. Opposed to these first two samples, the ones which underwent to a lower cross-linking priod to gold deposition, experienced only minor delamination after 50 peeling steps.

The protocol labeled as SU8/Au-C, results then to be the one with the lowest amount of cracking and wrinkling and at the same time one of the best performers at the peeling off test. On the basis of this analysis, we can indicate the third protocol, i.e. gold is evaporated after the soft-baking, but prior to UV-exposure, as the most reliable protocol for the fabrication of mechanically, optically and chemically stable Au electrodes on glass substrates.

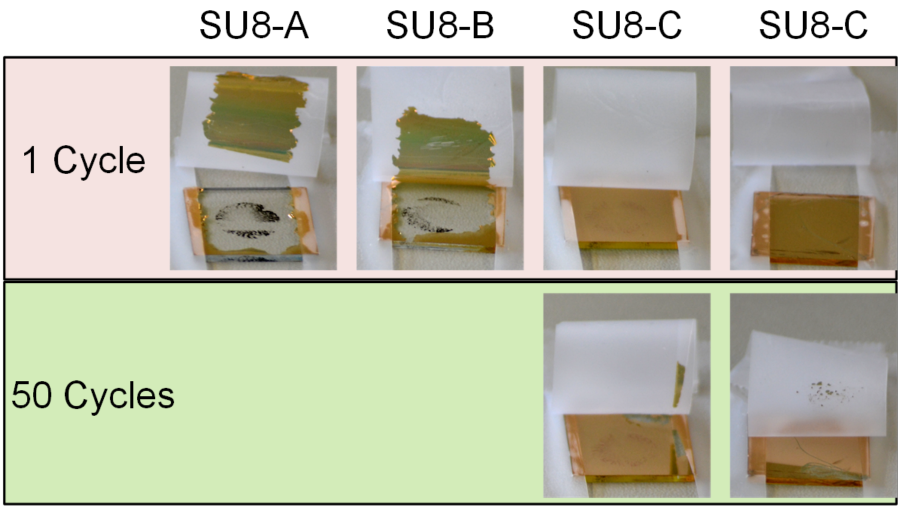

Figure 4.29: (a) Photographs of the different Au-SU8 samples after a peel-off test. SU8-A and SU8-B could bear only one cycle of peeling off, while their less cross-linked counterparts could bear up to 50 cycles.

4.4.3 Biocompatibility

A prerequisite for applying any material in a biomedical device is an evaluation of its biocompatibility. Since the effort of the doctoral thesis is the canalized to explore possibilities related to neuroelectronics, a consistent assessment of the biocompatibility of the considered films was obtained by plating acutely prepared hippocampal neurons of Sprague Dawley rats onto the adhesion layer films of evaporated chromium and spin coated SU8-A. To enhance cell attachments, both surfaces were incubated overnight in culturing medium, before further overnight incubation of PLL in borate buffer solutions. Neurons were characterized by fluorescence-based assay of viability (7,14,21,28 DIV) and electrophysiological characterization (14-18 DIV) similar to the ones described in Section 4.3.
While neurons grown on SU-8 or glass showed no difference in esterase activity or population levels of propidium iodide permeable cells as compared to glass, the difference from chromium at all time points assessed was significant, as presented in Figure 4.30, Panel (b). Furthermore, panels (c) shows the results of patch clamp recordings carried out after two weeks of culture incubation, which showed a slight but significant shift of action potential threshold in neurons plated on chromium versus glass controls, while no differences were found in firing rates for steps >75pA, or between neurons on SU-8 or glass. The bottom line of this analysis is the assessment of the full biocompatibility of SU-8 layers, as opposed to the toxic behavior of Chromium. With this final confirmation, the choice of SU-8 as an adhesion layer for bioelectronics applications is now

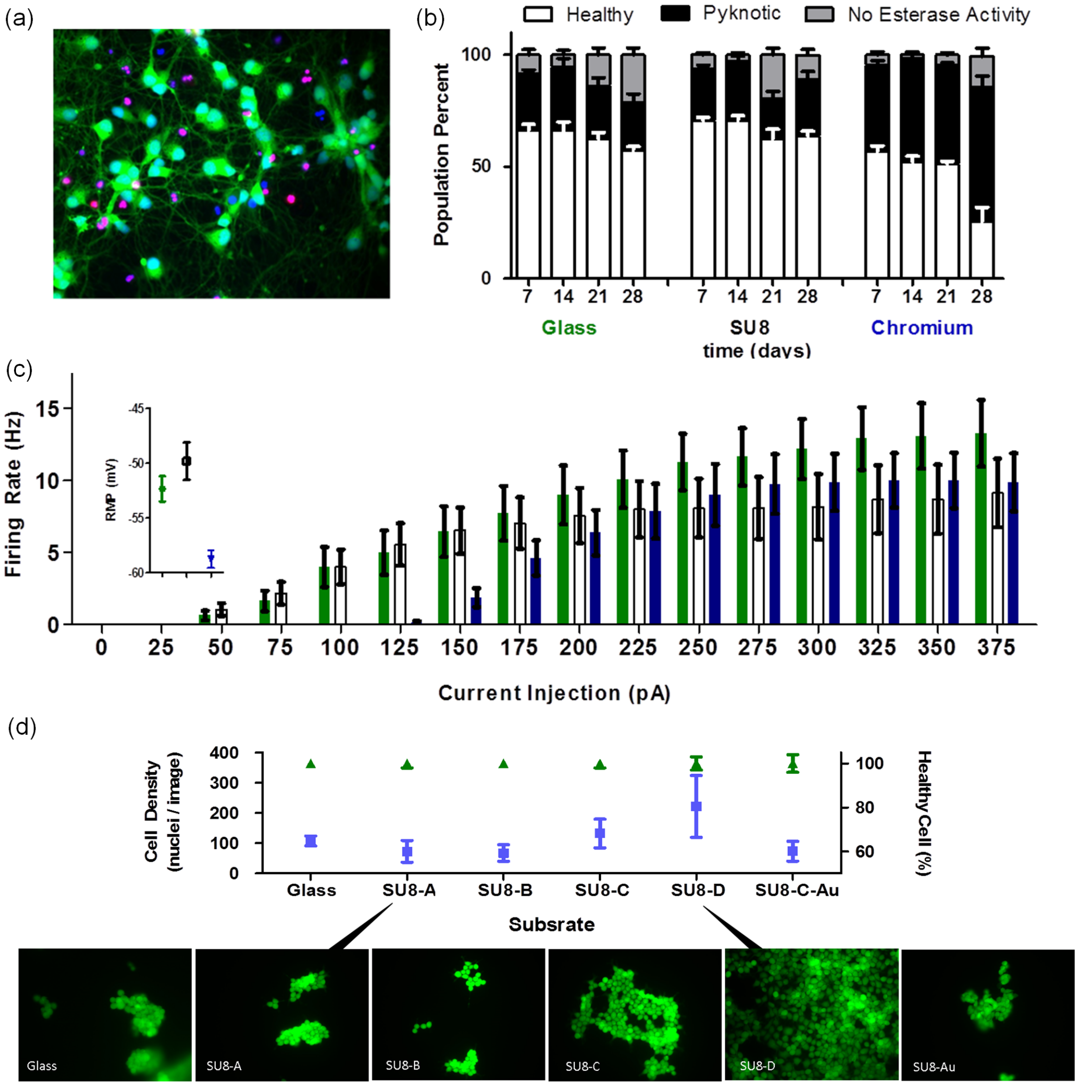

Figure 4.30: Panel (a) shows an example of composite fluorescence image including Hoechst, FDA and PI stains. The results of the analysis carried out on the glass, SU8-A and chromium are summarized in panel (b). As a further viability assay, the firing rate of the neurons at different injected currents is evaluated and reported in panel (c). Panel (d) is related to the biocompatibility of differently cured SU-8, and shows the HEK-cell density (blue markers, left hand scale) and the percentage of healthy cells (green markers, right hand scale), along with typical examples of microscope images of the cells proliferating on the samples

fully motivated.

One last step could be taken, however, to make the analysis even more thorough: checking whether the different SU-8 protocols lead to modifications in the cell viability and density. Testing all the Su8 cross-linking methods with the aid of neurons is, nevertheless, very expensive in terms of time, and once the biocompatibility of a generic SU8 cross-linking strategy was assessed, the comparison between the differently cured SU8 has been performed with the aid of HEK tumor line cells, as in Section 4.3. The results, summarized in Figure 4.30 (d), show that while each SU8 treatment is in essence fully biocompatible (the percentage of healthy cells is close to 100%), the cell density is remarkably different with different levels of cross-linking. Particularly, the samples subject to less intentional cross-link (namely, SU8-C and SU8-D) presented an enhanced cell density, which in the case of SU8-D is twice the density of the positive control on glass. Albeit surprising at a first glance, the phenomenon can be explained in terms of different adhesion forces.

When the SU8 is not fully cross-linked, the polymer is still soft and "sticky" to the touch, which might indicate stronger adhesion forces at the topmost interface. This occurrence can be verified with means of Force Scanning Probe Microscopy. In this technique, a probe (typically the cantilever of an atomic force microscope), is slowly brought in contact with the surface of the sample under test. In a first phase, while approaching, the deflection of the cantilever will be almost zero with respect to its resting position. When the probe will get few tens of nm away from the sample, the Van der Waals forces will be strong enough to abruptly attract the cantilever, which will "jump on" to contact the sample. Only from this point on the deflection of the cantilever will be proportional to the distance between the probe and the sample, becoming zero when the cantilever is completely horizontal. If the stage with the sample is now retracted from the tip, the AFM probe will deflect linearly with the distance and then, once the surface adhesive forces are compensated, "jump off" the surface and assume its resting position once again.

Since the cantilever can be approximated as a spring-and-mass system, the force can be evaluated through Hook's law as a direct proportion to the deflection: as a result, the deflection of the cantilever at the *jump off* can be directly related to the force which is necessary to separate the tip from the sample, once they are in contact. This procedure, summarized in the schematic in Figure 4.31 (a), can be seen as an operative definition of adhesive force, it is easy to implement and has been previously reported as a reliable method of investigation [138].

Figure 4.31 (b) presents the distributions of the adhesion forces obtained measuring a given sample in 1024 points showing that SU8-C and SU8-D present the highest average values of adhesion forces. It would have been reasonable to assume SU8-D would present an even higher adhesion force; however, it must be noted that it is impossible to guarantee non-intentional exposure to light of the samples: as a result, SU8-D covered glass slides might have been subject to partial cross-linking, which would justify the lower-than-expected adhesion force.

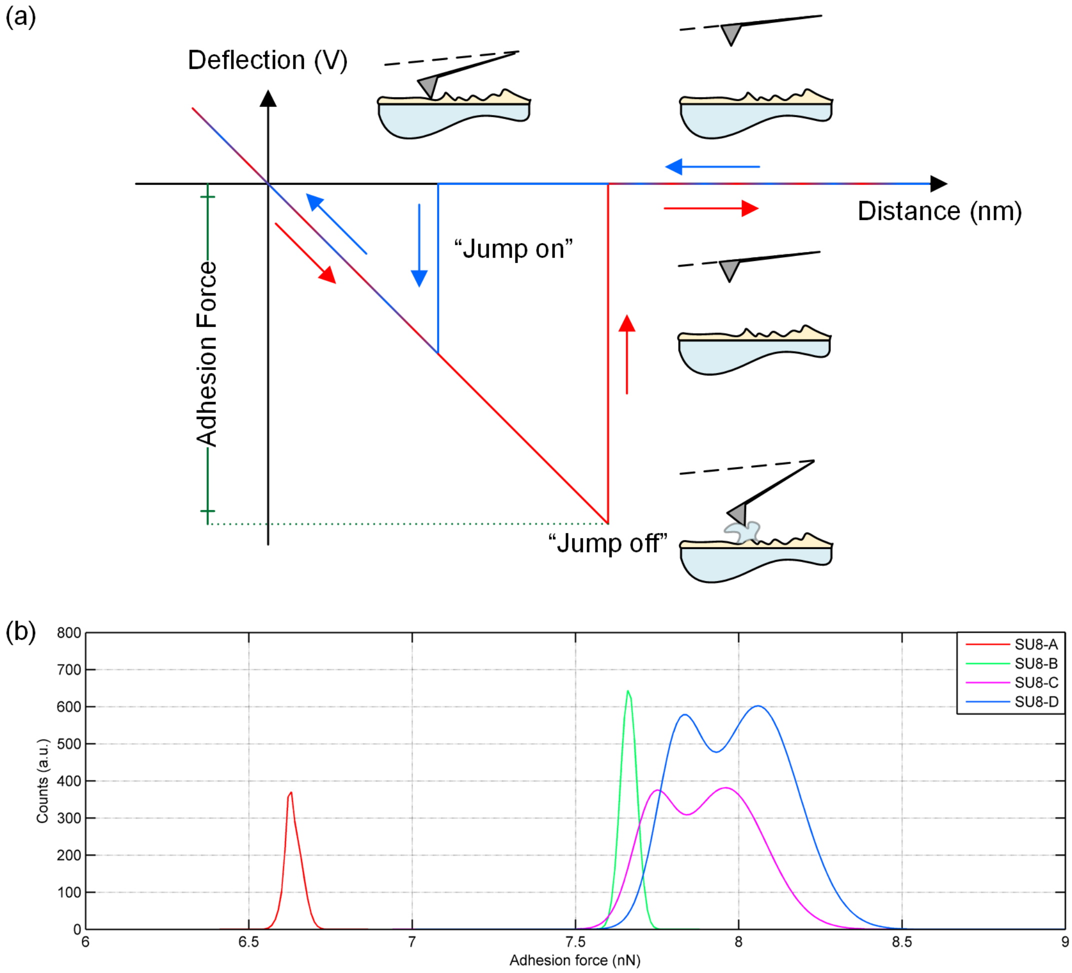

Figure 4.31: The drawing in Panel (a) shows the working principle of adhesion force microscopy, while panel (b) presents the distribution of adhesion forces over the differently treated SU8 samples

4.5 Summary

In this chapter we analyzed the several implications arising when Organic Photodetectors and probes for bioelectronics are taken away from controlled environments such as a glovebox and are implemented in the real world. First, we briefly enumerated and discussed the causes of degradation in an organic semiconductor, then we partially addressed the issue by clarifying the need for encapsulation. Given the absence of precise benchmarks for the maximum allowed WVTR and OTR for OPDs, we defined an operative benchmark oriented to our particular application. Afterwards, we showed the possibility to obtain effective in-line thin film encapsulation processes, with the use of materials and equipment compatible with the typical Organic Electronics devices process flow

We subsequently described a scenario where an organic optoelectronic device, or a simple electrode, is immersed in a physiological medium in order to be put in contact with cells or living tissues. We described the possible causes which might lead to a malfunctioning of the devices, basing the analysis on the degradation of the electrode materials over time, when immersed in biologically rich media. Since most of the metals are subject to sudden electro-optical changes and delamination, it was evident the need of an adhesive interlayer, in order to retain over time the original characteristics of the metals. Among the different possibilities, the commercially available photoresist SU-8 was preferred to classical adhesive layers composed of oxidative metals such as Chromium.

Although this choice led to an higher stability of the electro-optical characteristics of the metals, optical inspections showed that the SU-8 wrinkled and cracked after a prolonged exposure in culturing medium. By fine tuning the deposition protocol, however, it has been possible to find a combination of parameters which led to minimal deterioration of the surface. This characterization has been carried through a long term study of the stability of the transmittance spectrum and through full-sample imaging of the samples. To further assess the goodness of the chosen deposition protocol, a peel-test has been conducted, which confirmed the process choice.

Finally, the superior biocompatibility of SU-8 with respect to Chromium was demonstrated with fluorescence and electrophysiological assays on neurons, while the cell proliferation on the differently treated SU-8 samples was evaluated on HEK cells. This last experiment, led to the remarkable result of a particularly high cell proliferation on the least cross-linked samples, associated to higher adhesion forces measured through Force Scanning Probe Microscopy.

Chapter 5

Vertical Integration: In-Line Cross-Polarization

Main *leitmotiv* of this chapter is what we define *vertical integration.* This concept is related to the monolithic integration of devices with different functions aiming to minimize the insertion losses, to reduce the need for external components and for bonding techniques, and to optimize the general production process. The main objective of our vertical integration will be the realization of optical devices capable of generating/collecting light, while contemporaneously filtering it.

The distinction of overlapping optical signals can be effectuated with different techniques, some based on the time dependent amplitude of the optical wave, some on their different color (wavelength) and some based on their polarization. The latter class of methods has been attracting significant attention and now plays a crucial role in many sensing systems, allowing for the distinction of signals radiated from different sources in the same wavelength range. In the last 20 years, the exploitation of the polarization of light has been applied in many sectors of science and engineering, ranging from remote sensing to night vision, from astronomy to life sciences [7], [139]–[142]. In this Chapter we will first present some basic of Electromagnetic Field theory to introduce some helpful concepts and definitions which will be used throughout the whole chapter. Followingly, we will introduce an application in the field of bioelectronics which benefits the most from the use of light polarizers.

These devices are, however, rarely built on thin, flexible foils and, at the best of our knowledge, they were never embedded in organic optoelectronics. Whenever light polarizers are used in conjunction to OLEDs and/or OPDs, they are bond together through glues or adhesives [7], [82], which leads to clumsy processes, to significant insertion losses and a worse resolution.

Hereby, we introduce a novel method to realize fully integrated polarized OPDs and OLEDs (from now on also *pOPD* and *pOLED*) using two main solution processing techniques: nanoimprint lithography and spray-deposition. First, we realize a theoretical optimization of the structure with the aid of a multiphysics simulation software (COMSOL): we compare two strategies for the realization of such light polarizers and we simulate the performances with the use of three different metals. The polarizer is then fabricated and characterized. Afterwards, we discuss some strategies for the integration of the fabricated structures in OPDs and we will implement the most promising one. The JV characteristics of the obtained devices will be characterized and discussed. The following step will be the realization of polarized OLEDs, where spray-deposition process for a light emitting polymer will be optimized and the spray-deposited OLEDs will be characterized. Once working spray-deposited OLEDs are obtained, the technique is applied to build pOLEDs, and the final devices are evaluated separately and in conjunction with previously fabricated pOPDs.

These two novel devices are the fulfillment of the idea of *vertical integration*: summing up the capabilities of light generation/collection and filtering, with a small complexity added to the system, they indicate the direction to follow for the obtainment of fully-automated and cost-effective processes for lab on a chip applications.

5.1 Cross-Polarization Technique for LoC

5.1.1 Field Polarization

Light, in its plane wave approximation, is not only characterized by its wavelength and intensity, but also by another important quantity defined as “polarization”, which is related to the geometrical orientation of the field oscillation. To understand this concept, consider a plane wave propagating without attenuation in the z direction of a Cartesian[143], [144] :

$$\overrightarrow{E}(z,t) = \overrightarrow{A_e} e^{i(kz-\omega t)} = \left(\overrightarrow{A_e} + i\overrightarrow{B_e}\right) e^{i(kz-\omega t)} \begin{pmatrix} A_{ex} + iB_{ex} \\ A_{ey} + iB_{ey} \\ 0 \end{pmatrix} e^{i(kz-\omega t)}$$

$$\overrightarrow{H}(z,t) = \overrightarrow{A_h} e^{i(kz-\omega t)} \left(\overrightarrow{A_h} + i\overrightarrow{B_h}\right) e^{i(kz-\omega t)} = \begin{pmatrix} A_{hx} + iB_{hx} \\ A_{hy} + iB_{ey} \\ 0 \end{pmatrix} e^{i(kz-\omega t)}$$

Where $k = \frac{2\pi n}{\lambda}$ is the wavenumber and $\omega = 2\pi f$ is the angular frequency. Consider now the real part of the electric field (the considerations for the magnetic field will be analogous):

$$\overrightarrow{e} = \Re\left[\left(\overrightarrow{A} + i\overrightarrow{B}\right)e^{i(kz-\omega t)}\right] = \overrightarrow{A}\cos(\omega t) - \overrightarrow{B}\sin(\omega t) \tag{5.1}$$

Where, for simplicity of notation, A_e and B_e were substituted with A and B. The real part of the electric field can then be rewritten as

$$\begin{cases} e_x = A_x cos(\omega t) - B_x sin(\omega t) \\ e_y = A_y cos(\omega t) - B_y sin(\omega t) \end{cases} \tag{5.2}$$

Multiplying the first line of Eq. 5.2 by A_y and the second line by A_x and performing a member by member subtraction, and doing the same with B_y and B_x, respectively, we can write

$$(e_x A_y - e_y A_x) = (B_y A_x - B_x A_y)\sin(\omega t) \tag{5.3}$$

$$(e_x B_y - e_y B_x) = (A_x B_y - A_y B_x)\cos(\omega t) \tag{5.4}$$

By squaring both equation and summing the two members, it is possible to write the following:

$$(e_x A_y - e_y A_x)^2 + (e_x B_y - e_y B_x)^2 = (A_x B_y - A_y B_x)^2 \Rightarrow \tag{5.5}$$

$$\Rightarrow (A_y^2 + B_y^2)e_x^2 + (A_x^2 + B_x^2)e_y^2 - 2(A_x A_y + B_x B_y)e_y = (A_x B_y - A_y B_x)^2 \Rightarrow \tag{5.6}$$

$$\Rightarrow \frac{e_x^2}{(A_x^2 + B_x^2)^2} + \frac{e_y^2}{(A_y^2 + B_y^2)^2} - \frac{2(A_x B_x + B_x B_y)}{(A_y^2 + B_y^2)(A_x^2 + B_x^2)}e_y = \frac{(A_x B_y - A_y B_x)^2}{(A_y^2 + B_y^2)(A_x^2 + B_x^2)} \tag{5.7}$$

This equation, relating the x component to the y component of the electric field, describes an ellipse, as represented in Figure 5.1 (a). In this most general case, the EM field is said to be *elliptically polarized.* If the real and imaginary part of the electric field vector are orthogonal and equal in modulus (i.e. $B_x = A_y$ and $B_y = -A_x$), the third term of the first member cancels, and the equation semplifies to:

$$\frac{e_x^2}{(A_x^2 + B_x^2)^2} + \frac{e_y^2}{(A_y^2 + B_y^2)^2} = \frac{(A_x B_y - A_y B_x)^2}{(A_y^2 + B_y^2)(A_x^2 + B_x^2)} \tag{5.8}$$

This equation corresponds to a circumference, as represented in Figure 5.1 (b), and the field is said to be *circularly polarized.* Finally, in case the imaginary and real part of

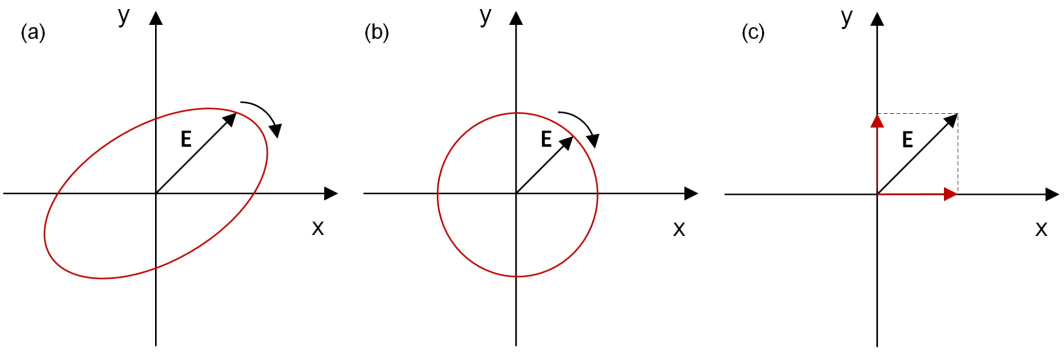

Figure 5.1: The figure represents the possible polarization states of a completely polarized, single wavelength, plane wave. The most general polarization form is described by an ellipse (a), which semplifies to a circumference when the real and imaginary part of the electric field vector have equal modulus and their directions are orthogonal (b) or to a line when the real and imaginary parts are in the same direction (c)

the electric field are parallel (i.e. $\overrightarrow{B} = \alpha\overrightarrow{A}$), Eq. 5.7 can be rewritten as:

$$A_y^2 e_x^2 + A_x^2 e_y^2 - 2A_x A_y e_y = \frac{\alpha A_x A_y - \alpha A_y Ax}{1+\alpha^2} \Rightarrow \tag{5.9}$$

$$(e_x A_y - e_y A_x)^2 = 0 \Rightarrow e_y = \frac{A_y}{A_x} e_x \tag{5.10}$$

This last equation describes a line, which is represented in Figure 5.1 (c) and the field is said to be *linearly polarized.*

It can be proved that a generic elliptically polarized field can be expressed as the linear combination of two linearly polarized waves [143], hence, every problem of perfectly polarized, single wavelength, electromagnetic field can be solved in terms of linear polarization.

5.1.2 Field Polarizer

Given a linearly polarized wave, though, it could assume any orientation in the plane. To define a coordinate frame, conventionally [143], [144], the concepts of *transverse electric (TE)* and *transverse magnetic(TM)* polarizations are introduced. Starting from an impinging wave, we can define the *incident plane* as the plane which contains the propagation vector before and after reflection/refraction at the surface of an object (see Figure 5.2). If the oscillation of the electric field of the EM wave lies on the incident plane, the wave will be said to be TM-polarized, while if the oscillation of the electric field lies in a plane orthogonal to the incident plane, the wave will be said to be TE-polarized.

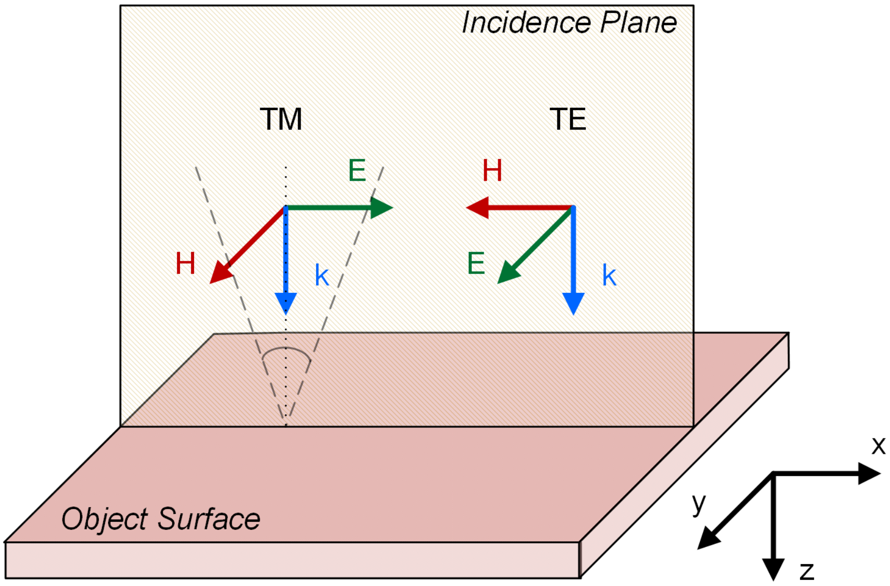

Figure 5.2: In this figure we define the *incidence plane* and, accordingly, the vectorial representation of a TM (left) and TE (right) plane wave

A generic wave is, in general, composed of a TE and a TM component (which in the coordinate system defined in Figure 5.2, correspond to y and x components, respectively). A *linear field polarizer* is defined a filter which, regardless from the input wave, yields an output wave composed of only one of the two components. For example, the functional definition of a TM field polarizer will be a vectorial operator such as:

$$\overrightarrow{E_{out}} = f_{polarizer}(\overrightarrow{E_{in}}) = \begin{pmatrix} E_{out_x} = E_{in_x} \\ E_{out_y} = 0 \end{pmatrix} \tag{5.11}$$

One of the possible physical descriptions of this mathematical function can be described as a *metamaterial* with anisotropic permittivity. Such a material will have to behave as an insulator in the x direction and as a perfect conductor in the y direction. To better understand why, please consider the conditions on the tangential electric field at an interface between two materials [143]:

$$(\overrightarrow{E_1} - \overrightarrow{E_2}) \times \hat{n} = \overrightarrow{J_s} \tag{5.12}$$

Where $\overrightarrow{E_1}$ is the electric field before the interface, $\overrightarrow{E_2}$ is the electric field after the interface and $\overrightarrow{J_s}$ is the surface current density. If the material is an insulator, the right hand side has to be zero and, consequently, the left hand side must be zero as well. As a result, the tangential field components before and after the interface are equal, as prescribed by the definition of linear field polarizer.

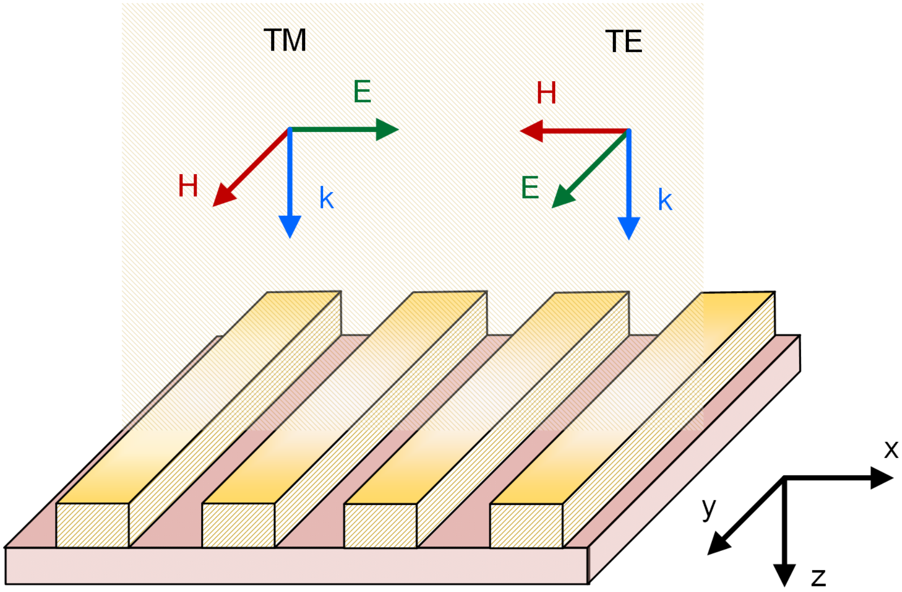

Figure 5.3: Grid grating with respect to TE and TM mode

Vice versa, if the second medium is a conductor, given the definition of electrical conductivity ($\sigma = \frac{J}{E}$), the higher σ, the lower the resulting electric field in the medium. As a result, if the metamaterial we are considering behaves as a Perfect Electric Conductor along the y-direction (i.e. $\sigma \rightarrow +\infty$), the resulting "output" field will be zero.
For real linear field polarizers, where the conductivity is not infinitive and the extinction of the undesired mode is not complete, it is customary to define an *Extintion Ratio (ER)*, as the ratio of the Transmittance of the TM mode to the Transmittance of the TE mode. The higher this figure of merit, the higher is the quality of the polarizer, since it is characterized by high transparency of the desired mode and high dumping of the unwanted one.

5.1.3 Wire Grid Polarizers

A good approximation of this theoretical principle can be obtained throughout the use of wire-grid polarizers (WGPs) [145], [146]. Consider the structure depicted in Figure 5.3, where metallic lines are deposited on top of a dielectric flat medium. The TE components of a generic field will be aligned to the metallic grid and will generate a motion of electrons along that direction: the free electrons will impact against the atoms of the lattice with a net energy transfer from the electromagnetic wave to the metal, which will in turn heat up. The higher the conductivity of the metal associated to excitations in a given wavelength, the more efficient is the energy transfer and the least part of the electric field will pass through the metallic line.

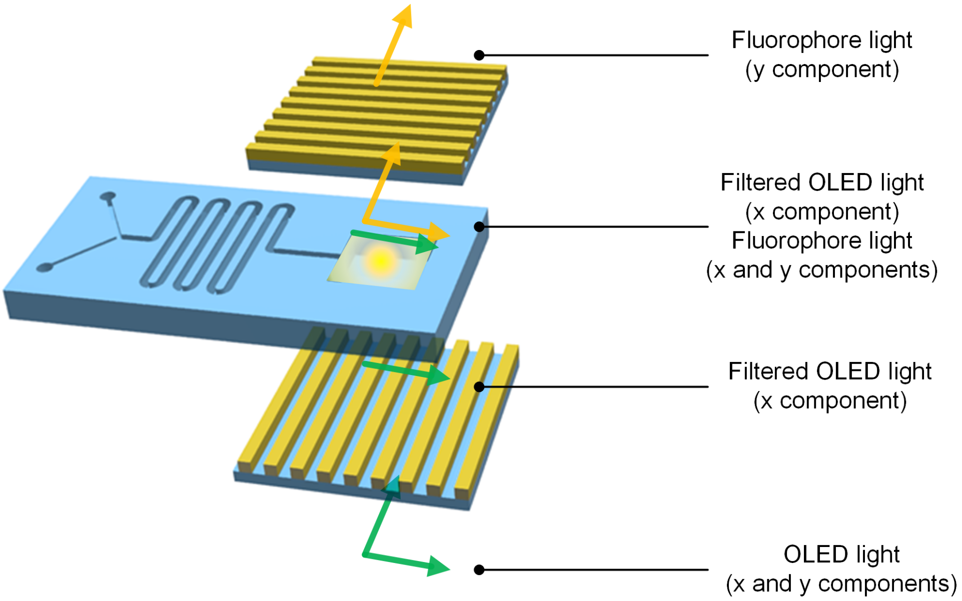

Figure 5.4: The figure schematically presents the concept of cross polarization. A unpolarized light is emitted by an OLED and immediately filtered by an y-oriented polarizer. The polarized wave excites fluorophores present in the reaction chamber, which, in turn, emit unpolarized light. The optical signal is then filtered by an x-oriented polarizer: the OLED light will be totally extinguished, while the y-oriented component of the light of the fluorophores will reach the OPD

On the other hand, the electric field components aligned along the x-direction (TM) cannot move the electrons far, since the metallic layer is interrupted after a distance which is a fraction of the wavelength: if the carriers are not accelerated, the energy transfer will be minimal (as in a dielectric) and the impinging EM wave can travel through the material. [146]

First attempts to the realization of such devices were performed through costly and complex lithography processes [145], but in the last years, the issue has been solved with the employment of soft-lithography techniques such as nanoimprint lithography [147]. WGPs fabricated with this procedure have very high extinction ratios (up to 4 orders of magnitude) and mechanical flexibility, since they can be fabricated directly on foil and, for this reason, are particularly intriguing for the purposes of this work.

5.1.4 Cross-Polarization Technique

A very interesting use of the polarization in biological applications is for the separation of optical excitation and re-emitted signal in fluorescence based studies, where the realization of compact, on-chip technologies would allow the development of many point of care assays [7], [148]. The working principle is summarized in Figure 5.4: the light generated by a light source is immediately filtered by y oriented linear polarizer and travels to the reaction chamber, where, in solution, there is a fluorophore. This substance is excited by the (x-polarized) light and re-emits unpolarized light at a wavelength slightly higher than the one of the exciting signal. The traveling optical wave will now be composed of two parts: the x-polarized light of the light source and the unpolarized light of the fluorophore. Installing another polarizer, this time oriented along the x-direction, leads the elimination of the x component from both optical signals. As a result, the original source signal is almost completely dimmed, while the light emitted by the analyte will still present its strong y component and can be detected by a photodetector. Effort has been put in the substitution of conventional sources and photodetectors with their organic counterparts. As to now, OLEDs for the excitation and OPDs for the detection of light have been already employed in cross-polarization analytic applications for the detection of a wide number of analytes [7], [8], [82], [149]. The main drawback of this technique, at the current state, resides in the fairly low integration of the components. In works similar to the one of Pais et al.[7], for instance, the OPD and the OLED are produced (by small molecule evaporation) on separate glass slides, they are mechanically bond to commercially available thin film polarizers and the resulting "polarized OPD" and "polarized OLED" are used to sandwich the microfluidic chip.

The ultimate goal we pursue in this work is the obtainment of fully-integrated structures, where the necessity of buying external components and bind them to the organic devices and/or to the microfluidic chips is limited to the minimum. For this reason, in this chapter we will design, simulate and fabricate monolithically integrated OPDs and OLEDs with embedded WGPs, which act, contemporaneously, as polarizers and as electrodes of the organic devices.

5.2 Wire Grid Polarizers (WGPs)

5.2.1 Simulations Background

In this section, we will simulate Wire Grid Polarizers with the aid of a Finite Element Modeling multiphysics simulation software (COMSOL). The structures we keep into consideration are based on the work of Ekinci et al. [145], and to the similar, successive works of Yang et al. [150] and Wang et al. [151].

Although many other structures are possible, this section is mainly focused on the two most simple ones, represented in Figure 5.5: a single layer WGP, in which metallic lines are deposited on top of a dielectric layer and immersed in air, and a bilayer WGP,

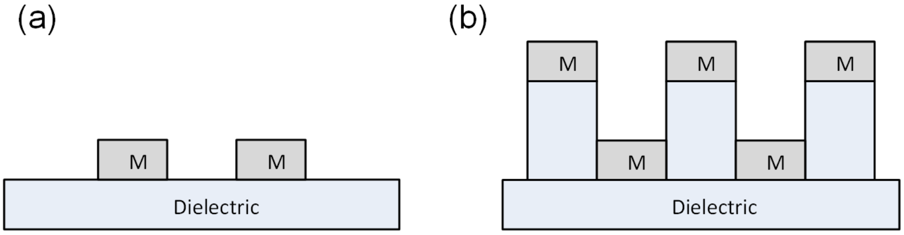

Figure 5.5: The sketches represent the two categories of wire grid polarizers we considered in this work: single layer WGPs (a) and bilayer WGPs (b)

in which a metal is deposited on the peaks and the troughs of dielectric grid lines. Through the whole section, both structures are simulated in terms of transmittance of the single modes and extinction ratio. We perform parametric variations, changing the pitch of the periodic cells, the utilized metal and the thickness of the metallic layer, in order to find clear design directions.

The simulations are performed with means of COMSOL multiphysics and the MatLab Link: MatLab has been used to evaluate the complex refractive index of the metals, with formulas and parameters based on the work of Rakic et al. [152] and to generate iteratively new geometries. The metals we simulated are Silver (Ag), Aluminum (Al) and Gold (Au), because of their wide employment in established process for organic and printed electronics [44], [45], [106].

To set up the problem, the basic geometry with parametrized dimension were defined in the COMSOL user interface. Since the metallic grating is a periodic structure, it is possible to define a “cell” with the basic system to be replicated an infinite number of time. In these situations, the solution of the electromagnetic problem is periodic as well, and it is possible to apply Floquet periodicity conditions to the boundaries. The excitation and the output of the system are defined in terms of port scattering parameters, i.e.:

$$\begin{pmatrix} b_1 \\ b_2 \end{pmatrix} = \begin{pmatrix} S_{11} & S_{12} \\ S_{21} & S_{22} \end{pmatrix} \begin{pmatrix} a_1 \\ a_2 \end{pmatrix} \tag{5.13}$$

Where $a_1 = E_1^+$ is the excitation field, $b_2 = E_2^-$ is the field at the output of the port (the transmitted field), $b_1 = E_1^-$ is the field which is backscattered and $a_2 = 0$, since in the considered system there is only one excited port. Using the port scattering parameters we are able to easily define the transmission and the reflection coefficients as:

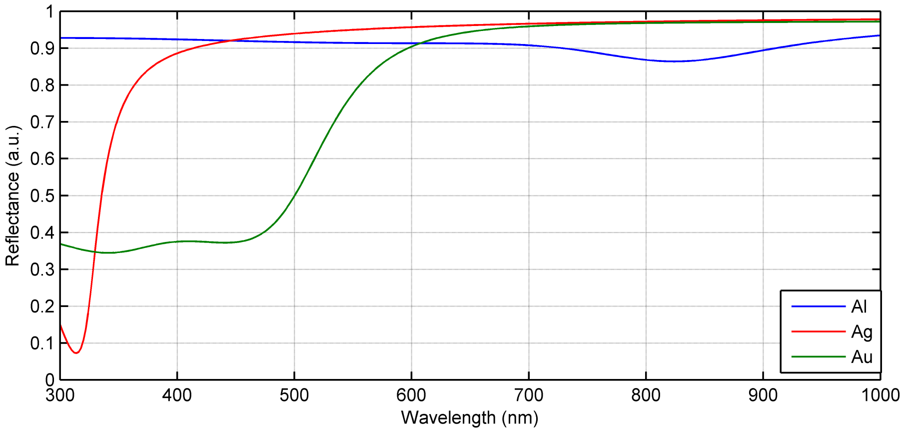

Figure 5.6: Reflectance of Ag, Al and Au in the optical range. The Plasmonic resonance peak of Au (in the blue range) and Ag (in the UV) are clearly visible

$$S_{21} = \frac{b_2}{a_1} = \frac{E_2^-}{E_1 * +} \Rightarrow |S_{21}|^2 = |\frac{E_2^-}{E_1^+}|^2 = T \tag{5.14}$$

$$S_{11} = \frac{b_1}{a_1} = \frac{E_1^-}{E_1 * +} \Rightarrow |S_{11}|^2 = |\frac{E_1^-}{E_1^+}|^2 = R \tag{5.15}$$

Once all the parameters are set, it is possible to perform some simple simulations: the first application case is the evaluation of Transmittance and Reflectance on unstructured 100 nm thick metallic films. As expectable, the transmission through the metals is negligible for every metal (data not shown), but the Reflectance plots are surprisingly informative. Figure 5.6 presents the reflectance of Ag, Al and Au in the wavelength range comprised between 300 and 1000 nm. The reflectance of Al is essentially flat, with a value of circa 90%, on the whole spectrum, with oscillations below the 5% of the average value. Ag, on the other hand, presents a sharp plasmonic resonance at a wavelength of 320 nm, with its reflectance decreasing below 10%; however, for wavelengths longer than 500 nm, Ag is able to reflect above 95% of the impinging light. Finally, Au presents a wide plasmonic resonance in the short-wave part of the visible range and an almost flat reflectance in the mid IR.

Starting from these considerations, some of the findings of the next subsections will intuitively explainable: in the metamaterial approximation presented in Section 5.1, the TE component of the plane waves is subject to boundary conditions proper of a bulk metal. The simulations are carried out by solving the complete Maxwell's equations set on a sub-wavelength optical structure, which is physically and numerically different

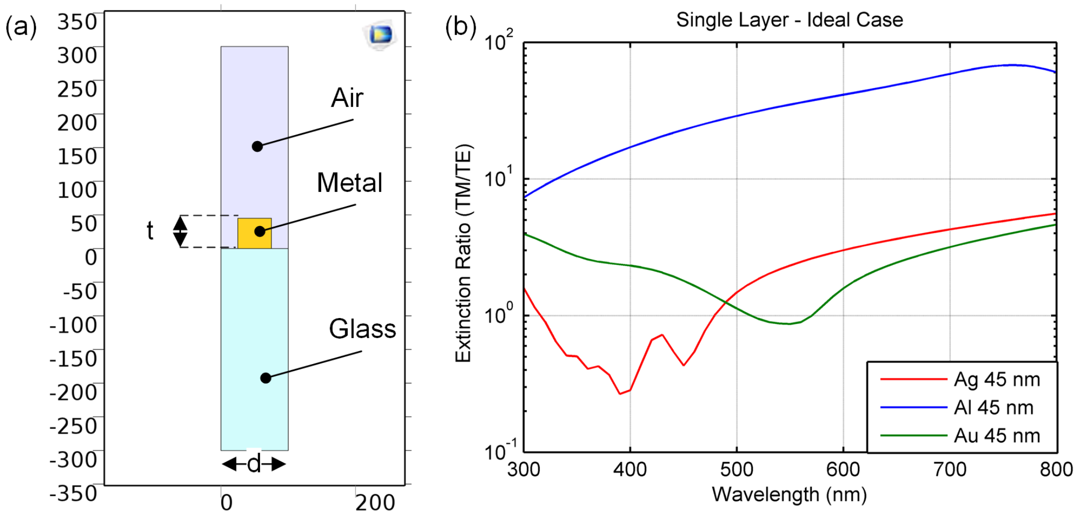

Figure 5.7: Panel (a) presents the geometry extracted from COMSOL with marks in correspondence to the two main parameters. Panel (b) presents the extinction ratio of polarizers obtained with a cell periodicity of 100 nm and a material thickness of 45 nm

from a flat metal layer. However, the results are, up to a certain extent, consistent with the reflectance curves, which conceptually validate the simple metamaterial model we proposed.

5.2.2 Single Layer Grid Polarizers

Starting from this last consideration, the first simulation we performed was a comparison between the three metals for a given material thickness and period of the structure. Figure 5.7 (a) shows the unit cell employed in COMSOL with the important parameters highlighted, namely, the period of the structure ($d = 100nm$) and the thickness ($t = 45nm$). Please note that we considered a duty cycle of 50% for the grid polarizers, hence, the width of the material line will be kept equal to $\frac{d}{2}$, unless differently stated. Panel (b) shows the simulation of the Extinction Ratios of the single layer WGPs with the defined parameters.

Al presents a steadily increasing curve, with the the ER rising for longer wavelengths and an absolute value comprised between 10 and 70 in the whole visible spectrum. This values of ER are relatively low, but can still be acceptable for some applications. Au and Ag, on the other hand, present curves which suffer from the presence of the resonance peak we introduced in the previous subsection. The plasmonic resonance is significant for both materials and the ER ratios are irregularly shaped (specially the one of Ag) and with very low absolute values. Only in the Near Infrared these two metals start to present behaviors more associable to linear polarizers, since the ER is

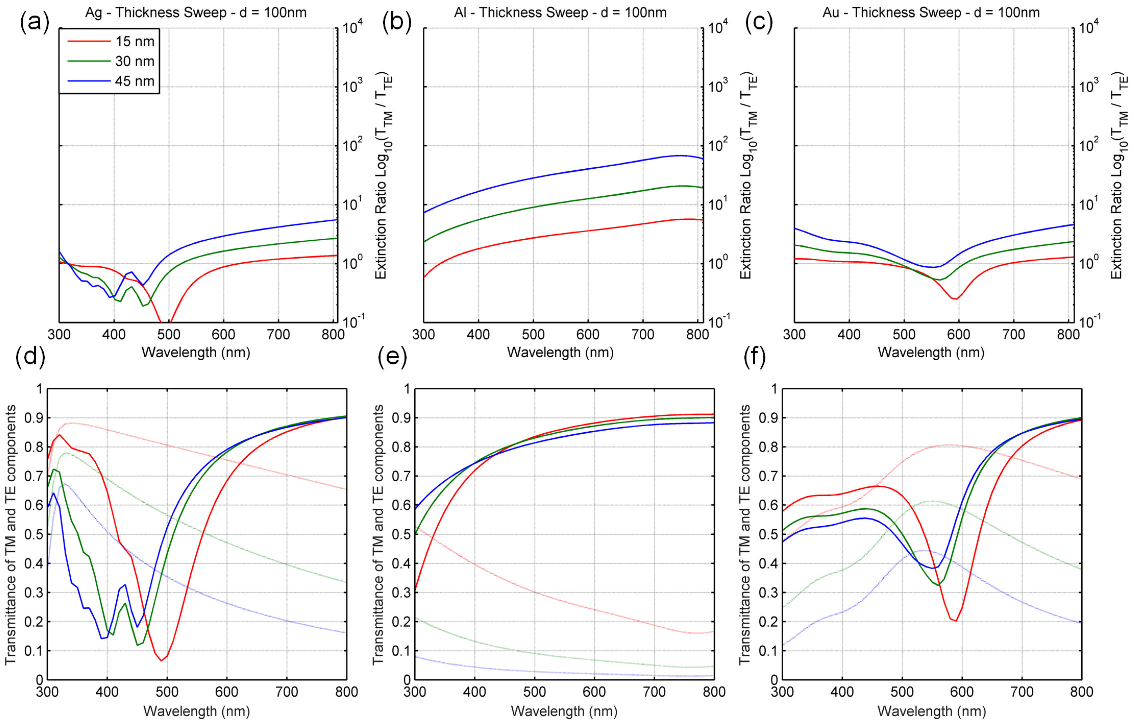

Figure 5.8: Panels (a) - (c) show the Extinction Ratios of single layer WGPs, while panels (d) - (f) present the transmission of the TM modes (solid lines) and TE modes (dashed lines) for different thicknesses and of Ag, Al and Au, respectively. The period of the cell is set to 100 nm.

rising, reaching a maximum value of 5.5 and 4.7 for Ag and Au, respectively. These values are very low for any practical application [149], rendering these last two materials, in this configuration, hardly usable as field polarizer. However, changing the thickness of the metal (t) or the period of the structure (d) might lead different results.

To verify this hypothesis, we first performed a thickness sweep, with values ranging from $15nm$ to $45nm$, fixing $d = 100nm$, and compared the results obtained with the different materials. The upper bound for the thickness of the metal layer was kept to 45 nm, since it is the maximum experimentally feasible thickness for this kind of nanostructures. The ER (a)-(c) and the transmission of TE and TM components (d)-(f) can be observed in Figure 5.8.

A common component to all the plots is that very thin metallic layers (i.e. 15 nm) result in a significant redshift of the plasmonic resonance for the TM transmission: when the thickness decreases, the trough for Ag shifts from $400nm$ towards $490nm$, while for Au, it is shifted from $590nm$ towards $550nm$. Remarkably, even Al, with a thickness of $15nm$, presents a very low transmission for the TM mode in the short wavelength range. The transmittance of the TM mode is one of the most important characteristics for a polarizing filter: the output TM field should be identical to the input one, or, in

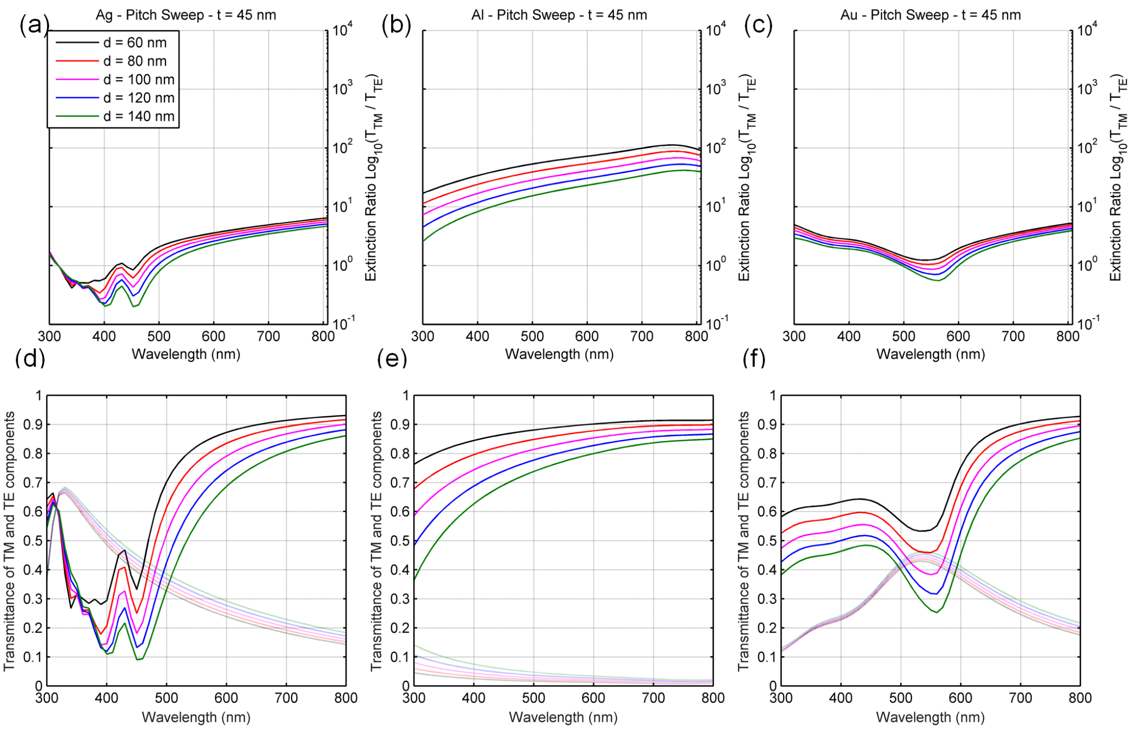

Figure 5.9: Panels (a) - (c) show the Extinction Ratios of single layer WGPs, while panels (d) - (f) present the transmission of the TM modes (solid lines) and TE modes (dashed lines) for different periods of the cells and for Ag, Al and Au, respectively. The thickness of the metallic layer is set to 45 nm

other words, the transmittance of the TM mode should be as close as possible to 1 and as constant as possible on the whole spectrum. This goal is achieved only by Al, which presents, for almost any thickness, a transmittance of the TM mode above 75%.

Concerning the extinction ratios, they are strongly affected by the plasmonic resonance of the TE mode, which is in correspondence to the resonance of the bulk material: Ag, especially in thin layers is almost translucent for TE polarized UV light, and a similar phenomenon is encountered for Au in the region around $550nm$. With these trends for the transmission of the TE modes, the effects on the ER are not surprising. The thinner the layer, the lower the extinction ratios in the longer wavelength region and the smaller is the effect of the plasmonic resonance.

Since the maximum thickness yielded the best results, the sweep on the pitch size was performed keeping the thickness constant to $45nm$, and varying the period of the structure from $60nm$ to $140nm$, with steps of $20nm$.

In Figure 5.9 it is possible to find the ER (a)-(c) and the transmission of TE and TM components (d)-(f) for different periods of the cell. In every material system, decreasing the pitch brings to the slight reduction of the TE transmission and to a significant amelioration of the transmittance of the TM mode. The effects are more accentuated in Al with respect to Ag and Au, where the concurrent decrease in the transmission of TE and increase in the transmission of TM lead the ER to double on the whole spectrum, while passing from a period of $140nm$ to a period of $60nm$.

The two trends analyzed so far, hence, give important design indications: in order to achieve better TM transmissions and higher ER, the pitch of the cell should be as small as possible and the thickness of the material should be as high as possible. However, also for a very narrow pitch of $60nm$ and a $45nm$ thick metal layer, the ER can barely be higher than 100.

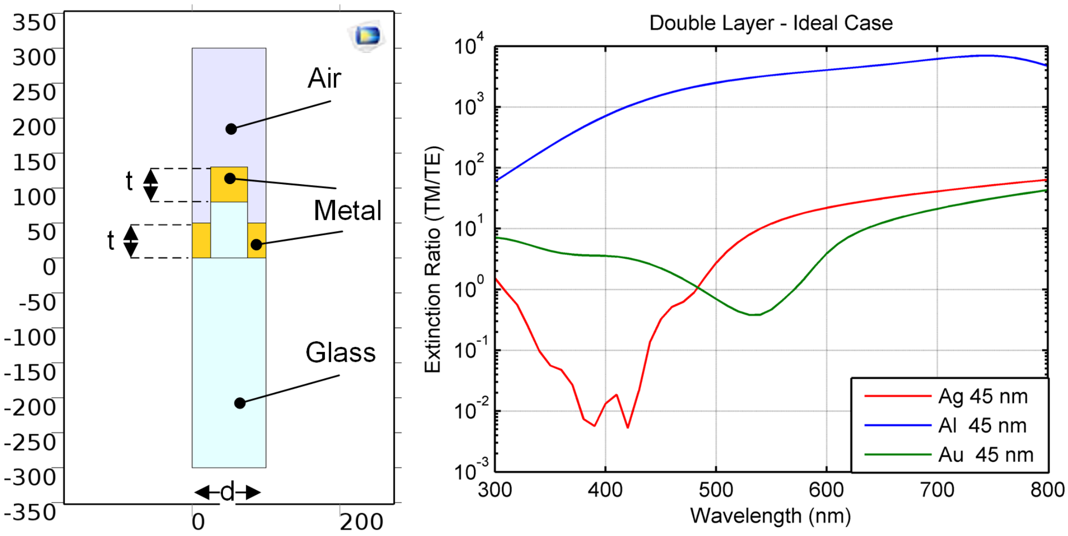

Figure 5.10: Panel (a) presents the geometry extracted from COMSOL with marks in correspondence to the parameters. Panel (b) presents the extinction ratio of polarizers obtained with a cell periodicity of 100 nm and a material thickness of 45 nm

5.2.3 Bilayer Grid Polarizers

The second strategy we investigated is the realization of *bilayer* WGPs. This kind of polarizers, although conceptually more complex, given the multilayered structure, are of much simpler practical implementation [151]. Indeed, while the single layer WGPs are normally realized with means of complex photolithography [145], the realization of bilayer WGPs is typically performed through soft lithography, as will be discussed in the next section.

Figure 5.10 (a) presents the geometry designed in the COMSOL user interface with the labels on the important parameters. The two metallic layers are, at least in this phase, always considered to be equal in thickness, in order to reduce the number of degrees of freedom. Furthermore, we set the total height of the pillar upon which the uppermost metal is formed equal to $80nm$. Such height has been chosen, as it is the typical depth of the tranches obtainable with our facilities. Figure 5.10 (b) presents the comparison between the extinction ratios of bilayer WGPs fabricated with a thickness of the metallic layer $t = 45nm$ and for the three different materials. The shape of the ERs for this new kind of polarizers is, besides the appearance of some minor shoulders, very similar to what presented in Figure 5.7 for the single layer WGPs. The magnitude of the extinction, nevertheless, is strikingly different: while the maximum theoretical ER for Al was slightly below 100 in a single layer WGP, a bilayer WGP reaches ER higher than 3000 in the red and near infrared parts of the spectrum. Even a polarizer made of Ag presents now extinction ratios higher than 60.

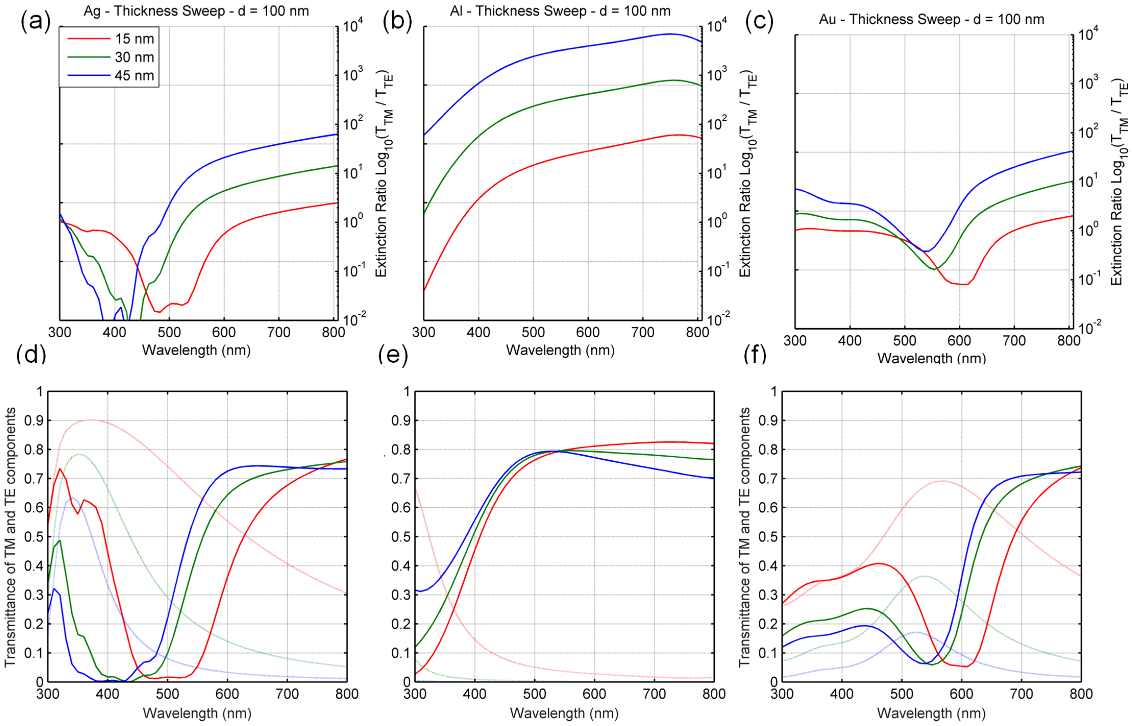

Figure 5.11: Panels (a) - (c) show the Extinction Ratios of double layer WGPs, while panels (d) - (f) present the transmission of the TM modes (solid lines) and TE modes (dashed lines) for different thicknesses and of Ag, Al and Au, respectively. The period of the cell is set to 100 nm.

As observed by Ekinci and coworkers [145], and easy to confirm using the results of our simulations, the ERs of bilayer grid polarizers are *higher* than the ERs obtainable by simply putting in tandem configuration two single layer WGPs. This is due to the insurgence of coupled modes between the two polarization layers, which are separated by distance smaller than the wavelength [153]. Once more, in order to find the correct design strategy, we carried out simulations for the three metals, by keeping the cell pitch constant to $d = 100nm$ and varying the thickness of the metal lines between $15nm$ and $45nm$.

The results of this simulations are summarized in Figure 5.11 and are remarkably different from the results presented for the single layer grid polarizers. As previously stated, the shape of the ER curves is similar, but for each material, the maximum extinction ratio in the IR region increased of up to two orders of magnitude.

For instance, the Al-WGP with the thinnest metal grids ($15nm$) has a peak extinction ratio higher than the $45nm$ thick single layer grid polarizer. Increasing the metal thickness, the polarization efficiency increases with a dramatic rate: considering once more the Al case, each parametrical step involved a one order of magnitude rise of the ER.

Moving the attention to Au and Ag, it is possible to observe a very similar effect, in addition to even stronger redshift of the ER trough for thinner layers. As the ER is calculated from the TE and TM transmittance rates, the lower panels of Figure 5.11 can give some further insight regarding this phenomenon: the plasmonic transparency induced in Ag, for instance, is even more marked than in the single layer WGP. The $45nm$ thick polarizer has now a very sharp peak which resembles even more closely the peak observable in the reflectance curve. A similar behavior is observed in Au-based WGPs, while Al, as now customary, is characterized by different features: although the transmittance of the TM mode is still high in most of the visible spectrum, in bilayer configuration, Al WGPs start to present cut-off behaviors in the UV region, particularly for very thin layers. The effect, however, is still negligible in the visible range, since the transmittance of the TM mode for wavelengths longer than $400nm$ is well above 50% an reaches a peak of 80% around $\lambda = 550nm$.

Adding up all the information gathered through these simulations, it is possible to finally give some ultimate indications for the design and fabrication of a well-performing WGP:

- Al is the best material for WGPs in the visible range. Bilayer WGPs made of Ag or Au might perform well in the IR range

- The thicker the metal layer, the more the structure will be similar to a bulk metal to the TE mode

- The narrower the pitch, the more the structure will be similar to a perfect dielectric to the TM mode

- Bilayer WGPs promote the ER by substantially dumping the transmission of the TE mode (up to 2 orders of magnitude, for a given thickness), at the cost of slightly sacrificing the transmission of the TM mode (Transmittance 10% lower than single layers)

We will use these indications for the design of the optimal WGP realizable with the available technology and we will compare the experimental results to the theoretical findings presented so far.

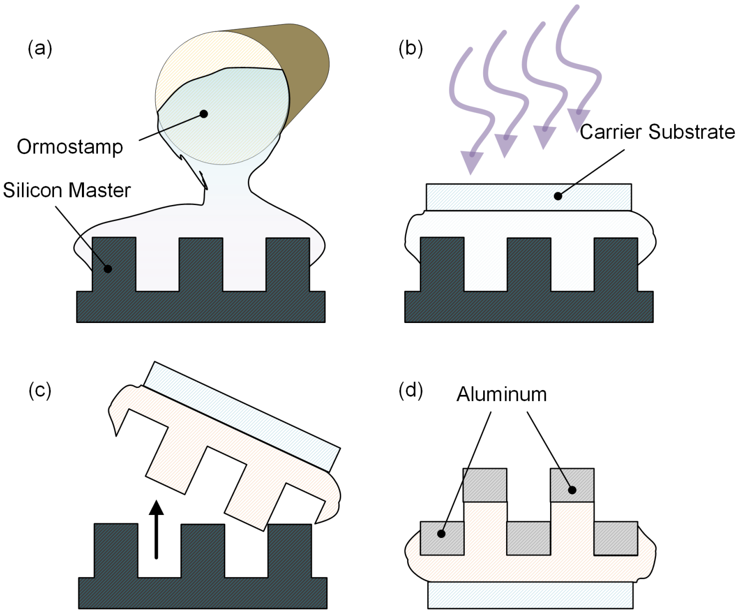

Figure 5.12: The schematic represents the process for the realization of a bilayer WGP. The process starts by replicating a master fabricated with conventional lithographic techniques in a Silicon wafer. An UV curable polymer is first poured onto the master (a) and then pressed down by a carrier substrate and exposed to light (b). The replica is peeled off (c) in order to be used as substrate for the WGP. As a last step (d), metal is thermally evaporated on top of the structure, and the two off-plane grid-lines are ready.

5.3 Fabrication of Visible Light Polarizers

5.3.1 Fabrication Steps of Bilayer WGPs

The fabrication of WGPs is performed in four main different stages, represented in the drawings of Figure 5.12. First an UV curable polymer is poured on a silicon master with the desired line pitch. In our case, as molding material we chose Ormostamp, because of its high transparent and its ability to conform to sub-100 nm features [154]. On top of the polymer is placed glass or PEN (from now on also *carrier substrate*) which will help the spreading of the polymer and will provide additional mechanical stability during the subsequent processing steps. The polymer is then exposed to an UV light dose, eventually thermally cured and peeled off from the silicon master. After peeling off, a negative replica of the master is ready. Since a negative replica of a grid-line structure with 50% duty cycle is identical to the original, there is no need to create a positive replica, reducing the number of process steps with respect to what introduced by Wang et al. [147].

Finally, although the Ormostamp replica is circa $50\mu m$ thick and is robust enough to be used as a stand-alone substrate, we preferred to keep the carrier material, to guarantee

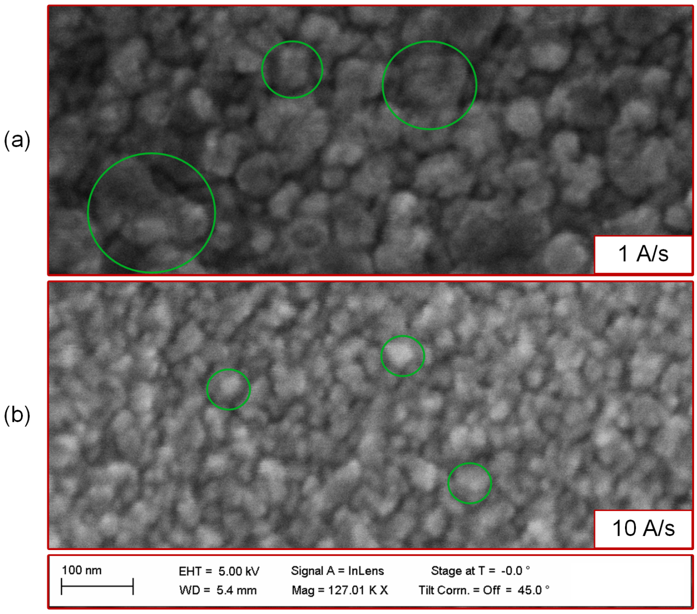

Figure 5.13: The figure shows SEM images of the surface of an evaporated Al film when the evaporation rate is (a) $1\text{Å}/sec$ and (b) $10\text{Å}/sec$.

more stability. The last step of the process is the direct physical vapor deposition of the target material: the metal will be deposited both on the peaks of the grid structure and in the valleys, naturally generating a bilayer grid.

The process is remarkable for many reasons: it is clean, does not need any dry or wet etch, the structure is self-assembled, there is no waste of material. There is, however, one major caveat, related to low-than-expected ERs, which will be evident in the next subsection. For the fabrication of our bilayer WGPs we used grid-lines with a period of $100nm$, a pillar height of $80nm$ and we evaporated $45nm$ of Al, in order to respect all the guidelines for the fabrication of a well-performing WGP we formulated at the end of Section 5.2.

5.3.2 Influence of the Evaporation Rate

Although the apparently simple fabrication process, the first attempts at the realization of WGPs were not entirely successful. It was possible to observe and measure a difference in the transmission of TM modes with respect to TE modes, but the ERs were in the order of few units. However, observing the evaporated metals at the Atomic Force Microscope (AFM) and at the Scanning Electron Microscope (SEM) gave some important insights.

The first information, deducible at a very first glance, was the big Al grain size. Figure 5.13 (a) presents the typical surface of an evaporated Al layer on Ormostamp, with

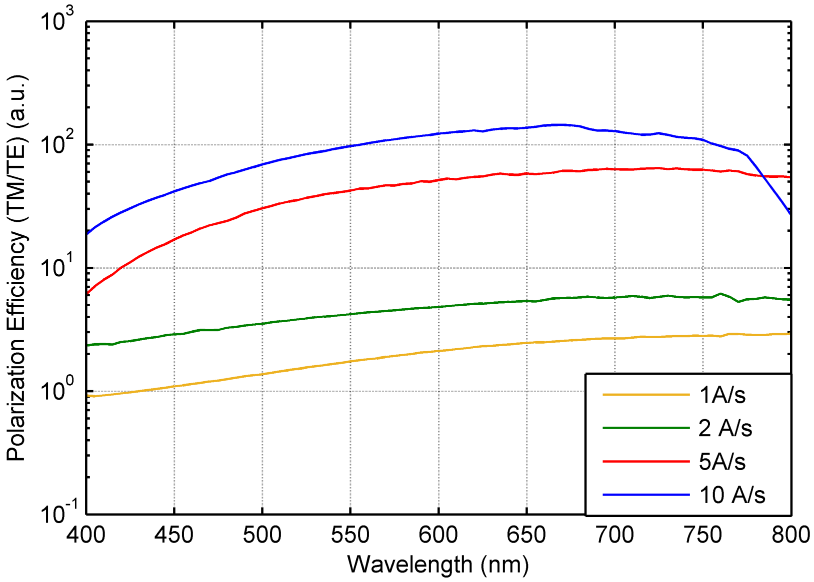

Figure 5.14: The plots show the measured ERs for WGPs produced with the methods described in this section and with different evaporation rates.

evaporation rate of 1 Å/sec: the circles indicate some representative particles, and do not mean to have any analytical indication. The average particle size has been, however, evaluated with means of the image-analysis software ImageJ, applied on SEM scans taken in different parts of the sample: with these processing conditions, the average particle size is found to be circa $58nm$. This grain size is clearly unacceptable: since the pitch of the periodic structure is $100nm$, the width of the troughs of the stamp will be $50nm$ in best case (i.e. in the case of a perfect replica). The big metal grains led to the formation of inhomogeneous lines and to an almost continuous Al film, more than an alternation of two separated grid lines.

One of the reasons behind this phenomenon is the evaporation rate at which the process is performed: if the rate is too slow, the heat emitted by the PVD crucible enhances the surface energy of the sample and promotes the formation of big agglomerations [58]. To avoid this issue, we tried different evaporation rates (namely, 1 Å/sec, 2 Å/sec, 5 Å/sec, 10 Å/sec), in order to find an optimal value which would yield smooth samples, but still guarantee accuracy on the metal thickness.

The best result, shown in Figure 5.13, was obtained with 10 Å/sec, which yielded an average grain size of $29nm$. To this evaporation rate, it is associated the best ER for a bilayer WGP produced within this work, as inferable from the plots in Figure 5.14: for increased evaporation rate, the quality of the grid polarizer steadily increases and almost saturates when passing from $5Å/sec$ to $10Å/sec$, and the ER of the latter grid polarizer exceeds 100.

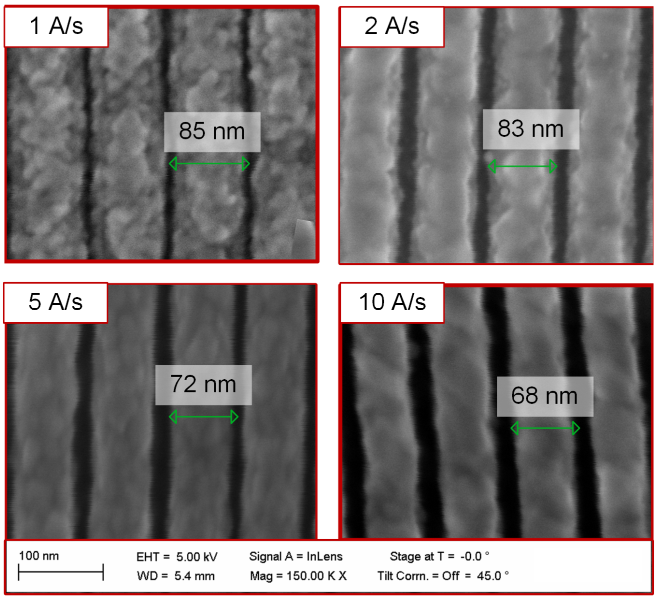

Figure 5.15: The plots show the extinction ratio of the fabricated bilayer WGPs as a function of the evaporation rate of Al

Nevertheless, although this value is good enough for analytical applications [7], it is almost two order of magnitude lower than the values estimated through the simulations, and no light has been yet shed on the causes of this strong divergence.

5.3.3 Simulation of Real Grid Polarizers

One of the reasons behind this significant difference between the simulations and the measured ER values resides in the non accurate reproduction of the geometrical constraints we set. Observing the lines fabricated with different evaporation rates, shown in Figure 5.15, it is possible to see how the duty cycle is never 50%, as simulated, but always above 65%. One more reason lies in the fact that the profile of the evaporated metal is not rectangular and is not as thick as $45nm$ everywhere. As pointed out by Ekinci and coworkers [145], the evaporation on top of the grids will assume a "mushroom shape" and will shield the grooves from receiving further metal. As a result, the bottom layer must be considered thinner than the nominal $45nm$.

Softwares based on the numerical solution of the Maxwell equations have very few constraints on the geometry of the structures to simulate. Exploiting this advantage, we took in account all the considerations developed so far: the duty cycle of the structure was increased to 68%, the thickness of the bottom layer reduced to $30nm$ and the profile of the Al on top of the grid lines was considered semi-elliptical. The only real constraint we were subject to is on the shape of the bottom metal layer, which needs

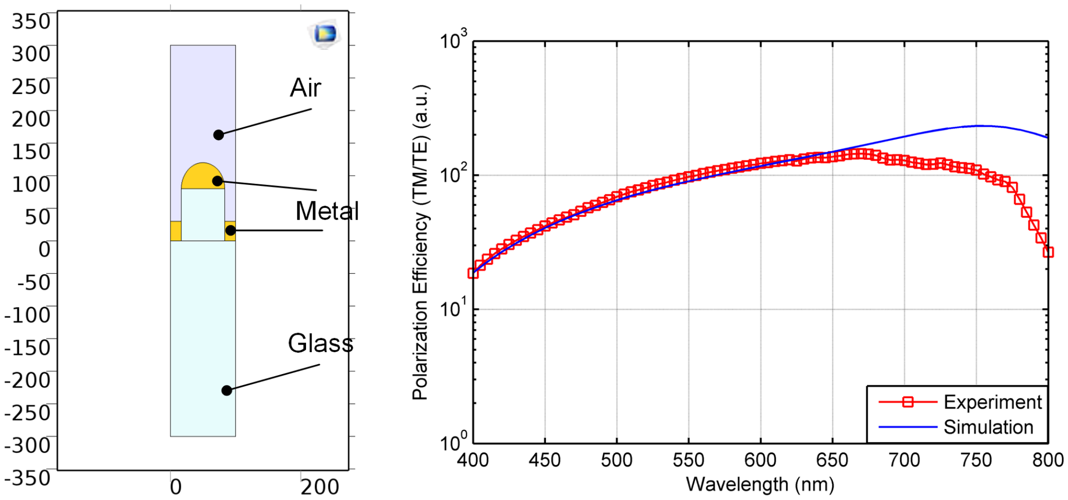

Figure 5.16: The diagram in panel (a) is the geometry of the simulated structure, as built in the User Interface of COMSOL. The plot in panel (b) shows the experimental curve of the fabricated WGP and the simulated spectrum after including the discussed changes

to be kept rectangular to avoid singularities of the EM field at the periodic boundary.

Figure 5.16 presents the single cell, as it has been drawn in the COMSOL interface and a plot with the simulated value and the experimental values reported for a WGP fabricated with Al evaporated at $10Å/sec$. It should be noted that the curves were not "fitted", since the simulation we defined and performed does not have any fitting parameter; the similarities between the curves are due to the experimental observations and to the intrinsic nature of the devices.

The experimental and the theoretical curves, however, diverge for wavelengths longer than $670nm$ and the difference becomes very significant (more than one order of magnitude) in the near infrared. We believe the behavior of the curve in that spectral region should be attributed to experimental limitations of the set-up used for the measurement, more than to real phenomena happening in the fabricated WGP. This is due to the fact that the commercial polarizer used to select between TE and TM mode becomes much less effective in the wavelength region around $700nm$ [155].

5.4 Integration of Polarizers with OPDs

5.4.1 Integration of Grid Polarizers with OPDs

We have so far hypothesized and proved the realizability of thin film polarizers by using a very simple soft lithography process and Al, a material totally compatible with the common processes used in Organic and Printed Electronics. The goal of the following

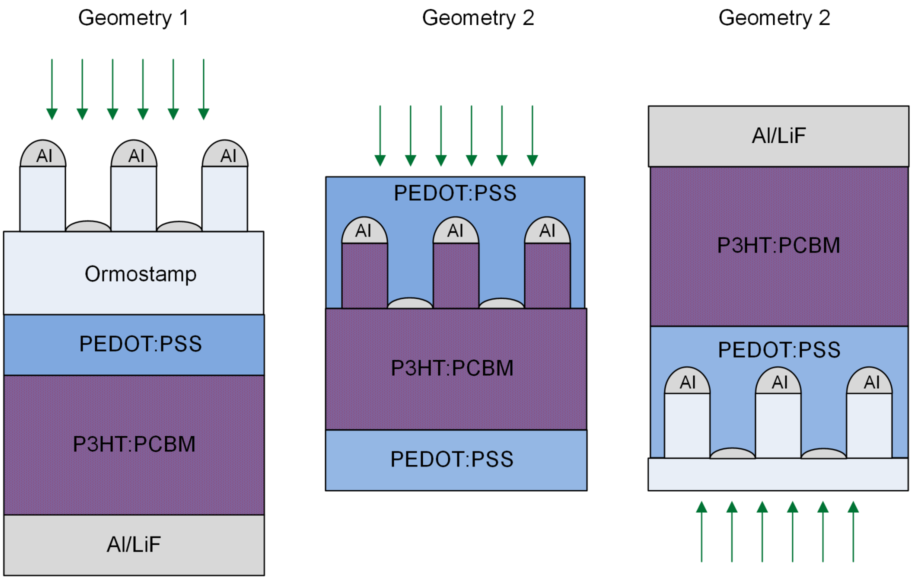

Figure 5.17: Description of the three most promising geometries for the integration of WGPs and OPDs. Geometry 1 uses the backside of the Ormostamp as a substrate to build the OPD; geometry 2 involves the nano-imprint of the P3HT:PCBM blend and the use of Al as a cathode; geometry 3 is based on the work-function modification of the Al with PEDOT:PSS to use it as an anode

part of this chapter is to demonstrate the possibility of the *vertical integration* of such structures, as well as integrating a light polarizer into a photodetector, is the most intuitive concept.

There are, however, several strategies to perform this kind of integration, which Figure 5.17 presents. In the first geometry we propose, the backside of the Ormostamp is used as a substrate for the fabrication of direct-structure OPD. The biggest advantage of this method is the simplicity of fabrication: the OPD can be produced with the procedures described in Chapter 3. Nevertheless, a number of drawbacks occur. The first, and most evident one, is that the Al layer is exposed to the environmental agents (or to culturing medium, in case of LoC applications). As extensively seen in Section 4.3, Al layers, when not encapsulated, are prone to oxidation and delamination. Additionally, building the polarizer on the opposite side with respect to the OPD, allows, diffused, unpolarized light to penetrate from the sides of the structures. This signals would be detected, constituting a source of noise, or, in some cases, even induce false positives.

The second geometry we propose is based on very different idea: the P3HT:PCBM blend can be patterned with means of nano-imprint lithography (as previously shown by Schmidt et al. [156]), and the Al lines could be evaporated directly on top of the evaporated blend. The main advantages of this techniques are the direct integration of the OPD and the polarizer, without any insertion loss. The use of Al as a cathode, without the need of any interlayer to adjust its work-function. However, the process is quite complex, delicate and sensitive to temperature. Furthermore, in order to be properly patterned, the blend must be as flat as possible, and the use of spray-deposition for the realization of the photoactive layer would be inhibited. Thus, it would be difficult to produce the thick blend layers needed to keep a low dark current [43]

Finally, the third geometry we propose is based on a hybrid approach: the WGP is fabricated on one side of the Ormostamp, just as described in the previous section, and the OPD is built *on top* of the polarizer. Through the spray-deposition of a layer of PEDOT:PSS it is possible to adapt the work-function of Al. To enhance the electrical conductivity of the polarizing film, in order to effectively use it as an anode electrode. Subsequently, the active layer is spray-deposited and the cathode electrode is composed by a PVD-formed LiF/Al layer, as in Section 3.3. This geometry does not present any evident drawback, while the advantages are manifold:

- the polarizer is in direct contact with the OPD: it acts as filter and electrode.
- it is to fabricate (through standard spray-deposition technique).
- the Al layer is encased on the one side by the photodiode and on the others by a thick Ormostamp layer. This leads to an enhanced barrier against water and oxygen (As shown in section 4.2).

The most important parameter for the choice of one geometry over the other, however, is how effectively the integrated WGP is able to block the TE mode and transmit the TE mode. Indeed, given the different combinations of refractive indexes, it is not safe to assume that the ERs of the three strategies will be the same. Thus, before opting for one of it, we simulated the transmission through the structures to have further ground for decision. However, as Ormostamp, P3HT:PCBM an PEDOT:PSS are not standard materials in the COMSOL library, it was necessary to extrapolate their characteristics from literature.

Ormostamp was considered to be a lossless medium with a refractive index extracted by the producer's data sheet, and its absolute value in the visible range is comprised between 1.525 and 1.49. Regarding P3HT and PCBM, they are widely studied materials in optics and electronics, hence both the real and imaginary part of the refractive indexes could be extracted from previous literature [157]–[161]. The blended material was obtained through the simple arithmetic average between the values of P3HT and PCBM, with a "virtual" semiconductor approach [162]. Finally, although PEDOT:PSS has been studied and employed in many applications during the last years [77], [117],

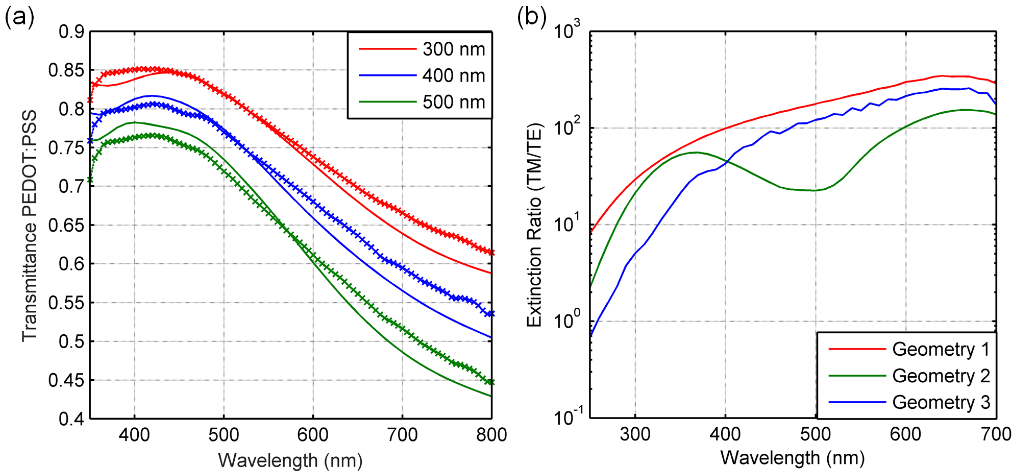

Figure 5.18: The left hand side panel (a) shows a comparison between simulated and experimentally measured transmittance of PEDOT:PSS layers. The plots on the right (b) show a comparison of the ERs obtained simulating the three geometries described in Figure 5.17. The transmission of TE and TM mode are influenced by the combinations of different refractive indexes

[163], the use of different ink formulations or post treatments can significantly influence its optical properties [164].

For these reasons, in order to ensure reasonable simulation results, basic parameters for this material were extracted from the work of Pettersson and coworkers [163], but they were modified to better fit our experimental results. Figure 5.18 (a) presents the measured (markers) and simulated (solid lines) transmittance curves for $300nm$, $400nm$ and $500nm$ thick PEDOT:PSS layers.

Figure 5.18 (b) shows the comparison between the ERs of all the considered geometries. The first geometry is, in essence, the case we saw at the end of the previous section, and outperforms the other two geometries. It has ER about twice the value of Geometry 2 and about three times the value of Geometry 3. On the other hand, the third geometry has a very similar shape, and ERs above 50 in the entire visible range, while the second geometry presents a wide trough in the central part of the spectrum, due to the interaction with the photoactive blend.

Besides these main differences, all the alternatives here proposed are valid approaches for the fabrication of integrated polarizers, although Geometry 1 and Geometry 3 present higher ERs in the region which is interesting for our OPDs applications. Between these two, Geometry 3 is the one which is entirely novel and presents more benefits, and it is our designated choice for the fabrication of polarized OPDs (pOPDs).

5.4.2 Fabrication and Characterization of pOPDs

The production of a pOPD, then, articulates as follow: after fabricating the WGP with means of soft lithography, a $200nm$ thick layer of PEDOT:PSS is spray deposited on top of the Al layers (Figure 5.19 (b)), followed by a $650nm$ thick layer of P3HT:PCBM (Figure 5.19 (c)). The device is then annealed at $120°C$ for 10 minutes and the PVD of a LiF/Al cathode electrode is performed on top. Microscope observations at each step show the strong difference between the reflected light in TE and TM mode, and prove that the performance of the WGP do not degrade during the production process. Once the devices are fabricated, they are ready to be characterized, and we evaluated their performances in terms of JV characteristics (in dark and under 1 sun TE and TM polarized) and EQE (monochromatic light TE and TM polarized). Figure 5.20 (c) and (d) show photographs of a complete device, acquired utilizing a camera polarizer aligned along the TE and TM direction, respectively. Remarkably, the use of the filter shows the creation of an optical window inside the Al electrode line, which confirms the intuitive idea of light polarizers we structured in Section 5.11: if the light is oriented orthogonally to the grid lines (d), the metamaterial will be optically equivalent to an Ormostamp window, while if the light is perpendicular to the grid lines (c) it will be equivalent to a reflective metallic layer.

Furthermore, Figure 5.20 shows in panels (a) and (b) the JV characteristics and the external quantum efficiencies of a typical pOPD. The dark current of the device is in line with other devices we showed throughout this work, and the illuminated TE and TM currents are discernibly different. The photocurrent is, however, one order of magnitude lower than the diodes we presented in previous sections, since most of the blue and part of the green light are cut off by the polarizer. This can be understood looking at the EQE in panel (b): instead of the classical high and flat response of the photodiode to light with wavelength comprised between $400nm$ and $600nm$, EQE has a rising profile, which follows the trend of the pristine WPG and reaches a peak around $600nm$, where both the TM light transmitted by the WGP and the EQE of a thick P3HT:PCBM photodiode are maximum.

The process could be further optimized: the reduction of line pitch of the WGP is a possible path, since the feasibility of lines with a pitch of $60nm$ has been already demonstrated [154]. Furthermore, the presence of a very high serial resistance indicates either interface problems or that one of the electrodes (realistically, the anode) has a relatively low conductivity, and a consequently increased resistance. As a result, a general optimization in the fabrication of the WGP could bring ameliorations in every component of the device: the polarizing part and the diode.

The ratio of the EQE at $600nm$ for the TM light to the EQE of the TE light is,

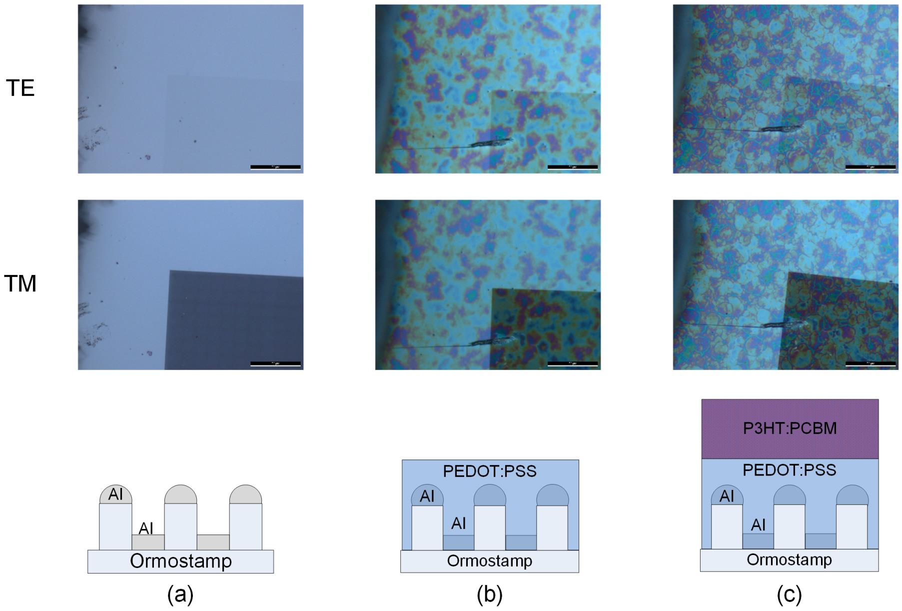

(a) (b) (c)

Figure 5.19: Microscope images acquired in reflection mode with a linear polarizer oriented in TE and TM mode at the different process steps. Panel (a) shows the WGP as evaporated, (b) shows the same sample after the spray-deposition of PEDOT:PSS, while (c) shows the result after the evaporation of a very thin layer of P3HT:PCBM (thicker layers would hide the underlying WGP)

nonetheless, above 50, which is still a remarkable result. To the best of our knowledge, what we report here is the first self-polarizing Organic Photodiode. We believe it paves the way to an entire new class of applications, and simultaneously, it is the realization of the objectives we defined at the beginning of the chapter.
This device, is the first example of a system which completely embraces the philosophy of *vertical integration*.

5.5 Integration of Polarizers with OLEDs

5.5.1 Process for Fully Spray-Deposited OLEDs

To complete a vertically integrated system, the ideal combination of a self polarized photodetector is the realization of a self polarized light source. In this direction, the most natural choice is the realization, in analogy to the pOPD, of a pOLED. The main difficulty resides in the implementation of a reliable and reproducible deposition process, usable for the realization of the very thin polymeric layers ($< 100nm$) needed for a well-performing OLED.

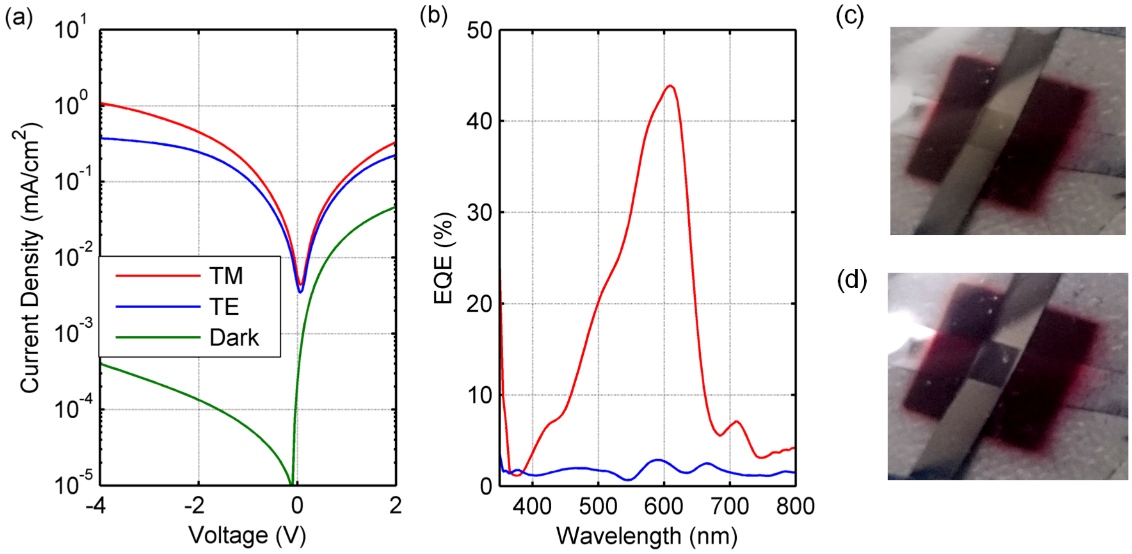

Figure 5.20: (a) JV characteristics and EQE (b) for a typical pOPD, under illumination with light polarized in TE and TM mode. For the JV characteristics, the illumination is 1 sun AM1.5G, while the EQE is measured with means of a monochromator. Panels (c) and (d) show a photograph taken with a polarization filter (in TE and TM mode, respectively) of the pOPD under ambient light.

Spray-deposition is once more the ideal candidate for the process defined above: via tuning of the ink formulation, we showed, in Section 3.4, the possibility of spray-depositing polymeric layers with thickness even lower than $20nm$. Furthermore, the deposition must be confined to a very small area of the sample and must be carried out onto a relatively rough surface (as the Al-WGP). Since the optimization of a spray-deposition process for OLEDs lies beyond the goals of the thesis, the obtainment of acceptable process conditions was conducted following a very simple procedure with relatively few iterations. For a given value of atomization pressure, we found the parameters which yielded a spray-deposited layer in the “intermediate" regime. We then swept the deposition time, in order to find the relationship between deposition time and layer thickness for a selected set of parameters.As presented in Figure 5.21, by using 1 bar of atomization pressure and 15 sec of deposition time, it was possible to achieve a $70nm$ thick layer with relatively low roughness.

The stack of a simple OLED is very similar to the stack used for OPDs: a semi-transparent electrode, PEDOT:PSS as work-function modifier, active layer, evaporated cathode. We first fabricated a control OLED, in which the PEDOT:PSS layer and the light emitting polymer (Super Yellow, PDY-132) were spin-coated on top of a pre-patterned ITO sample. Subsequently, we used the spray deposition parameters we

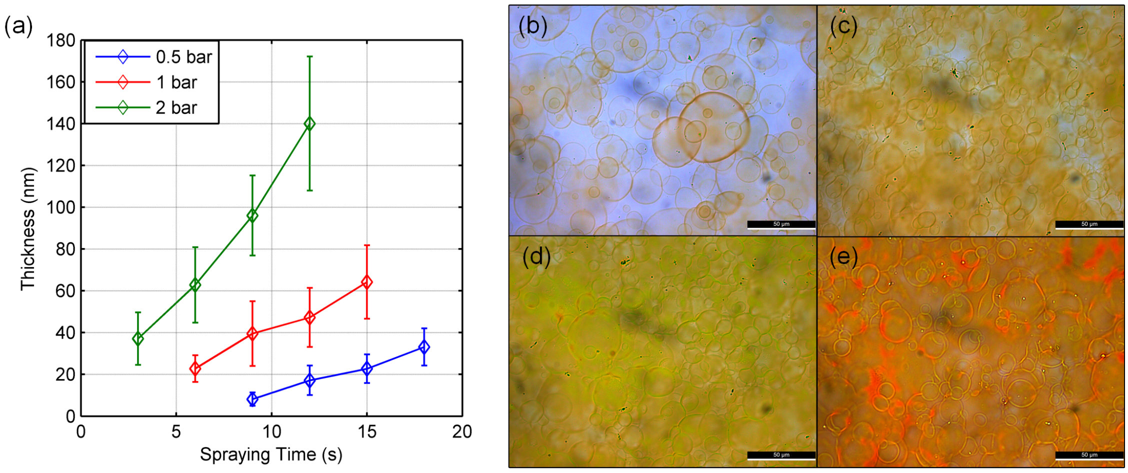

Figure 5.21: On the left hand side (a), there is a plot of the thickness and the roughness (error bars) of spray-deposited layers with different deposition parameters, as a function of time. On the right hand side, there are optical micrographs of films of different quality: too sparse (a), uniform ($t \approx 30nm$) (b), uniform ($t \approx 70nm$) (c), uniform ($t \approx 120nm$) (d). The scale bar is $50\mu m$ for every picture.

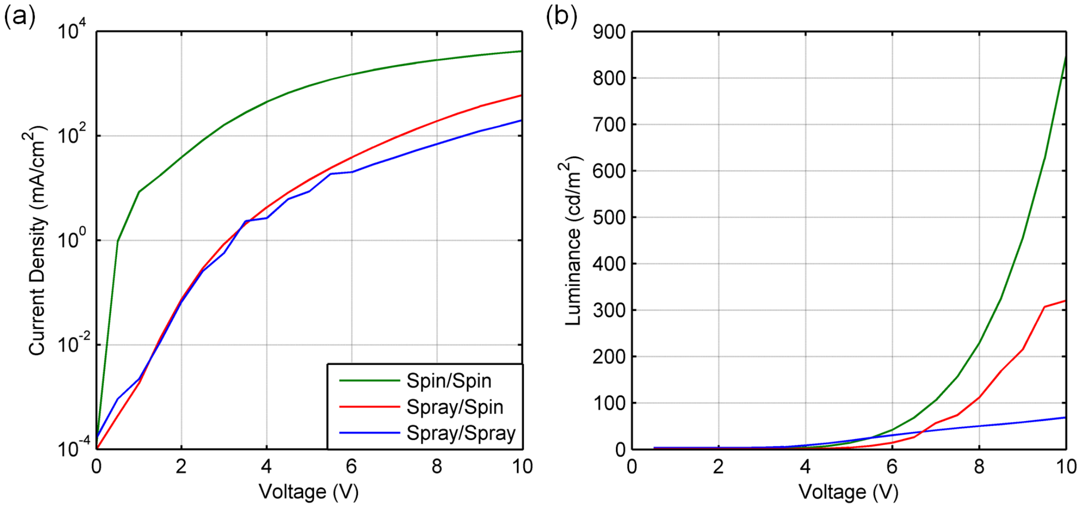

Figure 5.22: Current Density-Voltage characteristics (a) and the Luminance-Voltage characteristics (b) of three OLEDs categories: fully spin-coated on ITO electrodes, spin coated PDY-132 on spray-deposited PEDOT:PSS, fully spray-deposited

have developed to fabricate two set of OLEDs. The first one, features a spray-deposited conductive PEDOT:PSS electrode and spin-coated PDY-132, while the second one is fully sprayed. This last class of devices, if working, can be directly replicated on top ot the Al-WGP to obtain eventual pOLEDs. For every kind of OLED, the cathode was obtained by PVD deposition of a LiF/Al electrode, as previously described for the OPDs.

Figure 5.22 presents the Current Density-Voltage characteristics (a) and the Luminance-Voltage characteristics (b) of such devices. The control OLED presents a much higher current density with respect to the ones with spray-deposited electrodes, with a steeper growth in the low voltage region. This effect is direct derivation of the increased serial resistance due to the employment of PEDOT:PSS instead of ITO. Although this peculiarity of the PEDOT:PSS electrodes does not constitute a significant problem for OPDs, it represents a major drawback for OLEDs, where the efficient injection of charge is an important prerogative. The lower current is also reflected in the luminance characteristics, since this quantity is reduced to a third of the maximum value obtained by the control sample.

The introduction of spray-deposition for the active layer, does not significantly affect the current injection, but has dramatic influence on the emission of light. The most likely explanation to this phenomenon resides in the lower quality of the spray-deposited sample with respect to the spin-coated one. Droplet boundaries and surface irregularities influence the emission of light and might entirely hinder the functionality of the OLED [165]. As the goal of this section is to obtain OLEDs performing well enough to be integrated with WGPs, we applied the obtained process for the fabrication of pOLEDs, and since the final devices function properly, as we will shortly see, the further optimization of the deposition process is postponed to other works.

5.5.2 Fabrication and Characterization of pOLEDs

The processes developed so far were finally used for the realization of a self polarized OLED. First, the WGP has been fabricated as reported in Section 5.3, followed by the immediate deposition of a PEDOT:PSS work-fuction adaptation layer, the photoactive polymer PDY-132 and the evaporation of a LiF/Al cathode. The devices were encapsulated with epoxy glue and a thin glass lid, to prevent excessive deterioration during the characterization. Once the devices were complete their performances were evaluated in terms of JV and LV characteristics (data not shown) and spectral emission. Figure 5.23 (a) presents this latter feature of the pOLEDs: a commercial Glen-Thompson polarizer was placed on top of the OLED and positioned parallel to the polarization axis of the

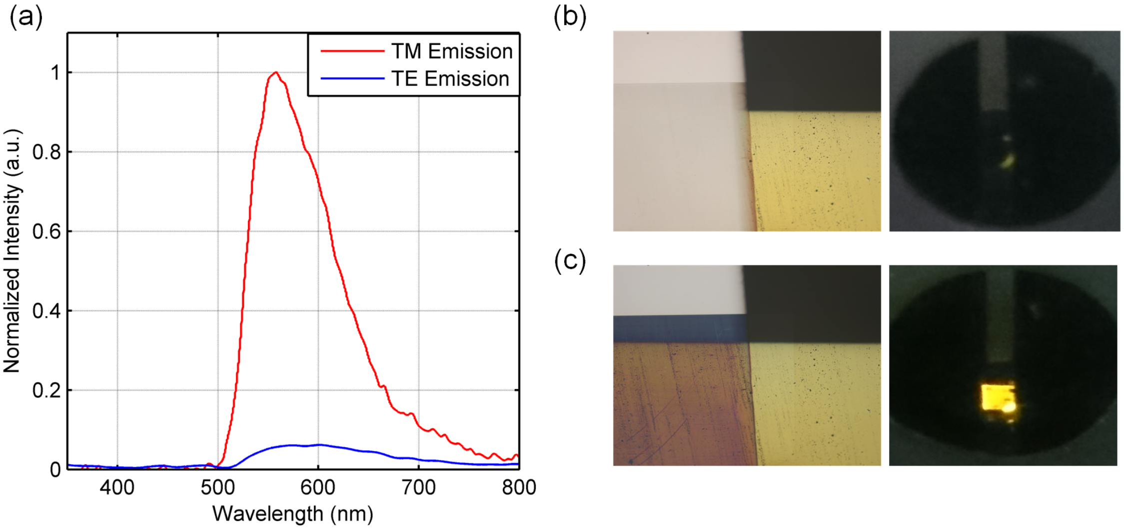

Figure 5.23: Panel (a) presents the emission spectrum recorded for a fabricated pOLED when a TM oriented and a TE oriented linear filter is placed on top of the device. Panels (b) and (c) show an optical micrograph at the intersection between the WGP and the cathode line (left hand side pictures) and a photo of the full device in the dark under 10V bias (right hand side pictures), with a TE and TM photographic filter, respectively

WGP. The emission light was examined with means of a CCD spectrometer. From the spectral characteristics, the polarizing nature of the devices is immediately evident: in the peak region, the TM emission is up to 15 times stronger than the TE, and the dichroism is very strong on the whole spectrum. Panels (b) and (c) show an optical micrograph and a full-sample photo (in the dark) of the samples, using a linearly polarizing photographic filter. Particularly interesting are the optical micrographs (left hand side). The images have been acquired in the point where the WGP is built and the top cathode ideally intersects the anode.

As noticed for the pOPDs, the rotation of the polarizer, opens an “optical window” in the aluminum line which would otherwise be almost fully reflective. Furthermore, the image helps to assess one of the most critical parts of the process: the alignment between the top and the bottom electrode. In this case, the alignment was good enough to consent a working device, nonetheless, in the points where the WGP is not perfectly aligned, there is the formation of hot spots of non-polarized light, as the one identifiable in the bottom right corner of the full-sample photographs.

One last remarkable observation is the following: the emission peak of the PDY-132-pOLED is almost exactly in correspondence of the of the EQE peak of the P3HT:PCBM pOPD. To exploit this advantage and to attain a full vertical integration (OLED / Polarizer / Polarizer / OPD), the devices were tested in conjunction.

The pOLED, placed at a distance of $1cm$ from the pOPD was excited with a square

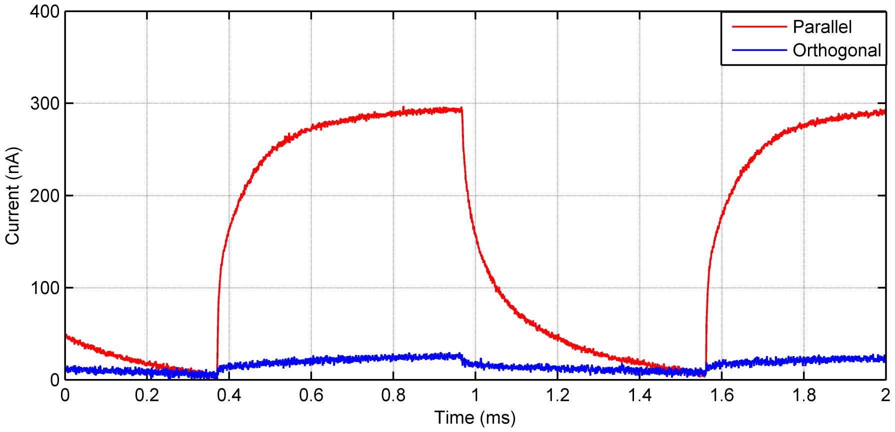

Figure 5.24: Response of the pOPD stimulated by the yellow emission of the pOLED at an AC frequency of 1kHz. The difference between TM-polarized and TE-polarized excitation is significant and discernible.

wave, and the current of the pOPD was amplified with a transimpedence amplifier and recorded with means of an oscilloscope. A typical time-current plot under parallel and orthogonal polarization is presented in Figure 5.24. Strikingly, when the pOLED's polarization axis is parallel to the one of the pOPD, the S/N ratio is circa 45, while when the polarization axis is orthogonal to the pOPD, it was measured to be circa 2. The rise time of the electrical signal is estimated to be circa $150\mu s$, suggesting that the cutoff frequency is not far from the one measured for the fully-solution processable OPDs presented in Chapter 3.

5.6 Summary

In this chapter we showed the feasibility of an approach based on the vertical integration of thin film components. The goal was to realize organic optoelectronic devices (OLEDs and OPDs) with embedded polarizers, and was achieved through a sequence of successive steps. First, we carried out multiphysics simulations of grid polarizers (WGPs) in single layer and bilayer configuration, comparing the quality of polarizers obtained with Ag, Al and Au. We found out, consistently with the specialized literature, that the thicker the metal layer and the narrower the pitch of the structure, the better the polarizer is. Al resulted to be the best material for the production of polarizers in the visible range, while bilayer WGPs were demonstrated to be up to two orders of magnitude more effective than their single layer counter parts.

Subsequently, we fabricated and characterized a soft-lithography made WGP, obtaining ERs much lower than the simulated ones. Investigating this issue with means of SEM scans, we identified the non-idealities of the real structure and we used the acquired knowledge to perform more realistic simulations.

The optimized WGPs were then embedded in OPDs and OLEDs, where they were employed as both field polarizers and anode electrode. The obtained devices were then characterized separately and in conjunction, showing good performances: the TM to TE ratio of the photocurrent induced in a polarized OPD (pOPD) by a polarized OLED (pOLED) was bigger than 20, and the two signals were perfectly discernible.

The devices are largely perfectible in the single parts. Nevertheless, the final outcome is a full vertically integrated system, with polarized OLEDs and OPDs, where every single part has been realized using simple and conventional production techniques. This proof of concept, then, lays the first stone for the reduction of the number of external devices needed for Lab-on-a-Chip applications and, if further improved, can provide a valid alternative to bulky polarizer in any polarimetric measurement system.

Chapter 6

Horizontal Integration: 3D printing and Organic Electronics

As natural complement to the concept of *Vertical Integration* described in Chapter 5, here we introduce the concept of *Horizontal Integration.* With this term, within the frame of this work, we define the idea of embedding several components in the same horizontal plane. In the field of bioelectronics, this concept is fully embraced by the Lab-on-a-Chip technology, which is a complex mix of readout electronics, sensors, actuators, micromechanics and microfluidics.

The fascinating objective we will try to pursue in this chapter is the realization of procedure to integrate organic electronic devices, meaning both sensors and actuators, directly onto microfluidic chips and to design an apparatus able to attain this goal with the maximal automation.

In order to understand why the current fabrication techniques are not suitable for this purpose, it is necessary to understand which are their real limitations. The first information to take in account of, is that the most widely used material for building microfluidic chips has been for a long time PolyDiMethylSiloxane (PDMS) [166], because of its proven biocompatibility [167], [168], mechanical flexibility [169] and the numerous techniques developed to bond it with a large set of materials [170].

One of the known drawbacks of this material, however, is the difficulty of direct patterning, because of its high viscous nature and the pronounced hydrophobicity. Among the most effective attempt to the develop a technique for the immediate patterning of this material is a work of Garra et al. [171], where a fluorine-based RIE process is developed to obtain the anisotropic etching of the material, which can be rendered very spatially selective with the aid of a stencil mask. This approach, although significantly better than the previously reported wet etching techniques in terms of precision and

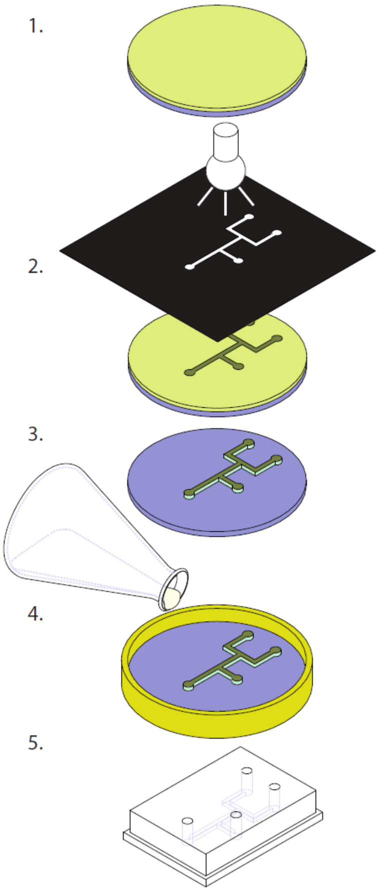

Figure 6.1: The diagrams show the classical steps needed in a soft lithography process: 1. Spin coating of the negative-tone photoresist, 2. UV light exposure 3. Photoresist development 4. Pouring of the elastometer (typically PDMS), 5. Cutting into shape and punching the inlets and outlets. Image taken from the work of Qi et al. [174]

accuracy, is extremely cumbersome, time consuming, and requires the use of expensive equipment. Although cleaner and more accurate techniques such as *bond detatch lithography* have been proposed in more recent times [172], the simplest and more often used technique for micropatterning of PDMS is the so-called *soft lithography* [173]. This approach relies on the remarkable property of PDMS to be able to reproduce micrometer-size features: when poured on a sample, PDMS fills the underlying microgaps and, if subject to proper curing, will retain the shape after the solvent dried up. Based on this principle, it was possible to develop the soft lithography technique [175], where a PDMS microfluidic channel is fabricated, starting from a CAD file in a defined sequence of steps. Very detailed protocols can be found in literature [176], but the in-depth analysis of this technique lies out of the purpose of this work. The basic process stages, however, are summarized in Figure 6.1, extracted from an interesting work by Qi et al [174]. First, a photolithographyc mask is created with the desired microfluidic structure and is impressed via UV light onto a negative-tone photoresist, previously spun on a silicon wafer. Once the film is crosslinked, it can be developed and cleaned: at the end of this delicate process, a master stamp, similar to the one used in Chapter 5 for the realization of the polarizers, is obtained. Afterwards, PDMS is poured on the master stamp, is degased and cured. Once the solved is dried up, it is possible to cut the PDMS chip in the wanted shape, peel it off and transfer it to a carrier substrate.

However, although this method leads to good and reproducible results, it is inherently slow and difficult to automate. Furthermore, a small change in the design requires a big effort and a long preparation time before it can be applied into finite products. The realization of multilayered chips is also limited by the use of this technology, since fabricating multiple levels made of a flexible material as PDMS avoiding the collapse of the channels is not easy to achieve. In addition, once the microfluidics chip is obtained, it needs to be connected to all the separate parts which compose a lab-on-a-chip system (inlets, outlets, pumps, electronics, heaters) and, while holes and cavities must be externally created to insert the components, the sealing of the channels must still be guaranteed to prevent the contamination of the experiments or, eventually, biohazard [166].

Finally, given the strong hydrophobicity of PDMS, the direct fabrication of solution processable electronic devices on a PDMS chip might be extremely challenging.

For these reasons, mostly related to the flexibility in design and the possibility of realizing arbitrary changes, there is the need of new technologies able to take over the old-fashioned, limited soft lithography approach. One of the most promising techniques in this field is the so called *3D printing*, part of the larger class of *additive manufacturing* technologies [173], [177].

In this chapter we will first make some general considerations on additive manufacturing as a consumer product and as a fabrication method for research and industry, then we will describe the three main 3D-Printing technologies. Afterwards, we will select one of these technologies and use it to fabricate a centimeter sized perfusion well with an integrated semi-transparent heater. The heater is produced with means of the integration of spray-deposition and 3D printing and it is a proof of concept which paves the way to an entire new class of devices for both consumer electronics and biosciences, where the electronic components do not need to be externally attached *to* the object, but they are fabricated *in* the object.

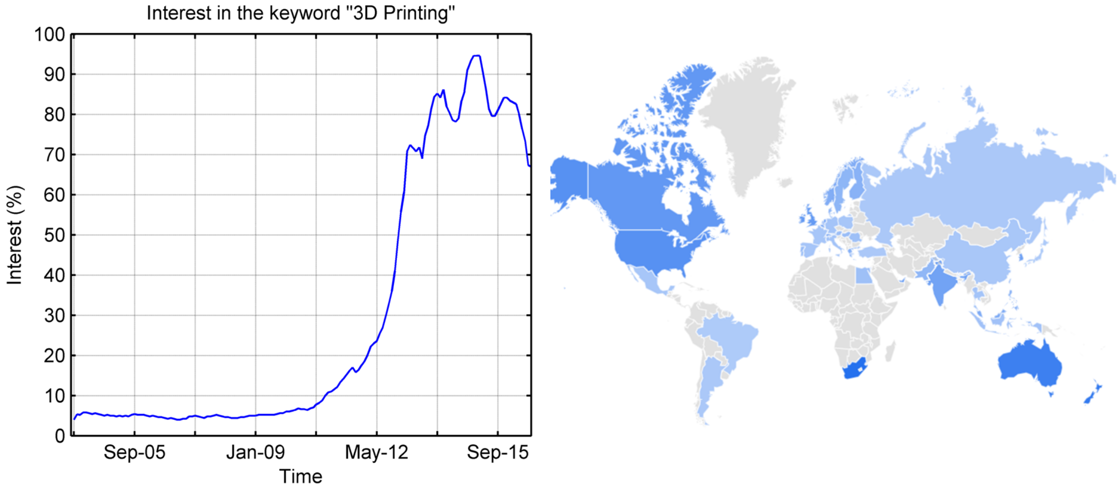

Figure 6.2: The plot on the left shows the relative interest in the keyword "3D Printing" according to *google.com* (Google Trends). Starting from early May 2012, the interest in the keyword has been steadily rising, reaching an apparent peak in mid 2015. In the right hand side, an heat-map of the world is presented: the darker the blue, the highest the research interest in a given country.

6.1 Additive Manufacturing

6.1.1 3D Printing

With the generic term 3D printing, or additive manufacturing, have been designated all those technologies aiming at the fabrication of solid objects through the deposition of a material, starting from a computer-based 3D model. This technology has recently attracted a paramount interest of research, industry and consumers. In the academia, the advancements in additive manufacturing led to the attainment of important results in the fields of bio-engineering [178] [179] [180], electronics [181] [182] [183] and structural engineering [184]. Figure 6.2 shows the trend in the interest for the keyword “3D Printing” according to the volume of researcher on the search engine *google.com*.

The extraction of the data has been performed through the instrument *Google Trends* and shows the global interest in the keyword and an heatmap with the distribution of the interest in the world. The interest in the topic started rising very recently, and was subject to a steady increase, leading to the reach of a peak in mid May 2015. Even more interestingly, the heatmap in the right hand side of Figure 6.2 shows how the interest is very well spread throughout most of the industrialized nations, including 18 of the 19 individually represented countries in the G20.

Given the current stunning interest and significance of the technology, however, it might be surprising to know that the first registered patent related to a 3D printing machine dates back to 1986 [185]. Instead of quickly moving towards the production of small consumer oriented machines, the 3D printers manufacturers only produced bulky, high-definition, high through-put machines commercialized until mid of the first decade of the 2000s, relegating these apparatuses to the fast prototyping and research in the big enterprise business.

The motivations behind this phenomenon are numerous but they are mostly related to the high prices of the printing apparatuses and materials and the “user unfriendly” modeling software tools [186]. One of the causes for the high prices of the equipment is the complex system behind the classic approaches for the additive manufacturing, namely the Stereolithography (SLA) and the Selective Laser Sintering (SLS). As we will see in the next subsection, both methods rely on techniques which are difficult to scale down, such as motorized high power light sources. A totally different approach to the production of 3D printed objects is constituted by the so-called Fused Deposition Modeling (FDM). An apparatus based on this newer, lower quality technology, can now be bought as a finite product or in form of a mountable kit for less than €500 [186].

The objective of this chapter is to show how to integrate additive manufacturing techniques with existing organic electronics processing methodologies, aiming at the fabrication of fully integrated smart objects. The main trade-off to solve is the one between the quality of the 3D-printed objects per se and the possibility of integrating the printing technique with other deposition methods.

Hence, in the next subsection we will briefly describe the most utilized different techniques for 3D printing, listing their advantages and drawbacks and we will motivate the choice of FDM as the most relevant technique for the work conducted in this thesis. Afterwards, we will focus in the obtainment of the proposed goal.

6.1.2 3D Printing Techniques

Selective Laser Sintering (SLS)

Figure 6.3 shows a conceptual drawing of a Selective Laser Sintering (SLS) machine. These apparatus are composed of to main cavities, where the material cartridge and the object holder are positioned. The working principle is based on the direct solidification of a powder with means of an high power laser pulse, and depending on the intensity of the laser, different material densities can be obtained, approaching, for very powerful lasers, 100%, i.e. the density of the bulk material from which the powder was obtained. The deposition happens in several steps: first, the material (which can be originated

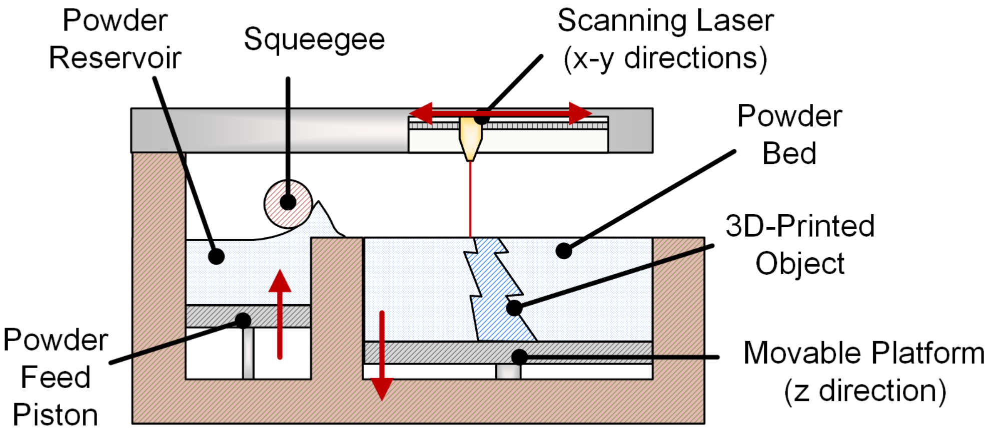

Figure 6.3: The diagram represents a typical SLS setup, with labels indicating the most important parts, namely the powder reservoir, the squegee, the scanning laser and the movable platform.

by plastics, resins or even metals) is spread on the movable platform by a squeegee; afterwards, a scanning pulsed laser performs the sintering, illuminating only the powder onto an accurately defined pattern. At this stage, there will be a part of the powder (the one exposed to light) which has been sintered and it is solidified, while all the remaining part will be unchanged, and could in principle be re-utilized. Once a first layer is completed, the movable platform will move down of the chosen z resolution (which can be as low as $10\mu m$) and the process starts again. By doing so, at the end of the printing process there will be a solid form immersed in a powder bed: the object can be simply removed from the container and washed over to be complete.
The biggest advantages of this technique reside in the possibility of obtaining extremely smooth finish, very high resolutions in every direction and the wide choice of materials. All these advantages, however, come at a cost: since both the mechanical and the optical parts have to be extremely accurated, SLS printers are the most expensive on the consumer market, starting, in the moment of writing, at €5000 for the most basic models. Furthermore, their complexity maxes them not prone to easy integration with other systems, and albeit perfect for the fabrication of stand-alone objects, cannot be employed for the purposes of this work.

Stereolithography (SLA)

Figure 6.4 shows a conceptual drawing of a Stereolithography (SLA) machine. These apparatus are conceptually similar to SLS, but simpler and with lower energetic demands, since they are based on photosensitive resins, rather than sinterable powders. In SLA printing, the movable platform is immersed into a photoactive resin; as in SLS

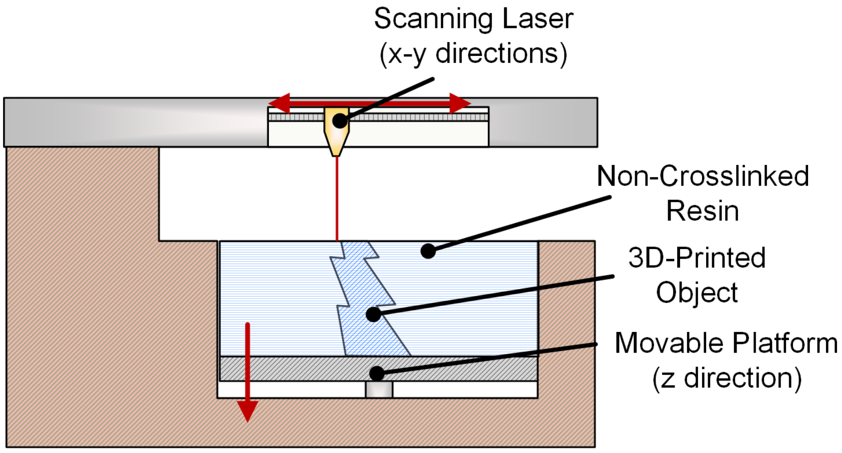

Figure 6.4: SLA setups are, as a matter of principle, very similar to SLS setups, although they rely on a substantially different physical principle. In this diagram we present the most important parts of an SLA apparatus, which are essentially the xy scanning laser and the movable z platform.

a laser is canned over the material to cross-link it in the desired pattern and once one layer is completed, the moving platform is shifted downwards of the selected z-step. Fresh material will be exposed on the surface of the reservoir and the exposure can be iterated for the fabrication of the successive layers. Although the functioning mechanism of SLA is similar to the one of SLS, the physical principles involved are very different: the former is based on the cross-linking of light curable polymers or resins (a low intensity process), the latter is based on the re-solidification of a powder (a high intensity process). The implications are contrasting: on the one hand SLA machines are simpler, lighter and less expensive (in the moment of writing, it the most basic models are priced around €3000), on the other hand the availability of the materials is poor. The choice of “cartridges” is limited and the prices are elevated. Furthermore, albeit SLA machines are simpler than SLS, they are still very delicate and integrated, factor which represents a major limitation for their implementation in in-line processes.

Fused Deposition Modeling (FDM)

Figure 6.5 shows a conceptual drawing of a Fused Deposition Modeling (FDM) machine. These apparatus are composed of a heated bed capable of moving in the X and Y directions and a crossbar able to move in the z direction, where the printing head is mounted. The printing process happens feeding a plastic filament into a heating element set at the melting temperature of the material. The liquid material is then pushed through a nozzle and reduced to a thinner filament. Moving the printing head, the nozzle scans a certain pattern and it is able to draw the desired shape on the heated

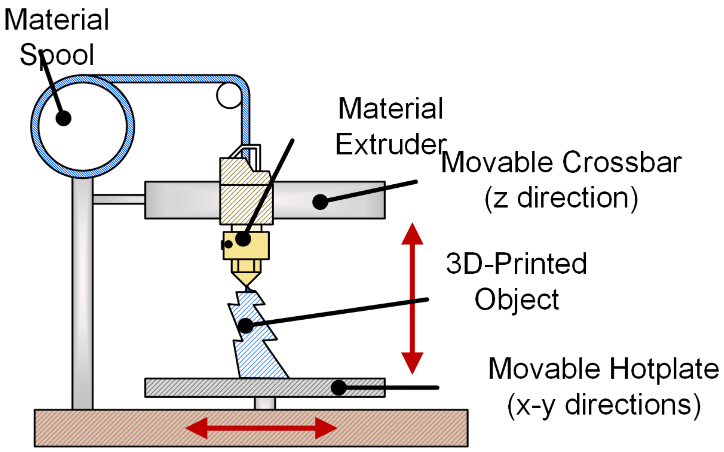

Figure 6.5: FDM is the simplest of the 3D printing methodologies. In this diagram is possible to observe the most important parts of an FDM printer, namely the extruder, the moving crossbar, the moving hotplate and the material spool.

bed.

The two main drawbacks of this technology are the low resolutions achievable (both in the lateral and the vertical directions), which are limited by the size of the orifice: a smaller orifice will be able to produce thinner lines, but will be more prone to clogging and failure. Furthermore, since each layer is obtained by the juxtaposition of polymeric lines, the possibilities to obtain flat layers and smooth finish are strongly hindered, and the typical surface will have a wavy profile, with oscillations in the range of the hundreds of microns. However, this technology presents some key advantages over the other two we presented in this section. Primarily, the choice of materials is wider than the one for SLA, the materials are cost-effective, easy to find and easy to self-synthesize. Furthermore, these printers are simply built and can be easily modified to be integrated into complex processes. Finally, they are inexpensive, rendering them a prime choice for small laboratories and the consumer user.

6.2 Integration of 3D-Printing and Spray-Deposition

6.2.1 Concept

The examples briefly introduced in Section 6.1 demonstrate how in a few years 3D-printing has become a mature technology and how the integration with discrete electronics is steadily progressing. However, albeit the technology is in an advanced state and the ability to produce layers as thin as few tens of microns has been achieved, the

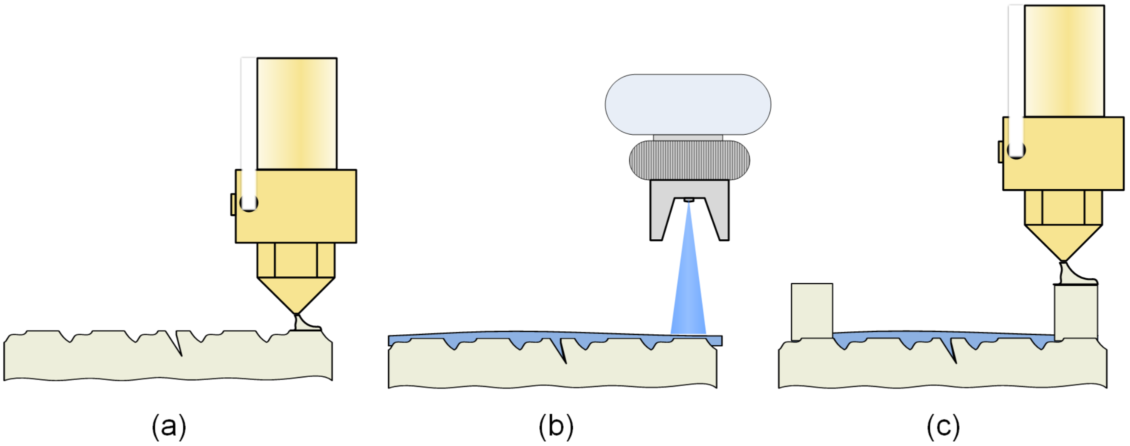

Figure 6.6: Proposed schematic for multi-technology integration. The substrate is first printed with means of FDM technology (a). A functional layer is then deposited through a conventional deposition technique, such as spray-deposition (b), and, finally,(c) the remaining parts of the 3D-printed structure are built above the spray-coated thin film. [187]

integration with existing organic electronic fabrication techniques is still poor. Technologies such as ink-jet printing, spin coating or spray deposition could, in principle be integrated in the printing apparatus in order to realize organic electronic devices *embedded* in the object. The drawings in Figure 6.6 present the concept of a similar process: an arbitrary substrate could be printed, then, with means of the chosen fabrication method, the functional layers could be produced and, as last step, the mechanical structure of the object could be completed. This procedure could then be iterated and used for the construction of more complex structures. Furthermore, with the correct choice of materials, the obtained device could be encapsulated and packaged, leading to a fully-integrated production system.

FDM seems to be the most natural choice to realize this kind of complex systems, given the simplicity of its mechanics and the wide choice of materials, although it presents a major caveat which has prevented so far the obtainment of such solutions. Differently from SLA and SLS, where the direct sintering or curing of the materials leads to smooth finish and elevated features accuracy, FDM relies on the juxtaposition and overlapping of few-hundred micron wide extruded lines, which renders wavy and rough structures [182], [183]. Such uneven substrates are not suitable for conventional deposition techniques (e.g. spin-coating), but the employment of more robust and conformal deposition methods, such as spray-deposition, could overcome this barrier. Besides the applications already cited in the previous parts of this thesis, this technique has been used in the last years for the realization of thin film devices with arbitrary shapes [74], on various substrates, ranging from conventional plastic foil [43] to the end

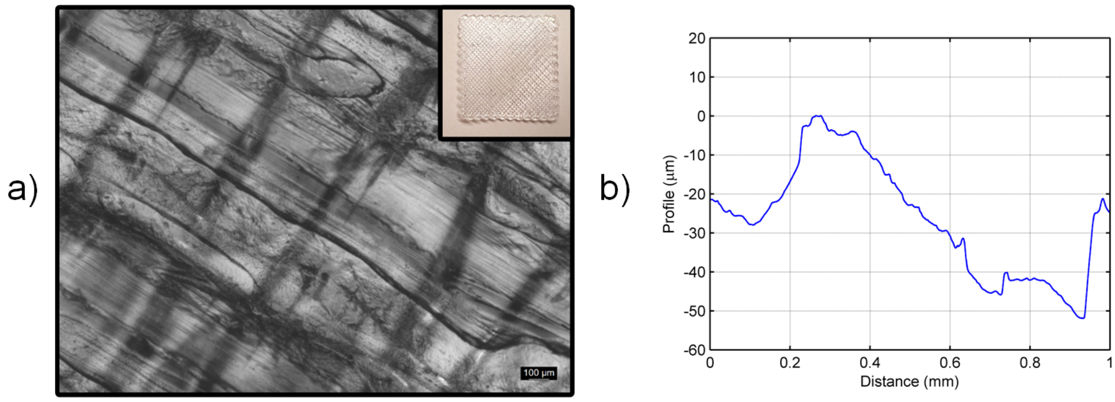

Figure 6.7: (a) Optical micrograph of an as-fabricated 3D printed sample, with a nominal thickness of 0.5mm and composed of two overlapping layers. The inset shows a photograph of the fabricated sample. (b) Surface profile of the typical surface of the same sample.

of an optical fiber [188] to cutlery [165].
The objective of this part of the thesis is to demonstrate the full integration of spray-deposition and 3D printing, by first overcoming the practical challenges imposed by the materials and the current technology and then designing and building a machine able to create fully printed objects.

The substrate designed to start the experiments is a $25 \times 25mm^2$ square sample, conceived to be comparable to the glass substrates used in the first part of the thesis work.The effective thickness of the sample is 0.5 mm and it is obtained by the overlapping of two polymeric layers, arranged in a criss-cross pattern, which, as expected, led to a high surface roughness. Figure 6.7 (a) shows an optical micrograph and a photograph of a typical sample made of a commercially available, semi-transparent ABS derivative (Bendlayő), while Figure 6.7 (b) shows the surface profile. In order to evaluate the RMS roughness, we employed a mechanical profilometer whose stylus was scanned in a direction orthogonal to the topmost polymeric lines. The evaluated RMS roughness is circa $15\mu m$, while the peak-to-trough difference can range between $50\mu m$.

6.2.2 Reduction of Surface Roughness

This surface roughness is prohibitive for the realization of any thin film device. As a reference, the typical length of commercially available CNTs rarely exceeds $5\mu m$ [189], and the high roughness of the sample would render the reach of a percolation threshold rather troublesome. To reduce the film roughness, three approaches based on previous literature have been elaborated and tested, and all of them exhibit the potential of being integrated in an in-line automated process. The three methods, presented graphically in

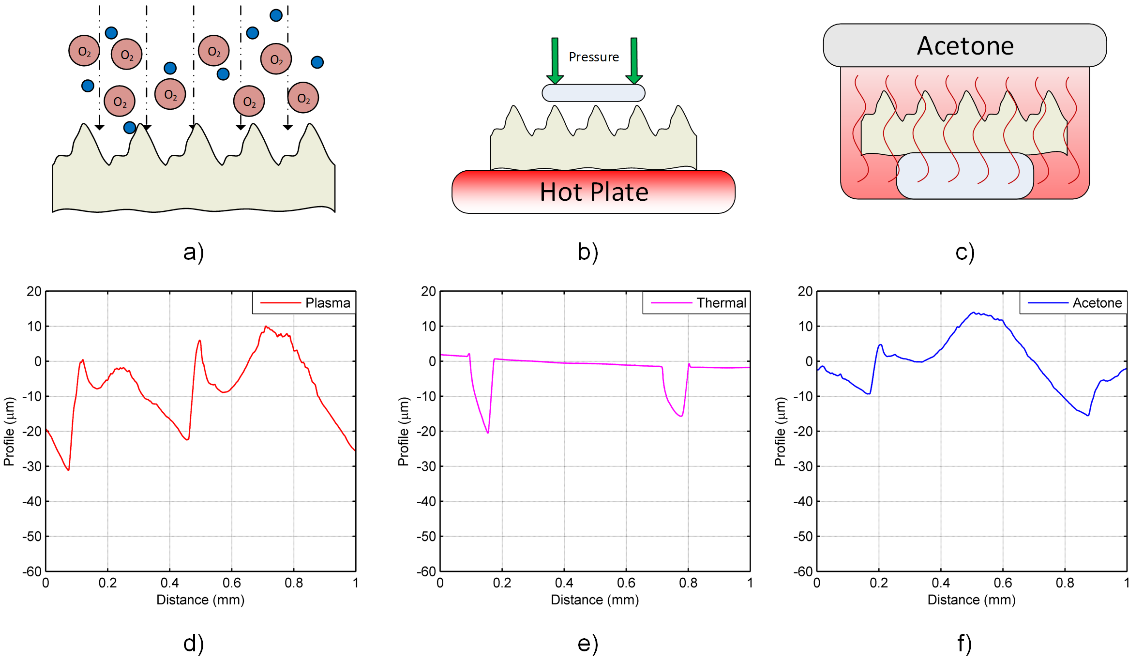

Figure 6.8: Three different approaches proposed for the planarization of the 3D printed structure. (a) Represents the use of a high power microwave oxygen plasma exposure for a prolonged time (b) Represents the use of mechanical force combined with thermal energy in order to partially melt the upper features and render them conformal to a flat mold (c) Represents the positioning of the sample in a solvent saturated atmosphere. Panels (d), (e) and (f) report a typical profile measured with the three different planarization approaches.

Figure 6.8, represent three main surface modification categories: a non-contact physical modification, a mechanical physical modification, and a chemical modification. From the first class of procedures, the use of a high power plasma treatment has been selected. The sample was placed in a remote microwave plasma chamber, where the plasma power was set to 200W and the process was conducted for variable durations comprised between 30 s and 300 s. Observing Figure 6.8 (d) can be inferred that the effect of the plasma treatment only minimally affects the film roughness and profile. With this method, the RMS roughness was reduced from an initial value of 14.6 ţm to 10.4 ţm, while the peak-to-trough amplitude was decreased from 51.85μm to 40.93μm. The change is significant (both quantities were diminished by more than 20%), but the absolute values are still to high to be employed in the targeted application.
The second planarization technique employed led to significantly better results. The utilized concept is the following: bringing the plastic sample close to its melting point, the application of a well regulated pressure on its surface through a flat mold would yield the juxtaposed lines to collapse and form a smooth surface. To this purpose, the

sample was heated up to 250°C and a flat mold was held on the top of the structure for 5 minutes with a constant pressure of 2.5 kPa. This particular pressure was the minimum sufficient to achieve a planarizing effect and it was chosen to be as low as possible to avoid any damage to the sample. What we observed with higher pressures and/or temperatures was the complete deformation of the sample, or in some extreme case, its perforation. With the optimized conditions, though, the results obtained through this process are of special appeal.Figure 6.8 (e) shows the mechanical profilometer scan of the surface, denoting a mostly flat finish and merged adjacent lines. The caveat lies in the fact that some among the widest troughs are not filled by the molten lines. This phenomenon keeps the RMS roughness and the peak-to-trough amplitude relatively high, with values of 6.5μm and a of 21.20μm, respectively.

The last planarization technique considered in this part, which proved to be effective in previous studies [190], consists in the exposure of the sample to a saturated atmosphere of Acetone. A glass support is placed in a container with liquid Acetone and the sampled is laid on it. Afterwards, the container is covered with a glass lid and heated up to 100°C in order promote the evaporation of the solvent. Once acetone starts to evaporate, it chemically etches the exposed surface of the sample, at the same time reducing the height of the lines and softening the 3D-printed object. If the polymer is exposed to the Acetone gas for too long, it liquefies. Once re-solidified, the original shape, geometry and dimensions were not kept, rendering this planarization method too destructive. However, once more it was possible to find a compromise duration of the process, identified with a 300 s lapse. After this time frame, the RMS roughness is remarkably reduced, with values almost comparable to the ones obtained with the second treatment class (7.5μm), while, as evident in Figure 6.8) (f) the peak-to-trough amplitude is still in the range of 30μm. The RMS roughness obtained through the methods presented so far, are summarized in Figure 6.9 (a) and are consistent with values reported by the specialized literature for similar approaches [190], [191]. Furthermore, optical inspection of the substrates led to a remarkable finding: the sampled exposed to any planarization technique were more transparent and less hazy than their untreated counterparts. To quantify this effect, we evaluated the transmittance in the visible spectrum, estimating a 35% increase of the average transmittance for the thermally treated sample, 23% for the chemically treated one, while the plasma treated ones were not significantly modified. The improvement of the transmittance seems to be closely related to the amelioration of the surface roughness, and a further enhancement is expected as a result of a better planarization.

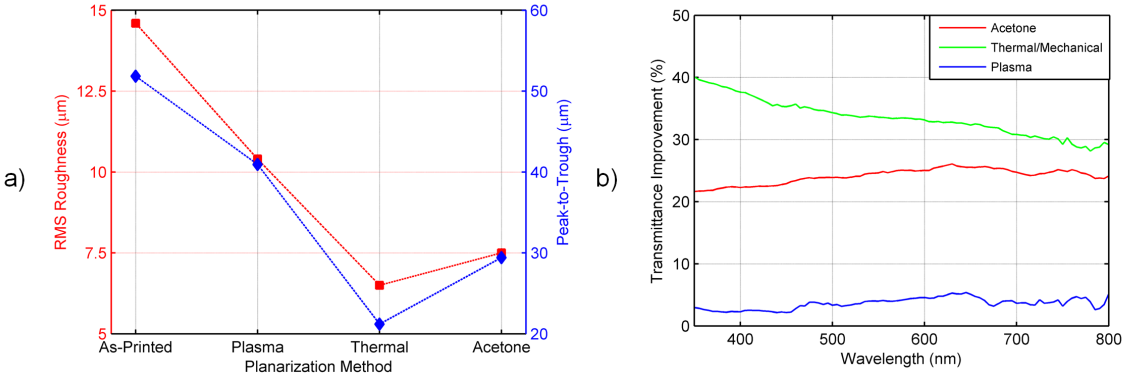

Figure 6.9: (a) RMS Roughness and Peak-to-Trough for the samples treated with different approaches. The best results are obtained for the thermal/mechanical method (b) Relative transmittance change with respect to the as-printed sample. The thermal treatment improves the average transmittance in the visible range of 35%.

6.2.3 Spray-Deposition of the Planarization Layer

Although the approaches presented so far were effective in planarizing the samples up to a certain extent, they present a main further limitation which is not due to the process outcome. The totality of the methods are difficult to implement into an integrated machine able to 3D-Print, planarize and spray-deposit the wanted material. Only the thermal one could be implemented with a relatively easy design, which would include the realization of ad hoc robotic arms, nonetheless.

An alternative could, however, be based on spray-deposition itself. As a matter of principle, an insulating material, deposited in a thick layer, could be used to fill the gaps between the adjacent lines without interfering with the subsequent functional layer. Moreover, the solvents utilized for the solution of the polymer, might lead to a milder version of the planarizing effect of Acetone. The range of materials possibly employable for this application is extremely wide, since any insulating material could be used, however our choice was guided by a non-technical resolution. During the 3D printing of the prototypes, many samples were disposed, because they had been destroyed by some harsh treatment or simply they were not needed anymore, which led to a relevant waste of material. However, since both ABS and Bendlay are soluble in organic solvents, the most straightforward solution to both issue (material waste and insulator for the planarization), was the choice of the substrate material as planarization polymer.

Bendlayő was found to be well soluble in organic solvents such as Toluene (Tol) and 1,2-Dichlorobenzene (DCB), which have been shown to be reliable and easy-to-control solvents for spray deposition [43], [73]. Moreover, their boiling points and vapor pressures are significantly different [192], which leads to two completely dissimilar behaviors during spray-deposition and to the necessity to define two separated processes.

As usual, the process optimization is based on the modification of some major parameters: nozzle-to-substrate distance, temperature, pressure and material flow rate. Contextually changing these quantities leads to different droplet size, film thickness and to different deposition regimes. The choice of the parameters should be performed in order to guarantee uniform layers, with an accurate thickness control. These last two prerogatives are essential for the spray-deposition of functional layers, although they assume special importance in the realization of planarization layers as well. The uniformity is directly related to the roughness of the film, while the deposition time, which regulates the thickness of the layer, is also responsible of the chemical etching effect.

Figure 6.10 presents the measured surface profiles of film spray-deposited on glass starting from 1% wt solutions of Bendlayő in Tol (a) and DCB (b), at the end of the tuning process. In case of DCB, a flat solid layer with a thickness of circa $1\mu m$ is obtained with a spraying duration of 10s, while the optimization process for the Toluene solution did not yield the desired result. This can be attributed to the lower boiling point and significantly higher vapor pressure of Toluene [192], which renders it less prone to a wet deposition regime and to a fine control of the spray-cone.

The regulation of the deposition time, moreover, also plays an important role. Figure 6.10 (c) presents the surface profile of layers obtained with a spraying time of 10 s, 30 s and 50 s.

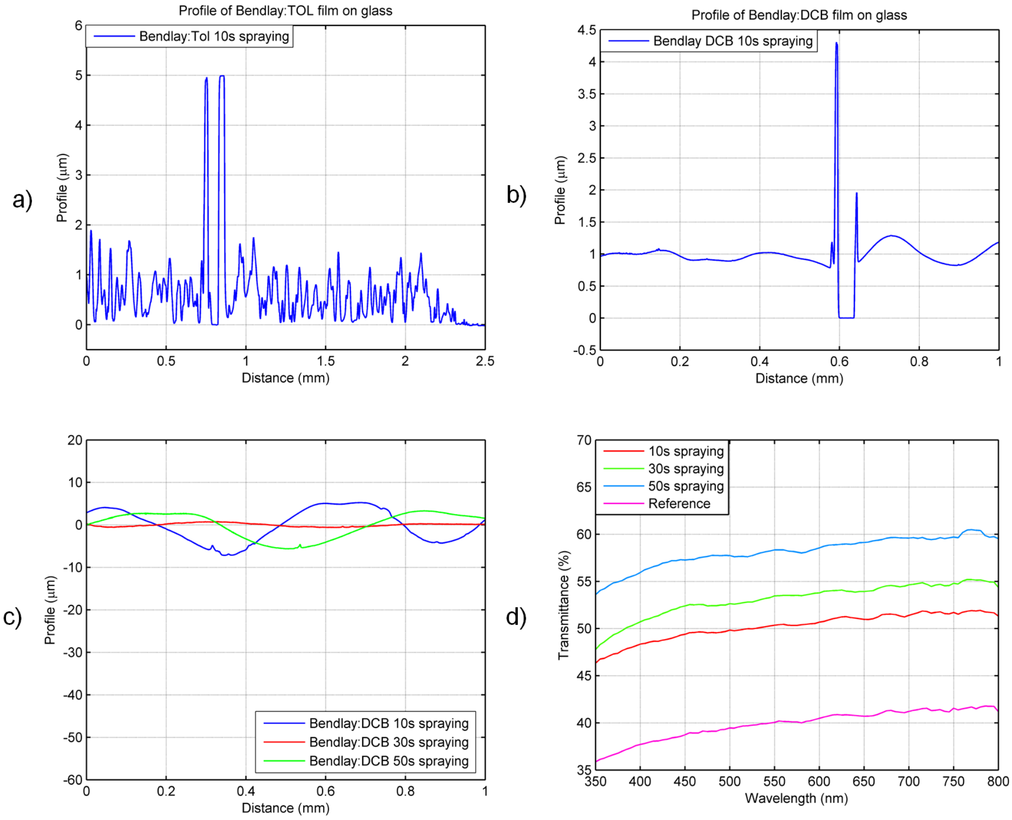

Figure 6.10: Profiles of spray-coated Bendlay on a glass sample when dissolved in (a) Toluene and (b) 1-2,Dichlorobenzene. (c) Surface profiles of spray-deposited Bendlay planarization layers on 3D-printed samples

In the first case, the substrates are not exposed to the deposited material and etching agent long enough to have a robust covering and a strong planarization. The layer is rippled and irregular, although much smoother than the as-prepared film. On the other extreme, 50 s of spraying time, the sample is over-etched and loses it consistency, leading to a melting and successive re-solidification, with a consequent increase in the surface roughness. In some trials, for this long spray duration, holes were generated, hence hindering the practical applicability of the method. The roughness values and the peak-to-trough amplitudes are reported in Table 6.1, along with the values obtained for the previous planarization methods. Finally, in analogy to what presented for the other planarization methods, Figure 6.10 (d) reports the transmittance spectra for the different deposition durations, with improvements quantifiable between 10% and 50% of the original value.

Finally, panels (a) and (b) of Figure 6.11 are Scanning Electron Microscope (SEM) scans of the edge of the spray-deposited regions, for 10s and 30s of spray time, respectively, and give a visual validation of the analytical data extrapolated from the

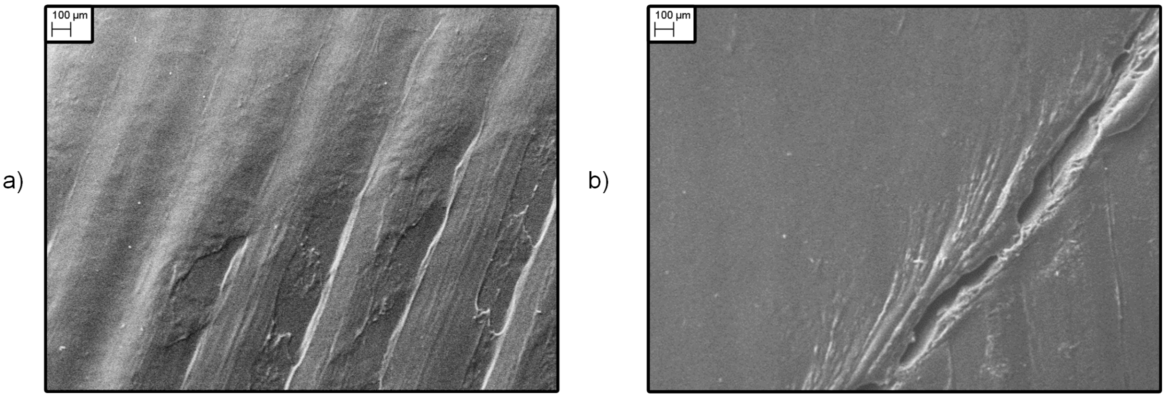

Figure 6.11: SEM scans at the border of the planarized area on a 3D-printed substrate for 10s and 30s of spraying duration, respectively.

	As Printed	**Plasma**	**Thermal**	**Acetone**	**10s Spray**	**30s Spray**	**50s Spray**
RMS Roughness (μm)	14.6	10.4	6.5	7.5	2.4	0.39	3.01
Peak-to-Trough (μm)	51.8	40.9	21.2	29.4	13.3	1.4	8.35

Table 6.1: Summary of RMS roughness and peak-to-trough amplitude for all the considered planarization methods

profilometer. In addition to this, it is evident from the SEM image how the separation between non-planarized and planarized part, when the spray-time is extended, becomes more abrupt, which hints to a strong etching behavior in addition to the deposition of material.

6.2.4 Spray-Deposited Conductive Films on 3D Printed substrate

The effectiveness of the planarization methods, must, however, be validated through the application to a practical case. To this purpose, we chose to deposit conductive nanomaterials on the planarized samples and to measure their sheet resistance as a figure of merit to define the quality of the layer. The first chosen material was a Sodium Dodecyl Sulfate of single walled carbon nanotubes (SDS-CNTs) and was spray-deposited first onto a non-planarized substrate. The resistance of this film ($5684\Omega/\square$) is used as a benchmark for the others, to quantify the improvement due to the planarization.

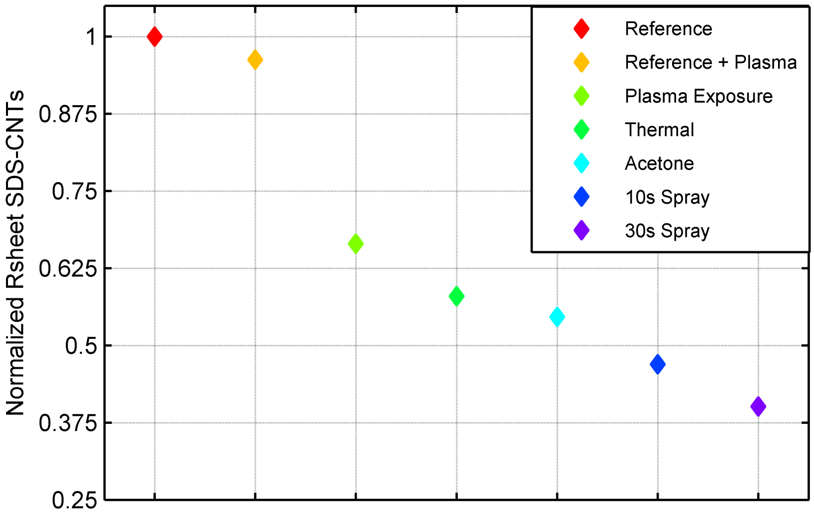

Figure 6.12: Sheet resistance of the spray-coated CNT films onto planarized 3D-printed samples, normalized to the sheet resistance value of the as printed substrate.

The plot in 6.12 presents the normalized sheet resistance of SDS-CNTs for the different planarization methods and shows how the film quality is significantly increased by the utilization of the different planarization techniques. The spray-deposition method resulted to be the most effective one, with an amelioration of the sheet resistance value above 60%, although all the other methods were comparably effective.

Since this approach resulted to function particularly well, it has been employed to show the feasibility of the spray-deposition of two other nanomaterials, namely PEDOT:PSS and Silver Nanowires (AgNW).Table 6.2, summarizes the results obtained with all the conductive nanomaterials and further assesses the effectiveness of the chosen method. Indeed, the planarizing effect leads to a reduction of the sheet resistance of one order of magnitude, approaching values described in literature for thin layers of PEDOT:PSS and AgNW on glass [109], [117]

6.2.5 Integrated Printer

The previous stages demonstrated the viability of the deposition of thin conductive films on 3D-printed structures which have been properly planarized. A final step towards the assessment of the technology proposed in this chapter is the realization of a complete system able to integrate the three functions (3D printing, planarization, spray-deposition of the active layer) and obtain the concept depicted in Figure 6.6.

Spraying Time	**Average $R_s(\Omega/\square)$**		
	CNTs	**PEDOT:PSS**	**AgNW**
0 s	5684	1401	475
10 s	2671	137	49
30 s	2541	123	48
Glass Ref	1444	105	25

Table 6.2: Average sheet resistance of CNTs, PEDOT:PSS and AgNW deposited on spray-planarized layers with different deposition times.

The starting point for the realization of such apparatus, was the purchase of a low-cost 3D printer kit. The Velleman-Kit K8200, produced by the belgian electronics wholesaler Velleman has an open source design, the parts are fully detailed and documented and is based on rigid extrusion profiles. Added up, all these characteristics make the printer fairly easy to assemble and prone to be tweaked, while, at the same time, the choice of a 3D printer in kit contains the overall cost of the equipment (which was lower than 500 €).

The assembled 3D printer is composed of an X-Y heatable stage, a crossbar motorized on the z axis where the FDM extruder is located and an Arduino-based control unit. In order to attach the spray-deposition gun, we designed an adapter able to attach to the crossbar and we printed it with the Velleman K8200 printer itself. With the printed adapter, it was possible to position the spray-gun right behind the FDM extruder in order to optimize the allocated space, obtaining the system presented by the photograph in Figure 6.13.

The commands provided to the printer, particularly the ones related to heating up of the extrusion nozzle, selection of the hot plate temperature and every detail related to the movement, are managed via an open source protocol (G-Code). Using this protocol, it is possible to write a sequence of instructions which the 3D printer uses, for instance, to move the heated plate and define a pattern.

The most widely used patterns for the realization of spray-deposited layers with a moving gun (or, in this case, with a moving plate) are based on a criss-cross path, organized in such a way the coverage of the sample is as uniform as possible. As a result, in addition to the parameters we considered so far, for the development of a large area spray-deposition process there will be the need of optimizing at least two more parameters: the distance between two parallel passes (which will define how spatially uniform will the layer be) and the velocity of the pass. In order to be able to perform

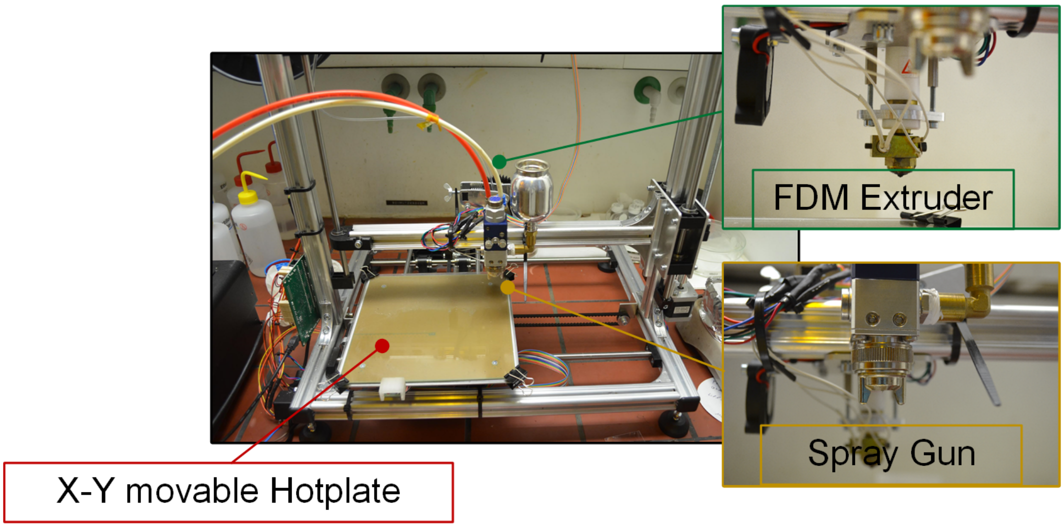

Figure 6.13: The photograph shows the integrated setup composed of the X-Y moving hotplate, an FDM extruder and a spray-deposition gun. The temperature can be set up to $80°C$, the z distance can be modified between 0 and 15 cm and the X-Y motors can be used contemporaneously to describe any arbitrary spray pattern

quick trials finalized at the process optimization, we developed a Matlab script, which, when prompted the input parameters (bed temperature, z crossbar positioning, sample size, pass pitch, velocity of the pass) would develop a diagram with the proposed path and a G-Code to send to the printer. An example of such an automatically generated pattern, optimized for the spray-deposition of PEDOT:PSS, on a $6 \times 6cm^2$ substrate is shown in Figure 6.14

6.3 Fabrication of a Fully-Printed Perfusion Chamber

6.3.1 Fabrication of a 3D-Printed Semitransparent Heater

A good example which embraces the capability of this approach and which can be built with a single conducting film is a semi-transparent thin-film heater [193], [194]. In these devices, the conducting film is only used for the transmission of heat through Joule effect, and are can be used for defrosting LCD panels and vehicle windows. Their integration into 3D-printed objects, however, could pave the way to the realization of self-heated and semi-transparent reaction chambers, which could turn to be particularly useful for lab-on-a-chip and life science applications [23], [195], and were considered to be of strong pertinence to the work carried out in this thesis. The heating chamber structure is summarized in 6.15 (a), and made of an inner chamber which is going to be planarized and where the heater is going to be spray-deposited, two round apertures

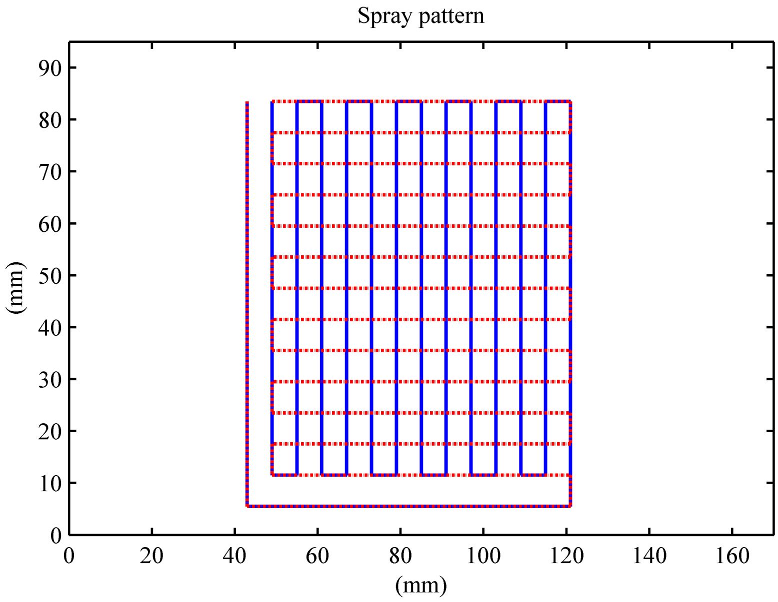

Figure 6.14: Criss-cross pattern generated via a Matlab code and associated to a G-Code to perform a uniform spray-deposition on a large area. The distance within the lines, the number of passes, the speed of the platform are all parameters which can be regulated and automatically set.

to allow the electric wires to reach the conductive thin film and a bigger rectangular aperture, designed to accommodate a commercial temperature sensor.

Figure 6.15 shows a photo of the complete device produced in-situ. Liquid silver has been successively added to the leads to enhance the electrical contact and the mechanical stability. To provide a comparison and to further show the need of planarization, two kind of devices were fabricated: a spray-planarized one (spray-planarization deposition time of 30 s), and an as-printed sample. For both classes of devices, first, a $25 \times 25 mm^2$, 0.5 mm thick substrate has been fabricated, in analogy with what reported in Section 6.2. Then, without removing the sample from the 3D-printer, the spray-planarization and the spray-deposition of the conducting material are performed in a sequence. The conducting material of choice we opted for is PEDOT:PSS, which provides lower sheet resistance than the CNT films and a better adhesion than AgNW, which are subject to delamination [23]. Finally, the process is completed through the printing of the overlying structure, which includes the sidewalls, with the vias for the leads and the housing of the commercial temperature sensor. The characterization of the heater has been performed by applying a cyclical voltage sweep to the devices, while the real-time temperature was recorded through a commercial sensor and the temperature distribution was obtained with means of a thermal IR-camera. Figure 6.16 (a) presents the temperature curves obtained for the planarized and the non-planarized

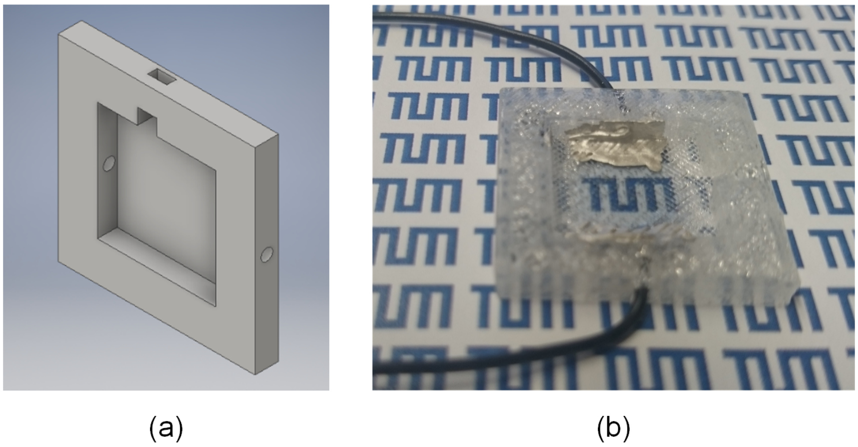
(a) (b)

Figure 6.15: (a) 3D schematic of the heating chamber with two round vias used to feed the electric wires to the conducting film and a slot for the housing of a commercial temperature sensor (b) the actual device, where silver paint has been added to enhance the electrical contact between the wires and the conducting film.

samples with respect to the voltage ramp. Remarkably, the temperature measured by the commercial sensor for the non-planarized sample is higher than the measured value for the planarized one, reaching $55°C$ and $50°C$, respectively. The IR-camera images, however, is more informative and provides an easy interpretation of the results. In the non-planarized sample, the heating is limited to a small area, which is aligned to the printing direction of the topmost layer. The conduction path lies within the few diagonal lines which connect the left silver paste pad to the right silver paste pad, symptom of a very limited conduction in the direction orthogonal to the 3D-printing pattern. The results for the planarized sample are strikingly different. The thermal camera shows a uniform heating throughout the whole sample and no preferred path is observable, finally affirming the successful planarization and deposition of the conductive layer.

To compare the dynamic results to literature, both class of devices were modeled through RC thermal equivalent circuits, differently tailored to take into account the structural differences between planarized and the non-planarized devices. The latter is, indeed, composed by only one thermal interface (PEDOT:PSS/3D-printed sample), while the former presents two (PEDOT:PSS/Planarization film and Planarization film/3D-printed sample). Although the non-planarized sample can be modeled through a simple first order model, the planarized one introduces some complexity and needs to be modeled through a second order model. One of the transient solutions for a circuit with two capacitors and shunt resistors is the linear combination of two exponentials,

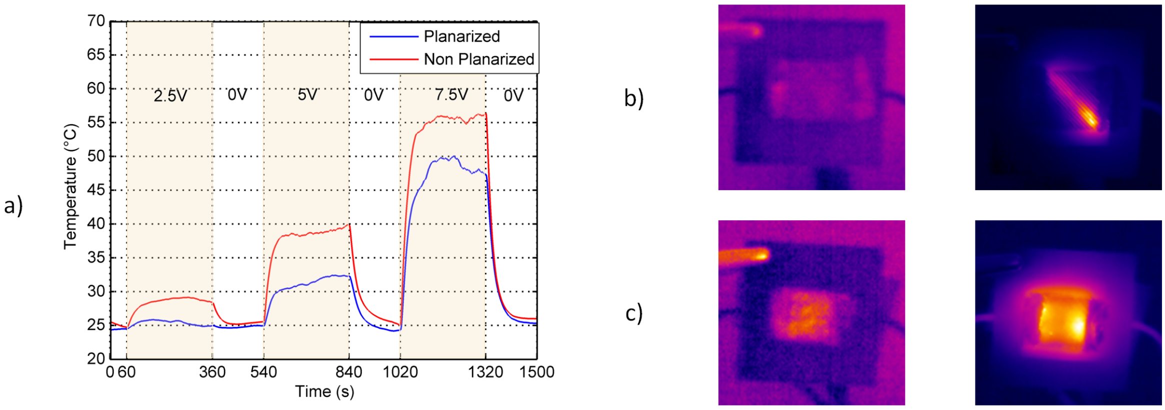

Figure 6.16: (a) Spot temperature curves measured on the heater for different voltages (b) Thermal IR-image of the non-planarized and the planarized sample (c) when 0V are applied (left hand side) and when 7.5V are applied (right hand side)

or in formulas:

$$T(t) = T_A(1 - e^{-\frac{t}{\tau_A}}) + T_B(1 - e^{-\frac{t}{\tau_B}}) \tag{6.1}$$

The numerical fitting, however, provides a negligible value of T_A, suggesting that a single pole approximation could be used. With means of this simplification, the comparison between these two classes of devices and the literature can be straightforwardly performed by evaluating the characteristic time constants. The non-planarized system and the planarized one, yielded time constants are 23.3 s and 29.5 s, respectively. The slower response of the planarized device is attributable to the larger effective area of the conductive layer and to the combination of the two interfaces, which leads to an overall higher thermal resistance and, hence, to a higher time constant. The response times for both the devices result slightly higher than what previously reported in literature for CNTs and AgNW on PET foil [193], [194], [196], [197]. This, however, is believed to be due the significantly lower thermal conductivity of PEDOT:PSS with respect to the aforementioned nanomaterials and to the thicker substrate, not to the employed fabrication process [198].

6.3.2 Concept of a Fully Printed Perfusion Chamber

These results show how the integration between 3D printing and thin film spray-deposition it is feasible and pave the way for the realization of more complex, albeit technologically similar, systems.

Figure 6.18 introduces one of these novel concepts: a fully-printed perfusion chamber. The microfluidic structure is 3D printed with means of FDM technology. After the fabrication of the first physical substrate, it is possible to spray-deposit an Or-

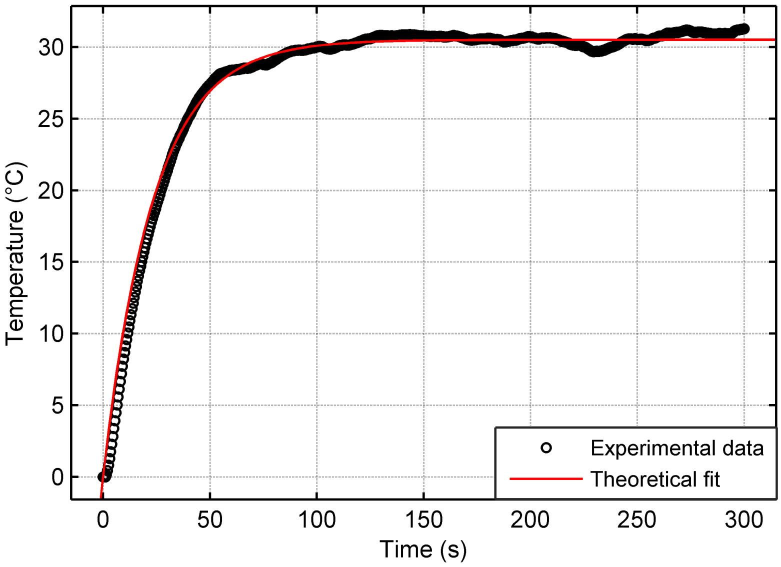

Figure 6.17: Experimental data (black circles) and typical theoretical fit to the proposed RC model

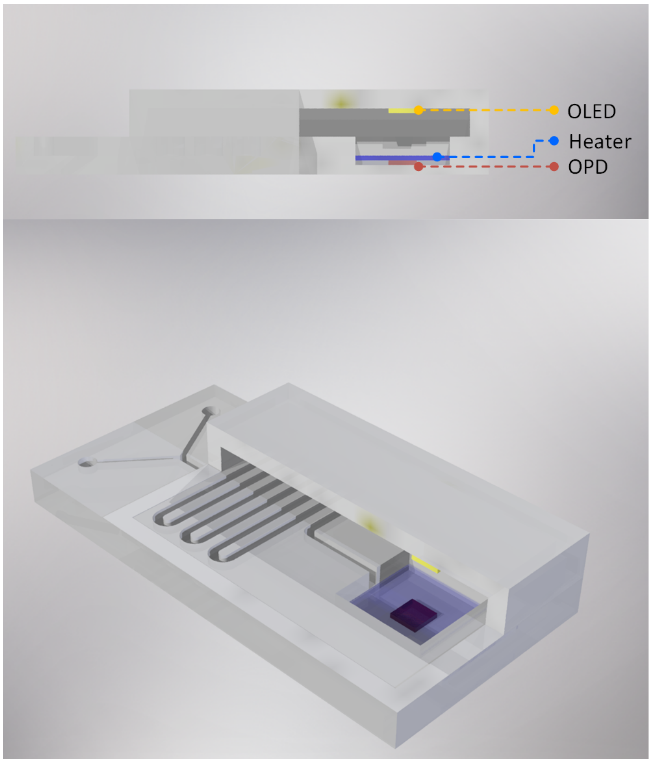

Figure 6.18: Section and 3D view of a concept for a fully printed perfusion chamber with in-sito heating and fluorescence viability control through OPD/OLED coupling

ganic Photodiode, by only changing the material in the reservoir of the spray gun: the techniques developed in Section 3.4, allow us to produce fully spray deposited OPDs, which is a consistent advantage in this process line. The encapsulation can be performed through the inline method developed in Section 4.2, while the heater can be produced as we just described. To complete the structure, it is possible to design and print a lid, necessary on the one hand to close the chamber, and, on the other hand as a support for the OLED. In case the excitation and fluorescence spectrum overlap too much, it would be possible to prepare polarization filters on foil and laminate them on the OLED and the OPD [147], or directly integrate them in the devices, as we discussed in Chapter 5. Everything described so far, is realizable utilizing only the technology developed and described in this work, without need of further assistance.

Nevertheless, given the inherent additive nature of the processes involved, it is possible to design stacked devices and, throughout the use of the pertinent stencils, it would be possible to fabricate even more complex structures in the perfusion chamber or at its inlets/outlets. Still employing spray technology only, for instance, it could be possible to integrate a CO_2 gas sensor [199], [200], along with a temperature sensor [201], to provide a feedback of the phenomena taking place in the chamber. On the outlet, it could be possible to integrate a spray-deposited pH sensor [16], in order to have more data to monitor the development of the cells and complement the fluorescence study.

The main issues related to the realization of a realistic design of the chamber, currently in progress, are related to the optimization of the dynamics of fluids: the chamber must be fed with nutrition medium, and the flow must be smooth and regular, in order to avoid cells rupture or delamination. The accurate choice of pumps and actuators is not enough to guarantee this kind of stability over a prolonged time lapse and for this reason, the need to find mechanicals solutions able to break the medium droplets and slow them down before arriving to the incubation chamber must be found.

6.4 Summary

After briefly introducing the state of the art in the production of microfluidic and Lab-on-a-Chip devices with conventional techniques such as photolithography and PDMS bonding, we introduced 3D printing as a promising technique to solve some of the major issues related to the classical processing. We postulated that 3D-Printing can be employed for a new generation of electronic and biotechnological devices and we defined a road map for the realization of 3D printed *smart objects* and biochips. To realize some of the points of this road map, we first showed how it is possible to spray-deposit thin conducting films on top of 3D printed structures. However, given the roughness of the 3D printed samples, we analyzed the necessity of planarization and compare three classical techniques presented in literature to a novel technique we implemented. This novel approach is based on the spray-deposition of a planarizing layer on top of the 3D printed sample and has some major qualities: it is remarkably effective, cost-effective, “green” (since it helps to recycle the byproducts of 3D printing) and easy to integrate in preexistent systems.

To prove this latter point, we developed a fully integrated printer able to perform 3D-printing, *spray planarization* and spray deposition of the desired material. This apparatus was then used for the fabrication of a fully printed heating chamber, obtained in one process run. This last finding paves the way to the realization of even more complex structures in the field of smart objects, but also in the intriguing field ob bioelectronics.

Chapter 7

Conclusion and Outlook

The main goal of this thesis was, as stated in the title, on the one hand, the design and the implementation of printed devices and objects for neuroelectronics, and, on the other hand, the development and optimization of processing techniques to facilitate (or enable) their fabrication.

In order to clarify the framework in which this thesis was set, we first gave a brief overview about the phenomena behind organic electronics and the peculiarities of this field of electronics, with its advantages and drawbacks. We described the main three fabrication techniques utilized throughout the work and then presented two applications where the use of organic and printed materials has been successfully employed to realize system not obtainable with conventional, rigid electronics.

Once the working principle and the potential of Organic Electronics was introduced, we focused, in the rest of the work, on realizing processes for the reliable implementation of devices to be employed in smart objects and in neuroelectronics. In the first experimental chapter of this dissertation (Chapter 3), we demonstrate the feasibility of OPDs employing spray-deposited CNT electrodes. The fabrication process presented several issues connected to the roughness and poor wettability of CNT networks, which were solved by analyzing the CNT/PEDOT:PSS interface and modifying the formulation of the PEDOT:PSS ink. At this stage, however, albeit the OPDs had solution processable anodes, the cathodes were still produced with means of PVD. To bypass this bottleneck, we developed a process for fully spray-deposited OPDs featuring PEDOT:PSS electrodes as both anode and cathode, and where, for the latter, the work-function has been modified through the spray-deposition of an ultrathin PEI layer. This methodology was finally applied for the realization of OPDs on printed Ag nanoparticles stripes, integrated into a complex system with a printed folded dipole antenna and an RFID chip.

In Chapter 4, we faced one of the major issues related to Organic Electronics: the poor durability of the devices. This issue is commonly solved with the usage of thick, rigid encapsulating barriers, which are stable and reliable, but hinder the flexibility of the substrates. To have have good encapsulations and at the same time retain this latter characteristic, we developed and tested a method based on the *in line* deposition of oxide barriers and spray-deposited polymers. The hybrid encapsulators, composed of eight alternated oxides and a thick polymeric film, allowed the OPDs to keep 40% of their original photocurrent one month after their fabrication.

In the second part of the chapter, we investigated in more detail the stability of one particular element common to almost any Organic Electronic device: one of the electrodes. We exposed some classical electrode materials (Ag, Al, Au and ITO) to culturing medium and characterized the modifications of conductivity, transmittance and work function over time. The prolonged immersion in a liquid medium, however, led to evident surface modifications, involving oxidation and delamination of the metal layers, which would be a significant problem in a real life application. To overcome this barrier, we employed a photocurable polymer (SU-8) as adhesion layer and we showed how, modifying the cross-linking procedure, it is possible to influence the stability of the polymer/metal system. Evaporating the metal layer on a partially cross-linked polymer resulted in much more stable layers with respect to the deposition on a fully cross-linked one, and the electro-optical properties of the thin film were not discernibly altered after 672 hours of immersion in culturing medium. To be able to use this solution in bioelectronics, however, the biocompatibility of SU-8 needed to be assessed, and this task was assolved through fluorescent and electrphysiologic assays. The results of these tests indicate that SU-8, processed with any protocol we tried, is as biocompatible as the glass control, with both HEK cells and neurons, confirming the potential of the introduced methodology as simple and effective alternative to oxidative metals as adhesion layers for Au or Ag.

Chapter 5 introduced the idea of vertical integration, and, as a proof of concept, wire grid polarizers were embedded in OPDs and OLEDs for the realization of self-polarized organic optoelectronic devices. To achieve this goal, the WGP structures were first simulated, fabricated and characterized. The results of the simulations, however, although in line with the results reported by similar works, were significantly discordant with the measurements of the practical devices, yielding Extinction Ratios up to two orders of magnitude higher than the experimental data. The reasons for it reside in the assumptions on the geometrical and physical structure of the simulated devices: the duty cycle of the grid was considered to be equal to 50%, and the thickness of the top and bottom layers were supposed to be equal. Literature research and SEM investigations showed how both assumptions were flawed, and by simple integration of more realistic parameters, the results of the simulations become strikingly similar to the measured devices. The fabricated WGPs were then employed as semi-transparent and polarization sensitive electrodes for OPDs and OLEDs, which were characterized both as stand-alone devices and in an OPD/OLED cross-polarization system, demonstrating how vertical integration can result in the reduction of the needed external components, with a limited trade-off on the performances.

The devices we introduced, defined pOLED and pOPD, at the best of our knowledge, have never been developed by any other research group, and as they are a proof of concept, they can be subject to major improvements. The main weak point of the developed process resides in the sub-optimal practical implementation of the WGPs: this aspect is reflected in both the relatively low polarization efficiency and the very high serial resistance presented by the pOPDs. A future optimization effort could be put onto the realization of smoother Al layers and sharper grid lines, which would lead to a contemporaneous amelioration of the grid lines performances as polarizers and as electrodes, improving the pOPD and pOLED devices as a whole.

Vertical integration is, however, not the only integration concept we developed. In Chapter 6 we introduced 3D printing as a viable technique for the realization of smart objects, through the horizontal integration of different devices and functionalities. We demonstrated that through a newly developed planarization method, it is possible to transform some areas of rough 3D printed objects in smooth surfaces ready for the deposition of organic thin films. In order to assess the technique, we spray-deposited thin conductive layers of CNTs, PEDOT:PSS and AgNW on top of non-planarized and planarized samples and measured the sheet resistance: the latter films presented an improvement in this figure of merit up to one order of magnitude, which we attribute to the shorter average conductive path on planarized samples.

Subsequently, we designed a system able to 3D-print and spray-deposit arbitrary materials, and we employed it for the fabrication of a fully-printed heating chamber. The structure is composed by a thin 3D-printed substrate, which is first planarized and then covered with a conductive layer of PEDOT:PSS; when this first layer is completed, the structure is ultimated via the composition of side-walls, which include holes for the contacting of the PEDOT:PSS film. By applying a DC voltage to the conductive layer, the current flow heats up the chamber due to Joule dissipation, and we proved how the planarization of the substrate substantially modifies the uniformity of the heater.

This proof of concept is a gateway for a number of possible novel applications: smart objects with embedded organic electronic devices might be widely employed in consumer electronics, but the concept of a semitransparent heated chamber can be directly applied to neurosciences. For instance, as a possible (and advisable) development of this technology, we propose the realization of a fully-printed perfusion chamber, where cells could be grown independently and out from the incubator and directly analyzed with means of fluorescence imaging performed with an OLED/OPD combination. The perfusion chamber might integrate pH, RH and temperature sensing capabilities, realized with means of solution processable electronics, along with energy harvesting components and printed antennas. The complexity of realizable systems is only bounded by the space which can be allocated on a single chip, in the horizontal plane or the vertical one and by the intrinsic limits of the spray-deposition technique.

This last observation hints to the final advice we give to a willing, interested reader. The limits of conventional processes, the boundaries of established technologies and the functionalities of existing devices are not where your research work stumbles, dwindles and stops. They are, in fact, where everything starts.

Appendix A

Materials and Methods

A.1 Fabrication

Preparation of CNTs

For the dispersion of CNTs in aqueous solution, SDS or CMC are solved in DI water in a weight ratio of 0.5 wt %. The CMC solution is stirred overnight for at least 12 h at room temperature, while the SDS solution only needs 1 h stirring. When the solutions are uniform, 0.05 wt % of SWNTs (Hanwha Nanotech) is added and the CMC and SDS solutions are sonicated with a horn sonicator for 30 minutes. Solutions are finally centrifuged at 15 000 rpm for 90 min, and the top 80% of material in each vial is utilized for the deposition.

Organic Material Solutions

The bulk heterojunction blend is obtained dissolving solid-phase regioregular poly(3-hexylthiophene-2,5-diyl) (Rieke Metals Inc.) and [6,6]-phenyl C61 butyric acid methyl ester (PCBM) (Solenne B.V.) in o-DCB (Sigma-Aldrich) with a 1 wt %:1 wt % ratio and stirred overnight (>12 h) at 60 řC. The PEDOT:PSS (CLEVIOS P VP CH 8000) solutions were sprayed in a dilution of either 1:3 with DI water or 1:3 in isopropyl alcohol (Sigma-Aldrich). The highly conductive PEDOT:PSS utilized for the top electrodes was a mixture of PEDOT:PSS (CLEVIOS PH 1000) and Ethylene Glycol.

Spray-Deposition of OPDs

Table A.1 summarizes the most important parameters employed in the deposition of the materials: spray atomization temperature, nozzle-to-sample distance, hot-plate

Material	Pressure (bar)	Temperature (°C)	Distance (cm)
PEDOT:PSS (HCL)	0.5	45	15
PEDOT:PSS (Electrode)	1	120	25
PEI	1	40	15
P3HT:PCBM	1	120	15
Bendlay (Planarization)	1	80	15

Table A.1: Spray-deposition parameters for PEDOT:PSS (HCL and Electrode), PEI, P3HT:PCBM and planarization layer

temperature. Concerning the evaporation of the cathodic material, when performed, it was composed of a $1nm$ thick LiF layer, followed by an $120nm$ thick Al one. The evaporation rates were 0.1 Åand 1 Å, respectively.

Ormostamp Replica Fabrication

The Ormostamp replicas were obtained with a process similar to what described by Nagel et al [154]. The resin is poured onto the original stamp, and a carrier sample (either glass or plastic foil) is placed on the material. Gravity and capillary forces make the resin spread and fill the master's nanometric features. Once the resin is fully spread, it is exposed to UV light dose of $1000mJcm^2$. Afterwards, the carrier substrate together with the cured polymer can be peeled off from the master by lifting the glass with tweezers and a scalpel. The replica is then thermally cured at 130°C for 30 minutes and slowly ramped down to ambient temperature.

A.2 Characterization

Thin Film characterization

The sheet resistance was measured with a custom-made four-points probe and a Keithley 4200 semiconductor parameter analyzer. The topography, average thickness and uniformity of all the spray-coated layers (PEDOT:PSS, highly conductive PEDOT:PSS, PEI and P3HT:PCBM) were evaluated with means of an AFM (JEOL JSPM-5200), a mechanical profilometer (Veeco Dektak 150) and a white light interferometer (Veeco

NT9080). To perform this last measurement, a thin Al layer (15 nm) was evaporated on the deposited material, to enhance the reflection of white light. The work-function was measured with respect to a highly ordered pyrolytic graphite (HOPG) through a Kelvin Probe with a golden reference electrode (KP Technology Ltd., KP020).

OPDs characterization

The transmittance of the single films and the EQE of the fabricated OPDs were evaluated using a 300W xenon arc lamp choppered at 210 Hz, passing through an Oriel Cornerstone 260 $\frac{1}{4}m$ monochromator and a calibrated photodetector. The output signal was connected to a transimpedence amplifier and fed to a lock-in amplifier. The JV-characterization of the OPDs were performed by means of a Keithley 2602 sourcemeter, under a sun simulator with AM1.5G illumination or in a dark current box. Finally, the cut-off frequency was evaluated by extracting the amplitude of the photocurrent induced by a square wave green emission.

References

[1] M. Berggren and A. Richter-Dahlfors, "Organic bioelectronics", *Advanced Materials*, vol. 19, no. 20, pp. 3201–3213, 2007, ISSN: 09359648. DOI: `10.1002/adma.200700419`.

[2] G. Scarpa, A. L. Idzko, S. Götz, and S. Thalhammer, "Biocompatibility Studies of Functionalized Regioregular Poly(3-hexylthiophene) Layers for Sensing Applications", *Macromolecular Bioscience*, vol. 10, no. 4, pp. 378–383, 2010, ISSN: 16165187. DOI: `10.1002/mabi.200900412`.

[3] D. Khodagholy, T. Doublet, M. Gurfinkel, P. Quilichini, E. Ismailova, P. Leleux, T. Herve, S. Sanaur, C. Bernard, and G. G. Malliaras, "Highly conformable conducting polymer electrodes for in vivo recordings.", *Advanced materials (Deerfield Beach, Fla.)*, vol. 23, no. 36, H268–72, Oct. 2011, ISSN: 1521-4095. DOI: `10.1002/adma.201102378`. [Online]. Available: `http://www.ncbi.nlm.nih.gov/pubmed/21826747`.

[4] V. D. Bhatt, S. Teymouri, K. Melzer, A. Abdellah, Z. Guttenberg, and P. Lugli, "Biocompatibility Tests on Spray Coated Carbon Nanotube and PEDOT:PSS Thin Films", *IEEE Transactions on Nanotechnology*, vol. 15, no. 3, pp. 373–379, 2016, ISSN: 1536-125X. DOI: `10.1109/TNANO.2016.2535780`. [Online]. Available: `http://ieeexplore.ieee.org/lpdocs/epic03/wrapper.htm?arnumber=7422111`.

[5] G. G. Malliaras, "Organic bioelectronics: A new era for organic electronics", *Biochimica et Biophysica Acta - General Subjects*, vol. 1830, no. 9, pp. 4286–4287, 2013, ISSN: 03044165. DOI: `10.1016/j.bbagen.2012.10.007`. [Online]. Available: `http://dx.doi.org/10.1016/j.bbagen.2012.10.007`.

[6] G. Malliaras and M. R. Abidian, "Organic Bioelectronic Materials and Devices", *Advanced Materials*, vol. 27, no. 46, pp. 7492–7492, 2015, ISSN: 09359648. DOI: `10.1002/adma.201504783`. [Online]. Available: `http://doi.wiley.com/10.1002/adma.201504783`.

[7] A. Pais, A. Banerjee, D. Klotzkin, and I. Papautsky, "High-sensitivity, disposable lab-on-a-chip with thin-film organic electronics for fluorescence detection.", *Lab on a chip*, vol. 8, no. 5, pp. 794–800, May 2008, ISSN: 1473-0197. DOI: `10.1039/b715143h`. [Online]. Available: `http://www.ncbi.nlm.nih.gov/pubmed/18432351`.

[8] A. Banerjee, A. Pais, I. Papautsky, and D. Klotzkin, "A polarization isolation method for high-sensitivity, low-cost on-chip fluorescence detection for microfluidic lab-on-a-chip", *IEEE Sensors Journal*, vol. 8, no. 5, pp. 621–627, 2008, ISSN: 1530437X. DOI: `10.1109/JSEN.2008.918961`.

[9] E. Kraker, A. Haase, B. Lamprecht, G. Jakopic, C. Konrad, and S. Köstler, "Integrated organic electronic based optochemical sensors using polarization filters", *Applied Physics Letters*, vol. 92, no. 3, pp. 10–13, 2008, ISSN: 00036951. DOI: `10.1063/1.2837410`.

[10] A. Steude, M. Jahnel, M. Thomschke, M. Schober, and M. C. Gather, "Controlling the Behavior of Single Live Cells with High Density Arrays of Microscopic OLEDs", *Advanced Materials*, n/a–n/a, 2015, ISSN: 09359648. DOI: `10.1002/adma.201503253`. [Online]. Available: `http://doi.wiley.com/10.1002/adma.201503253`.

[11] A. K. Bansal, S. Hou, O. Kulyk, E. M. Bowman, and I. D. W. Samuel, "Wearable organic optoelectronic sensors for medicine", *Advanced Materials*, pp. 7638–7644, 2014, ISSN: 15214095. DOI: `10.1002/adma.201403560`.

[12] D. Khodagholy, T. Doublet, P. Quilichini, M. Gurfinkel, P. Leleux, A. Ghestem, E. Ismailova1, T. Herve, S. Sanaur, C. Bernard, and G. G. Malliaras, "In vivo recordings of brain activity using organic transistors", *Nature communications*, vol. 4, 2013. DOI: `10.1038/ncomms2573`.

[13] V. Benfenati, S. Toffanin, S. Bonetti, G. Turatti, A. Pistone, M. Chiappalone, A. Sagnella, A. Stefani, G. Generali, G. Ruani, D. Saguatti, R. Zamboni, and M. Muccini, "A transparent organic transistor structure for bidirectional stimulation and recording of primary neurons.", *Nature materials*, vol. 12, no. 7, pp. 672–80, 2013, ISSN: 1476-1122. DOI: `10.1038/nmat3630`.

[14] M. R. Antognazza, N. Martino, D. Ghezzi, P. Feyen, E. Colombo, D. Endeman, F. Benfenati, and G. Lanzani, "Shedding Light on Living Cells", *Advanced Materials*, pp. 7662–7669, 2014, ISSN: 15214095. DOI: `10.1002/adma.201403513`.

[15] D. Ghezzi, M. R. Antognazza, R. Maccarone, S. Bellani, E. Lanzarini, N. Martino, M. Mete, G. Pertile, S. Bisti, G. Lanzani, and F. Benfenati, “A polymer optoelectronic interface restores light sensitivity in blind rat retinas”, no. March, pp. 1–7, 2013. DOI: `10.1038/NPHOTON.2013.34`. [Online]. Available: `http://dx.doi.org/10.1038/nphoton.2013.34`.

[16] A. M. Münzer, K. Melzer, M. Heimgreiter, and G. Scarpa, “Random CNT network and regioregular poly(3-hexylthiophen) FETs for pH sensing applications: A comparison”, *Biochimica et Biophysica Acta - General Subjects*, vol. 1830, no. 9, pp. 4353–4358, 2013, ISSN: 03044165. DOI: `10.1016/j.bbagen.2013.01.023`. [Online]. Available: `http://dx.doi.org/10.1016/j.bbagen.2013.01.023`.

[17] K. Melzer, A. M. Münzer, E. Jaworska, K. Maksymiuk, A. Michalska, and G. Scarpa, “Polymeric ion-selective membrane functionalized gate-electrodes: Ion-selective response of electrolyte-gated poly (3-hexylthiophene) field-effect transistors”, *Organic Electronics: Physics, materials, applications*, vol. 15, no. 2, pp. 595–601, 2014, ISSN: 15661199. DOI: `10.1016/j.orgel.2013.12.016`. [Online]. Available: `http://dx.doi.org/10.1016/j.orgel.2013.12.016`.

[18] K. Deisseroth, “Optogenetics”, *Nature Methods*, vol. 8, no. 1, pp. 26–29, 2011, ISSN: 1548-7091. DOI: `10.1038/nmeth.f.324`. [Online]. Available: `http://www.nature.com/doifinder/10.1038/nmeth.f.324`.

[19] S. Royer, B. V. Zemelman, M. Barbic, A. Losonczy, G. Buzski, and J. C. Magee, “Multi-array silicon probes with integrated optical fibers: Light-assisted perturbation and recording of local neural circuits in the behaving animal”, *European Journal of Neuroscience*, vol. 31, no. 12, pp. 2279–2291, 2010, ISSN: 0953816X. DOI: `10.1111/j.1460-9568.2010.07250.x`.

[20] F. Pisanello, L. Sileo, I. A. Oldenburg, M. Pisanello, L. Martiradonna, J. A. Assad, B. L. Sabatini, and M. De Vittorio, “Multipoint-emitting optical fibers for spatially addressable in vivo optogenetics”, *Neuron*, vol. 82, no. 6, pp. 1245–1254, 2014, ISSN: 10974199. DOI: `10.1016/j.neuron.2014.04.041`. arXiv: `NIHMS150003`. [Online]. Available: `http://dx.doi.org/10.1016/j.neuron.2014.04.041`.

[21] V. S. Polikov, P. A. Tresco, and W. M. Reichert, “Response of brain tissue to chronically implanted neural electrodes”, *Journal of Neuroscience Methods*, vol. 148, no. 1, pp. 1–18, 2005, ISSN: 01650270. DOI: `10.1016/j.jneumeth.2005.08.015`.

[22] M. R. Antognazza, M. Di Paolo, D. Ghezzi, M. Mete, S. Di Marco, J. F. Maya-Vetencourt, R. Maccarone, A. Desii, F. Di Fonzo, M. Bramini, A. Russo, L. Laudato, I. Donelli, M. Cilli, G. Freddi, G. Pertile, G. Lanzani, S. Bisti, and F. Benfenati, "Characterization of a Polymer-Based, Fully Organic Prosthesis for Implantation into the Subretinal Space of the Rat", *Advanced Healthcare Materials*, pp. 1–12, 2016, ISSN: 21922640. DOI: `10.1002/adhm.201600318`. [Online]. Available: `http://doi.wiley.com/10.1002/adhm.201600318`.

[23] C. D. Chin, V. Linder, and S. K. Sia, "Lab-on-a-chip devices for global health: Past studies and future opportunities", *Lab Chip*, vol. 7, no. 1, pp. 41–57, 2007, ISSN: 1473-0197. DOI: `10.1039/B611455E`. [Online]. Available: `http://xlink.rsc.org/?DOI=B611455E`.

[24] F. C. Krebs, H. Spanggard, T. Kjær, M. Biancardo, and J. Alstrup, "Large area plastic solar cell modules", *Materials Science and Engineering: B*, vol. 138, no. 2, pp. 106–111, Mar. 2007, ISSN: 09215107. DOI: `10.1016/j.mseb.2006.06.008`. [Online]. Available: `http://linkinghub.elsevier.com/retrieve/pii/S0921510706002935`.

[25] T. Aernouts, P. Vanlaeke, W. Geens, J. Poortmans, P. Heremans, S. Borghs, R. Mertens, R. Andriessen, and L. Leenders, "Printable anodes for flexible organic solar cell modules", *Thin Solid Films*, vol. 451-452, pp. 22–25, Mar. 2004, ISSN: 00406090. DOI: `10.1016/j.tsf.2003.11.038`. [Online]. Available: `http://linkinghub.elsevier.com/retrieve/pii/S0040609003015773`.

[26] A. Abdellah, B. Fabel, P. Lugli, and G. Scarpa, "Spray deposition of organic semiconducting thin-films: Towards the fabrication of arbitrary shaped organic electronic devices", *Organic Electronics*, vol. 11, no. 6, pp. 1031–1038, Jun. 2010, ISSN: 15661199. DOI: `10.1016/j.orgel.2010.02.018`. [Online]. Available: `http://linkinghub.elsevier.com/retrieve/pii/S1566119910000844`.

[27] S. E. Shaheen, R. Radspinner, N. Peyghambarian, and G. E. Jabbour, "Fabrication of bulk heterojunction plastic solar cells by screen printing", *Applied Physics Letters*, vol. 79, no. 18, p. 2996, 2001, ISSN: 00036951. DOI: `10.1063/1.1413501`. [Online]. Available: `http://scitation.aip.org/content/aip/journal/apl/79/18/10.1063/1.1413501`.

[28] LG, *LG 55EG9600*, 2016. [Online]. Available: `http://www.lg.com/us/tvs/lg-55EG9600-oled-4k-tv`.

[29] OSRAM, *OSRAM Butterfly*, 2016. [Online]. Available: `http://www.osram-oled.com/oled/en/applications/reference-projects/butterfly-oled/index.jsp`.

[30] A. Köhler and H. Bässler, *Electronic Processes in Organic Semiconductors, An Introduction.* Wiley-VCH Verlag GmbH & Co. KGaA, 2015, ISBN: 9783527332922.

[31] A. Pochettino, "SUI FENOMZNI IIX LUMINESCENZA IN ALCUNE SOSTANZE ORGANICHE", *Società Italiana di Fisica*, pp. 118–127, 1906.

[32] M. Pope, H. P. Kallmann, and P. Magnante, "Electroluminescence in Organic Crystals", *The Journal of Chemical Physics*, vol. 38, no. 8, p. 2042, 1963, ISSN: 00219606. DOI: `10.1063/1.1733929`. [Online]. Available: `http://scitation.aip.org/content/aip/journal/jcp/38/8/10.1063/1.1733929`.

[33] J. H. Burroughes, D. D. Bradley, A. R. Brown, R. N. Marks, K. Mackay, R. Friend, P. Burns, and A. Holmes, "Light-Emitting Diodes Based on Conjugated Polymers", *Nature*, vol. 347, 1990.

[34] C. K. Chiang, C. R. Fincher, Y. W. Park, A. J. Heeger, H. Shirakawa, E. J. Louis, S. C. Gau, and A. G. MacDiarmid, "Electrical conductivity in doped polyacetylene", *Physical Review Letters*, vol. 39, no. 17, pp. 1098–1101, 1977, ISSN: 00319007. DOI: `10.1103/PhysRevLett.39.1098`.

[35] A. Heeger, A. G. MacDiarmid, and H. Shirakawa, "The Nobel Prize in chemistry, 2000: conductive polymers", *Stockholm, Sweden: Royal Swedish Academy of Sciences*, pp. 1–16, 2000. DOI: `http://www.nobelprize.org/nobel{\_}prizes/chemistry/laureates/2000/advanced-chemistryprize2000.pdf`. [Online]. Available: `http://scholar.google.com/scholar?hl=en%7B%5C&%7DbtnG=Search%7B%5C&%7Dq=intitle:The+Nobel+Prize+in+Chemistry+,+2000+:+Conductive+polymers%7B%5C#%7D1`.

[36] J. K. Jeong, J. H. Jeong, J. H. Choi, J. S. Im, S. H. Kim, H. W. Yang, K. N. Kang, K. S. Kim, T. K. Ahn, H.-j. Chung, M. Kim, B. S. Gu, J.-s. Park, Y.-g. Mo, H. D. Kim, and H. K. Chung, "12.1-Inch WXGA AMOLED Display Driven by Indium-Gallium-Zinc Oxide TFTs Array", *SID Symposium Digest of Technical Papers*, pp. 1–4, 2008, ISSN: 0097-966X. DOI: `10.1889/1.3069591`.

[37] S.-I. Na, S.-S. Kim, J. Jo, and D.-Y. Kim, "Efficient and Flexible ITO-Free Organic Solar Cells Using Highly Conductive Polymer Anodes", *Advanced Materials*, vol. 20, no. 21, pp. 4061–4067, 2008, ISSN: 09359648. DOI: `10.1002/adma.200800338`. [Online]. Available: `http://doi.wiley.com/10.1002/adma.200800338`.

[38] H. A. M. Van Mullekom, J. A. J. M. Vekemans, E. E. Havinga, and E. W. Meijer, *Developments in the chemistry and band gap engineering of donor-acceptor substituted conjugated polymers*, 1. 2001, vol. 32, pp. 1–40, ISBN: 3140247265. DOI: `10.1016/S0927-796X(00)00029-2`.

[39] A. Miller and E. Abrahams, "Impurity conduction at low concentrations", *Physical Review*, vol. 120, no. 3, pp. 745–755, 1960, ISSN: 0031899X. DOI: `10.1103/PhysRev.120.745`. arXiv: `PhysRev.120.745 [10.1103]`.

[40] J. M. Montero, J. Bisquert, G. Garcia-Belmonte, E. M. Barea, and H. J. Bolink, "Trap-limited mobility in space-charge limited current in organic layers", *Organic Electronics: Physics, materials, applications*, vol. 10, no. 2, pp. 305–312, 2009, ISSN: 15661199. DOI: `10.1016/j.orgel.2008.11.017`. [Online]. Available: `http://dx.doi.org/10.1016/j.orgel.2008.11.017`.

[41] W. Honda, S. Harada, T. Arie, S. Akita, and K. Takei, "Wearable, human-interactive, health-monitoring, wireless devices fabricated by macroscale printing techniques", *Advanced Functional Materials*, vol. 24, no. 22, pp. 3299–3304, 2014, ISSN: 16163028. DOI: `10.1002/adfm.201303874`.

[42] J. T. Smith, B. O'Brien, Y. K. Lee, E. J. Bawolek, and J. B. Christen, "Application of flexible OLED display technology for electro-optical stimulation and/or silencing of neural activity", *IEEE/OSA Journal of Display Technology*, vol. 10, no. 6, pp. 514–520, 2014, ISSN: 1551319X. DOI: `10.1109/JDT.2014.2308436`.

[43] A. Falco, L. Cinà, G. Scarpa, P. Lugli, and A. Abdellah, "Fully-Sprayed and Flexible Organic Photodiodes with Transparent Carbon Nanotube Electrodes.", *ACS applied materials & interfaces*, Jun. 2014, ISSN: 1944-8252. DOI: `10.1021/am5022123`. [Online]. Available: `http://www.ncbi.nlm.nih.gov/pubmed/24914700`.

[44] K.-J. Baeg, M. Binda, D. Natali, M. Caironi, and Y.-Y. Noh, "Organic Light Detectors: Photodiodes and Phototransistors.", *Advanced materials (Deerfield Beach, Fla.)*, vol. 25, pp. 4267–4295, Mar. 2013, ISSN: 1521-4095. DOI: `10.1002/adma.201204979`.

[45] A. Abdellah, D. Baierl, B. Fabel, P. Lugli, and G. Scarpa, "Exploring spray technology for the fabrication of organic devices based on poly(3-hexylthiophene)", *Nanotechnology, 2009. IEEE-NANO 2009. 9th IEEE Conference on*, pp. 831–934, 2009.

[46] A. Abdelhalim, A. Abdellah, G. Scarpa, and P. Lugli, “Fabrication of carbon nanotube thin films on flexible substrates by spray deposition and transfer printing”, *Carbon*, vol. 61, pp. 72–79, Sep. 2013, ISSN: 00086223. DOI: `10.1016/j.carbon.2013.04.069`. [Online]. Available: `http://linkinghub.elsevier.com/retrieve/pii/S0008622313003783`.

[47] S. Kim, J. Yim, X. Wang, D. D. Bradley, S. Lee, and J. C. DeMello, “Spin- and Spray-Deposited Single-Walled Carbon-Nanotube Electrodes for Organic Solar Cells”, *Advanced Functional Materials*, vol. 20, no. 14, pp. 2310–2316, Jun. 2010, ISSN: 1616301X. DOI: `10.1002/adfm.200902369`. [Online]. Available: `http://doi.wiley.com/10.1002/adfm.200902369`.

[48] C. N. Hoth, S. a. Choulis, P. Schilinsky, and C. J. Brabec, “High Photovoltaic Performance of Inkjet Printed Polymer:Fullerene Blends”, *Advanced Materials*, vol. 19, no. 22, pp. 3973–3978, Nov. 2007, ISSN: 09359648. DOI: `10.1002/adma.200700911`. [Online]. Available: `http://doi.wiley.com/10.1002/adma.200700911`.

[49] W. Wang, F. Zhang, L. Li, M. Gao, and B. Hu, “Improved Performance of Photomultiplication Polymer Photodetectors by Adjustment of P3HT Molecular Arrangement”, *ACS Applied Materials & Interfaces*, p. 151 001 120 726 009, 2015, ISSN: 1944-8244. DOI: `10.1021/acsami.5b07522`. [Online]. Available: `http://pubs.acs.org/doi/10.1021/acsami.5b07522`.

[50] F.-C. Chen, S.-C. Chien, and G.-L. Cious, “Highly sensitive, low-voltage, organic photomultiple photodetectors exhibiting broadband response”, *Applied Physics Letters*, vol. 97, no. 10, p. 103 301, 2010, ISSN: 00036951. DOI: `10.1063/1.3488017`. [Online]. Available: `http://scitation.aip.org/content/aip/journal/apl/97/10/10.1063/1.3488017`.

[51] E. Stavrinidou, P. Leleux, H. Rajaona, M. Fiocchi, S. Sanaur, and G. G. Malliaras, “A simple model for ion injection and transport in conducting polymers”, *Journal of Applied Physics*, vol. 113, no. 24, p. 244 501, 2013, ISSN: 00218979. DOI: `10.1063/1.4812236`. [Online]. Available: `http://ieeexplore.ieee.org/articleDetails.jsp?arnumber=6547956`.

[52] J. Puigdollers, “Pentacene thin-film transistors with polymeric gate dielectric”, *Organic Electronics*, vol. 5, no. 1-3, pp. 67–71, 2004, ISSN: 15661199. DOI: `10.1016/j.orgel.2003.10.002`.

[53] S. H. Park, A. Roy, S. Beaupre, S. Cho, N. Coates, J. S. Moon, D. Moses, M. Leclerc, K. Lee, and A. J. Heeger, "Bulk heterojunction solar cells with internal quantum efficiency approaching 100%", *Nat. Photonics*, vol. 3, no. 5, pp. 297–303, 2009, ISSN: 1749-4885. DOI: `10.1038/nphoton.2009.69`.

[54] N. Grossiord, J. M. Kroon, R. Andriessen, and P. W. Blom, "Degradation mechanisms in organic photovoltaic devices", *Organic Electronics*, vol. 13, no. 3, pp. 432–456, 2012, ISSN: 15661199. DOI: `10.1016/j.orgel.2011.11.027`. [Online]. Available: `http://dx.doi.org/10.1016/j.orgel.2011.11.027`.

[55] J. Ahmad, K. Bazaka, L. J. Anderson, R. D. White, and M. V. Jacob, "Materials and methods for encapsulation of OPV: A review", *Renewable and Sustainable Energy Reviews*, vol. 27, pp. 104–117, 2013, ISSN: 13640321. DOI: `10.1016/j.rser.2013.06.027`.

[56] D. Feili, M. Schuettler, T. Doerge, S. Kammer, and T. Stieglitz, "Encapsulation of organic field effect transistors for flexible biomedical microimplants", *Sensors and Actuators, A: Physical*, vol. 120, no. 1, pp. 101–109, 2005, ISSN: 09244247. DOI: `10.1016/j.sna.2004.11.021`.

[57] D. B. Hall, P. Underhill, and J. M. Torkelson, "Spin Coating of Thin and Ultrathin Polymer Films", *Liquid Film Coating*, vol. 38, no. 12, p. 7, 1998. DOI: `10.1007/978-94-011-5342-3{\_}20`.

[58] S. Wolf and R. N. Tauber, *Silicon Processing for the VLSI Era, Vol. 1: Process Technology*, 1st. Lattice Press, 1986.

[59] C. B. Walsh and E. I. Franses, "Ultrathin PMMA films spin-coated from toluene solutions", *Thin Solid Films*, vol. 429, no. 1-2, pp. 71–76, 2003, ISSN: 00406090. DOI: `10.1016/S0040-6090(03)00031-2`.

[60] C. Extrand, "Spin Coating of Very Thin Polymer Films", *Polymer Engineering and Science*, vol. 34, no. 5, p. 390, 1994. DOI: `10.1002/pen.760340503`.

[61] D. F. S. Petri, "Characterization of spin-coated polymer films", *Journal of the Brazilian Chemical Society*, vol. 13, no. 5, pp. 695–699, 2002, ISSN: 01035053. DOI: `10.1590/S0103-50532002000500027`.

[62] C.-W. W. Liang, W.-F. F. Su, and L. Y. Wang, "Enhancing the photocurrent in poly(3-hexylthiophene)/[6,6]-phenyl C[sub 61] butyric acid methyl ester bulk heterojunction solar cells by using poly(3-hexylthiophene) as a buffer layer", *Appl. Phys. Lett.*, vol. 95, no. 13, p. 219 902, 2009, ISSN: 00036951. DOI: `10.1063/1.3242006`. [Online]. Available: `http://scitation.aip.org/content/`

aip/journal/apl/95/13/10.1063/1.3242006$%5Cbackslash$nhttp://scitation.aip.org/content/aip/journal/apl/95/21/10.1063/1.3267145$%5Cbackslash$n%3CGo%20to%20ISI%3E://000270458000075$%5Cbackslash$n%3CGo$%5Cbackslash$nto$%5Cbackslash$nISI%3E://000270458000075.

[63] W. W. Flack, D. S. Soong, A. T. Bell, and D. W. Hess, "A mathematical model for spin coating of polymer resists", *Journal of Applied Physics*, vol. 56, no. 4, pp. 1199–1206, 1984, ISSN: 00218979. DOI: 10.1063/1.334049.

[64] D. E. Bornside, C. W. Macosko, and L. E. Scriven, "Spin coating: One-dimensional model", *Journal of Applied Physics*, vol. 66, no. 11, pp. 5185–5193, 1989, ISSN: 00218979. DOI: 10.1063/1.343754.

[65] M. Singh, H. M. Haverinen, P. Dhagat, and G. E. Jabbour, "Inkjet printing-process and its applications", *Advanced Materials*, vol. 22, no. 6, pp. 673–685, 2010, ISSN: 09359648. DOI: 10.1002/adma.200901141.

[66] G. Azzellino, a. Grimoldi, M. Binda, M. Caironi, D. Natali, and M. Sampietro, "Fully inkjet-printed organic photodetectors with high quantum yield.", *Advanced materials (Deerfield Beach, Fla.)*, vol. 25, no. 47, pp. 6829–33, Dec. 2013, ISSN: 1521-4095. DOI: 10.1002/adma.201303473. [Online]. Available: http://www.ncbi.nlm.nih.gov/pubmed/24105887.

[67] H. Sirringhaus, T. Kawase, R. H. Friend, T. Shimoda, M. Inbasekaran, W. Wu, and E. P. Woo, "High-resolution inkjet printing of all-polymer transistor circuits.", *Science (New York, N.Y.)*, vol. 290, no. 5499, pp. 2123–2126, 2000, ISSN: 0883-7694. DOI: 10.1557/mrs2001.127.

[68] A. Albrecht, A. Rivadeneyra, A. Abdellah, P. Lugli, and F. Salmero, "Inkjet printing and photonic sintering of silver and copper oxide nanoparticles for ultra-low-cost condctive patterns", *Journal of Materials Chemistry C*, pp. 3546–3554, 2016, ISSN: 20507526. DOI: 10.1039/c6tc00628k.

[69] A. Falco, J. F. Salmeron, F. Loghin, A. Abdelhalim, P. Lugli, and A. Rivadeneyra, "Optimization of Process Parameters for Inkjet Printing of CNT Random Networks on Flexible Substrates", in *Nanotechnology, 2016 IEEE-NANO IEEE Conference on Nanoelectronics*, 2016, (Accepted).

[70] Y. W. Enrique J. Lavernia, *Spray Atomization and Deposition.* Wiley, 1996.

[71] R. C. Tenent, T. M. Barnes, J. D. Bergeson, A. J. Ferguson, B. To, L. M. Gedvilas, M. J. Heben, and J. L. Blackburn, “Ultrasmooth, Large-Area, High-Uniformity, Conductive Transparent Single-Walled-Carbon-Nanotube Films for Photovoltaics Produced by Ultrasonic Spraying”, *Advanced Materials*, vol. 21, no. 31, pp. 3210–3216, Aug. 2009, ISSN: 09359648. DOI: `10.1002/adma.200803551`. [Online]. Available: `http://doi.wiley.com/10.1002/adma.200803551`.

[72] S. F. Tedde, J. Kern, T. Sterzl, J. Fürst, P. Lugli, and O. Hayden, “Fully spray coated organic photodiodes.”, *Nano letters*, vol. 9, no. 3, pp. 980–3, Mar. 2009, ISSN: 1530-6984. DOI: `10.1021/nl803386y`. [Online]. Available: `http://www.ncbi.nlm.nih.gov/pubmed/19239203`.

[73] C. Girotto, D. Moia, B. P. Rand, and P. Heremans, “High-Performance Organic Solar Cells with Spray-Coated Hole-Transport and Active Layers”, *Advanced Functional Materials*, vol. 21, no. 1, pp. 64–72, Jan. 2011, ISSN: 1616301X. DOI: `10.1002/adfm.201001562`. [Online]. Available: `http://doi.wiley.com/10.1002/adfm.201001562`.

[74] A. Abdellah, K. S. Virdi, R. Meier, M. Döblinger, P. Müller-Buschbaum, C. Scheu, P. Lugli, and G. Scarpa, “Successive Spray Deposition of P3HT/PCBM Organic Photoactive Layers: Material Composition and Device Characteristics”, *Advanced Functional Materials*, vol. 22, no. 19, pp. 4078–4086, Oct. 2012, ISSN: 1616301X. DOI: `10.1002/adfm.201200548`. [Online]. Available: `http://doi.wiley.com/10.1002/adfm.201200548`.

[75] D. Vak, S.-S. Kim, J. Jo, S.-H. Oh, S.-I. Na, J. Kim, and D.-Y. Kim, “Fabrication of organic bulk heterojunction solar cells by a spray deposition method for low-cost power generation”, *Applied Physics Letters*, vol. 91, no. 8, p. 081 102, 2007, ISSN: 00036951. DOI: `10.1063/1.2772766`. [Online]. Available: `http://scitation.aip.org/content/aip/journal/apl/91/8/10.1063/1.2772766`.

[76] K. X. Steirer, J. J. Berry, M. O. Reese, M. F. van Hest, A. Miedaner, M. W. Liberatore, R. Collins, and D. S. Ginley, “Ultrasonically sprayed and inkjet printed thin film electrodes for organic solar cells”, *Thin Solid Films*, vol. 517, no. 8, pp. 2781–2786, Feb. 2009, ISSN: 00406090. DOI: `10.1016/j.tsf.2008.10.124`. [Online]. Available: `http://linkinghub.elsevier.com/retrieve/pii/S0040609008012972`.

[77] D. Baierl, L. Pancheri, M. Schmidt, D. Stoppa, G.-F. Dalla Betta, G. Scarpa, and P. Lugli, “A hybrid CMOS-imager with a solution-processable polymer as photoactive layer.”, *Nature communications*, vol. 3, p. 1175, Jan. 2012, ISSN:

2041-1723. DOI: `10.1038/ncomms2180`. [Online]. Available: `http://www.ncbi.nlm.nih.gov/pubmed/23132025`.

[78] P. Büchele, M. Richter, S. F. Tedde, G. J. Matt, G. N. Ankah, R. Fischer, M. Biele, W. Metzger, S. Lilliu, O. Bikondoa, J. E. Macdonald, C. J. Brabec, T. Kraus, U. Lemmer, and O. Schmidt, "X-ray imaging with scintillator-sensitized hybrid organic photodetectors", *Nature Photonics*, vol. 9, no. 12, pp. 843–848, 2015, ISSN: 1749-4885. DOI: `10.1038/nphoton.2015.216`. [Online]. Available: `http://dx.doi.org/10.1038/nphoton.2015.216$%5Cbackslash$nhttp://www.nature.com/nphoton/journal/v9/n12/pdf/nphoton.2015.216.pdf$%5Cbackslash$nhttp://www.nature.com/doifinder/10.1038/nphoton.2015.216`.

[79] G. H. Gelinck, A. Kumar, D. Moet, J. L. Van Der Steen, U. Shafique, P. E. Malinowski, K. Myny, B. P. Rand, M. Simon, W. Rütten, A. Douglas, J. Jorritsma, P. Heremans, and R. Andriessen, "X-ray imager using solution processed organic transistor arrays and bulk heterojunction photodiodes on thin, flexible plastic substrate", *Organic Electronics: Physics, materials, applications*, vol. 14, no. 10, pp. 2602–2609, 2013, ISSN: 15661199. DOI: `10.1016/j.orgel.2013.06.020`. [Online]. Available: `http://dx.doi.org/10.1016/j.orgel.2013.06.020`.

[80] G. H. Gelinck, A. Kumar, D. Moet, J.-l. P. J. V. D. Steen, A. J. J. M. V. Breemen, S. Shanmugam, A. Langen, J. Gilot, P. Groen, R. Andriessen, M. Simon, W. Ruetten, A. U. Douglas, R. Raaijmakers, P. E. Malinowski, and K. Myny, "X-Ray Detector-on-Plastic With High Sensitivity Using Low Cost , Solution-Processed Organic Photodiodes", *IEEE Transaction on Electron Devices*, vol. 63, no. 1, pp. 197–204, 2016, ISSN: 0018-9383. DOI: `10.1109/TED.2015.2432572`.

[81] A. Banerjee, Y. Shuai, R. Dixit, I. Papautsky, and D. Klotzkin, "Concentration dependence of fluorescence signal in a microfluidic fluorescence detector", *Journal of Luminescence*, vol. 130, no. 6, pp. 1095–1100, 2010, ISSN: 00222313. DOI: `10.1016/j.jlumin.2010.02.002`. [Online]. Available: `http://dx.doi.org/10.1016/j.jlumin.2010.02.002`.

[82] G. Williams, C. Backhouse, and H. Aziz, "Integration of Organic Light Emitting Diodes and Organic Photodetectors for Lab-on-a-Chip Bio-Detection Systems", *Electronics*, vol. 3, no. 1, pp. 43–75, 2014, ISSN: 2079-9292. DOI: `10.3390/electronics3010043`. [Online]. Available: `http://www.mdpi.com/2079-9292/3/1/43/`.

[83] J. Xue, "Carrier transport in multilayer organic photodetectors: I. Effects of layer structure on dark current and photoresponse", *Journal of Applied Physics*, vol. 95, no. 4, p. 1859, 2004, ISSN: 00218979. DOI: `10.1063/1.1640453`. [Online]. Available: `http://link.aip.org/link/?JAP/95/1859/1%7B%5C&%7DAgg=doi`.

[84] M. Pope and C. E. Swenberg, "Electronic processes in organic solids", *Annual Review of Physical Chemistry*, vol. 35, pp. 613–655, 1984, ISSN: 0031-9155. DOI: `10.1088/0031-9155/27/3/001`.

[85] M. Chandross, Y. Shimoi, and S. Mazumdar, "Systematic characterization of excited states in p -conjugated polymers", no. November, pp. 85–90, 1997.

[86] C. Lee, G. Yu, and A. Haeger, "Persistent photoconductivity in poly(pphenylenevinylene): Spectral response and slow relaxation", *Physical Review B*, vol. 47, no. 23, 1993.

[87] M. Knupfer, "Exciton binding energies in organic semiconductors", *Applied Physics A: Materials Science and Processing*, vol. 77, no. 5, pp. 623–626, 2003, ISSN: 09478396. DOI: `10.1007/s00339-003-2182-9`.

[88] P. Schilinsky, C. Waldauf, and C. J. Brabec, "Recombination and loss analysis in polythiophene based bulk heterojunction photodetectors", *Applied Physics Letters*, vol. 81, no. 20, p. 3885, 2002, ISSN: 00036951. DOI: `10.1063/1.1521244`. [Online]. Available: `http://link.aip.org/link/APPLAB/v81/i20/p3885/s1%7B%5C&%7DAgg=doi`.

[89] L. Li, F. Zhang, J. Wang, Q. An, Q. Sun, W. Wang, J. Zhang, and F. Teng, "Achieving EQE of 16,700% in P3HT:PC71BM based photodetectors by trap-assisted photomultiplication", *Scientific Reports*, vol. 5, p. 9181, 2015, ISSN: 2045-2322. DOI: `10.1038/srep09181`. [Online]. Available: `http://www.nature.com/doifinder/10.1038/srep09181`.

[90] J. Y. Oh, W. S. Jang, T. I. Lee, J.-m. Myoung, H. K. Baik, and H. Koo, "Driving vertical phase separation in a bulk-heterojunction by inserting a poly (3-hexylthiophene) layer for highly efficient organic solar cells Driving vertical phase separation in a bulk-heterojunction by inserting a poly 3-hexylthiophene ... layer fo", *Applied Physics Letters*, vol. 98, 2011. DOI: `10.1063/1.3541648`.

[91] P. E. Keivanidis, P. K. H. Ho, R. H. Friend, and N. C. Greenham, "The Dependence of Device Dark Current on the Active-Layer Morphology of Solution-Processed Organic Photodetectors", *Advanced Functional Materials*, vol. 20, no. 22, pp. 3895–3903, Nov. 2010, ISSN: 1616301X. DOI: `10.1002/adfm.201000967`. [Online]. Available: `http://doi.wiley.com/10.1002/adfm.201000967`.

[92] G. Gruner, “Carbon nanotube films for transparent and plastic electronics”, *Journal of Materials Chemistry*, vol. 16, no. 35, pp. 3533–3539, 2006.

[93] Q. Cao and J. A. Rogers, “Ultrathin Films of Single-Walled Carbon Nanotubes for Electronics and Sensors: A Review of Fundamental and Applied Aspects”, *Advanced Materials*, vol. 21, no. 1, pp. 29–53, Jan. 2009, ISSN: 09359648. DOI: `10.1002/adma.200801995`.

[94] L. Hu, D. S. Hecht, and G. Grüner, “Carbon Nanotube Thin Films: Fabrication, Properties, and Applications”, *Chemical Reviews*, vol. 110, no. 10, pp. 5790–5844, Oct. 2010. DOI: `10.1021/cr9002962`. [Online]. Available: `http://dx.doi.org/10.1021/cr9002962%20http://pubs.acs.org/doi/full/10.1021/cr9002962`.

[95] D. Zhang, K. Ryu, X. Liu, E. Polikarpov, J. Ly, M. E. Tompson, and C. Zhou, “Transparent, Conductive, and Flexible Carbon Nanotube Films and Their Application in Organic Light-Emitting Diodes”, *Nano Letters*, vol. 6, no. 9, pp. 1880–1886, 2006. DOI: `10.1021/nl0608543`.

[96] Y.-M. Chien, F. Lefevre, I. Shih, and R. Izquierdo, “A solution processed top emission OLED with transparent carbon nanotube electrodes.”, *Nanotechnology*, vol. 21, no. 13, p. 134 020, Apr. 2010, ISSN: 1361-6528. DOI: `10.1088/0957-4484/21/13/134020`. [Online]. Available: `http://www.ncbi.nlm.nih.gov/pubmed/20208120`.

[97] C. M. Trottier, P. Glatkowski, P. Wallis, and J. Luo, “Properties and characterization of carbon-nanotube-based transparent conductive coating”, *Journal of the Society for Information Display*, vol. 13, no. 9, p. 759, 2005, ISSN: 10710922. DOI: `10.1889/1.2080514`. [Online]. Available: `http://doi.wiley.com/10.1889/1.1828693`.

[98] D.-Y. Cho, K. Eun, S.-H. Choa, and H.-K. Kim, “Highly flexible and stretchable carbon nanotube network electrodes prepared by simple brush painting for cost-effective flexible organic solar cells”, *Carbon*, vol. 66, pp. 530–538, Jan. 2014, ISSN: 00086223. DOI: `10.1016/j.carbon.2013.09.035`.

[99] T. M. Barnes, J. D. Bergeson, R. C. Tenent, B. a. Larsen, G. Teeter, K. M. Jones, J. L. Blackburn, and J. van de Lagemaat, “Carbon nanotube network electrodes enabling efficient organic solar cells without a hole transport layer”, *Applied Physics Letters*, vol. 96, no. 24, p. 243 309, 2010, ISSN: 00036951. DOI: `10.1063/1.3453445`. [Online]. Available: `http://link.aip.org/link/APPLAB/v96/i24/p243309/s1%7B%5C&%7DAgg=doi`.

[100] M. Tinkham, "Energy gap interpretation of experiments on infrared transmission through superconducting films", *Physical Review*, vol. 104, p. 845, 1956. [Online]. Available: `http://prola.aps.org/abstract/PR/v104/i3/p845%7B%5C_%7D1`.

[101] A. Falco, "Spray-deposition of polymer and CNT thin-films for organic optoelectronics", 2013.

[102] B. B. Parekh, G. Fanchini, G. Eda, and M. Chhowalla, "Improved conductivity of transparent single-wall carbon nanotube thin films via stable postdeposition functionalization", *Applied Physics Letters*, vol. 90, no. 12, p. 121 913, 2007, ISSN: 00036951. DOI: `10.1063/1.2715027`. [Online]. Available: `http://link.aip.org/link/APPLAB/v90/i12/p121913/s1%7B%5C&%7DAgg=doi`.

[103] V. Robbiano, A. Abdellah, L. Santarelli, A. Falco, S. El-molla, L. V. Titova, D. N. Purschke, F. A. Hegmann, F. Cacialli, and P. Lugli, "Analysis of Sprayed Carbon Nanotube Films on Rigid and Flexible Substrates", in *Nanotechnology, 2014. IEEE-NANO IEEE Conference on Nanoelectronics*, 2014, pp. 650–654, ISBN: 9781479956227.

[104] P. Vacca, M. Petrosino, R. Miscioscia, G. Nenna, C. Minarini, D. Della Sala, and A. Rubino, "Poly(3,4-ethylenedioxythiophene):poly(4-styrenesulfonate) ratio: Structural, physical and hole injection properties in organic light emitting diodes", *Thin Solid Films*, vol. 516, no. 12, pp. 4232–4237, 2008, ISSN: 00406090. DOI: `10.1016/j.tsf.2007.12.143`.

[105] V. Chirila, G. Marginean, and W. Brandl, "Effect of the oxygen plasma treatment parameters on the carbon nanotubes surface properties", *Surface and Coatings Technology*, vol. 200, no. 1-4, pp. 548–551, Oct. 2005, ISSN: 02578972. DOI: `10.1016/j.surfcoat.2005.01.089`. [Online]. Available: `http://linkinghub.elsevier.com/retrieve/pii/S0257897205001763`.

[106] D. Baierl, B. Fabel, P. Gabos, L. Pancheri, P. Lugli, and G. Scarpa, "Solution-processable inverted organic photodetectors using oxygen plasma treatment", *Organic Electronics*, vol. 11, no. 7, pp. 1199–1206, Jul. 2010, ISSN: 15661199. DOI: `10.1016/j.orgel.2010.04.023`. [Online]. Available: `http://linkinghub.elsevier.com/retrieve/pii/S1566119910001400`.

[107] M. Petrosino and P. Vacca, "The effect of ITO surface energy on OLED electrical properties", *... , 2007. IWPSD 2007. ...*, pp. 1–4, 2007. [Online]. Available: `http://ieeexplore.ieee.org/xpls/abs%7B%5C_%7Dall.jsp?arnumber=4472590`.

[108] J.-Y. Lee, S. T. Connor, Y. Cui, and P. Peumans, "Solution-processed metal nanowire mesh transparent electrodes.", *Nano letters*, vol. 8, no. 2, pp. 689–92, Feb. 2008, ISSN: 1530-6984. DOI: `10.1021/nl073296g`. [Online]. Available: `http://www.ncbi.nlm.nih.gov/pubmed/18189445`.

[109] D.-S. Leem, A. Edwards, M. Faist, J. Nelson, D. D. C. Bradley, and J. C. de Mello, "Efficient organic solar cells with solution-processed silver nanowire electrodes.", *Advanced materials (Deerfield Beach, Fla.)*, vol. 23, no. 38, pp. 4371–5, Oct. 2011, ISSN: 1521-4095. DOI: `10.1002/adma.201100871`. [Online]. Available: `http://www.ncbi.nlm.nih.gov/pubmed/21861269`.

[110] T. Someya, Y. Kato, S. Iba, Y. Noguchi, T. Sekitani, H. Kawaguchi, and T. Sakurai, "Integration of Organic FETs With Organic Photodiodes for a Large Area , Flexible , and", *2502 IEEE TRANSACTIONS ON ELECTRON DEVICES*, vol. 52, no. 11, pp. 2502–2511, 2005.

[111] L. Yang, T. Zhang, H. Zhou, S. C. Price, B. J. Wiley, and W. You, "Solution-Processed Flexible Polymer Solar Cells with Silver Nanowire Electrodes", pp. 4075–4084, 2011.

[112] M. Schmidt, A. Falco, M. Loch, P. Lugli, and G. Scarpa, "Spray coated indium-tin-oxide-free organic photodiodes with PEDOT:PSS anodes", *AIP Advances*, vol. 4, no. 10, p. 107 132, Oct. 2014, ISSN: 2158-3226. DOI: `10.1063/1.4899044`. [Online]. Available: `http://scitation.aip.org/content/aip/journal/adva/4/10/10.1063/1.4899044`.

[113] L. La Notte, D. Mineo, G. Polino, G. Susanna, F. Brunetti, T. M. Brown, A. Di Carlo, and A. Reale, "Fabrication of Fully-Spray-Processed Organic Photovoltaic Modules by using an Automated Process in Air", *Energy Technology*, vol. 1, no. 12, pp. 757–762, Dec. 2013, ISSN: 21944288. DOI: `10.1002/ente.201300107`. [Online]. Available: `http://doi.wiley.com/10.1002/ente.201300107`.

[114] Y. Zhou, C. Fuentes-Hernandez, J. Shim, J. Meyer, a. J. Giordano, H. Li, P. Winget, T. Papadopoulos, H. Cheun, J. Kim, M. Fenoll, a. Dindar, W. Haske, E. Najafabadi, T. M. Khan, H. Sojoudi, S. Barlow, S. Graham, J.-L. Bredas, S. R. Marder, a. Kahn, and B. Kippelen, "A Universal Method to Produce Low-Work Function Electrodes for Organic Electronics", *Science*, vol. 336, no. 6079, pp. 327–332, 2012, ISSN: 0036-8075. DOI: `10.1126/science.1218829`.

[115] Y. Zhou, C. Fuentes-Hernandez, J. W. Shim, T. M. Khan, and B. Kippelen, "High performance polymeric charge recombination layer for organic tandem solar cells", *Energy & Environmental Science*, vol. 5, no. 12, p. 9827, 2012, ISSN: 1754-5692. DOI: `10.1039/c2ee23294d`. [Online]. Available: `http://xlink.rsc.org/?DOI=c2ee23294d`.

[116] S. Stolz, M. Scherer, E. Mankel, R. Lovrini, J. Schinke, W. Kowalsky, W. Jaegermann, U. Lemmer, N. Mechau, and G. Hernandez-Sosa, "Investigation of solution processed ultra-thin electron injection layers for organic light-emitting diodes.", *ACS applied materials & interfaces*, 2014, ISSN: 1944-8252. DOI: `10.1021/am500287y`. [Online]. Available: `http://www.ncbi.nlm.nih.gov/pubmed/24703464`.

[117] A. Falco, A. Zaidi, P. Lugli, and A. Abdellah, "Spray deposition of Polyethylenimine thin films for the fabrication of fully-sprayed organic photodiodes", *Organic Electronics*, vol. 23, pp. 186–192, 2015, ISSN: 15661199. DOI: `10.1016/j.orgel.2015.05.003`. [Online]. Available: `http://linkinghub.elsevier.com/retrieve/pii/S1566119915001949`.

[118] J. G. Simmons, "Conduction in thin dielectric films", *Journal of Physics D: Applied Physics*, vol. 4, no. 5, pp. 613–657, 2002, ISSN: 00223727. DOI: `10.1088/0022-3727/4/5/202`.

[119] D. Barkhouse, O. Gunawan, T. Gokmen, T. Torodov, and D. Mitzi, "Device characteristics of a 10.1% hydrazine-processed Cu2ZnSn(Se,S)4 solar cell", *Prog. Photovolt: Res. Appl.*, vol. 15, pp. 659–676, 2012, ISSN: 10627995. DOI: `10.1002/pip`. arXiv: `1303.4604`. [Online]. Available: `http://dx.doi.org/10.1002/pip.1160`.

[120] M. Manceau, A. Rivaton, J. L. Gardette, S. Guillerez, and N. Lematre, "The mechanism of photo- and thermooxidation of poly(3-hexylthiophene) (P3HT) reconsidered", *Polymer Degradation and Stability*, vol. 94, no. 6, pp. 898–907, 2009, ISSN: 01413910. DOI: `10.1016/j.polymdegradstab.2009.03.005`. arXiv: `arXiv:1011.1669v3`.

[121] J. W. Arbogast, A. P. Darmanyan, C. S. Foote, Y. Rubin, F. N. Diederich, M. M. Alvarez, S. J. Anz, and R. L. Whetten, "Photophysical Properties of C60", *J. Phys. Chem.*, no. 10, pp. 11–12, 1991, ISSN: 0022-3654. DOI: `10.1021/j100154a006`.

[122] J. G. Wijmans and R. W. Baker, "The solution-diffusion model: a review", *Journal of Membrane Science*, vol. 107, no. 1-2, pp. 1–21, 1995, ISSN: 03767388. DOI: `10.1016/0376-7388(95)00102-I`.

[123] A. Dameron, S. Davidson, B. Burton, P. Carcia, R. McLean, and S. George, "Gas diffusion barriers on polymers using multilayers fabricated by Al2O3 and rapid SiO2 atomic layer deposition", *The Journal of Physical Chemistry C*, vol. 112, pp. 4573–4580, 2008, ISSN: 1932-7447. DOI: `10.1021/jp076866`. [Online]. Available: `http://pubs.acs.org/doi/abs/10.1021/jp076866+`.

[124] A. S. Da Silva Sobrinho, G. Czeremuszkin, M. Latrèche, G. Dennler, and M. R. Wertheimer, "A study of defects in ultra-thin transparent coatings on polymers", *Surface and Coatings Technology*, vol. 116-119, pp. 1204–1210, 1999, ISSN: 02578972. DOI: `10.1016/S0257-8972(99)00152-8`.

[125] T. N. Chen, D. S. Wuu, C. C. Wu, C. C. Chiang, H. B. Lin, Y. P. Chen, and R. H. Horng, "Effects of plasma pretreatment on silicon nitride barrier films on polycarbonate substrates", *Thin Solid Films*, vol. 514, no. 1-2, pp. 188–192, 2006, ISSN: 00406090. DOI: `10.1016/j.tsf.2006.02.039`.

[126] S. Schubert, H. Klumbies, L. Müller-Meskamp, and K. Leo, "Electrical calcium test for moisture barrier evaluation for organic devices", *Review of Scientific Instruments*, vol. 82, no. 9, 2011, ISSN: 00346748. DOI: `10.1063/1.3633956`. arXiv: `/dx.doi.org/10.1063/1.3633956 [http:]`.

[127] R. Paetzold, A. Winnacker, D. Henseler, V. Cesari, and K. Heuser, "Permeation rate measurements by electrical analysis of calcium corrosion", *Review of Scientific Instruments*, vol. 74, no. 12, pp. 5147–5150, 2003, ISSN: 00346748. DOI: `10.1063/1.1626015`.

[128] J. Meyer, P. Görrn, F. Bertram, S. Hamwi, T. Winkler, H. H. Johannes, T. Weimann, P. Hinze, T. Riedl, and W. Kowalsky, "Al2O3/ZrO2 Nanolaminates as ultrahigh gas-diffusion barriersa strategy for reliable encapsulation of organic electronics", *Advanced Materials*, vol. 21, no. 18, pp. 1845–1849, 2009, ISSN: 09359648. DOI: `10.1002/adma.200803440`.

[129] J. H. Choi, Y. M. Kim, Y. W. Park, J. W. Huh, B. K. Ju, I. S. Kim, and H. N. Hwang, "Evaluation of gas permeation barrier properties using electrical measurements of calcium degradation", *Review of Scientific Instruments*, vol. 78, no. 6, 2007, ISSN: 00346748. DOI: `10.1063/1.2747168`.

[130] T. Ameri, G. Dennler, C. Waldauf, P. Denk, K. Forberich, M. C. Scharber, C. J. Brabec, and K. Hingerl, "Realization, characterization, and optical modeling of inverted bulk-heterojunction organic solar cells", *Journal of Applied Physics*, vol. 103, no. 8, 2008, ISSN: 00218979. DOI: `10.1063/1.2902804`.

[131] D. Baierl, "A Hybrid CMOS-Imager with Integrated Solution-Processable Organic Photodiodes", no. November, p. 171, 2012, ISSN: 2041-1723. DOI: `10.1038/ncomms2180`.

[132] M. Es-saheb, A. A. Elzatahry, E. S. M. Sherif, A. S. Alkaraki, and E. R. Kenawy, "A novel electrospinning application for polyvinyl chloride nanofiber coating deposition as a corrosion inhibitor for aluminum, steel, and brass in chloride solutions", *International Journal of Electrochemical Science*, vol. 7, no. 7, pp. 5962–5976, 2012, ISSN: 14523981.

[133] W. S. Rapson, "Skin Contact with Gold and Gold-Alloys", *Contact Dermatitis*, vol. 13, no. 2, pp. 56–65, 1985. DOI: `DOI10.1111/j.1600-0536.1985.tb02505.x`. [Online]. Available: `%3CGo%20to%20ISI%3E://A1985AQQ2900003`.

[134] A. Falco, B. Matarese, P. Feyen, F. Benfenati, J. C. de Mello, and P. Lugli, "Investigation of the stability and biocompatibility of commonly used electrode materials in organic neuro-optoelectronics", *IEEE Transactions on Nanotechnology*, 2016.

[135] M. Agirregabiria, F. J. Blanco, J. Berganzo, M. T. Arroyo, a. Fullaondo, K. Mayora, and J. M. Ruano-López, "Fabrication of SU-8 multilayer microstructures based on successive CMOS compatible adhesive bonding and releasing steps.", *Lab on a chip*, vol. 5, no. 5, pp. 545–552, 2005, ISSN: 1473-0197. DOI: `10.1039/b500519a`.

[136] D. Fischer, Y. Li, B. Ahlemeyer, J. Krieglstein, and T. Kissel, "In vitro cytotoxicity testing of polycations: Influence of polymer structure on cell viability and hemolysis", *Biomaterials*, vol. 24, no. 7, pp. 1121–1131, 2003, ISSN: 01429612. DOI: `10.1016/S0142-9612(02)00445-3`.

[137] C. Brunot, L. Ponsonnet, C. Lagneau, P. Farge, C. Picart, and B. Grosgogeat, "Cytotoxicity of polyethyleneimine (PEI), precursor base layer of polyelectrolyte multilayer films", *Biomaterials*, vol. 28, no. 4, pp. 632–640, 2007, ISSN: 01429612. DOI: `10.1016/j.biomaterials.2006.09.026`.

[138] R. Jones, H. M. Pollock, J. A. S. Cleaver, and C. S. Hodges, "Adhesion forces between glass and silicon surfaces in air studied by AFM: Effects of relative humidity, particle size, roughness, and surface treatment", *Langmuir*, vol. 18, no. 21, pp. 8045–8055, 2002, ISSN: 07437463. DOI: `10.1021/la0259196`.

[139] S. L. Jacques, "Optical properties of biological tissues: a review.", *Physics in medicine and biology*, vol. 58, no. 11, R37–61, 2013, ISSN: 1361-6560. DOI: `10.1088/0031-9155/58/11/R37`. [Online]. Available: `http://iopscience.iop.org/article/10.1088/0031-9155/58/11/R37`.

[140] T. Novikova, A. Pierangelo, A. De Martino, A. Benali, and P. Validire, "Polarimetric Imaging for Cancer Diagnosis and Staging", *Optics and Photonics News*, vol. 23, no. 10, p. 26, 2012, ISSN: 1047-6938. DOI: `10.1364/OPN.23.10.000026`.

[141] F. Snik, J. Craven-Jones, M. Escuti, S. Fineschi, D. Harrington, A. De Martino, D. Mawet, J. Riedi, and J. S. Tyo, "An overview of polarimetric sensing techniques and technology with applications to different research fields", *Spie*, vol. 9099, 90990B, 2014, ISSN: 1996756X. DOI: `10.1117/12.2053245`. [Online]. Available: `http://proceedings.spiedigitallibrary.org/proceeding.aspx?doi=10.1117/12.2053245`.

[142] S. Yin and P. Ruffin, *Fiber Optic Sensors. Wiley Encyclopedia of Biomedical Engineering.* 2006.

[143] G. Franceschetti, *Campi Elettromagnetici.* Bollati Boringhieri, 1983.

[144] J. D. Jackson, *Classical electrodynamics.* John Wiley & Sons Ltd., 1962.

[145] Y. Ekinci, H. H. Solak, C. David, and H. Sigg, "Bilayer Al wire-grids as broadband and high-performance polarizers.", *Optics express*, vol. 14, no. 6, pp. 2323–34, Mar. 2006, ISSN: 1094-4087. [Online]. Available: `http://www.ncbi.nlm.nih.gov/pubmed/19503570`.

[146] E. Hecht, *Optics*, 4th. Addison-Wesley, 2002.

[147] L. Wang, H. Schift, J. Gobrecht, Y. Ekinci, P. M. Kristiansen, H. H. Solak, and K. Jefimovs, "High-throughput fabrication of compact and flexible bilayer nanowire grid polarizers for deep-ultraviolet to infrared range", *Journal of Vacuum Science & Technology B: Microelectronics and Nanometer Structures*, vol. 32, no. 3, p. 031 206, May 2014, ISSN: 2166-2746. DOI: `10.1116/1.4874318`. [Online]. Available: `http://scitation.aip.org/content/avs/journal/jvstb/32/3/10.1116/1.4874318`.

[148] E. P. Kartalov, J. F. Zhong, A. Scherer, S. R. Quake, C. R. Taylor, and W. F. Anderson, “High-throughput multi-antigen microfluidic fluorescence immunoassays”, *BioTechniques*, vol. 40, no. 1, pp. 85–90, 2006, ISSN: 07366205. DOI: `10.2144/000112071`.

[149] E. Manna, T. Xiao, J. Shinar, and R. Shinar, *Organic Photodetectors in Analytical Applications*, 3. 2015, vol. 4, pp. 688–722, ISBN: 1515294870. DOI: `10.3390/electronics4030688`. [Online]. Available: `http://www.mdpi.com/2079-9292/4/3/688/`.

[150] Z. Y. Yang and Y. F. Lu, “Broadband nanowire-grid polarizers in ultraviolet-visible-near-infrared regions.”, *Optics express*, vol. 15, no. 15, pp. 9510–9, 2007, ISSN: 1094-4087. DOI: `10.1364/OE.15.009510`. [Online]. Available: `http://www.ncbi.nlm.nih.gov/pubmed/19547298`.

[151] L. Wang, H. Schift, P. M. Kristiansen, K. Jefimovs, H. H. Solak, J. Gobrecht, and Y. Ekinci, “Bilayer wire-grid polarizers for DUV to IR fabricated using EUV interference and nanoimprint lithography”, *8th Annual IEEE International Conference on Nano/Micro Engineered and Molecular Systems, IEEE NEMS 2013*, vol. 1, no. c, pp. 1232–1235, 2013. DOI: `10.1109/NEMS.2013.6559941`.

[152] a. D. Rakic, a. B. Djurisic, J. M. Elazar, and M. L. Majewski, “Optical properties of metallic films for vertical-cavity optoelectronic devices.”, *Applied optics*, vol. 37, no. 22, pp. 5271–83, Aug. 1998, ISSN: 0003-6935. [Online]. Available: `http://www.ncbi.nlm.nih.gov/pubmed/18286006`.

[153] V. I. Belotelov, A. N. Kalish, A. K. Zvezdin, A. V. Gopal, and A. S. Vengurlekar, “FabryPerot plasmonic structures for nanophotonics”, *Journal of the Optical Society of America B*, vol. 29, no. 3, p. 294, 2012, ISSN: 0740-3224. DOI: `10.1364/JOSAB.29.000294`.

[154] R. D. Nagel, T. Haeberle, M. Schmidt, P. Lugli, and G. Scarpa, “Large Area Nano-transfer Printing of Sub-50-nm Metal Nanostructures Using Low-cost Semi-flexible Hybrid Templates.”, *Nanoscale research letters*, vol. 11, no. 1, p. 143, 2016, ISSN: 1931-7573. DOI: `10.1186/s11671-016-1346-4`. [Online]. Available: `http://www.ncbi.nlm.nih.gov/pubmed/26976429`.

[155] Thorlabs, *Thorlabs - Dichroic Film Polarizer*. [Online]. Available: `https://www.thorlabs.com/newgrouppage9.cfm?objectgroup%7B%5C_%7Did=7081`.

[156] M. Schmidt and P. Lugli, “Nanopatterning of P3HT : PCBM for organic solar cell realization”, pp. 3–6, 2015.

[157] G. Juka, K. Geneviius, R. Österbacka, K. Arlauskas, T. Kreouzis, D. Bradley, and H. Stubb, "Initial transport of photogenerated charge carriers in pi-conjugated polymers", *Physical Review B*, vol. 67, no. 8, p. 081 201, 2003, ISSN: 1550-235X. DOI: `10.1103/PhysRevB.67.081201`. [Online]. Available: `http://prb.aps.org/abstract/PRB/v67/i8/e081201`.

[158] P. W. M. Blom, V. D. Mihailetchi, L. J. A. Koster, and D. E. Markov, "Device physics of polymer:Fullerene bulk heterojunction solar cells", *Advanced Materials*, vol. 19, no. 12, pp. 1551–1566, 2007, ISSN: 09359648. DOI: `10.1002/adma.200601093`.

[159] W. H. Lee, S. Y. Chuang, H. L. Chen, W. F. Su, and C. H. Lin, "Exploiting optical properties of P3HT:PCBM films for organic solar cells with semitransparent anode", *Thin Solid Films*, vol. 518, no. 24, pp. 7450–7454, 2010, ISSN: 00406090. DOI: `10.1016/j.tsf.2010.05.021`.

[160] G. Dennler, K. Forberich, M. C. Scharber, C. J. Brabec, I. Tomi, K. Hingerl, and T. Fromherz, "Angle dependence of external and internal quantum efficiencies in bulk-heterojunction organic solar cells", *Journal of Applied Physics*, vol. 102, no. 5, 2007, ISSN: 00218979. DOI: `10.1063/1.2777724`.

[161] H. Hoppe and N. S. Sariciftci, "Organic solar cells: An overview", *J. Mater. Res.*, vol. 19, no. July 2004, pp. 1924–1945, 2004, ISSN: 0884-2914. DOI: `10.1557/JMR.2004.0252`. [Online]. Available: `http://dx.doi.org/10.1557/JMR.2004.0252`.

[162] B. V. Popescu, D. H. Popescu, P. Lugli, S. Locci, F. Arca, S. F. Tedde, M. Sramek, and O. Hayden, "Modeling and simulation of organic photodetectors for low light intensity applications", *IEEE Transactions on Electron Devices*, vol. 60, no. 6, pp. 1975–1981, 2013, ISSN: 00189383. DOI: `10.1109/TED.2013.2259239`.

[163] L. A. Pettersson, S. Ghosh, and O. Inganäs, "Optical anisotropy in thin films of poly(3,4-ethylenedioxythiophene)poly(4-styrenesulfonate)", *Organic Electronics*, vol. 3, no. 3-4, pp. 143–148, 2002, ISSN: 15661199. DOI: `10.1016/S1566-1199(02)00051-4`. [Online]. Available: `http://www.sciencedirect.com/science/article/pii/S1566119902000514`.

[164] L. Zhao, S. Zhao, Z. Xu, D. Huang, J. Zhao, Y. Li, and X. Xu, "The Effects of Improved Photoelectric Properties of PEDOT:PSS by Two-Step Treatments on the Performance of Polymer Solar Cells Based on PTB7-Th:PC ₇₁ BM", *ACS Applied Materials & Interfaces*, acsami.5b09561, 2015, ISSN: 1944-8244. DOI: `10.1021/acsami.5b09561`. [Online]. Available: `http://pubs.acs.org/doi/10.1021/acsami.5b09561`.

[165] A. Sandström, A. Asadpoordarvish, J. Enevold, and L. Edman, “Spraying light: ambient-air fabrication of large-area emissive devices on complex-shaped surfaces.”, *Advanced materials (Deerfield Beach, Fla.)*, vol. 26, no. 29, pp. 4975–80, Aug. 2014, ISSN: 1521-4095. DOI: `10.1002/adma.201401286`. [Online]. Available: `http://www.ncbi.nlm.nih.gov/pubmed/24831222`.

[166] J. C. Mcdonald, D. C. Duffy, J. R. Anderson, and D. T. Chiu, “Review - Fabrication of microfluidic systems in poly (dimethylsiloxane)”, *Electrophoresis*, vol. 21, pp. 27–40, 2000, ISSN: 01730835 (ISSN). DOI: `10.1002/(SICI)1522-2683(20000101)21:1<27::AID-ELPS27>3.0.CO;2-C`.

[167] S. K. Sia and G. M. Whitesides, “Microfluidic devices fabricated in poly(dimethylsiloxane) for biological studies”, *Electrophoresis*, vol. 24, no. 21, pp. 3563–3576, 2003, ISSN: 01730835. DOI: `10.1002/elps.200305584`.

[168] T. Fujii, “PDMS-based microfluidic devices for biomedical applications”, *Microelectronic Engineering*, vol. 61-62, pp. 907–914, 2002, ISSN: 01679317. DOI: `10.1016/S0167-9317(02)00494-X`.

[169] M. E. Vlachopoulou, G. Kokkoris, C. Cardinaud, E. Gogolides, and A. Tserepi, “Plasma etching of poly(dimethylsiloxane): Roughness formation, mechanism, control, and application in the fabrication of microfluidic structures”, *Plasma Processes and Polymers*, vol. 10, no. 1, pp. 29–40, 2013, ISSN: 16128850. DOI: `10.1002/ppap.201200008`.

[170] D. Cai and A. Neyer, “Cost-effective and reliable sealing method for PDMS (PolyDiMethylSiloxane)- based microfluidic devices with various substrates”, *Microfluidics and Nanofluidics*, vol. 9, no. 4-5, pp. 855–864, 2010, ISSN: 16134982. DOI: `10.1007/s10404-010-0596-1`.

[171] J. Garra, T. Long, J. Currie, T. Schneider, R. White, and M. Paranjape, “Dry etching of polydimethylsiloxane for microfluidic systems”, *Journal of Vacuum Science & Technology A: Vacuum, Surfaces, and Films*, vol. 20, no. 3, p. 975, 2002, ISSN: 07342101. DOI: `10.1116/1.1460896`.

[172] A. L. Thangawng, R. S. Ruoff, M. a. Swartz, and M. R. Glucksberg, “An ultrathin PDMS membrane as a bio/micro-nano interface: Fabrication and characterization”, *Biomedical Microdevices*, vol. 9, no. 4, pp. 587–595, 2007, ISSN: 13872176. DOI: `10.1007/s10544-007-9070-6`.

[173] A. K. Au, W. Huynh, L. F. Horowitz, and A. Folch, “3D-Printed Microfluidics”, *Angewandte Chemie - International Edition*, vol. 55, no. 12, pp. 3862–3881, 2016, ISSN: 15213773. DOI: `10.1002/anie.201504382`.

[174] D. Qi, D. J. Hoelzle, and a. C. Rowat, "Probing single cells using flow in microfluidic devices", *European Physical Journal-Special Topics*, vol. 204, no. 1, pp. 85–101, 2012, ISSN: 1951-6355. DOI: `10.1140/epjst/e2012-01554-x`. [Online]. Available: `%3CGo%20to%20ISI%3E://WOS:000302814400008$%5Cbackslash$nhttp://www.springerlink.com/content/a2328n4n8v173470/fulltext.pdf`.

[175] D. Qin, Y. Xia, and G. M. Whitesides, "Rapid prototyping of complex structures with feature sizes larger than 20 μm", no. 11, pp. 47–49, 1996.

[176] M. Lake, M. Lake, C. Narciso, K. Cowdrick, T. Storey, S. Zhang, J. Zartman, and D. Hoelzle, "Microfluidic device design, fabrication, and testing protocols", *Protocol Exchange*, no. July, pp. 1–26, 2015, ISSN: 2043-0116. DOI: `10.1038/protex.2015.069`. [Online]. Available: `http://www.nature.com/protocolexchange/protocols/4049`.

[177] B. C. Gross, J. L. Erkal, S. Y. Lockwood, C. Chen, and D. M. Spence, "Evaluation of 3D printing and its potential impact on biotechnology and the chemical sciences", *Analytical Chemistry*, vol. 86, no. 7, pp. 3240–3253, 2014, ISSN: 15206882. DOI: `10.1021/ac403397r`.

[178] J. M. Williams, A. Adewunmi, R. M. Schek, C. L. Flanagan, P. H. Krebsbach, S. E. Feinberg, S. J. Hollister, and S. Das, "Bone tissue engineering using polycaprolactone scaffolds fabricated via selective laser sintering", *Biomaterials*, vol. 26, no. 23, pp. 4817–4827, 2005, ISSN: 01429612. DOI: `10.1016/j.biomaterials.2004.11.057`. [Online]. Available: `http://linkinghub.elsevier.com/retrieve/pii/S0142961204011068`.

[179] M. S. Mannoor, Z. Jiang, T. James, Y. L. Kong, K. a. Malatesta, W. O. Soboyejo, N. Verma, D. H. Gracias, and M. C. McAlpine, "3D printed bionic ears", *Nano Letters*, vol. 13, no. 6, pp. 2634–2639, 2013, ISSN: 15306984. DOI: `10.1021/nl4007744`.

[180] M. K. Gupta, F. Meng, B. N. Johnson, Y. L. Kong, L. Tian, Y.-W. Yeh, N. Masters, S. Singamaneni, and M. C. McAlpine, "3D Printed Programmable Release Capsules", *Nano Letters*, vol. 15, no. 8, pp. 5321–5329, 2015, ISSN: 1530-6984. DOI: `10.1021/acs.nanolett.5b01688`. [Online]. Available: `http://pubs.acs.org/doi/abs/10.1021/acs.nanolett.5b01688`.

[181] S. Ready, F. Endicott, G. L. Whiting, T. N. Ng, E. M. Chow, and J. Lu, "3D Printed Electronics", *2013 International Conference on Digital Printing Technologies*, pp. 9–12, 2013.

[182] K. H. Church, H. Tsang, R. Rodriguez, P. Defembaugh, and R. Rumpf, “Printed circuit structures, the evolution of printed circuit boards”, *IPC APEX EXPO Conference and Exhibition 2013, APEX EXPO 2013*, vol. 2, pp. 1242–1261, 2013. [Online]. Available: `http://www.scopus.com/inward/record.url?eid=2-s2.0-84883568107%7B%5C&%7DpartnerID=tZOtx3y1`.

[183] E. a. Rojas-Nastrucci, T. Weller, V. L. Aida, F. Cai, and J. Papapolymerou, “A study on 3D-printed coplanar waveguide with meshed and finite ground planes”, *Wamicon 2014*, pp. 1–3, 2014. DOI: `10.1109/WAMICON.2014.6857792`. [Online]. Available: `http://www.scopus.com/inward/record.url?eid=2-s2.0-84905964565%7B%5C&%7DpartnerID=tZOtx3y1`.

[184] A. E. Jakus, S. L. Taylor, N. R. Geisendorfer, D. C. Dunand, and R. N. Shah, “Metallic Architectures from 3D-Printed Powder-Based Liquid Inks”, *Advanced Functional Materials*, pp. 6985–6995, 2015, ISSN: 1616301X. DOI: `10.1002/adfm.201503921`.

[185] Hull, *Apparatus for production of three-dimensional objects by stereolithography*, 1986.

[186] T. Wohlers and T. Gornet, “History of additive manufacturing”, *Wohlers Report 2014*, pp. 1–23, 2014.

[187] A. Falco, M. Petrelli, E. Bezzeccheri, A. Abdelhalim, and P. Lugli, “Towards 3D-Printed Organic Electronics: Planarization and Spray-Deposition of functional layers onto 3D-printed objects”, *Organic Electronics*, vol. 39, pp. 340–347, 2016. DOI: `10.1016/j.orgel.2016.10.027`.

[188] M. Binda, D. Natali, A. Iacchetti, and M. Sampietro, “Integration of an Organic Photodetector onto a Plastic Optical Fiber by Means of Spray Coating Technique”, *Advanced Materials*, vol. 25, no. 31, pp. 4335–4339, Jun. 2013, ISSN: 09359648. DOI: `10.1002/adma.201301285`.

[189] L. Hu, D. S. Hecht, and G. Grüner, “Carbon Nanotube Thin Films: Fabrication, Properties, and Applications”, *Chemical Reviews*, vol. 110, no. 10, pp. 5790–5844, Oct. 2010. DOI: `10.1021/cr9002962`. [Online]. Available: `http://dx.doi.org/10.1021/cr9002962%20http://pubs.acs.org/doi/full/10.1021/cr9002962`.

[190] L. Galantucci, F. Lavecchia, and G. Percoco, “Experimental study aiming to enhance the surface finish of fused deposition modeled parts”, *CIRP Annals - Manufacturing Technology*, vol. 58, no. 1, pp. 189–192, 2009, ISSN: 00078506.

DOI: `10.1016/j.cirp.2009.03.071`. [Online]. Available: `http://linkinghub.elsevier.com/retrieve/pii/S0007850609000778`.

[191] A. Boschetto and L. Bottini, “Roughness prediction in coupled operations of fused deposition modeling and barrel finishing”, *Journal of Materials Processing Technology*, vol. 219, pp. 181–192, 2015, ISSN: 09240136. DOI: `10.1016/j.jmatprotec.2014.12.021`. [Online]. Available: `http://www.sciencedirect.com/science/article/pii/S0924013614005172`.

[192] T. E. Daubert and R. P. Danner, *Physical and thermodynamic properties of pure chemicals : data compilation*, Taylor & Francis, Ed. Washington, DC, 1989.

[193] B. Y.-h. Yoon, J.-w. Song, D. Kim, J. Kim, J.-k. Park, and S.-k. Oh, “Transparent Film Heater Using Single-Walled Carbon Nanotubes **”, pp. 4284–4287, 2007, ISSN: 09359648. DOI: `10.1002/adma.200701173`.

[194] D. Kim, L. Zhu, D. J. Jeong, K. Chun, Y. Y. Bang, S. R. Kim, J. H. Kim, and S. K. Oh, “Transparent flexible heater based on hybrid of carbon nanotubes and silver nanowires”, *Carbon*, vol. 63, pp. 530–536, 2013, ISSN: 00086223. DOI: `10.1016/j.carbon.2013.07.030`. [Online]. Available: `http://dx.doi.org/10.1016/j.carbon.2013.07.030`.

[195] C. H. Ahn, J.-W. Choi, G. Beaucage, J. H. Nevin, J.-B. Lee, A. Puntambekar, and J. Y. Lee, “Lab on a Chip for Point-of-Care Clinical Diagnostics”, *Proceedings of the IEEE*, vol. 92, no. 1, pp. 154–173, 2004, ISSN: 0018-9219. DOI: `10.1109/JPROC.2003.820548`.

[196] D. Jung, D. Kim, K. H. Lee, L. J. Overzet, and G. S. Lee, “Transparent film heaters using multi-walled carbon nanotube sheets”, *Sensors and Actuators A: Physical*, vol. 199, pp. 176–180, 2013, ISSN: 09244247. DOI: `10.1016/j.sna.2013.05.024`. [Online]. Available: `http://www.sciencedirect.com/science/article/pii/S0924424713002793`.

[197] S. De, T. M. Higgins, P. E. Lyons, E. M. Doherty, P. N. Nirmalraj, W. J. Blau, J. J. Boland, and J. N. Coleman, “Silver Nanowire Networks as Flexible, Transparent, Conducting Films: Extremely High DC to Optical Conductivity Ratios”, *ACS Nano*, vol. 3, no. 7, pp. 1767–1774, 2009, ISSN: 1936-0851. DOI: `10.1021/nn900348c`. [Online]. Available: `http://pubs.acs.org/doi/abs/10.1021/nn900348c`.

[198] J. Park, A. Lee, Y. Yim, and E. Han, "Electrical and thermal properties of PEDOT:PSS films doped with carbon nanotubes", *Synthetic Metals*, vol. 161, no. 5-6, pp. 523–527, 2011, ISSN: 03796779. DOI: `10.1016/j.synthmet.2011.01.006`. [Online]. Available: `http://www.sciencedirect.com/science/article/pii/S0379677911000129`.

[199] A. Abdelhalim, A. Falco, F. Loghin, P. Lugli, J. F. Salmeron, and A. Rivadeneyra, "Flexible NH3 Sensor Based on Spray Deposition and Inkjet Printing", in *IEEE Sensors 2016*, 2016, (Accepted).

[200] A. Abdellah, S. Member, A. Yaqub, C. Ferrari, B. Fabel, P. Lugli, and G. Scarpa, "Spray Deposition of Highly Uniform CNT Films and Their Application in Gas Sensing", *2011 11th IEEE International Conference on Nanotechnology*, pp. 1118–1123, 2011.

[201] E. Cagatay, A. Falco, A. Abdellah, and P. Lugli, "Carbon Nanotube Based Temperature Sensors Fabricated by Large-Scale Spray Deposition", in *Microelectronics and Electronics (PRIME), 2014 10th Conference on Ph. D. Research in*, 2014, pp. 2–5, ISBN: 9781479949946.

List of Publications

Journal Articles

[1] A. Falco, M. Petrelli, E. Bezzeccheri, A. Abdelhalim, and P. Lugli, “Towards 3D-Printed Organic Electronics: Planarization and Spray-Deposition of functional layers onto 3D-printed objects”, *Organic Electronics*, Vol. 39, pp.340-347, 2016. DOI: 10.1016/j.orgel.2016.10.027

[2] A. Falco, B. Matarese, P. Feyen, F. Benfenati, J. C. de Mello, and P. Lugli “Investigation of the stability and biocompatibility of commonly used electrode materials in organic neurooptoelectronics”, *IEEE Transactions on Nanotechnology*, Vol. 15, no. 5, pp. 746-753, 2016. DOI: 10.1109/TNANO.2016.2536946.

[3] A. Abdellah, A. Falco, U. Schwarzenberger, G. Scarpa, and P. Lugli, “Transfer Printed P3HT/PCBM Photoactive Layers: From Material Intermixing to Device Characteristics”, *ACS Applied Materials & Interfaces*, Vol.8, no. 4, pp. 2644-2651, 2016. DOI: 10.1021/acsami.5b10539.

[4] A. Falco, A. Zaidi, P. Lugli, and A. Abdellah, “Spray deposition of Polyethylenimine thin films for the fabrication of fully-sprayed organic photodiodes”, *Organic Electronics*, vol. 23, pp. 186-192, 2015. DOI: 10.1016/j.orgel.2015.05.003.

[5] M. Schmidt, A. Falco, M. Loch, P. Lugli, and G. Scarpa, “Spray coated indium-tin-oxide-free organic photodiodes with PEDOT:PSS anodes”, *AIP Advances*, vol. 4, no. 10, pp. 107132, 2014. DOI: 10.1063/1.4899044..

[6] A. Falco, L. Cinà, G. Scarpa, P. Lugli, and A. Abdellah, “Fully-Sprayed and Flexible Organic Photodiodes with Transparent Carbon Nanotube Electrodes.”,*ACS Applied Materials & Interfaces*, Vol. 6, no. 13, pp. 10593-10601, 2014. DOI: 10.1021/am5022123.

Conference Proceedings

[1] A. Falco, J. F. Salmeron, F. Loghin, A. Abdelhalim, P. Lugli, and A. Rivadeneyra, "Optimization of Process Parameters for Inkjet Printing of CNT Random Networks on Flexible Substrates", *Nanotechnology, 2016 IEEE Conference on Nanoelectronics*, 2016. (Accepted)

[2] A. Abdelhalim, A. Falco, F. Loghin, P. Lugli, J. F. Salmeron, and A. Rivadeneyra, "Flexible NH3 Sensor Based on Spray Deposition and Inkjet Printing", *Sensors, 2016 IEEE Conference on Sensors*, 2016. (Accepted)

[3] A. Falco, E. Bezzeccheri, R. Nagel, R. Liguori, A. Rubino, and P. Lugli, "Simulation and Fabrication of Polarized Organic Photodiodes", *Sensors, 2016 IEEE Conference on Sensors*, 2016. (Accepted)

[4] E. Bezzeccheri, S. Colasanti, A. Falco, R. Liguori, and P. Lugli "Comparative modeling of vertical and planar organic phototransistors with 2D drift-diffusion simulations", *VIII INTERNATIONAL CONFERENCE ON TIMES OF POLYMERS AND COMPOSITES*, 2016. DOI: 10.1063/1.4949659.

[5] P. Lugli, A. Abdellah, A. Abdelhalim, A. Albrecht, M. Becherer, E. Cagatay, A. Falco, F. Loghin, S. El-molla, J. F. Salmeron, and A. Rivadeneyra "Fabrication , characterization and modeling of flexible electronic components based on CNT networks", *2016 IEEE International Symposium on Circuits and Systems (ISCAS)*, 2016. DOI: 10.1109/ISCAS.2016.7527502.

[6] A. Falco, P. Lugli, B. Matarese, J. C. D. Mello, P. Feyen, and F. Benfenati, "Investigation of the stability and biocompatibility of commonly used electrode materials in organic neuro- optoelectronics", *Nanotechnology, 2015 IEEE Conference on Nanoelectronics*, 2015. DOI: 10.1109/NANO.2015.7388938.

[7] V. Robbiano, A. Abdellah, L. Santarelli, A. Falco, S. El-molla, L. V. Titova, D. N. Purschke, F. A. Hegmann, F. Cacialli, and P. Lugli, "Analysis of Sprayed Carbon Nanotube Films on Rigid and Flexible Substrates", *Nanotechnology, 2014 IEEE Conference on Nanoelectronics*, 2014. DOI: 10.1109/NANO.2014.6968021.

[8] E. Cagatay, A. Falco, A. Abdellah, and P. Lugli, "Carbon Nanotube Based Temperature Sensors Fabricated by Large-Scale Spray Deposition", *Microelectronics and Electronics (PRIME), 2014 10th Conference on Ph. D. Research*, 2014. DOI: 10.1109/PRIME.2014.687273.

Submitted Works

[1] A. Falco, A. Rivadeneyra, P. Lugli, and J. F. Salmeron, “Fully Printed single-chip RFID tag with light detection capabilities”, *IEEE Sensors Journal*, Submitted in August 2016.

[2] F. Loghin, S. Colasanti, A. Weise, A. Falco, A. Abdelhalim, P. Lugli, and A. Abdellah “Scalable spray deposition process for highly uniform and reproducible CNT-TFTs”, *IOP Flexible and Printed Electronics*, Submitted in June 2016.

Acknowledgment

Thanking everyone who ever contributed to make this thesis possible, doing it properly and doing it in one page, is an inhuman challenge. I will have to try, though, since after such a long thesis, I should prove you I am able to synthesize, as well.

I will start by thanking Prof. Paolo Lugli. It is customary to write "because of the great opportunity he gave me", but that is not the only reason I want to thank him for. I would like to thank him he has always been supportive and patient; and, probably even more importantly, he has been a never-stopping source of inspiration and motivation.
I would like to thank Dr. Giuseppe Scarpa as well, as without his contribution, probably this voyage would have never started. I wish our ways had not parted so early, but I am glad I had the chance to work with you. I would also love to thank everyone in the OLIMPIA Network, where I met extraordinary colleagues and beautiful people. Furthermore, I need to thank Ms. Lucia Weik (the most willing and helping person in the whole world), Rosi Mittermeier (our guardian angel), Dr. Bernhard Fabel and Dr. Markus Becherer for doing their best to run the lab.
Special thanks must be sent to Prof. Alfredo Rubino, since although the distance and our unpredictable schedules, he has always been there: science, sport, music, literature; the topic was never important, our conversations were. To the late Prof. Salvatore Bellone, who taught me how passion and dedication are the keys to achieve your goals, I send my many thanks. Prof, if I will ever be half the man you were, it will be also because of you.

In this short and non exhaustive list, I cannot forget my friend and mentor Alaa, my adventures buddies Flo and Azeem, my misadventure buddy Simone, my italian-gang-member Emanuele, "los Tontos" Almu&Pepe, the grill-master Emmanuel, my loved and hated friends Bruno and Paul. If I missed anyone, please, do not be offended, finding adjectives and periphrases for each of you is rather troublesome.

How could I forget about my students? Asheque, Mattia and Michael: I will write it here, you will not hear me saying that again, but I am sorry I made you work so

much. I still feel a special connection to you, and I hope it will not dwindle. Also, I would like to thank my flat-mates, especially the ones who have been with me for the whole trip, making me feel at home. Thanks a lot, Janine, Karo and Marco.
Furthermore, I am thankful to my old friends, those who were living hundreds of km away, but kept on seeking me, helping me, supporting me. Peppe, Dario, Vincenzo, Lello, Marianna, Margherita, Apple-Gigi and everyone else (you are a lot... you know that!), it would have been hard without you.
I also say thank you to all the people I have found, the ones I have lost, the ones I have found again. I am thankful to the thief who stole my wallet in Singapore, since he reminded me to be always vigilant. Thanks to my hair (unfortunately almost gone), to coffee, orange juice, beer, whiskey and water... especially for the day after. Special thanks to adhesive tape: without you, I would have been lost.

Then it comes the turn of that special person, Angela, who has been by travel companion in these beautiful and dreadful years. I will not thank you for what you did for me, I do not want to do it, and, I hope, I will never have to.
Dulcis in fundo, I am very thankful to those who have always been there, and who will always be there for me. Thanks mum, thanks dad, thanks for giving me wings and space to fly by myself, while being there all the time, ready to grab me when I was falling. Thanks, Luigi, because you are and will always be my reference. And also because time passes by, we grow up, our bodies get old, but we will keep on being the usual idiots.
And thank you, whoever you are, for having read it all. As you could have imagined from the very beginning, one page could have never been enough.

Ringraziamenti

Ringraziare le persone che hanno reso possibile questa tesi di dottorato, farlo senza fretta e farlo in una sola pagina, è un'impresa a dir poco improba. Però devo provarci: d'altro canto, dopo una tesi così lunga, dovrò pur provare a fare un esercizio di sintesi, no?

Ringrazio, innanzitutto, il Professor Paolo Lugli. La prassi prevede che io debba scrivere "per la magnifica opportunità che mi ha dato", ma non è solo questo. Lo ringrazio per il continuo supporto e per l'enorme pazienza dimostrata in più di un'occasione. Ma, soprattutto, lo ringrazio per essere una costante fonte di ispirazione e motivazione.
Un grosso ringraziamento va anche al Dottor Giuseppe Scarpa, poiché, anche se il nostro percorso assieme si è fermato prima del tempo, questo lavoro non sarebbe stato possibile senza il suo apporto iniziale. Ringrazio, in questo contesto, anche tutto il Network OLIMPIA, nel quale ho trovato straordinari colleghi e bellissime persone. Non posso non ringraziare, poi, Lucia Weik (la persona più disponibile del mondo), Rosi Mittermeier (il nostro angelo custode), il Dottor Bernhard Fabel ed il Dottor Markus Becherer per aver fatto del loro meglio per amministrare il laboratorio.
Ringrazio il Professor Alfredo Rubino, perché nonostante la distanza è sempre stato lì, che si volesse parlare di scienza o di sport, di musica o di letteratura. Ringrazio il Professor Salvatore Bellone, il quale mi ha insegnato che la passione e l'impegno sono i fattori principali per raggiungere i propri obiettivi. Prof, se mai dovessi diventare metà della persona che lei fu, sarà stato anche merito suo.

Ringrazio il mio amico e mentore Alaa, i miei compagni di avventura Florin ad Azeem, il mio compagno di sventure Simone, il mio compagno di merende Emanuele, “los Tontos” Almu&Pepe, il bracista Emmanuel, i miei amici-nemici Bruno e Paul. Ringraziavi tutti ad uno ad uno sarebbe difficile, quindi, vi prego, non offendetevi se non siete in questa lista.
Come fare a non ringraziare i miei studenti? Asheque, Mattia e Michael: lo dico ora, e non ve lo ripeterò mai più, mi dispiace avervi fatto lavorare tanto. Ho con voi una connessione speciale che spero non scompaia mai. Ringrazio, poi, i miei coinquilini,

soprattutto quelli che sono stati con me fin dall'inizio di questo viaggio, per avermi fatto sentire a casa. Grazie Janine, Karo e Marco.

Vorrei poi ringraziare i miei amici di sempre, quelli che nonostante fossero a centinaia di km, mi hanno sempre cercato, aiutato, supportato. Peppe, Dario, Vincenzo, Lello, Marianna, Margherita, Gigi-Apple e tutti gli altri (siete tanti... e lo sapete!), sarebbe stato difficile senza di voi.
Grazie, poi, a tutte le persone trovate, a quelle perdute ed a quelle ritrovate. Grazie anche a te che mi hai rubato il portafogli a Singapore, per avermi aiutato a non dimenticare che bisogna esser sempre attenti, in ogni contesto. Grazie ai miei capelli (ormai andati), al caffè, al succo d'arancia, alla birra, al whisky e all'acqua; soprattutto per il giorno dopo. Un sentito grazie al nastro adesivo: senza di te sarei stato perduto.

C'è poi Angela, la persona speciale che è stata la mia compagna di viaggio per questi anni belli e difficili. Non ti ringrazio per tutto ciò che mi hai dato, non voglio farlo, e spero di non doverlo fare mai.
Dulcis in fundo, ringrazio coloro che ci sono sempre stati e che ci saranno sempre. Grazie mamma, grazie papà, per avermi dato le ali e lasciato spazio per volare da solo, restando però sempre lì, pronti ad afferrarmi nelle non rare cadute. Grazie Luigi perché sei e resterai il mio riferimento. E perché il tempo passa, i nostri corpi invecchiano, ma noi resteremo sempre i soliti idioti.

E grazie a te, chiunque tu sia, per aver letto. Come potevi immaginare fin dall'inizio, una sola pagina non sarebbe mai bastata.